MODELING DYNAMIC RUPTURES WITH HIGH RESOLUTION FAULT ZONE PHYSICS

BY

XIAO MA

DISSERTATION

Submitted in partial fulfillment of the requirements
for the degree of Doctor of Philosophy in Civil Engineering
in the Graduate College of the
University of Illinois at Urbana-Champaign, 2019

Urbana, Illinois

Doctoral Committee:

Assistant Professor Ahmed E. Elbanna, Chair and Director of Research
Associate Professor Rosa M. Espinosa Marzal
Assistant Professor David S. Kammer, ETH Zurich
Professor C. Armando Duarte
Professor Philippe H. Geubelle

Abstract

Earthquakes are among the costliest natural hazards on earth. The dynamical instabilities responsible for the onset and propagation of these events are linked to fundamental physics, friction, fracture, heating, and compaction of fluid filled granular materials and rocks in the subsurface subjected to extreme geophysical conditions. Due to the wide range of spatial and temporal scales characteristic of the earthquake source processes, computational modeling of these processes continue to be a major challenge.

In this research, we address this challenge by developing new models that shed novel insights into the different faces of complexity of the earthquake source. We first introduce the investigation of a complex fault zone structure and its effect on earthquake dynamic rupture mode transition. We show, for the first time, that the existence of soft inclusions off the fault plane may promote supershear transition under low prestress conditions. Secondly, we look further into the material behavior within the fault zone and develop a non-equilibrium statistical thermodynamics-based viscoplastic framework for modeling granular systems within the Shear Transformation Zone theory. Thirdly, we present a new hybrid computational algorithm for modeling earthquake ruptures in complex fault zone structures. This method has the potential capability to bridge the spatial and temporal scales in earthquake models by leveraging advantages of both domain based and boundary based numerical schemes. Finally, we demonstrate the powerful capability of the hybrid approach by applying the method to solve a computationally challenging problem in earthquake dynamic rupture modeling by explicitly representing small scale secondary fault branches. We then discuss the potential future research direction along the lines of previous studies such as applying the developed numerical frameworks for solving complicated fault zone problems that couldn't be solved by traditional numerical schemes; extending the hybrid scheme to simulate long term earthquake cycles incorporating geometric complexity and material nonlinearity. This research work will expand our understanding of earthquake rupture and will help us gain new insights into the complexity of earthquake mechanisms.

To my parents.

Ke Xiao and Wenli Ma

Acknowledgments

First of all, I would like to express my sincere gratitude to my advisor Prof. Ahmed Elbanna for the continuous guidance and support of my doctoral study and research, for his patience, motivation, enthusiasm and immense knowledge.

I would like to thank the Department of Civil and Environmental Engineering at University of Illinois at Urbana-Campaign for providing the high quality of education courses and academic resources. I am also grateful to all colleagues in MSC lab for offering suggestions and help to my research. I am also grateful for the my doctoral committee members for their time and guidance.

Finally, I would like to thank my family: my mother Ke Xiao and my mother Wenli Ma for unconditionally support though all my life, this would never be possible without your love.

To my parents, I dedicate this work to.

Contents

Chapter 1

Introduction

Earthquakes are one of the biggest natural hazards to mankind costing thousands of lives and billions of dollars each year. Its effect comes in various form such as: shaking and ground rupture, landslides, fires, soil liquefaction, tsunami, floods, as well as significant human impacts both emotionally and financially. Understanding earthquake initiation, propagation, and arrest mechanisms as well as identifying any precursors that could be helpful for forecasting are among the highly sought-after problems in the science community. Normally, one may resort to field data in order to find clues for an answer. Unfortunately, the data is scarce when it comes to magnitude 7 earthquakes and larger as strong ground motion seismometers have not been around for more than 50 years. During that period, we have recorded a few $M9+$, several tens of $8 < M < 9$, and a few hundred $7 < M < 8$. Thus, simulations are needed to fill in this gap and provide scenarios for what to expect in a large earthquake. Nonetheless, high fidelity and physics-based simulation of earthquake processes is a computationally challenging task. Earthquakes are highly nonlinear and multiscale phenomena. This multiscale feature exists both in space and time. Spatially, a moderate-size earthquake typically propagates over tens of kilometers. However, the physical processes governing the rupture propagation operates within a narrow region at the rupture tip called the process zone, which may not exceed a few millimeters in size [1]. Temporally, the time required for stress buildup and the attainment of the right condition for the initiation of friction instability during the interseismic period may be tens to hundreds of years. However, an earthquake only lasts for few to tens of seconds. This multiscale feature is a fundamental challenge in earthquake modeling

With the increasing power of computers, computational earthquake dynamics is emerging as a key component in understating the earthquake rupture. A variety of numerical methods have been proposed in the past decades for simulating the earthquake dynamic rupture, such as finite difference (FD) [2, 3, 4, 5, 6, 7, 8], finite elements (FE) [9, 10, 11], boundary integral (BI) [12, 13, 14, 15, 16], spectral element (SE) [17, 18], finite volume (FV) [19] discontinues galerkin [20, 21]. The computa-

tional framework may be divided into two categories: domain-based methods and boundary integral methods. Domain-based methods are quite flexible in handling material nonlinearities and small-scale heterogeneities as well as complexities of fault geometry. The major limitation of these methods stems from the need to discretize the entire domain demanding a large computational cost. On the other hand, boundary integral techniques, which confine the calculations to the fault plane and reduce the dimensions of the problem by one. The main limitation of this method, however, is that it is applicable only to linear-elastic bulks. One might envision combining the domain based method and the boundary integral method together taking both advantages of both [22].

In my PhD study, we are initially motivated by the complex fault geometry and material nonlinearity within the fault zone. In Chapter 2, inspired by that velocity structure in the vicinity of pre-existing fault networks is heterogeneous, we design a fault zone model with off-fault low velocity inclusions and conduct a set of dynamic rupture simulations. We investigate the supershear rupture transition in homogeneous medium and medium with presence of off-fault low velocity inclusion. We show that the existence of the low velocity off-fault inclusion promotes the supershear transition, and decrease the supershear transition length. We establish the robustness of these conclusions by conducting a parametric study about the effect of the low velocity inclusion thickness, off-fault distance, layer extension, position, the fault strength level and material contrasts.

In the inclusion study (Chapter 2), we adopted a slip-weakening friction law for modeling the shear stress-slip law on the fault surface. Admittedly, this friction model is a simple idealization of the frictional interface. This motivates us to investigate further extensions that account for the complex rheology of the fault zone material, specifically fault gouge. Gouge is a highly-granulated material which is formed in many fault zones due to the fragmentation of the intact country rocks as the fault develops under progressive shearing. Studies have shown extreme localization of slip within gouges layers that in some cases may be less than a few millimeters thick. A more realistic and physics-based material model would give more insight of material behavior within the fault gouge. In Chapter 3, we develop a thermodynamically consistent framework for amorphous plasticity in 2D finitely deformed granular medium using the concept of compactivity. First we derive a continuum formulation for the shear transformation zone (STZ) theory using the first and second laws of thermodynamics. Then we consider a layer of granular materials sheared between two parallel planes and subject it to a constant pressure at the top and bottom. Then we investigate the generic shear band localization using the developed framework. We show a good agreement between the developed complex pattern of shear

bands and experimental observations. The model provides us with a predictive tool to investigate factors affecting the shear localization such as the dilatancy effect, the inertia effect, confining pressure, initial compactivity, the layer thickness. We also identify a brittle to ductile transition that may vary as a function of dilatancy, pressure and initial disorder.

With the capability of modeling the fault gouge using the developed physic-based continuum model, there exists another changeling problem in earthquake simulations, which is the resolution of the multiscale nature of the earthquake source, which exists in both space and time. Spatially, an earthquake may involve several kilometers of fault rupture, whereas the fault gouge where most of the displacement is accommodated, may be on the order of few millimeters. Temporally, the time it takes for the stresses to accumulate and initiate an instability is several orders of magnitude larger than the sudden release of energy during an earthquake episode. Therefore, a numerical model needs to be developed to resolve this wide range of spatial and temporal scales. In Chapter 4, we have developed a hybrid numerical scheme by integrating the Finite Element method (FEM) and Spectral boundary integral method (SBIE). We first introduce the coupling of the FEM and SBIE method through consistent exchange of boundary information. Then we validate the accuracy of the hybrid method using the Southern California Earthquake Center (SCEC) Dynamic rupture verification exercises. We further show the capability and accuracy of the hybrid method solving problems that are too computationally expensive for the domain-based FEM method, and also not amenable for solution by the SBI method alone.

In Chapter 5, we demonstrate the powerful capability of the hybrid approach by applying the hybrid method to solve a computationally challenging problem by investigating the dynamics of rupture propagation on a fault plane with multiple short branches mimicking the fish bone architecture idealized in [23, 24]. By explicit representation of these small scale branches, we have found out that the secondary faults increase the overall energy dissipation leading to a reduction in the slip, peak slip rate, and rupture propagation on the main fault. Moreover, the activation of the secondary faults may lead to backward propagating ripples in the slip rate that increases slip far from the rupture tip. Rupture activation, propagation, and arrest on the secondary branches lead to a strongly heterogeneous normal and shear stress field on the main fault. We also observed promotion of high-frequency generation and high-frequency fluctuations on the computed seismograms due to the interaction of the seismic waves generated by the secondary branches. We further look into the effect of characteristics of the secondary faults on the dynamic rupture by conducting a set of parametric studies.

Finally, potential directions of future work are proposed in Chapter 6. One of the most promising future direction of study is extending the hybrid scheme to be able to conduct long term earthquake sequence incorporating geometry complexity and material nonlinearity. Meanwhile, another important potential future direction is to investigate fault branching and damage evolution. In this chapter, we will show some ongoing work and provide future study directions.

Chapter 2

Effect of off-fault low-velocity elastic inclusions on supershear rupture dynamics

The content of this chapter has been published on Geophysical Journal International [25].

Ma, X. & Elbanna, A. Effect of off-fault low-velocity elastic inclusions on supershear rupture dynamics. Geophysical Journal International, 203(1), 664-677 (2015).

2.1 Introduction

The velocity structure in the vicinity of pre-existing fault networks is, in general, heterogeneous [26]. In particular, faults zones are usually composed of rocks and granular materials that have experienced different cycles of damage and healing. This leads to time dependent variations in the magnitude of elastic moduli and the wave speeds [27]. The existence of a heterogeneous material structure is expected to affect rupture propagation on the embedded fault segments due to wave reflection, transmission and diffraction from the boundaries of the different layers and inclusions.

Of the different complexities that may arise in the velocity structure near pre-existing faults, the properties of low-velocity zones (LVZs) have been extensively studied. Examples include LVZs around San Andreas [28, 29, 30], San Jacinto [31, 32], Landers [33, 34, 35], Hector Mine [36], Calico [37, 38], Nojima [39], and North Anatolian [40] fault zones.

The implications of the existence of a LVZ adjacent to the fault surface, within an otherwise homogeneous medium, have been explored using spontaneous dynamic rupture models [41, 42, 43, 44, 45]. The velocity reduction within the LVZ, relative to the country rock, may vary in the range of 20%-60%. It was found that the trapped waves in the low velocity zone alter the shear stress on the fault plane and affect both the dynamic rupture mode [44] and rupture characteristics including supershear propagation. [42, 44, 45]. The enhanced supershear transition observed in simulations with LVZs [45] suggests that more heterogeneous velocity structure must be considered when investigating rupture speed.

Supershear rupture propagation has been inferred from seismic observations for natural faults. in several large strike-slip earthquake, including the 1979 Imperial Valley earthquake [46, 47], the 1999 Kocaeli (Izmit) earthquake [48, 49], the 1999 Duzce earthquake [46, 49, 50], the 2001 Kokoxili (Kunlun) earthquake [51, 52, 53, 54], and the 2002 Denali earthquake [55, 56].

The transition from rupture velocity less than Rayleigh velocity to rupture velocity greater than shear wave velocity has been studied using dynamic rupture simulations [57, 58, 59, 60, 61, 62, 43, 63, 64, 65, 66, 67, 68, 69, 70, 71, 72, 73, 74, 75, 45, 76]. The primary mechanism for the supershear transition is known as Burridge-Andrews mechanism [57, 58] in which a daughter crack is nucleated at the S wave shear stress peak ahead of the propagating Mode II rupture.

In order for the Burridge-Andrews mechanism to take place on a homogeneous fault in 2-D models, the prestress must be high enough. The strength parameter S [58, 59] has to be smaller than $S_{crit} = 1.77$. Previous work has shown that heterogeneities on the fault surface, including variations in the prestress or fracture energy, may enable supershear propagation at lower prestress values than what are theoretically predicted under homogeneous conditions. The effect of off-fault heterogeneities in the form of off-fault plasticity and damage has also been recently investigated [45]. The influence of off-fault material heterogeneities, as may be represented by inclusions or layered structure, is the focus of this study.

Material gradient and contrasts may not be confined to the vicinity of fault surfaces. Velocity anomalies in the form of lenses with lower or higher wave speeds than the surrounding medium may exist at some distance from the fault surface. In this case, additional interfaces, introduced by the boundaries of the domain with the different rigidity, produce multiple reflections in the wave field as well as diffraction and refraction effects. These modulations may influence the rupture process and increase the complexity of the dynamic response.

In this study we model dynamic rupture propagation on a slip weakening fault in an elastic domain with an embedded inclusion of a lower rigidity. This softer inclusion may not be directly adjacent to the fault surface and it may have a limited extension relative to the fault length. Section 2 describes the model setup and parameters selection. In Section 3 we show the simulation results regarding the influence of the embedded soft inclusion on the supershear transition as well as rupture propagation characteristics. We examine the robustness of our findings with respect to variations in the soft inclusion thickness,

the off-fault distance, material contrast degree and the stress level effect. In Section 4, we discuss the implications of our results in the context of other observational and computational models involving LVZs and supershear ruptures. We summarize our conclusions in Section 5.

2.2 Model Setup

We consider a planar fault in a linear elastic isotropic medium under inplane strain conditions. The medium has a shear modulus μ_1 everywhere except for the inclusion that possesses a smaller shear modulus μ_2 . The inclusion geometry is chosen to be rectangular with a width H_2, a length H_3 , and is located at a distance H_1 from the fault. The medium geometry is symmetric about the fault plane. Absorbing boundary conditions are applied at the four boundaries of the domain to mimic an infinite extension in all direction.

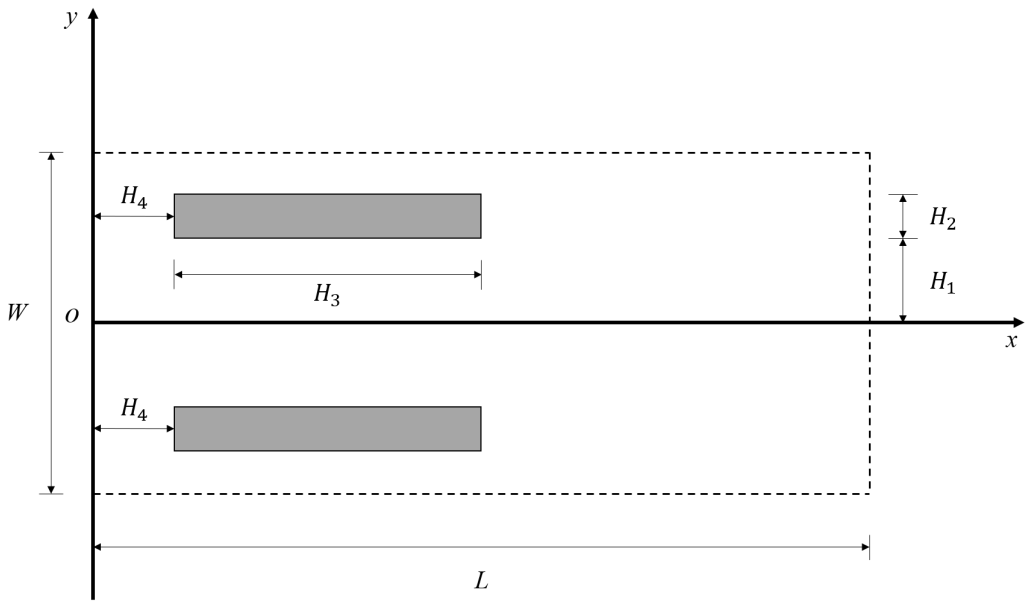

Figure 2.1: The model geometry. The simulated domain has an aspect ratio of L/W. A slip weakening fault of length L bisects the domain and acts as a horizontal symmetry line. Light gray layers represent the location of the soft inclusions. H_1 defines the distance between the fault and the material boundary. H_2 defines the thickness of the soft layer. H_3 defines the length of the soft layer.H_4 defines the off-edge distance of the soft layer inclusion.In most cases investigated here we set $H_4 = 0$. Absorbing boundary conditions are used for all edges to simulate an infinite extension in all direction.

The fault friction is governed by linear slip-weakening law [Ida, 1972; Palmer and Rice, 1973], where

the frictional shear strength Γ decreases linearly as a function of slip δ from its static value τ_s to the dynamic value τ_d over a characteristic slip d_c (Eqn. 2.1). We keep the friction law parameters the same in all our simulations. We choose the static friction coefficient to be 0.6, the dynamic friction coefficients to be 0.5 and the characterize slip weakening distance to be 0.2m

$$\Gamma(\delta) = \begin{cases} \tau_d + (\tau_s - \tau_d)/(1 - \delta/d_c), \delta \leq d_c \\ \tau_d, \delta < d_c \end{cases} \tag{2.1}$$

The static strength τ_s and the dynamic strength τ_d are the products of the effective normal stress by the corresponding static and dynamic friction coefficients, respectively. We discuss the implications of the choice of this particular friction law compared to other formulations, such as rate and state friction, in section 4.

We solve the dynamic rupture problem under 2-D plane strain conditions using the finite element program Pylith [77]. A uniform mesh with 25m grid size has been found to be adequate for resolving the process zone within the range of parameter values explored in this study. We conduct a mesh convergence study with 12.5m and 6.25m element sizes. The results are not affected by the mesh refinement. Table 2.1 summarizes the different parameter values. The fundamental length scale in this problem is given by Eqn. 2.2.

$$L_{nuc} = \frac{\mu_1 d_c}{(\tau_s - \tau_d)} \tag{2.2}$$

where μ_1 is the shear modulus of the homogeneous domain, d_c is the slip weakening distance, τ_s and τ_d are the static and dynamic shear strength values, respectively. This length scale L_{nuc} is proportional to the universal nucleation length predicted for linear slip-weakening friction [78] in a homogeneous medium with a shear modulus μ_1 .

To start the dynamic rupture, we overstress the fault beyond its static frictional strength in a limited region extending for 1.5 km to ensure the immediate dynamic propagation. In previous studies, it was pointed out that the nucleation procedure may affect the subsequent dynamic rupture evolution [63, 66]. We discuss the implications of the abrupt nucleation adopted here as compared to other nucleation procedures including quasi-static nucleation in section 4.

2.3 Results

In this section we first examine some observations related to supershear propagation in a homogenous medium. Then, we investigate the influence of the existence of an off-fault low velocity lens on the

Table 2.1: Model Discretization and Constitutive Parameters

Medium and Discretization Parameters	**Value**
Shear Modulus of the background domain μ	30 GPa
S wave velocity(background),c_s	3.464 $km \cdot s^{-1}$
P wave velocity(background),c_p	6.0 $km \cdot s^{-1}$
Mass density for all layers,ρ	2670 $kg \cdot m^{-3}$
Fault length,L	100 km
Domain width,W	30 km
Fault	$\{x, y \vert y = 0, 0 < x < 100km\}$
Overstress region on the fault	$\{x, y \vert y = 0, 0 < x < 1.5km\}$
Spatial grid space $\Delta x = \Delta y$	25 m
Wave velocity contrast	20-60%
Fault Constitutive Parameters	**Value**
Magnitude of the effective normal stress,σ_n^{eff}	50.0 MPa
Overstressed region initial shear stress	31.0 MPa
Static friction coefficient,μ_s	0.6
Dynamic friction coefficient,μ_d	0.5
Static Strength,τ_s	30.0 MPa
Dynamic Strength,τ_d	25.0 MPa
Strength Parameter,S	Varies
Characteristic slip-weakening distance,d_c	0.2 m

rupture mode and transition to supershear.

2.4 Supershear rupture propagation in a homogeneous medium

Dunham [64] identified conditions under which supershear transition may occur on a slip weakening fault through the Burridge-Andrews mechanism. Using the strength parameter $S = (\tau_s - \tau_o)/(\tau_o - \tau_d)$ which defines the degree of stressing of the fault relative to its strength limits, Dunham [64] showed that for 2D elasticity, S has to be less than 1.77 in order for the supershear transition to occur under homogeneous conditions. The transition length to supershear increases as the strength parameter value increases and becomes infinite when $S = 1.77$. We verified these findings in our numerical simulations. However, due to the abrupt nucleation procedure adopted here, the transition length is generally smaller than the values predicted by Dunham [64].

Moreover, due to the lack of a healing mechanism in the slip weakening law formulation, only crack like ruptures may propagate [79]. If strong heterogeneities in the prestress or material properties exist, pulse like ruptures may develop due to the arrest waves sent from these strong heterogeneities [60]. Furthermore, if a pulse like rupture is nucleated in a 2D model using rate dependent friction, it

may continue to propagate through regions governed by rate-independent slip weakening friction [80]. However, in general, self-healing pulse like ruptures are not compatible with slip weakening friction.

We have found that supershear pulses may propagate on uniformly stressed 2D slip weakening faults embedded in a homogeneous medium. These conditions preclude the influence of heterogeneities in the bulk, prestress, or friction law. Figure 2.2 shows the space-time evolution of slip rate distribution on the fault for a case with $S = 1$. Initially the rupture propagates in the crack like mode. Through the Burridge-Andrews mechanism, a daughter crack is nucleated ahead of the main rupture tip [See the insert]. This daughter crack propagates in both directions and eventually its rear tip joins the main rupture. However, shortly after this coalescence, the slip rate behind the leading front arrests and a supershear pulse is detached. This pulse propagates intact for the remainder of the simulation time.

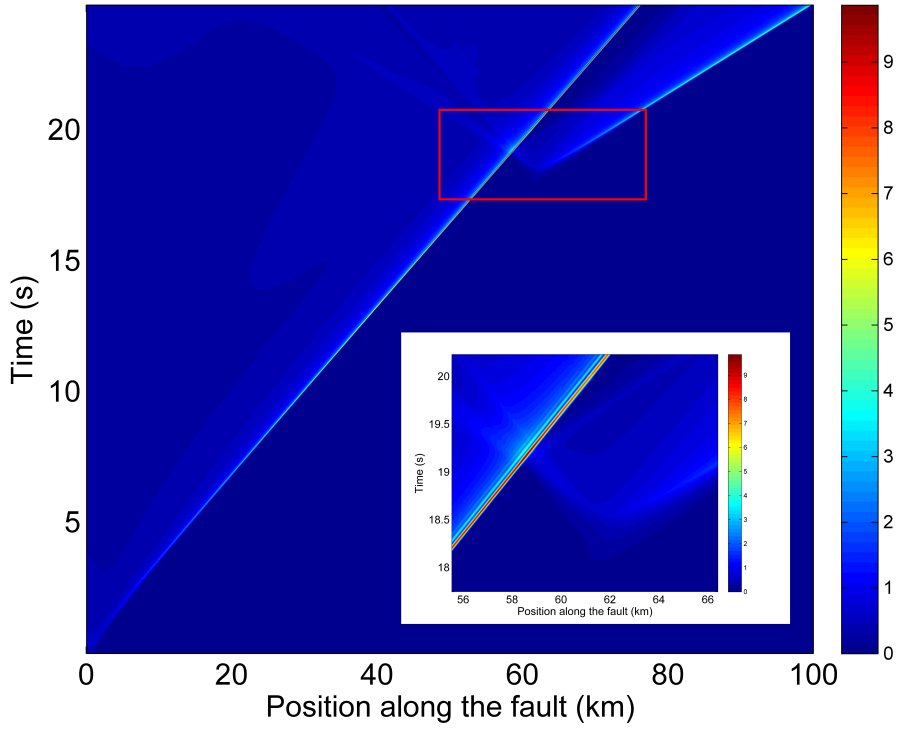

Figure 2.2: Space-time contour of slip rate for homogeneous medium.The nucleation of the daughter crack occurs when the main rupture tip is located at approximately 55km. Once nucleated, the daughter crack propagates into two directions, and its rear tip joints the main rupture front. A detached Supershear rupture is formed shortly after the coalescence.

In Figure 2.3 we plot the slip rate and shear stress distribution on the fault plane shortly after the supershear pulse detachment. The main rupture continues to propagate in a crack like mode. However, the fault unloads in the vicinity of the trailing edge of the supershear pulse and the shear stress drops below the level of dynamic shear strength (25 MPa). Within the actively slipping regions this does not happen and the shear stress is bounded from below by the minimum strength level specified by the slip weakening law.

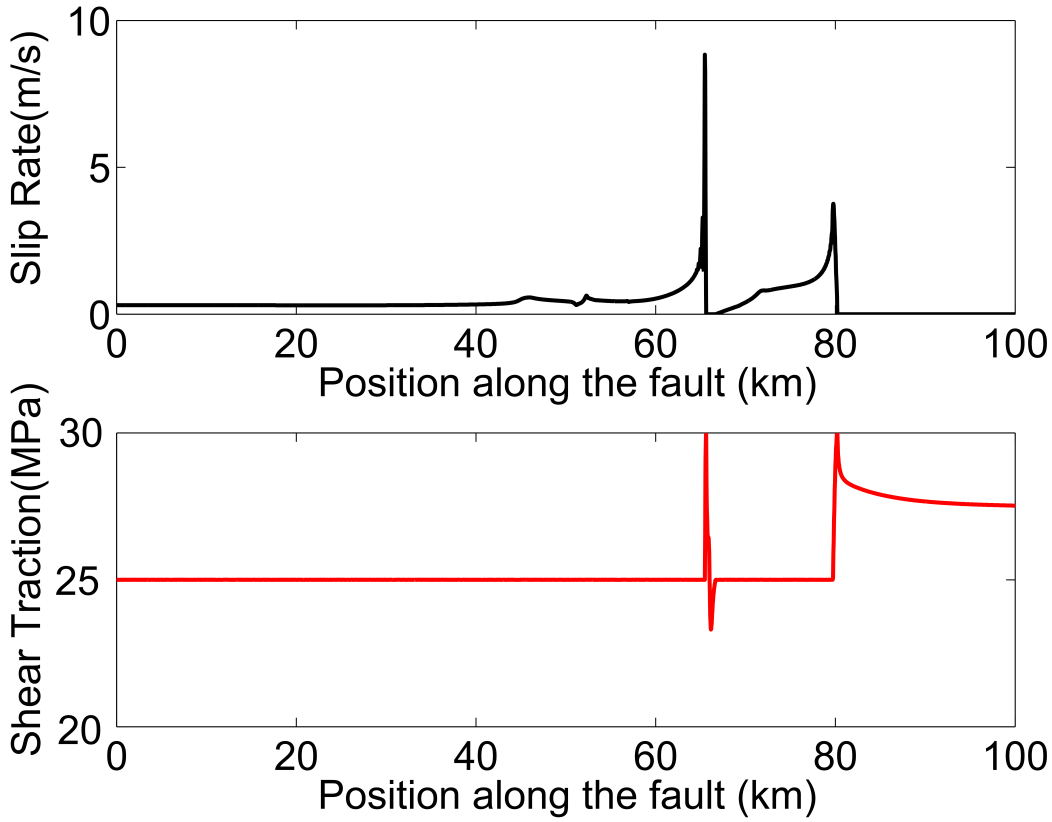

Figure 2.3: Snapshots of slip rate and shear traction on the fault surface after the detachment of the Supershear pulse.The first rupture front represents the Supershear rupture front. Due to the slip rate arrest around 65 to 68 km, the shear traction drops below 25MPa (The prescribed dynamic frictional stress).

In the absence of heterogeneities, why would a supershear pulse develop? To answer this question we computed the rupture tip driving force [Appendix A]. The rate of change of the driving force is given by:

$$\frac{dF}{dt} = \frac{1}{l}\int_0^l (\tau_o - \tau)\dot{u}dx \tag{2.3}$$

where l is the length of actively slipping region, τ_o is the prestress level,τ is the current value of shear stress, $\dot{u}$ is the slip rate and the integration is taken over the fault surface. The evolution of the rate of change of the driving force is shown in Figure 2.4.

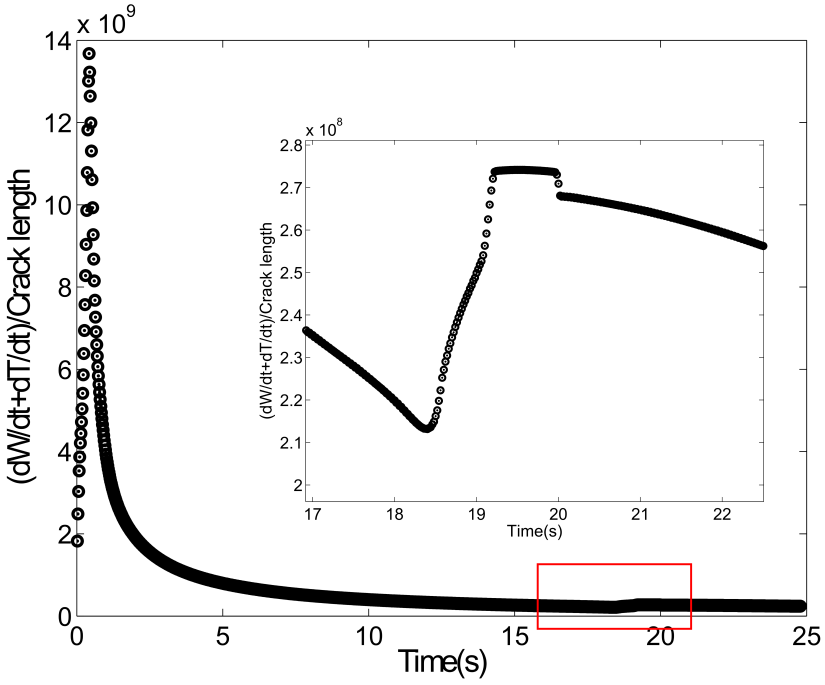

Figure 2.4: Evolution of driving force on the fault surface during the simulation. The jump represents the Supershear occurrence of the nucleation of the daughter crack.The driving force stays constant for some time and then drop due to the detachment of the Supershear pulse.

The abrupt nucleation leads to an initial sharp increase in the crack tip driving force. The rate of change of the force is high in this region. As the crack expands the crack driving force increases but the rate of change of the crack driving force decreases. For a steadily propagating slip pulse the crack driving force is a constant [81]. This corresponds to a propagating rupture with zero change in its driving force. We hypothesize that cracks are driven towards a similar state with the driving force increases at a progressively decreasing rate as the crack expands. This is probably a more favorable state from the energetic perspective. When the daughter crack nucleates, it disrupts the pattern and the rate of change of the tip driving force increases. Through the detachment of the slip pulse and the breakdown of the rupture to smaller regions, the rate of change of the driving force decreases again. Hence, we conjecture that the detachment of the pulse is more favorable because it leads to an overall smaller crack driving force than if the rupture continues to propagate as an intact crack.

2.5 Supershear rupture propagation in the presence of off-fault low velocity inclusion

The existence of an off-fault heterogeneity with a lower shear modulus than the surrounding bulk enriches the wave field by introducing additional boundary surfaces. The waves emanating from the rupture and propagating though the heterogeneous medium are modulated by the reflection and the refraction at the different material interfaces. These modulations include changes in wave amplitudes, phase angles and polarities. In Figure 2.5, we plot the reflection coefficient for the SV wave at both the lower and upper boundaries of a hypothetical soft layer for the case corresponding to a mismatch in P-wave speed = 20%. We consider different values of the incidence angle. Waves reflected from the lower boundary of the soft layer have the same polarity as the incident wave for the whole range of incidence angles we considered here. Thus, these waves enhance the rupture propagation. On the other hand, the waves reflected from the upper boundary of the soft layer have negative reflection coefficients for incidence angles less than 10°. When these waves are transmitted back to the fault zone, their reversed polarity impedes the rupture and may lead to temporary rupture arrest and formation of slip pulses as we will discuss shortly. This scenario is different from when the low velocity layer is adjacent to the fault plane. In this case, only reflections from the top layer are present leading to rupture decoherence [44, 45].

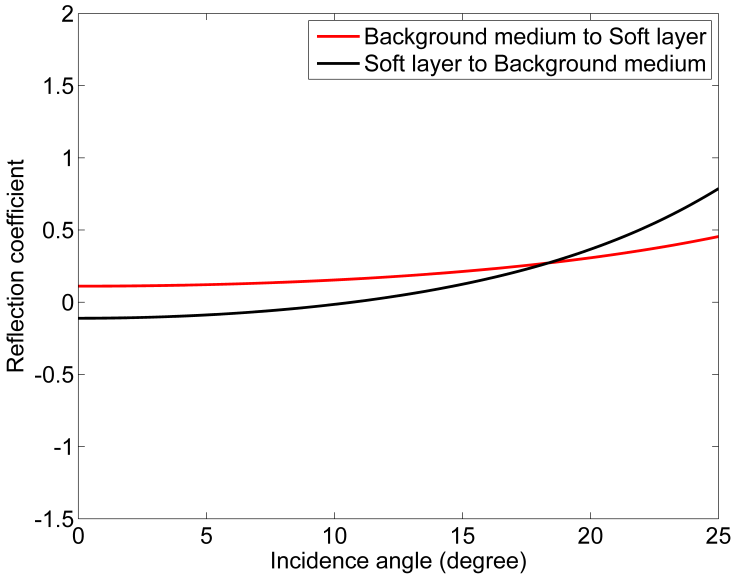

Figure 2.5: Reflection coefficient for incident SV waves at boundary between background medium and soft layer with velocity reduction of 20% ,Red line shows the incident wave background medium to soft layer and black line shows the incident wave from soft layer to background medium respectively.The reflected SV wave is considered.The incident angle of SV waves are plotted below the first critical angel.The phase is zero for this range of incident angels. Formulas of reflection coefficients are taken from [82]

We first consider a fault case with strength parameter $S = 1$. In a homogeneous medium, we observe that the rupture jumps into supershear after propagating for a distance 55.5 km.

The existence of the soft heterogeneity reduces the supershear transition distance. The extent of the effect depends on many factors such as the soft inclusion thickness, the soft inclusion extension, the soft inclusion distance from the fault and the velocity reduction in the soft inclusion. These factors determine the amplitudes of the waves reflected from the soft layer to the fault zone as well as the perturbations in the nucleation size of the daughter crack. The width of the soft inclusion, in particular, determines the difference in arrival times, as observed on the fault surface, between the different waves reflected from the two boundaries of the soft layer. For a soft inclusion of length 20 km and width $H_2 = 2R$, where R is the nucleation length scale, the transition distance to supershear is reduced to only 15 km compared to more than 55 km for the homogeneous case. This reduction may be attributed to two reasons. First, the waves reflected from the bottom boundary of the soft

inclusion have the same polarity as the incident wave and thus they enhance the rupture propagation. This thickness of the soft inclusion $H_2 = 2R$ is big enough to delay the arrival of the reflected waves from the top boundary. Since these waves have an opposite polarity they interfere destructively with the rupture. When the soft inclusion thickness is smaller (e.g. $H_2 = R$) these waves arrive sooner to the fault surface and compete with the enhanced effect carried by the reflected waves from the bottom boundary. In this case, the transition distance is close to its value in the homogeneous case.

The second reason is that the nucleation length for a crack is proportional to the rigidity of the domain (Eqn. 2.2). The existence of a soft inclusion reduces the effective rigidity of the medium compared to the homogeneous case. Thus the nucleation size of the daughter crack will be smaller in the presence of a soft inclusion. This is shown in Figure 2.6(a). There, we track the width of the region for which the peak shear stress is equal to the static strength. We define the nucleation size of the daughter crack as the size of this region just before it becomes disjoint. Based on this definition, we have found that the nucleation length of the daughter crack is reduced from 375m, for the homogeneous medium, to 225m, for the case with softer inclusion. The nucleation size of the daughter crack is generally smaller than what is predicted for quasi-static nucleation (Eqn. 2.1). This is because the nucleation of the daughter crack is enhanced by the dynamic stress field of the primary crack.

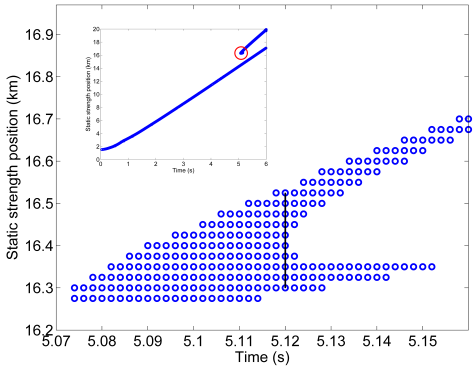

(a)

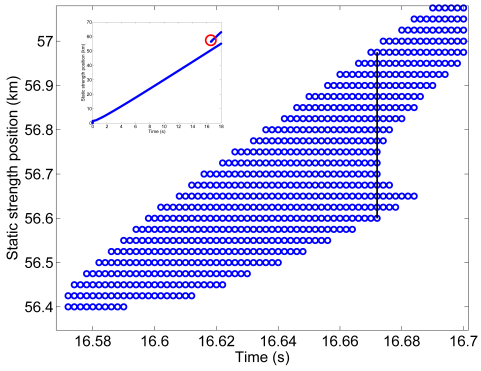

(b)

Figure 2.6: Growth of the daughter crack in the presence (a) and absence (b) of soft inclusion. Here the location of the fault points where the shear stress is equal to the static frictional stress (30MPa) is plotted. The nucleation length of the daughter crack in the soft layer inclusion case is 225km while in the homogeneous case is 375km.

Figure 2.7 shows the variation of the rupture speed for the homogeneous and heterogeneous cases. We compute the rupture speed by recording the location of the rupture tip at each time step. To eliminate numerical artifacts associated with the finite space time discretization, we fit the tip position-time curve with a polynomial of degree 9. By differentiating the smoother curve that resulted from the fitting process, the instantaneous rupture tip speed is computed as shown in Figure 2.7. We have also depicted the shear wave speed as well as the Rayleigh wave speed for the fault zone material on the same plot.

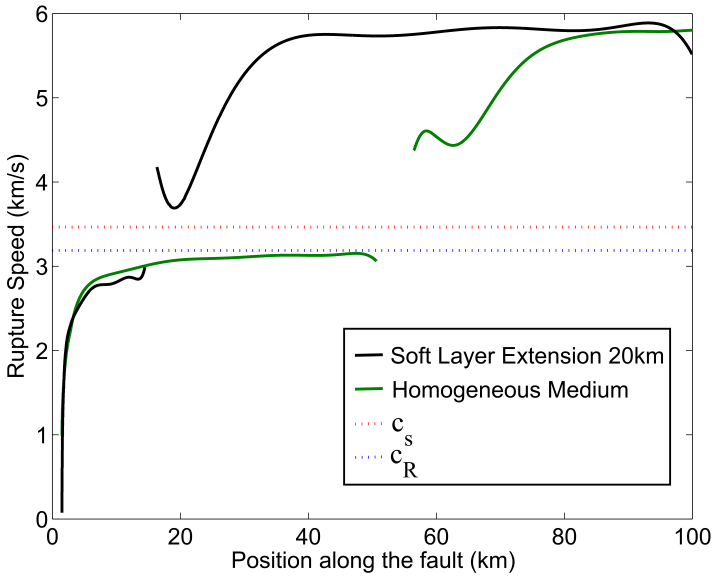

Figure 2.7: Variation of rupture speed for homogeneous medium and medium with soft layer inclusion. The jump represents the nucleation of daughter crack through the Burridge-Andrews mechanism. The dip after the jump represents the mechanism for Supershear rupture to form. The nucleation of daughter crack for homogeneous medium is 55km, for medium with soft layer inclusion is 15m.

In both cases, the supershear transition occurs discontinuously through the nucleation of a daughter crack as predicted by the Burridge-Andrews mechanism. The discontinuity in the rupture speed plot corresponds to the nucleation of the supershear tip. For the homogeneous case, the supershear rupture transition occurs at 55 km whereas for the soft layer case the supershear transition happens at approximately 15 km. In both cases prior to the supershear jump, the rupture travels at sub-Rayleigh wave speed. There is no propagation through the so called 'Energetically Forbidden Zone' defined by the range of velocities between the shear wave and Rayleigh wave speed [83].

Another feature of the rupture speed plot (Figure 2.7) is the existence of a dip shortly after the transition to supershear. This is related to the details of the supershear transition process. Shortly after it is formed, the daughter crack joins the main rupture and the leading rupture tip propagates at supershear velocity while the main rupture tip is still propagating at lower velocity. As a result the distance between the leading edge and the main rupture front continues to increase leading eventually to the detachment of a supershear pulse. This mechanism occurs in both the homogeneous and layered cases (Figure 2.7). This suggests that the formation of the detached pulse is essentially due to energetic reasons (See Section 3.1) rather than due to the reflections from the soft inclusion. After

the detachment, the rupture propagation speed of the slip pulse increases till it saturates at a speed between $\sqrt{2}c_s$ and c_p of the fault zone [55].

Figure 3.7 shows that the space time evolution of the slip rate on the fault surface in the two cases. For the case of homogeneous medium the slip rate is smoother. The multiple reflections from the different interfaces in the medium with a low velocity zone lead to visible oscillations in the slip. These oscillations may become large enough (depending on the material contrast) to lead to the temporary arrest of the rupture behind the leading edge and the formation of a train of pulses (not shown here).

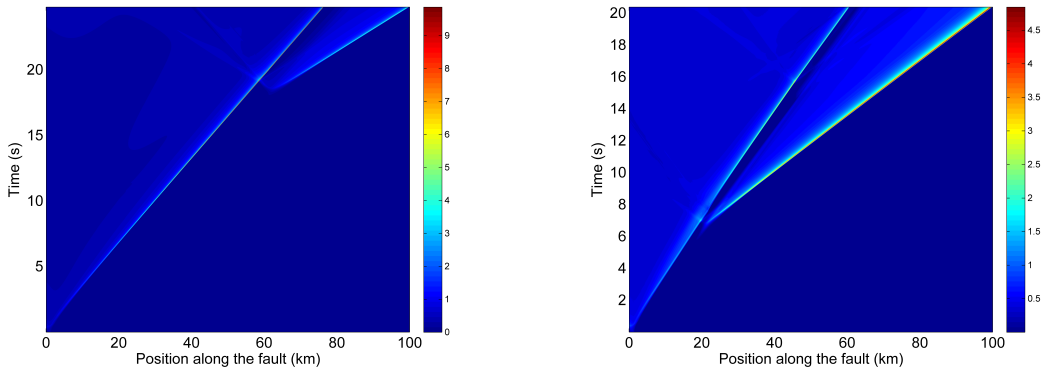

(a) (b)

Figure 2.8: Space-time contours of slip rate on the fault surface (a) homogeneous medium (b) medium with 20km soft layer inclusion.The homogeneous medium has smoother slip rate profile (no oscillations in the slip rate behind the Supershear front)

Figure 3.8 shows the evolution of maximum slip rate for both the homogeneous and inhomogeneous media. The existence of the embedded soft inclusion leads to the saturation of the maximum slip rate at 1.2 m/s during the sub-Rayleigh propagation. After the supershear jump, and as the rupture propagates into the homogeneous medium, the maximum slip rate starts to increase again. In the homogeneous case, on the other hand, the maximum slip rate increase monotonically up to 9 m/s in the sub-Rayleigh regime. The sudden jump in the maximum slip rate profile in both cases point to the supershear transition. The end of the drop following this jump refers to the detachment of supershear slip pulse. These observations suggest that the presence of an embedded soft layer inclusion to the occurrence of supershear transition at lower slip than in the homogeneous case. Also the magnitude of the maximum slip rate is smaller in the soft layer case than the homogeneous case

even though the rupture propagates faster in the former than in the latter. Same observation applies to the rate of change of the maximum slip rate. Although both tips are propagating in the same homogeneous medium (after the soft inclusion stops), the maximum slip rate increases at a faster rate in the homogeneous case than in the case with low velocity lens. This points to the necessity of accounting for the rupture history when estimating rupture quantities such as slip and maximum slip rate

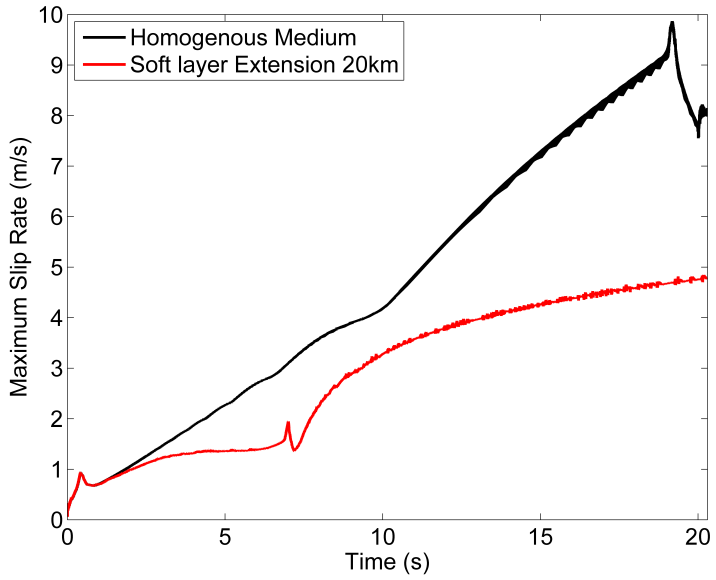

Figure 2.9: Evolution of Maximum Slip rate for homogeneous medium and medium with 20km soft layer inclusion ($H_1 = R$, $H_2 = 2R$, Material Contrast =20%, $L_{nuc} = R$)

In the following sections we investigate the soft inclusion effects in further details. We explore the effect of the soft inclusion thickness, off-fault distance, extension, and material contrast on the supershear transition.

2.6 Effect of Soft inclusion thickness and Off-fault distance

In this section, we investigate the effect of soft layer thickness (H_2) and off-fault distance (H_1) on the supershear transition length. For this purpose, we assume that the inclusion extends for the full length of the fault. We normalized these two quantities by R. For $H_2/R = 1$, we vary H_1/R between 1 and 8. As shown in Figure 2.10, the more distant the soft layer is from the fault surface, the longer the transition distance to supershear propagation is. On the other hand, for $H_1/R = 1$, we vary H_2/R between 1 and 8. In this case, as the thickness of the soft layer increases, the transition length decreases.

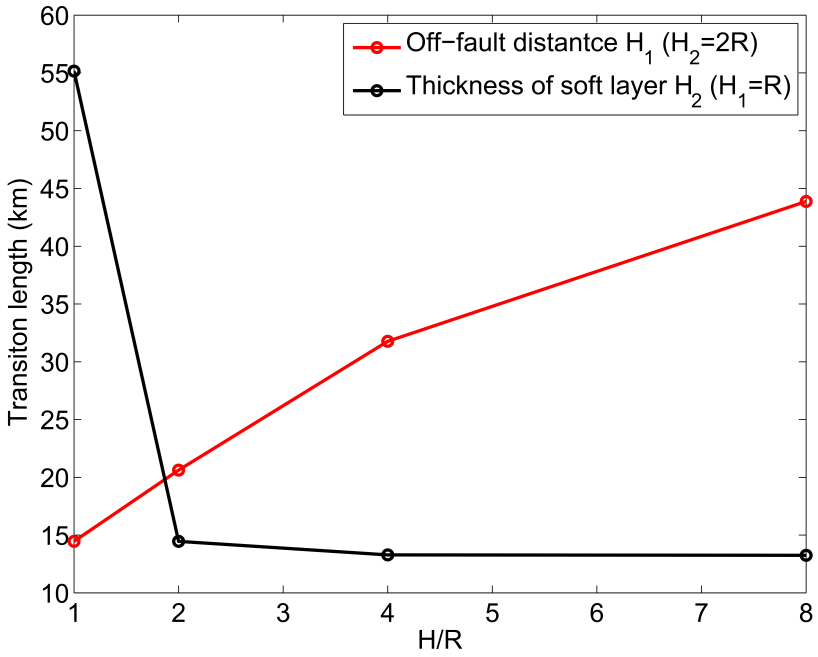

Figure 2.10: Variation of supershear transition length with different values of off-fault distance (H_1) and soft layer thickness (H_2), With $H_2 = 2R$, red line shows transition length to supershear rupture under various off-fault distance H_1. With $H_1 = R$, black line shows transition length to supershear rupture under various soft layer thickness H_2

These observations are explained as follows. The waves reflected from the top and bottom surfaces of the soft layer have opposite polarities (Figure 3.4). The travel time for a ray emanating from the rupture, reflected from one of these interfaces, and arriving back at the fault surface, depends on the layer thickness as well as its distance from the surface. The more distant the soft layer is from the fault surface, the longer this travel time will be. This has two consequences: (1) there is a delay in the arrival of the waves reflected from the bottom surface. These waves enhance the rupture propagation and accelerate the supershear transition. Their delay, on the other hand, increases the transition length; and (2) the difference in the arrival time between the waves reflected from the two boundaries of the soft layer decreases. In particular, the waves reflected form the upper boundary of the soft layer have reversed polarity and hence they interfere destructively with the propagating rupture as well as with the waves reflected from the bottom boundary delaying the rupture acceleration into supershear.

The increase in the soft layer thickness, on the other hand, enhances the supershear transition and

shortens the transition length. This is because as the soft layer thickness increases, the difference in arrival time, as observed at a point on the fault surface, between the waves reflected from the top and bottom boundaries of the soft layer increases. The delayed arrival of the waves reflected from the upper boundary reduces their destructive interference effect (Section 3.2) allowing more time for the rupture to interact with the waves reflected from the bottom boundary. The latter, having the same polarity as the incident waves, enhances the propagation dynamics and accelerates the rupture transition into supershear. This is shown in Figure 2.10, where the transition length changes significantly as H_2 changes from R to $2R$ but nearly saturates thereafter. This saturation reflects the observation that increasing the soft layer thickness beyond a certain limit is ineffective in changing the transition length. This is because any further delay in the arrival of the reversed polarity waves from the top boundary of the soft layer is irrelevant if the supershear transition has already happened. The trend in Figure 2.10 suggests that variations in the distance of the soft layer from the fault surface have a strong impact on the transition length. On the other hand, the effect of the layer thickness is only relevant for a limited range of thickness values. Increasing the layer thickness beyond a certain value, for a given off-fault distance, has a negligible effect on the supershear transition.

2.7 Effect of Soft layer extension

The low velocity layer may extend to different lengths. It may be an inclusion of a finite extension or a layer extending throughout the full fault length.

Figure 3.10 compares snapshots of slip rate in two cases: (a) a soft layer extending full length, and (b) a soft layer extending only for 20 km. Both cases have a strength parameter $S = 1$ and the velocity reduction is 20%. For both cases, the supershear transition distance is approximately 15 km. This suggests that accelerated supershear transition is insensitive to the length of the soft layer as long as the length of the soft layer is larger than a critical value. This value is set by the velocity contrast and the distance of the soft layer from the fault surface. Moreover, the rupture continues to propagate as supershear into the homogeneous medium after the truncation of the soft layer at 20km long. We discuss the implications of this on conditions for accelerated supershear transition under heterogeneous conditions in Section 4.

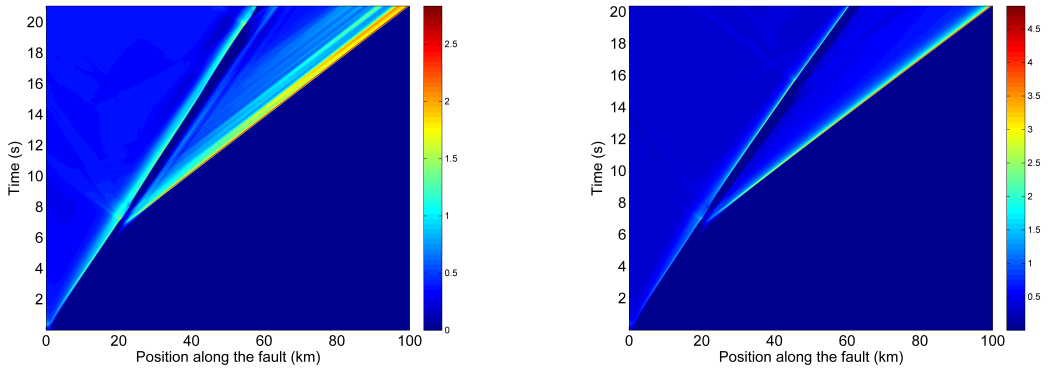

(a) (b)

Figure 2.11: Space-time contour of slip rate during rupture propagations. (a) Soft layer extend to the full length of the domain (100km) (b) Soft layer extend only 20km from the left edge of the domain. Case (a) exhibits more oscillations in the slip rate profile behind the supershear rupture front.

There are, however, a few differences between the two cases. Most notably, the rupture propagating into the homogeneous medium, after the soft layer is truncated, shows a smoother slip rate profile with no oscillations behind the first rupture front. This is not the case when the soft layer extends to the full length of the fault. In this case, the oscillations in the slip rate are caused by the multiple reflections of the waves from the soft layer boundaries. The truncation of the soft layer eliminates the cause of theses oscillations.

In Figure 2.12 we compare the rupture speeds for the two cases. Initially, both ruptures have essentially the same rupture speed. However, for the case of the truncated soft layer the rupture speed is slightly higher. This suggests that wave reflections from the upper boundary of the fully extended soft layer interferes destructively with the wave field surrounding the crack tip and slightly lower its propagation speed. These reflections are absent in the case of soft layer extending only for 20 km.

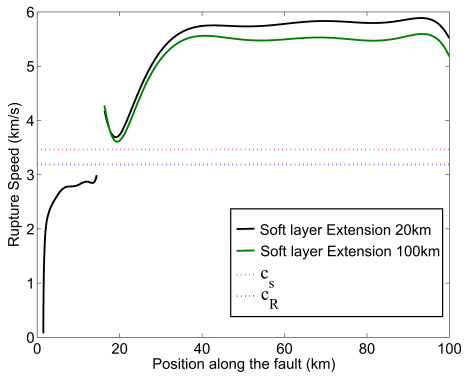

Figure 2.12: Variation of rupture speed for medium with soft layer extending full length and a medium with soft layer only extending 20km.

In Figure 2.13 we compare the evolution of maximum slip rate when the soft layer has a limited extension of 20 km and when it extends to the full length of the fault. The two cases are identical up to 7s of propagation time. There is a very small difference in the time of supershear transition (see the first peak in the maximum slip rate profile) between the two cases. The supershear transition is slightly delayed in the case of soft layer that is extending for the full length. In this case, wave reflections from the boundaries of the soft layer limit the maximum slip after supershear transition to approximately 2.7 m/s. However, in the case of the 20 km long soft layer, the magnitude of the maximum slip rate increases as the rupture propagates into the homogeneous medium.

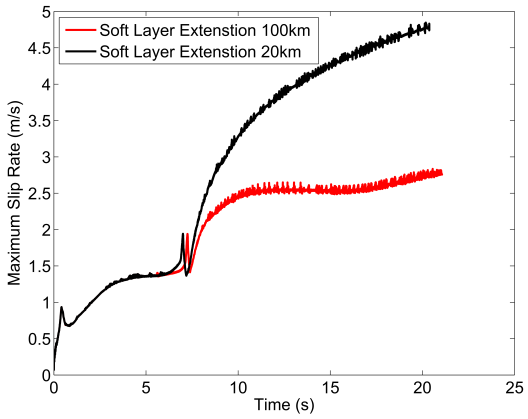

Figure 2.13: Evolution of Maximum Slip rate for soft layer extend 100km and medium with soft layer extended 30km.

2.8 Effect of Soft zone position

In this section we investigate how the position of the soft zone affects the supearshear transition characteristics. We conduct simulations with soft layer starting from the left edge (i.e. adjacent to the nucleation zone) and extending to only 10km. We repeat the simulation with the same soft layer length but make it extend from 20km to 30km. As it was shown previously [Section 3.2], a soft layer extending 20km from the start of the nucleation site has reduced the transition length to approximately 15km. For the soft layer starting from the edge and extending 10km, the supershear transition length (45 km) is slightly reduced compared to the homogeneous case but is much longer than the case with 20 km long soft layer. On the other hand, the transition length corresponding to the shifted soft layer is only 23.4 km. Figure 3.13 shows the space-time evolution of slip rate distribution on the fault for the two cases. The enhanced supershear transition for the case of shifted soft layer may be explained as follows. As the rupture propagates from the left, the S-wave stress peak grows. Waves reflected from the bottom boundary of the shifted layer interfere with the stress peak after the latter has had some time to grow. This interference further strengthens the stress peak and accelerates the transition. This suggests that the same heterogeneity may have different effects on the rupture dynamics depending on its position relative to the spatiotemporal evolution of the crack. If the rupture encounters a favorable off-fault heterogeneity, it will transition faster to supershear. This is similar to the effect of a favorable prestress heterogeneity on the fault surface that was previously discussed by Lapusta and Liu [67].

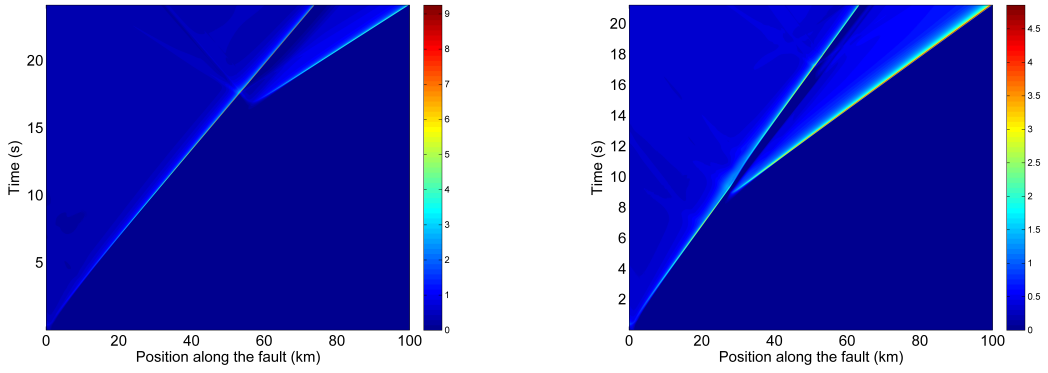

(a) (b)

Figure 2.14: Space-time contours of slip rate (a) soft layer 10km from beginning (b) soft layer 10km shifted to 20 to 30km

2.9 Effect of Stress level S ratio and Material contrast

In this section we investigate the effect of stress level ratio S and material contrast on supershear transition characteristics. The limiting value of strength parameter S for supershear rupture to occur in homogeneous 2D elastic media is 1.77. The existence of a soft layer violates the assumption of medium homogeneity and introduces additional interfaces for wave reflection and refraction. In this case, the limiting S value may be different from the homogeneous medium and it may be even non-existent. Indeed, [45] showed that the existence of LVZ adjacent to the fault surface enhances the supershear transition mechanism. Here, we present a few examples showing that rupture may transition into supershear, or continue to propagate as supershear, under stress values that are lower than the limiting case predicted theoretically for the homogeneous media.

We consider a soft layer that is 20 km long. We examined different prestress distributions. In one case, the value of the strength parameter is $S = 1$ for first 30km of the fault length and $S = 2$ for the remaining 70km. We also considered a case with $S = 2.5$ for the last 70 km of the fault length. The choice of the soft layer length and the extent of $S = 1$ regime was to insure that supershear transition will happen within the elevated stress region.

Figure 2.15 shows that the evolution of the rupture speed with respect to the distance along the fault for the two cases just described in addition to a reference case in which $S = 1$ uniformly along the whole fault length. The three cases behave exactly the same before the supershear transition happens This is expected as the rupture conditions are identical in this regime In all cases, the transition distance to supershear is 15 km. After the transition to supershear, the three cases develop a detached supershear slip pulse. This is signaled by the existence of a dip in the rupture speed profile [Please see Section 3.1 for further discussion on this]. As the rupture tip approaches the location at which the prestress abruptly changes (30 km), the three cases start to deviate from one another. Waves emitted from the propagating rupture sense variations in the prestress field, even before the rupture tip reaches the lower stress region. Some of these waves are reflected back carrying this information about the reduced prestress to the rupture tip. As a result, the rupture propagation speed decreases for the cases with increased strength parameters. Nonetheless, the difference in the rupture speed after the transition to supershear in all cases is small. Moreover, the rupture continues to propagate supershear even with $S = 2.5$. This suggests that supershear ruptures, once formed, may persist to propagate in low stress regions that are unfavorable for supershear transition in homogeneous conditions. The

existence of off-fault material heterogeneity accelerates the transition to supershear. The supershear propagation may persist thereafter even if the prestress is reduced. We discuss the implications of this on supershear transition in understressed faults in Section 4.

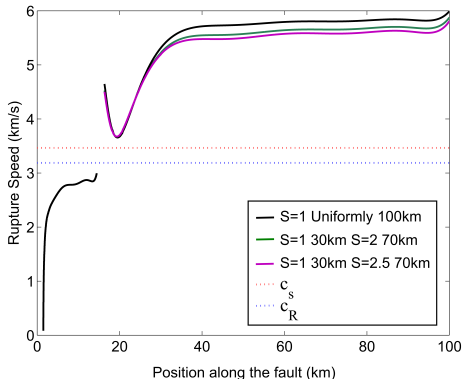

Figure 2.15: Variation of rupture speed for $S = 1$ uniformly 100km, $S = 1$ for 30km, $S = 2$ for the rest 70km and $S = 1$ for 30km $S = 2.5$ for the rest 70km. The domain is with 20km length soft layer inclusion.

The evolution of the maximum slip rate in the three cases is shown in Figure 2.16.The three cases behave exactly the same until the rupture reaches the location of change in the prestress (at 8 seconds). The maximum slip rate, unlike the rupture speed, shows a stronger dependence on the local stress conditions. For the cases of $S = 2$ and $S = 2.5$ the maximum slip rate drops instantaneously in response to the imposed prestress drop. The drop in the maximum slip rate is higher for the case with $S = 2.5$ than for the case with $S = 2.0$.

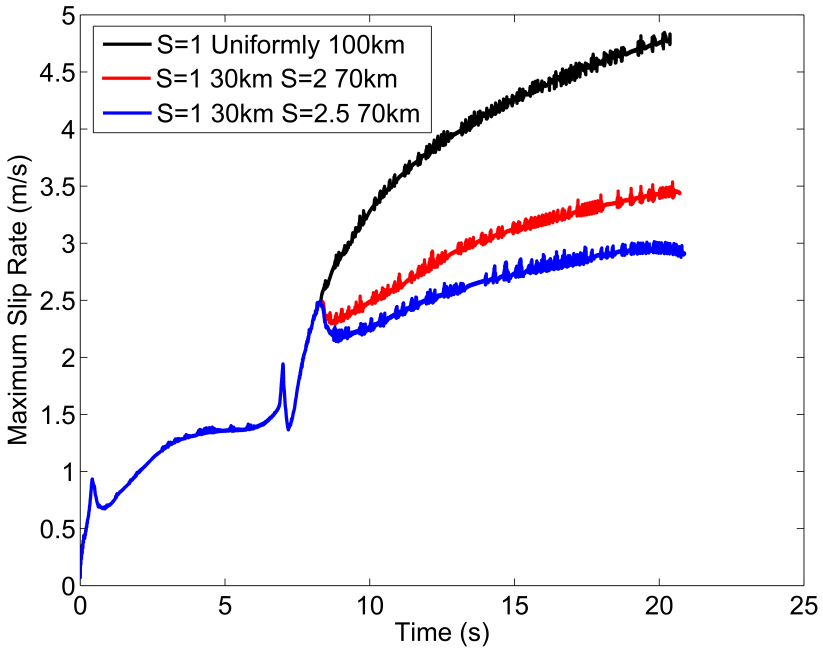

Figure 2.16: Maximum slip rate for $S = 1$ uniformly 100km, $S = 1$ for 30km and $S = 2$ for the rest 70km and $S = 1$ for 30km $S = 2.5$ for the rest 70km. The domain is with 20km length soft layer inclusion.

We also investigate the possibility of supershear transition under uniformly lower prestress levels if the velocity reduction in the soft layer increases. For this purpose we carry out simulation with the soft layer extending parallel to the full length of the fault. We considered several values of velocity reduction ranging from 20% to 60%. Figure 2.17 shows that it is possible with higher material contrast to generate supershear ruptures even if the strength parameter is uniform and equal to 2.5 along the fault length. The transition length to supershear propagation increases, however, as the material contrast decreases. For example, we have found that the supershear transition length, under uniform prestress conditions, is approximately 14 km for the case with material contrast 60% and $S = 2$. This transition length increases to 66 km and 176 km for cases with 40% and 20% velocity reduction in the soft layer respectively. For 0% velocity reduction (homogeneous medium) the transition length is predicted theoretically to be infinite. We thus hypothesize that in the presence of an off-fault soft layer, supershear may happen under any stress level but the transition length diverges, for $S > 1.7$, as the material contrast between the soft inclusion and the medium approaches zero. A possible mechanism is that the continuous reflections from the soft layer to the fault surface enhance the building up of the shear stress ahead of the rupture front, and eventually lead to the nucleation of the daughter crack through the Burridge-Andrews mechanism. If the rigidity of the soft layer approaches zero, it may be

taken as an analog of a free surface. Supershear transition due to free surface has been investigated for strike slip faults by Kaneko and Lapusta [69]. Our observations suggest that supershear transition may occur at low prestress values if a free surface exists parallel to the rupture propagation direction. We discuss the implications of this particular observation on rupture propagation on normal fault flats as well as the strike slip faults in Section 4.

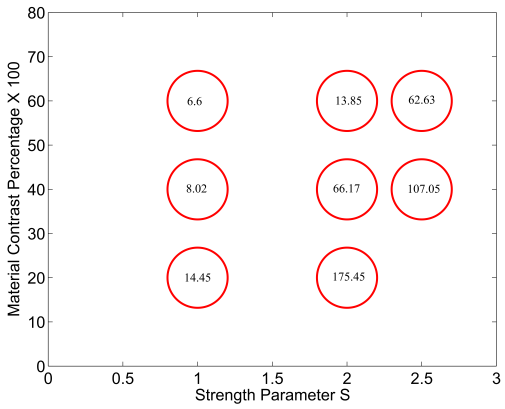

Figure 2.17: Values of Transition length with respect to Material Contrast and Strength Parameter S.

2.10 Discussion

Identifying conditions under which supershear transition may occur during earthquake propagation is crucial for the development of a better understanding of earthquake physics as well as the estimation of ground motions. Supershear ruptures tend to be more destructive since the resulting waves travel longer distances with less attenuation than in their sub-shear counterparts [55]. Heterogeneities in the Earth's crust are manifested in different forms. These include heterogeneities in the prestress, material properties and friction laws. Exploring the interplay between different sources of heterogeneities and the dynamics of the rupture process is essential for the development of more realistic rupture models.

In this study, we explored the influence of the existence of an off-fault material heterogeneity, represented by an off-fault low velocity lens, on the rupture dynamics on a slip weakening frictional interface. Our primary focus is on its effects on transition to supershear. Previous studies focused on other sources of heterogeneities such as variations in the prestress [67] or fracture energy [84]. Our investigation is similar to Harris and Day [42], Huang and Ampuero [44], and [45], where the authors explored the influence of a low velocity zone adjacent to the fault surface. A point of departure for our approach is that we allow the low velocity layer to be placed at a finite distance from the fault

surface. Moreover, the low velocity zone may be present in the form of a velocity anomaly within a limited region and need not extend throughout the length of the domain.

Velocity structure in the upper crust is generally heterogeneous [26]. It is most natural to think of low velocity zones to be present in the immediate vicinity of pre-existing faults as a result of the damage caused by previous earthquakes. However, there may be situations in which the low velocity zone exists near but not immediately adjacent to the fault surface. Examples include (i) faults in the shallow parts of the crust near sedimentary basins, (ii) a member of a fault network in which the damaged zone adjacent to a nearby fault has lower rigidity than the damage zone in its immediate vicinity. Moreover, recent developments in the unified velocity structure models [26] show that spatially heterogeneous velocity structure is more common than what was originally thought of. With increased resolution and better detection methods, we will be able to identify more fine scale variations in this heterogeneous structure.

Different friction models have been developed to describe the evolution of fault strength. These include the slip weakening models [85, 86, 78], the rate and state friction [87, 88], and the shear transformation zone theory [89, 90, 91, 92]. Rate dependent models such as the Deterich-Ruina formulation or STZ friction models capture the evolution in fault strength in response to velocity changes and naturally accounts for healing as the slip rate is reduced. These features have important implications for rupture mode classification [93, 94]. Linear slip weakening models, on the other hand, do not naturally allow for fault healing and are insensitive to rate effects. Nonetheless, it is possible to map the parameters of slip weakening friction to the corresponding parameters in the logarithmic rate and state law [67]. Thus, the results of the current study, derived based on linear slip weakening friction, are expected to hold, at least qualitatively, if a more sophisticated logarithmic rate and state description is used.

The dynamic friction used in this study is equal to 0.5. This leads to a reasonable value of static stress drop (2.5 MPa) [95]. However, this is relatively high compared to the expected strength level for mature faults. Due to the heat flow anomaly and lack of evidence for melting on mature faults [96, 97, 98], the actual value for dynamic friction is expected to be as low as 0.1 or 0.2. Several mechanisms have been proposed to account for the ultra-low dynamic friction including flash heating [98, 99], pore fluid pressurization [98, 100], silica gel formation [98] and nanoparticle lubrication [101]. We thus expect the heat generation associated with our friction model to be high and possibly consistent only with slip on dry and less mature faults [102] where traces of pseudotachylytes have been documented.

We appreciate, however, that the rapid transition from high static friction to low dynamic friction is important for enabling rupture propagation in relatively low prestress conditions [103]. The details of this transition has direct implications for the rupture mode classification and generation of self-healing slip pulses [79, 104]. We plan to extend this study to account for strong rate weakening friction in future investigations.

Slip pulses have been observed in dynamic rupture simulations under different conditions. These include models with strong rate weakening friction [93], strong material or prestress heterogeneities [60], low velocity zones [44], and heterogeneous friction conditions [80]. Here, we show that it is possible to generate a sustained slip pulse on a slip weakening fault within a homogeneous elastic medium as a consequence of the supershear transition. We hypothesized that the detachment of the supershear pulse in this case is more favorable from an energetic point of view as it enables rupture propagation with a smaller crack tip driving force. A similar observation of supershear slip pulse was made by Festa and Villote [63] who investigated the influence of nucleation procedure on supershear transition.

In this study we nucleated the rupture abruptly by overstressing a region of the fault beyond its static frictional strength. This artificial nucleation leads to the rupture propagating dynamically from the beginning. This is different from the more natural quasi-static nucleation of real earthquakes. However, it is not rare that an earthquake may be triggered dynamically due by waves emitted from another earthquake [105, 106, 107]. In this case the nucleation will not be quasi-static. Moreover, this procedure is routinely used in generating laboratory earthquakes [108]. Different nucleation protocols may affect the subsequent rupture propagation. In this study, we used the same nucleation procedure as well as the same nucleation parameters in all the simulations. Thus the artifacts that may be produced by the abrupt rupture initiation is common to all the results and any observed variations may be attributed to changes in the other model parameters such as the soft layer thickness, or off-fault distance, or material contrast.

The operation of most mature faults under overall low prestress [103] poses a paradox for supershear ruptures. On one hand, analytical and computational models predict that a relatively high prestress value ($S < 1.77$) is required for supershear transition to occur within a finite distance on slip weakening frictional faults in 2D homogenous elastic media [64]. Meanwhile, if supershear rupture propagation occurs on a mature fault it must then occur at a much lower prestress. A possible resolution to this paradox include the existence of favorable heterogeneities in the fault prestress [67], heterogeneities in

the fracture energy [64], or the existence of low velocity zone adjacent to rate and state frictional fault [45]. Here, we present an additional mechanism which is the existence of off-fault soft heterogeneities. The reflection of waves from the bottom boundary of the off-fault low velocity region enhances the supershear transition and leads to the building up of stresses ahead of the rupture tip at a much lower background stress. We showed that as the velocity contrast between the inclusion and the background medium increases, the transition to supershear decreases. Moreover we report supershear propagation at prestress values corresponding to $S > 1.77$. This may suggest that the velocity structure near the fault surface plays an important role in determining the rupture propagation speed. Accounting for these heterogeneities will give more insight into conditions for supershear transition beyond what is possible from homogeneous models or heterogeneities limited to the fault surface only.

If the elastic moduli of the soft layer are taken to zero in the limit, the soft layer bottom boundary will approach the free surface condition. We observe that the transition length decreases as the material contrast between the soft layer and the background layer increases. Moreover, we show that as the material contrast increases, the prestress value at which supershear propagation becomes possible decreases. The existence of a free surface parallel to the rupture strike may enable supershear transition at much lower prestress values than what is predicted for the full space case. This situation is relevant to rupture propagation along flat portions in normal faults as well as propagation along the strike of subduction zones. We plan to investigate this topic further in future studies.

Future extension of this study may include the consideration of more realistic friction constitutive models such as rate and state friction with enhanced coseismic weakening, modeling the existence of off-fault stiff inclusions, and representing more complex off-fault velocity structure. These investigations will also have implications for engineered composite materials in which the heterogeneous structure modulates the effective fracture toughness [109].

2.11 Conclusion

We have analyzed the supershear transition induced by an off-fault low velocity zone using simulations of spontaneous dynamic rupture on a fault governed by a linear slip-weakening friction law embedded in 2D elastic medium. We have analyzed factors that control the transition length to supershear rupture including the thickness of the soft layer, the contrast in the wave velocity between the soft inclusion and the rest of the domain, the stress level on the fault and the length and position

of the soft layer. We have shown that

1. For the same prestress value, the transition to supershear rupture may occur at much smaller distances due to the existence of the soft layer.

2. For the same material contrast, the transition length decreases with the increase of the soft layer thickness (at a fixed off-fault distance) but increases with the increase of the distance between the layer and fault plane (at a fixed soft layer thickness).

3. The maximum reduction in the transition length happens if the soft layer extends to a distance that is slightly larger than the transition length value predicted for a soft layer that has the same length as the fault. That is, the extension of the soft layer beyond this value has a negligible effect on the transition length.

4. Supershear propogation may happen at a much low prestress in the existence of an off-fault soft layer. The transition length, however, increases as the velocity contrast between the soft layer and the medium decreases.

Chapter 3

Strain Localization in Dry Sheared Granular Materials

The content of this chapter has been published on Physical Review E.[110].

Ma, X. & Elbanna, A. Strain localization in dry sheared granular materials: A compactivity-based approach. Physical Review E 98 (2): 022906 (2018).

3.1 Introduction

Fault gouge is a highly-granulated material which is formed in many fault zones due to the fragmentation of the intact country rocks as the fault develops under progressive shearing. Studies have shown extreme localization of slip within gouges layers that in some cases may be less than a few millimeters thick [111, 112, 113, 114, 115, 116]. Origin and evolution dynamics of this shear banding at lab and field scales are not yet fully understood.

Strain localization in granular material has been identified and studied extensively, mostly at low strain rates, using the tri-axial apparatus and direct double-shear test machines [117, 118, 119, 120, 121, 122]. Localization has been cited as a mechanism for material weakening in fault zones and has been linked to strain softening and changes in frictional rate sensitivity [120]. These rheological changes play a critical role in determining the stability of sliding during nucleation and subsequent propagation of earthquakes and control a variety of source parameters including strength drop, slip weakening distance and energy partitioning [119, 121, 123, 124]. Understanding the interplay between strain localization dynamics and fault zone constitutive response is thus crucial for resolving several outstanding challenges in earthquake physics.

Strain localization in sheared fault gouge has also been studied numerically [125, 126]. The focus was primarily on thermal mechanisms for strain localization including pore fluid thermal pressurization and chemical decomposition of carbonate rich gouge due to shear heating. These models were limited to idealized 1D geometry in the direction perpendicular to the mathematical fault plane. Daub

and Carlson [127], Hermundstad et al. [128] investigated athermal shear localization in gouge due to inhomogeneous plastic deformation. Lieou et al. [129], Konik and Elbanna [130] have extended this framework to investigate the influence of grain fragmentation and acoustic vibrations on strain localization dynamics respectively. These models were also limited to 1D idealization of fault zones. Field and lab observations suggest that shear bands have complicated structure including Riedel, boundary and Y-shears. Such complexity is beyond the capacity of 1d models. Here, we present a continuum 2D model for strain localization in viscoplastic gouge layers to capture the evolution of this complex texture.

Our primary theoretical tool for investigating fault zone inelasticity is the Shear Transformation Zone (STZ) framework [131]. The shear transformation zone (STZ) theory is a continuum model of plastic deformation in amorphous solids that quantifies local configurational disorder [131]. The basic assumption in the theory is that plastic deformation occurs at rare non-interacting localized spots known as shear transformation zones (STZs). An internal state variable, the effective temperature, or compactivity [129, 132], describes fluctuations in the configurational states of the granular material and controls the density of STZs [129]. In hard sphere granular systems, changes in compactivity are related to the evolution of porosity [129]. This approach coarse-grains granular simulations while retaining important physical concepts. The STZ framework has been recently extended to resolve additional several granular-specific mechanisms, such as grain breakage [133], and compaction under vibration [130, 134] beyond what is possible using classical friction and granular plasticity laws [135, 136]. Elbanna and Carlson [137] have also extended the flash heating theory [124] to fault gouge within the STZ framework.

The main contribution of this study is the development of thermodynamically consistent framework for amorphous plasticity in 2D finitely deformed granular media using the concept of compactivity. Compactivity was first introduced by Sir Sam Edwards [138] as an alternative for Gibb's temperature to describe packing of hard spheres where volume not energy is the relevant thermodynamic variable. Lieou and Langer [139] extended that concept to describe far from equilibrium dynamics of assemblies of hard spheres. They considered one-dimensional uniformly deformed systems. Here we extend their formulation to higher dimensions and implement it in a finite element framework allowing for spatial heterogeneities and investigation of initiation and evolution of complex shear bands as well as changes in granular material strength with slip.

The remainder of the study is organized as follows. In Section 3.2 we review the basic elements

of the STZ theory. In Section 3.3 we discuss the implementation of the STZ theory into a finite strain visco-plastic finite element framework. In Section 3.4, we present our numerical results for the evolution of shear bands, and factors affecting the shear band localization. In Section 3.5, we discuss the implications of our findings for fault zone dynamics and multiscale modeling of earthquakes. We summarize our conclusions in Section 3.6.

3.2 Continuum Shear Transformation Zone (STZ) theory

Shear Transformation Zone (STZ) theory is a nonequilibrium statistical thermodynamic framework for describing plastic deformations in amorphous materials by quantifying local disorder. It has been applied to a variety of systems including granular fault gouge [127, 128, 140, 141], glassy materials [131, 142, 143, 144], thin film lubricants [145], and hard spheres [139]. The theory, with just a few parameters, has successfully reproduced a large number of experiments and molecular dynamics simulations for glassy materials, including strain localization patterns (e.g. [132, 139, 144, 146, 147]). Recently, the theory was extended to model shear flow of granular materials with breakable particles [133], incorporating flash heating effects [137] as well as acoustic fluidization under low normal stresses [148]. Furthermore, the theory has been implemented to investigate conditions for stability of sliding and strain localization in granular layers subjected to shear and vibrations [130, 134] and has pointed to the possible effect of vibrations in transition from rapid slip to slow slip and eventually stable sliding; a mechanism that may play a role in tremor-slow slip interaction [134].

A basic feature of granular materials is that particles move and rearrange in response to applied stress. Molecular dynamics simulations of glassy materials [131] and discrete element models of granular materials [149] reveal that plastic irreversible deformation is concentrated in localized regions which came to be called shear transformation zones (STZs). These regions undergo slow configurational rearrangement by flipping between two orientations, anti-aligned and aligned with the direction of optimally oriented shear stresses [131]. This occurs on longer time scales than the scale of kinetic vibrations of the particles. Thus the thermodynamics of the system may be described by decomposing the system into a configuration subsystem and a kinetic-vibrational subsystem and the two are weakly coupled. A reservoir may also be introduced with which the granular system may exchange heat.

A single STZ transition is represented by an irreversible rearrangement of a cluster of particles, whereby the particles locally exchange nearest neighbor relationships. While an arbitrary motion in a granular

assembly may be decomposed into affine (i.e. a linear map) and non-affine components, it is the irreversible non-affine rearrangements (i.e. topological changes) of the particles that characterize an STZ. The creation, annihilation, and transition of STZs may be due to mechanical forcing, acoustic vibrations, or thermal fluctuations (for nanoparticles). In this study, we focus on athermal STZ dynamics that is mainly caused by shearing.

A state variable, the compactivity χ, is introduced to measure the degree of configurational disorder in the system and to set the number of STZs. The compactivity is formally defined as the change in the volume (per unit reference volume) V_p for a unit change in the system configurational entropy S_c: $\chi = \partial V_p / \partial S_c$ [139]. In the following subsections, we present a formulation for a compactivity-based Shear Transformation Zone theory in a finite deformation framework.

3.2.1 Finite deformation Kinematics

We introduce a continuous mapping from a reference undeformed configuration X to a current deformed configuration x:

$$\mathbf{x} = (\mathbf{X}, t) \tag{3.1}$$

We define the deformation gradient:

$$\mathbf{F} = \nabla \mathbf{x} \tag{3.2}$$

We adopt a multiplicative decomposition of the deformation gradient [150, 151, 152] such that:

$$\mathbf{F} = \mathbf{F}^e \mathbf{F}^p \quad \text{with} \quad J = |\mathbf{F}|, \quad J^e = |\mathbf{F}^e| \quad \text{and} \quad J^p = |\mathbf{F}^p| \tag{3.3}$$

Accordingly:

$$J = J^e J^p \tag{3.4}$$

The gradient of the velocity field:

$$\mathbf{L} = \nabla v = \dot{\mathbf{F}} \mathbf{F}^{-1} \tag{3.5}$$

From Eq. 3.3 and Eq. 3.5:

$$\begin{aligned} \mathbf{L} &= (\dot{\mathbf{F}}^e \mathbf{F}^p + \mathbf{F}^e \dot{\mathbf{F}}^p) {\mathbf{F}^p}^{-1} {\mathbf{F}^e}^{-1} \\ &= \dot{\mathbf{F}}^e {\mathbf{F}^e}^{-1} + \mathbf{F}^e \dot{\mathbf{F}}^p {\mathbf{F}^p}^{-1} {\mathbf{F}^e}^{-1} \\ &= \mathbf{L}^e + \mathbf{F}^e \mathbf{L}^p {\mathbf{F}^e}^{-1} \end{aligned} \tag{3.6}$$

We may write: $\mathbf{L}^e = \mathbf{D}^e + \mathbf{W}^e$ and $\mathbf{L}^p = \mathbf{D}^p + \mathbf{W}^p$ where $\mathbf{D}$ is the symmetric component and $\mathbf{W}$ is the skew symmetric component. We further assume that $\mathbf{W}^p = 0$ then:

$$\mathbf{L} = \mathbf{L}^e + \mathbf{F}^e\mathbf{D}^p\mathbf{F}^{e^{-1}} \tag{3.7}$$

3.2.2 STZ Kinematics

Let the symbol α denote the orientation of an STZ, which is the orientation of the axes along which its "±" states are defined as shown schematically in Fig 3.1. Let $N_{\pm}^{\alpha}$ indicates the number of STZs oriented in the "+" or "-" states. The master rate equations for STZs could be written as:

$$\tau_o \dot{N}_{\alpha}^{\pm} = R(\pm s_{\alpha})N_{\alpha}^{\mp} - R(\mp s_{\alpha})N_{\alpha}^{\pm} + \tilde{\Gamma}(\frac{1}{2}N^{eq} - N_{\alpha}^{\pm}) \tag{3.8}$$

where $\tau_o = a/\sqrt{P/\rho_G}$ is the inertial time scale [139] and $\tilde{\Gamma} = \Gamma + \rho$ is the attempt frequency. Here Γ and ρ denote the mechanical and vibration noise strengths, respectively. In this study, we don't consider the vibration noise strengths by taking $\rho = 0$. R denotes the STZ flipping rates, and N^{eq} indicates the equilibrium number of STZs. The first two terms in Eq. 3.8 represent the process of flipping of STZs from one state to another. The third term represents the creation and annihilation of STZs.

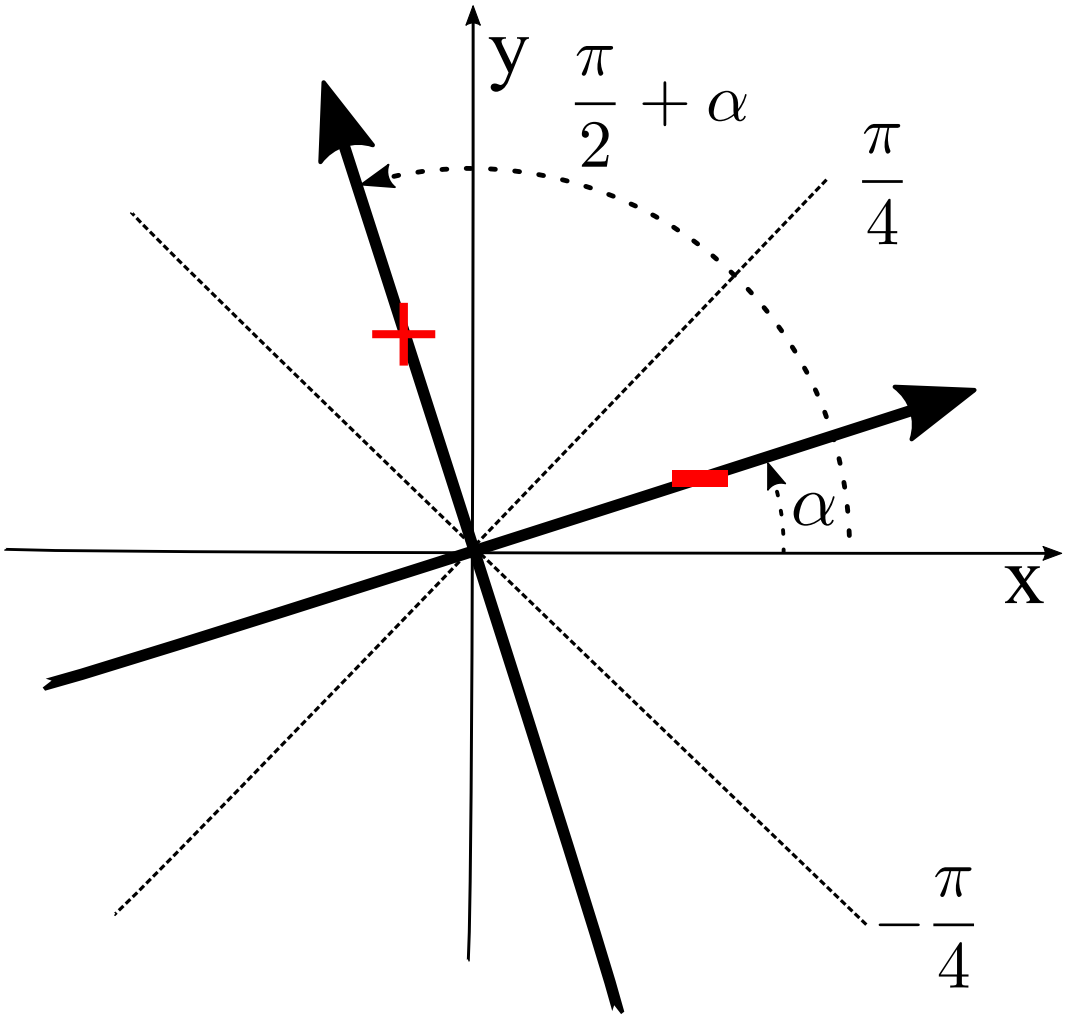

Figure 3.1: Schematic drawing of an STZ transition. The STZs are classified into two states "+" or "-". The "+" state is that an STZ's angle between the direction of its elongation and the y axis is smaller than $\pi/4$. The "-" state is that an STZ's angle between the direction of its elongation and the x axis is smaller than $\pi/4$

We assume that the total plastic strain rate tensor is decomposed into deviatoric and volumetric parts as follows:

$$\mathbf{D}^p_{tot} = \mathbf{D}^p_{dev} + \mathbf{D}^p_{vol} \tag{3.9}$$

The flow direction of the deviatoric part of the plastic strain rate $\mathbf{D}^p_{dev}$ must be proportional to a traceless tensor d_{ij}. For two-dimensional systems, Pechenik [153] showed that:

$$d_{ij}^{\alpha} = 2\hat{e}_i^{\alpha}\hat{e}_j^{\alpha} - \delta_{ij} \tag{3.10}$$

where $\hat{\mathbf{e}}$ is a unit vector at an angle α relative to the maximum shear stress, with $-\pi/4 < \alpha < \pi/4$. If the maximum shear stress is at an angle ϕ with respect to the x axis, then $s_{ij} = \bar{s}d_{ij}^{\phi}$, where s is the deviatoric stress and $\bar{s} = \sqrt{s_{ij}s_{ij}/2}$ is the second invariant of the stress tensor.

The deviatoric part of plastic rate tensor D_{ij}^{p} is the superposition of all of the microscopic shear strain rates accumulating through the STZ transitions and may be written as:

$$\tau_o D_{ij}^{p} = \frac{\epsilon_o}{N}\Big\langle d_{ij}^{\alpha}[R(s^{\alpha})N_{-}^{\alpha} - R(-s^{\alpha})N_{+}^{\alpha}]\Big\rangle \tag{3.11}$$

Here, ϵ_0 is a shear increment of order unity. The angle bracket $< \cdot >$ denotes an average over STZ orientations α consistent with the "$\pm$" constraints (see [153] for more details). The traceless, symmetric tensor d_{ij}^{α} projects these transitions onto the i, j axes. Expanding terms in Eq. 3.11:

$$\tau_o D_{ij}^{p} = \frac{\epsilon_o}{N}\Big\langle d_{ij}^{\alpha}\Big\{\frac{1}{2}[R(s^{\alpha}) - R(-s^{\alpha})][N_{+}^{\alpha} + N_{-}^{\alpha}] - \frac{1}{2}[R(s^{\alpha}) - R(-s^{\alpha})]][N_{+}^{\alpha} - N_{-}^{\alpha}]\Big\}\Big\rangle \tag{3.12}$$

We assume that $R(s^{\alpha}) + R(-s^{\alpha})$ and $R(s^{\alpha}) - R(-s^{\alpha})$ depend only weakly on the orientation and may be replaced by an α-independent function of the magnitude of the stress [154], We introduce the following intensive quantities:

$$\Lambda = \frac{1}{N}\int [N_{+}^{\alpha} + N_{-}^{\alpha}]d\alpha \tag{3.13}$$

$$m_{ij} = \Big\langle d_{ij}^{\alpha}\Big[\frac{N_{+}^{\alpha} - N_{-}^{\alpha}}{N_{+}^{\alpha} + N_{-}^{\alpha}}\Big]\Big\rangle \tag{3.14}$$

$$\frac{1}{2}[R(s^{\alpha}) + R(-s^{\alpha})] \approx \frac{1}{2}[R(\bar{s}) + R(-\bar{s}))] \equiv C(\bar{s}) \tag{3.15}$$

$$\Big\langle d_{ij}^{\alpha}\Big[\frac{R(s^{\alpha}) - R(-s^{\alpha})}{R(s^{\alpha}) + R(-s^{\alpha})}\Big]\Big\rangle \approx \frac{s_{ij}}{\bar{s}}\Big[\frac{R(\bar{s}) - R(-\bar{s})}{R(\bar{s})) + R(-\bar{s})}\Big] \equiv \frac{s_{ij}}{\bar{s}}\mathcal{T}(\bar{s}) \tag{3.16}$$

Here Λ is the total STZ density given by the total number of STZs normalized to N,where N is the total number of grains or particles in the same volume. m_{ij} is a deviatoric tensor that describe the average STZ orientation bias. The rate parameter $C(\bar{s})$ describes the flipping rate bias, and $\mathcal{T}(\bar{s})$ is the orientational rate bias.

Using the preceding definition of Λ, m_{ij}, $C(\bar{s})$ and $\mathcal{T}(\bar{s})$. We could write out the STZ governing

equations:

$$\tau_o D^p_{ij} = \epsilon_0 C(\bar{s})\Lambda[\frac{s_{ij}}{\bar{s}}\mathcal{T}(\bar{s}) - m_{ij}] \tag{3.17}$$

$$\tau_o \dot{m}_{ij} = 2C(\bar{s})(\frac{s_{ij}}{\bar{s}}\mathcal{T} - m_{ij}) - \Gamma m_{ij} - \tau_0 \frac{\dot{\Lambda}}{\Lambda} m_{ij} \tag{3.18}$$

$$\tau_o \dot{\Lambda} = \Gamma(\Lambda^{eq} - \Lambda) \tag{3.19}$$

3.2.3 Laws of Thermodynamics

First Law of Thermodynamics

$$\dot{U}_{int} = W_{ext} \tag{3.20}$$

Here, $\dot{U}_{int}$ is the rate of change of the total internal energy, W_{ext} is the conventional external work rate due to surface traction and body forces. The internal energy may be expanded as:

$$\dot{U}_{int} = \dot{U}_c + \dot{U}_k + \dot{U}_R \tag{3.21}$$

where U_c is the strain energy (associated with elasticity of loading device or elasticity of the particles), U_k is the kinetic-vibrational energy associated with the thermodynamics Gibbs temperature and heat flow, and U_R is the reservoir energy (assuming that the subsystem is connected to the environment and there is an exchange of heat between the two). All energies are measured per unit volume of the intermediate configuration for algebraic convenience as will be shown later.

The external work rate is given by:

$$\begin{aligned} W_{ext} &= \int_{\partial V} \sigma \mathbf{n}.\mathbf{v} da + \int_V \mathbf{b}.\mathbf{v} dV \\ &= \int_V (\nabla.\sigma).\mathbf{v} dV + \int_V \sigma : \nabla \mathbf{v} dV + \int_V \mathbf{b}.\mathbf{v} dV \\ &= \int_V (\sigma : \mathbf{L}^e + \sigma : \mathbf{F}^e \mathbf{L}^p \mathbf{F}^{e^{-1}}) dV \\ &= \int_V (\sigma : \mathbf{L}^e + \mathbf{F}^{e^T} \sigma \mathbf{F}^{e^{-T}} : \mathbf{D}^p) dV \\ &= \int_V (\sigma : \mathbf{L}^e + J^{e^{-1}} J^e \mathbf{F}^{e^T} \sigma \mathbf{F}^{e^{-T}} : \mathbf{D}^p) dV \\ &= \int_V (\sigma : \mathbf{L}^e + J^{e^{-1}} \mathbf{M} : \mathbf{D}^p) dV \end{aligned} \tag{3.22}$$

Here σ is the Cauchy stress, $\mathbf{n}$ is the normal direction vector to the surface, and $\mathbf{b}$ is the body force

density. We have used the divergence theorem, Eq. 3.7, and imposed static equilibrium $\nabla.\sigma + \mathbf{b} = 0$ [1]. An important result of the the above analysis is that the stress conjugated to the inelastic strain rate tensor is $\mathbf{M} = J^e \mathbf{F}^{e^T} \sigma \mathbf{F}^{e^{-T}}$. This is a consequence of the finite deformation analysis. We may recognize this stress as the Mandel stress routinely used in plasticity theories [155]. At small elastic strain, as in this study, the Mandel stress reduces to Cauchy stress.

Assuming that an energy density exists for each of the components of the internal energy and recognizing the arbitrariness of the considered differential volume, the first law of thermal dynamics takes the following local form:

$$\begin{aligned} J^{e^{-1}}(\dot{\psi}_c + \dot{\psi}_k + \dot{\psi}_R) &= \sigma : \mathbf{L}^e + J^{e^{-1}} \mathbf{s}^* : \mathbf{D}^p_{dev} - J^{e^{-1}} P tr \mathbf{D}^p \\ &= \sigma : \mathbf{L}^e + J^{e^{-1}} \mathbf{s}^* : \mathbf{D}^p_{dev} - J^{e^{-1}} P tr \mathbf{D}^p \end{aligned} \tag{3.23}$$

Here, $\mathbf{s}^*$ is the deviatoric component and P is the hydrostatic component of the Mandel stress. Rearranging terms, and accounting for the symmetry of the Cauchy stress σ, the local form of the first law of thermodynamics becomes:

$$\dot{\psi}_c + \dot{\psi}_k + \dot{\psi}_R = \frac{1}{2} J^e \sigma : \dot{\mathbf{C}}^e + \mathbf{s}^* : \mathbf{D}^p_{dev} - P tr \mathbf{D}^p \tag{3.24}$$

where $\mathbf{C}^e$ is the Cauchy-Green Strain tensor.

Constitutive equation specialization

The total entropy of the system S_{tot} is partitioned into entropy of configuration subsystem S_c (associated with the slow arrangement of the particles), entropy of the kinetic subsystem S_k (associated with the fast vibrational degrees of freedom of the particles) and the entropy of the reservoir S_R as stated in Eq. 3.25.

$$S_{tot} = S_c + S_k + S_R \tag{3.25}$$

We may also write the energy density of the different energy components in the system as follows:

[1] We may consider inertia effects and use instead: $\nabla.\sigma + \mathbf{b} = \rho\ddot{u}$. This in turn introduces an extra term $\int (\rho\ddot{u}).v dV = \frac{1}{2}\frac{d}{dt}(\int \rho v^2 dV)$. This rate of change of the kinetic energy of the propagating waves may be moved to the other side of energy balance equation to modify the energy rate of the kinetic subsystem $\dot{\psi}_k$. This will not change the remainder of the thermodynamic derivation

The elastic strain energy density:

$$\psi_c = \psi_c(\mathbf{C}^e) \tag{3.26}$$

The kinetic energy density:

$$\psi_k = \psi_k(S_k) \tag{3.27}$$

The reservoir energy density:

$$\psi_R = \psi_R(S_R) \tag{3.28}$$

Furthermore, the plastic volumetric strain may be written as:

$$V_p = V_p(S_c, \{\Omega\}) \tag{3.29}$$

Here Ω are STZ internal variables such as STZ density and orientations. Taking the time derivative of 3.29:

$$\dot{V}_p = \chi \dot{S}_c + \sum \frac{\partial V_p}{\partial \Omega} \dot{\Omega} \tag{3.30}$$

Here we have used the definition of compactivity:

$$\chi = \frac{\partial V_p}{\partial S_c} \tag{3.31}$$

We may also set:

$$\dot{V}^p = tr\mathbf{D}^p_{tot} \tag{3.32}$$

Second Law of Thermodynamics The total entropy is a non-decreasing function of time:

$$\dot{S} = \dot{S}_c + \dot{S}_k + \dot{S}_R \geq 0 \tag{3.33}$$

Using the aforementioned constitutive dependencies, the fact that $\dot{\psi_{\mathbf{k}}} = \theta_k \dot{S}_k$ where $\theta_k = \partial \psi_k / \partial S_k$ is the kinetic temperature, and the energy balance equation to eliminate S_c, the entropy rate statement reduces to:

$$\left\{ \begin{array}{l} \mathbf{s}^* : \mathbf{D}^p_{dev} - P \sum \frac{\partial V_p}{\partial \Omega} \dot{\Omega} \\ (\frac{1}{2} J^e \sigma - \frac{\partial \psi_e}{\partial \mathbf{C}^e}) : \dot{\mathbf{C}}^e \\ - \theta_k \dot{S}_k - \dot{\psi}_R + P\chi(\dot{S}_R + \dot{S}_k) \end{array} \right\} \geq 0 \tag{3.34}$$

To satisfy this inequality we must have:

$$\sigma = 2J^{e^{-1}} \frac{\partial \psi_e}{\partial \mathbf{C}^e} \tag{3.35}$$

We further request that dissipation is strictly non-negative:

$$\mathcal{D} = \mathbf{s}^* : \mathbf{D}^p_{dev} - P \sum \frac{\partial V_p}{\partial \Omega} \dot{\Omega} \geq 0 \tag{3.36}$$

Finally, for the reservoir and kinetic vibrational subsystems we have:

$$-\theta_k \dot{S}_k - \dot{\psi}_R + p\chi(\dot{S}_k + \dot{S}_R) = (-\theta_k + P\chi)(\dot{S}_k + \dot{S}_R) - \dot{\psi}_R(1 - \frac{\theta_k}{\theta_R}) \geq 0 \tag{3.37}$$

where we have used the identity: $\dot{\psi}_R = \theta_R \dot{S}_R$ and θ_R is the reservoir temperature. The inequality 3.37 may then be satisfied by taking:

$$\dot{\psi}_R = -A\big(1 - \frac{\theta_k}{\theta_R}\big) \tag{3.38}$$

$$\dot{S}_k + \dot{S}_R = B(-\theta_k + P\chi) \tag{3.39}$$

where A and B are positive coefficients.

Assuming that the kinetic temperature is always in equilibrium with the reservoir temperature, thus:

$$\dot{\psi}_R = 0 \tag{3.40}$$

$$\theta_k \dot{S}_k = B(-\theta_k + P\chi) \tag{3.41}$$

$$\dot{\psi}_k = \theta_k \dot{S}_k = B(-\theta_k + P\chi) \tag{3.42}$$

Substituting back into the energy balance equation we have:

$$P\chi \dot{S}_c = -P \sum \frac{\partial V_p}{\partial \Omega} \dot{\Omega} + \mathbf{s}^* : \mathbf{D}^p_{dev} - B(-\theta_k + P\chi) \tag{3.43}$$

Moreover:

$$\chi \dot{S}_c = \chi\big(\frac{\partial S_c}{\partial \chi} \dot{\chi} + \sum \frac{\partial S_c}{\partial \Omega} \dot{\Omega}\big) = c_o \dot{\chi} + \chi \sum \frac{\partial S_c}{\partial \Omega} \dot{\Omega} \tag{3.44}$$

Using 3.44 in 3.43 yields:

$$Pc_o\dot{\chi} = -P\chi\sum\frac{\partial S_c}{\partial\Omega}\dot{\Omega} - P\sum\frac{\partial V_p}{\partial\Omega}\dot{\Omega} + \mathbf{s}^* : \mathbf{D}^p_{dev} - B(-\theta_k + P\chi) \tag{3.45}$$

Where we have introduced the parameter $\mathbf{c_o}$ to approximate $\chi\frac{\partial \mathbf{S_c}}{\partial\chi}$. In general, $\mathbf{c_o}$ may depend on χ but we will assume it to be approximately constant in the susequent calculations. Furthermore, the equations governing the evolution of the set of internal variables $\mathbf{\Omega}$, namely 3.18 and 3.19 , are stiff differential equations as they do not have a prefactor Λ, typically a very small number, compared to the equation governing the plastic strain rate 3.17. Thus, we may assume that the internal variables Ω evolve on a much faster time scale than the compactivity and invoke a stationarity approximation $\dot{\Omega} = 0$ as in previous work [129]. The above equation then simplifies to:

$$Pc_o\dot{\chi} = \mathbf{s}^* : \mathbf{D}^p_{dev} - B(-\theta_k + P\chi) \tag{3.46}$$

The thermal transport coefficient B may be determined from steady state condition $\dot{\chi} = 0$ and $\chi = \hat{\chi}$ uniformly:

$$B = \frac{\mathbf{s}^* : \mathbf{D}^p_{dev}}{-\theta_k + P\hat{\chi}} \tag{3.47}$$

Thus we arrive at the evolution equation for the compactivity:

$$Pc_o\dot{\chi} = (\mathbf{s}^* : \mathbf{D}^p_{dev})(1 - \frac{-\theta_k + P\chi}{-\theta_k + P\hat{\chi}}) \tag{3.48}$$

We assume isothermic conditions and without loss of generality we take $\theta_k = 0$. Rearranging terms we derived the compactivity evolution equation:

$$\dot{\chi} = \frac{\mathbf{s}^* : \mathbf{D}^p_{dev}}{Pc_o}(1 - \frac{\chi}{\hat{\chi}}) \tag{3.49}$$

The above equation states that only a fraction of the external work rate $\mathbf{s}^* : \mathbf{D}^p_{dev} = s^*_{ij}D^p_{ij}$ is dissipated to increasing χ as it is driven toward its steady state value $\hat{\chi}$ [156]. This fraction is given by $1 - \chi/\hat{\chi}$. The coefficient c_o sets a scale for the amount of work required to increase the compactivity. The larger c_o the slower the evolution of χ is. The steady state value of the effective temperature is rate dependent in the limit of high strain rates $\hat{\chi}(q) = A/\log(q_0/q)$, where $q = \tau_o\dot{\gamma}$ is the dimensionless strain rate [127, 147, 148, 156]. However, at strain rates significantly below a critical value, given by the inverse of the inertial time scale τ_o^{-1} , this rate dependence is weak and the steady state is almost

a constant χ_∞ [129, 130]. For the parameters used in this study, the critical strain rate is of the order of $10^7/s$ which is orders of magnitudes higher than the strain rate of interest here. We will therefore adopt the approximation that $\hat{\chi} = \chi_\infty$ and thus our results represent the rate-independent limit.

3.2.4 STZ Isotropic Plasticity Model

Here we follow Pechnick [153] and Langer [154] in their formulation of the isotropic plasticity model within the effective temperature framework and adapt it to the compactivity based formulation.

The rate of orientational bias tensor $\dot{m}_{ij}$ evolution equation Eq. 3.18 is a stiff differential equation, there is no prefactor on the right-hand side to produce slow relaxation as the term Λ in the plastic strain rate D^p_{ij} governing equations Eq. 3.17. Therefore, we may set $\dot{m}_{ij} = 0$ and replace m_{ij} by its instantaneous equilibrium value for which the right hand size of Eq. 3.18 vanishes. Moreover, for an isotropic system in which the only orientations are set by the stress tensor s_{ij}, we must have:

$$m_{ij} \to \frac{s_{ij}}{\bar{s}} M(\bar{s}) \tag{3.50}$$

where $M(\bar{s})$ is the stationary solution of Eq. 3.18.

To make further progress in solving Eq. 3.18 we must constrain the expression for the mechanical noise strength term Γ. We invoke the Pechenik hypothesis [153] that states that Γ is directly proportional to the plastic work done per STZ:

$$\Gamma = \frac{\tau_0 s_{ij} D^p_{ij}}{\epsilon_0 s_0 \Lambda} = \frac{2 s_{ij}}{s_0} C(\bar{s}) [\frac{s_{ij}}{\bar{s}} \mathcal{T}(\bar{s}) - m_{ij}] \tag{3.51}$$

where s_0 is an as-yet undetermined factor with the dimension of stress.

Using Equations 3.50 and 3.51 in Eq. 3.18, the stationary solution of Eq. 3.18, $M(\bar{s})$, is as follows:

$$M(\bar{s}) = \frac{s_0}{2\bar{s}}[1 + \frac{\bar{s}}{s_0}\mathcal{T}(\bar{s})] - \frac{s_0}{2\bar{s}}\sqrt{[1 + \frac{\bar{s}}{s_0}\mathcal{T}(\bar{s})]^2 - 4\frac{\bar{s}}{s_0}\mathcal{T}(\bar{s})} \tag{3.52}$$

Simplifying the above equation, we find $M(\bar{s})$ to be:

$$M(\bar{s}) \to \begin{cases} \mathcal{T}(\bar{s}) & \bar{s}/s_0\mathcal{T}(\bar{s}) < 1 \\ s_0/\bar{s} & \bar{s}/s_0\mathcal{T}(\bar{s}) \geq 1 \end{cases} \tag{3.53}$$

Thus, s_0 turns out to play the role of the minimum flow stress.

We now turn to Eq. 3.36 to discover additional constraints on our constitutive response from the dissipation inequality. If N is the total number of STZs and v_z the excess volume per STZ, then the total volume V can be expressed as:

$$V = N\Lambda v_z + V_1[S_C - S_z(\Lambda, M)] \tag{3.54}$$

where S_z denotes the entropy associated with the STZs. Then from [157]:

$$S_z(\Lambda, M) = NS_0(\Lambda) + N\Lambda\psi(M) \tag{3.55}$$

where

$$S_0(\Lambda) = -\Lambda\ln(\Lambda) + \Lambda \tag{3.56}$$

$$\psi(M) = \ln 2 - \frac{1}{2}(1+M)\ln(1+M) - \frac{1}{2}(1-M)\ln(1-M) \tag{3.57}$$

With two internal variables STZ density Λ and STZ orientational bias tensor m_{ij}, we could rewrite Eq. 3.36 as:

$$\mathcal{D} = s_{ij}D^p_{ij} - P\frac{\partial V_p}{\partial\Lambda}\dot{\Lambda} - P\frac{\partial V_p}{\partial m_{ij}}\dot{m}_{ij} \geq 0 \tag{3.58}$$

Using Eqs. 3.54, 3.55, 3.56 and 3.57 to write the dissipation rate $\mathcal{D}$ as:

$$\begin{aligned} \frac{\tau_0\mathcal{D}}{v_z N} =& -\Gamma P\chi\Lambda m_{ij}\frac{d\psi}{dm_{ij}} \\ &+ 2\Lambda C(\bar{s})[\frac{s_{ij}}{\bar{s}}\mathcal{T}(\bar{s}) - m_{ij}](\frac{\epsilon_0}{v_z}s_{ij} + P\chi\frac{d\psi}{dm_{ij}}) \\ &- P\Gamma(\Lambda^{eq} - \Lambda)\Big\{1 + \chi[\ln\Lambda - \psi(M) + m_{ij}\frac{d\psi}{dm_{ij}}]\Big\} \end{aligned} \tag{3.59}$$

We could replace the m_{ij} in Eq. 3.59 with $\frac{s_{ij}}{\bar{s}}M(\bar{s})$:

$$\begin{aligned}\frac{\tau_0\mathcal{D}}{v_z N} =& -\Gamma P\chi\Lambda M(\bar{s})\frac{d\psi}{dM(\bar{s})}\frac{s_{ij}s_{ij}}{\bar{s}} \\ &+ 2\Lambda C(\bar{s})[\mathcal{T}(\bar{s}) - M(\bar{s})](\frac{\epsilon_0}{v_z} + \frac{P\chi}{\bar{s}}\frac{d\psi}{dM(\bar{s})})\frac{s_{ij}s_{ij}}{\bar{s}} \\ &- P\Gamma(\Lambda^{eq} - \Lambda)\Big\{1 + \chi[\ln\Lambda - \psi(M(\bar{s})) + M(\bar{s})\frac{d\psi}{dM(\bar{s})}\frac{s_{ij}s_{ij}}{\bar{s}^2}]\Big\}\end{aligned} \tag{3.60}$$

Since $\mathcal{D} \geq 0$, all three terms should be individually non-negative. The first term is automatically satisfied as:

$$\frac{d\psi}{dM} = -\frac{1}{2}\ln(\frac{1+M}{1-M}) = -\tanh^{-1}(M) \tag{3.61}$$

For the second term we need:

$$\mathcal{T} = \tanh(\frac{\epsilon_0\bar{s}}{v_z P\chi}) \tag{3.62}$$

Recalling the definition of $\mathcal{T}$ in Eq.3.16 and the symmetry of rate factors, we may assume $R(\bar{s}) = \exp(\frac{\epsilon_0\bar{s}}{v_z P\chi})$. Thus, higher stresses activate more transitions, while higher configurational disorder is reflective of a very noisy system, thereby reducing the transition rate. Assuming that reverse STZ transitions are negligible $R(-\bar{s}) \approx 0$, we may replace $C(\bar{s}) \approx \frac{1}{2}R(\bar{s}) = \frac{1}{2}\exp(\frac{\epsilon_0\bar{s}}{v_z P\chi})$ and $\mathcal{T}(\bar{s}) \approx 1$

The third term of Eq.3.60 may be cast as $-\frac{\partial F(\Lambda,M)}{\partial\Lambda}(\Lambda^{eq} - \Lambda) \geq 0$, assuming $F(\Lambda, M)$ represents a free energy-like function for the configurational subsystem. Using the non-negativity condition, we get:

$$\Lambda^{eq} = \exp[-\frac{1}{\chi} + \psi(M) - M\frac{d\psi}{dM}\frac{s_{ij}s_{ij}}{\bar{s}^2}] \approx 2\exp(-\frac{1}{\chi}) \tag{3.63}$$

The equilibrium density of STZs is given by a Boltzmann-like factor in the compactivity. Furthermore, the STZ density Λ evolve on much faster time scale relative to the compactivity χ. This may be justified by looking at the evolution equation of compactivity 3.49 which depends on plastic strain rate. The evolution of the latter 3.17 is directly proportional to STZ density while the evolution equation of Λ is not. Therefore, We can assume Λ to be always at their instantaneous equilibrium values.

$$\Lambda = \Lambda^{eq} = 2\exp(-\frac{1}{\chi}) \tag{3.64}$$

Now we could derive the final form of the plastic strain rate tensor:

$$\tau_0 D^p_{ij} = \frac{1}{2}\epsilon_0 R(\bar{s})\Lambda^{eq}\frac{s_{ij}}{\bar{s}}[1 - M(\bar{s}))] \tag{3.65}$$

Expanding the expression for $M(\bar{s})$ and substitute the expression for $R(\bar{s})$, $\mathcal{T}(\bar{s})$ and Λ^{eq} we have:

$$D_{ij}^{p} = \begin{cases} \tau_0^{-1}\epsilon_0 \exp(-1/\chi)\exp(\frac{\epsilon_0 \bar{s}}{v_z P \chi})[1 - \frac{s_0}{\bar{s}}]\frac{s_{ij}}{\bar{s}} & \bar{s} \geq s_0 \\ 0 & \bar{s} < s_0 \end{cases} \tag{3.66}$$

Where s_0 is the minimum flow stress. The above formula indicates that no plasticity occurs if $\bar{s} < s_0$. Thus, it is possible to interpret $\bar{s} = s_0$ as the initial (local) yield surface equation. The value of s_0 is a function of many system variables including the grain shape, surface roughness, contact temperature, etc. Here we assume s_0 to linearly depend on the first invariant of the stress tensor I_1 as commonly observed in frictional geological materials. That is, we define $s_0 = \alpha_1 - \alpha_2 I_1/3$, in which α_1 is the cohesion of material and α_2 is the tangent of the internal friction angle of the material [158]. The assumption we are making here is that there is no plastic flow when the stress level is lower than the stress threshold should be considered as only an approximation. In future work, we plan to expand the model to incorporate more physical processes that enable plastic flow below the stress threshold. This includes for example, creep [137], acoustic vibrations [129, 130], and granular fluidity [159, 160]. For example, it was shown previously that acoustic vibrations, may tend to fluidize the granular system, analogous to temperature effects in glasses, and enable plastic flow at stresses less than the mechanical minimum flow stress [130, 148].

The volumetric strain rate is directly proportional to the rate of compactivity. As stated in Eq. 3.44 with the assumption that $\dot{\Lambda} = 0$ and $\dot{m}_{ij} = 0$:

$$\dot{V}_p = \frac{\partial V_p}{\partial S_c}\frac{\partial S_c}{\partial \chi}\dot{\chi} = \chi\frac{\partial S_c}{\partial \chi}\dot{\chi} = \alpha_{eff}\dot{\chi} \tag{3.67}$$

where α_{eff} is an effective volume expansion coefficient. Assuming volumetric deformation to be isotropic, the inelastic volume strain rate tensor is given by:

$$\mathbf{D}_{vol}^{p} = \alpha_{eff}\dot{\chi}\mathbf{I} \tag{3.68}$$

Here, $\mathbf{I}$ is the identity tensor.

3.3 Numerical implementation

We implement the STZ constitutive model within a finite deformation finite element framework provided by Moose platform from Idaho National Lab. The Multi-Physics Object Oriented Simulation Environment (Moose) [161] provides a flexible platform to solve multi-physics problems implicitly and in a tightly coupled manner on unstructured meshes. Moose framework is built on top of libraries including the Libmesh finite element library [162] and PETSc solver library [163]. The solution of the nonlinear equations of motion (dynamic equilibrium) is done using Jacobian-free Newton-Krylov (JFNK) approach [164]. The algorithm for the plastic strain rate and stress update (material model update) is summarized in Appendix B.

Model Setup: We consider a layer of granular materials sheared between two parallel planes and subjected to a constant pressure at the top and the bottom as shown in Fig. 3.2(a). To mimic an infinite long strip, periodic boundary conditions are enforced at the left and right boundaries. At the center of the granular material, we introduce a perturbation in the local disorder by defining a circular inclusion with higher initial compactivity (aka less dense) than the surrounding bulk. To ensure the quality of the solution, an h-refinement study has been conducted to verify convergence with increasing resolution. The material properties that are used in the simulation are summarized in Table 3.1.

Table 3.1: List of parameters used in the simulations for the default case. Simulation with different initial compactivity χ, confining pressure P and the effective heat capacity c_o were also carried out and are indicated in the respective sections

Symbol	**Description**	**Value**	**Remark**
E	Young's Modulus	7GPa	Range: 100 MPa (loose aggregate) - 70 GPa (grain scale)
ν	Poisson ratio	0.4	Range: 0.2-0.45 [165]
h	Layer thickness	0.2m	Arbitrary
w	Width of the granular material	0.2m	Arbitrary
α_1	Cohesion	0.0	Neglect cohesion
α_2	Tangent of the internal friction angle	0.6	Typical value for sand (www.geotchdata.info)
ρ	Material density	1600 kg/m^3	[166]
ϵ	STZ plastic strain	1.0	Corresponding to a particle sliding a distance equal to its diameter
c_o	Effective volume capacity	0.025	Range for dilative materials: 0.001$\sim$1.0 leading to volumetric strains between 0.01% $\sim$10% [129]
α_{eff}	Effective volume expansion coefficient	0.025	Taken as same value as c_o
$\hat{\chi}$	Steady-State dimensionless compactivity	0.08	Material system specific. May be adjusted to fit experiments on steady state dilation [129, 167].
χ_o	Initial compactivity	0.04	Depends on initial preparation. Adjustable parameter [129].
a	Grain size	1.0×10^{-4}m	Constrained by sample particle size distribution
P	Confining Pressure	10 MPa	Constrained by experiments or depth

The loading in each simulation is a two-stage process. In the first loading step we solve a static equilibrium problem for the applied pressure at the top and bottom (assuming periodic boundary conditions at the sides). Then we apply the shear loading. To achieve a constant strain rate, we adopt a ramp loading technique in which we change the strain rate from zero to the prescribed constant value over a finite period of time using a fifth order of polynomial in time. This ensures a smooth profile for the displacement, velocity and acceleration at the top and bottom boundaries throughout the loading history. Since our simulation is fully dynamic, this ramping reduces the effect of waves that may be

generated due to an abrupt change in the loading rate during the elastic regime. We assume periodic boundary conditions for the compactivity on the lateral sides, and zero flux condition across the top and bottom boundaries of the granular layer.

3.4 Results

3.4.1 Generic Shear band localization

With the circular inclusion having a slightly higher compactivity than the rest of the granular layer, plasticity starts in that zone first. Due to the interdependence between the compactivity and inelastic strain rate (Eq. 3.49, 3.66), this positive feedback causes localization of the plastic deformation in the inclusion and favors the regions in its immediate vicinity to accommodate further inelasticity. This leads to the nucleation of shear bands from the circular inclusion and their subsequent growth. As shown in Fig. 3.2(b), the resulting localization pattern, as measured by the distribution of the compactivity, agrees well with the schematic describing field observation as summarized in [119]. In particular, our numerical results capture the Riedel "R1", boundary and Y-bands.

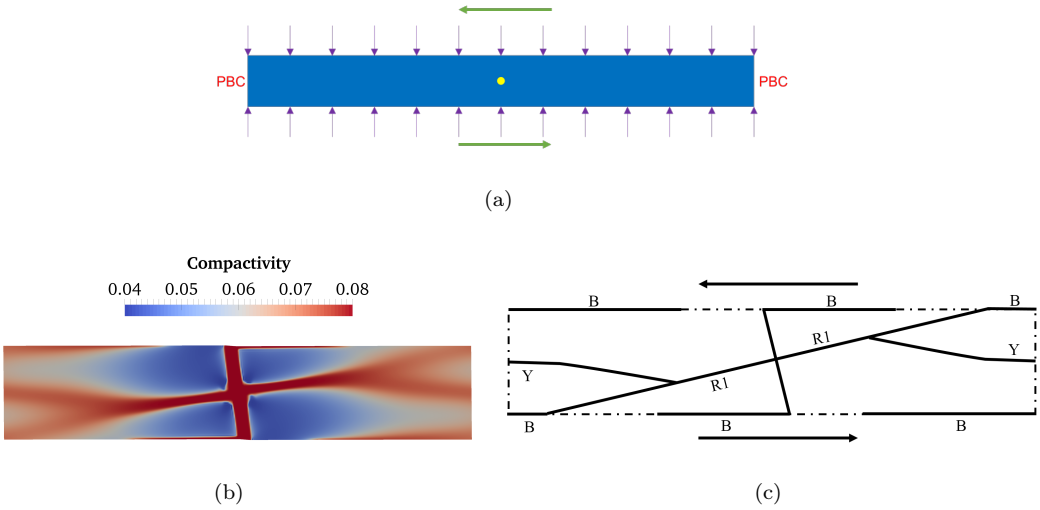

Figure 3.2: (a) The setup of the simulated gouge layer. The layer is 2.0 m long and 0.2 m wide. Pressure is applied on the top and bottom surfaces. Shear loading is applied on the top and bottom boundaries. The shear loading is left lateral as indicated by the green arrow. Periodic boundary conditions are imposed on the lateral edges. The yellow circle is an inclusion introduced to trigger localization by having a higher initial compactivity than the background fault gouge (indicated by blue color).(b) The distribution of compactivity at steady state from the numerical simulation. In particular, the numerical simulations generically capture the "R1, Y" and boundary shear bands. The results have qualitative agreement with results in [119]. (c) A schematic drawing illustrating the distribution of shear bands ("R1, Y" and Boundary shear bands) from the numerical simulations. B: Boundary Shear Band; Y: "Y" Shear Band; R1: "R1" Shear Band (Simulation Parameters: $\chi_o = 0.04$, $c_o = 0.025$, $P = 10$ MPa)

To further explore the relation between the stress slip response and shear bands propagation, we show in Fig. 3.3 the evolution of the localization patterns and its correlation with different stages in the stress slip plot. Initially, the response of the layer is elastic. With the initiation of plasticity in the central inclusion, the global response does not change much. However, with progressive shearing, the region with inelastic strain grows and diagonal bands start to propagate. With the localization of plastic deformation in the growing shear bands, the local inelastic strain rate increases causing the initiation of strain softening. This continues as the diagonal bands (primary and secondary R bands) propagate towards the top and bottom boundaries of the sample where new boundary bands start to develop. As the stress response approaches the steady state, the through-going Y-band becomes more visible. Interestingly, the Y-band seems to emanate from the primary Riedel shear band by curving out of it at some point during the softening stage before becoming fully developed. This picture of the

stress slip response alongside the compactivity evolution and localization bands development agrees qualitatively with the experimental observations of strength and microstructure evolution discussed in [120].

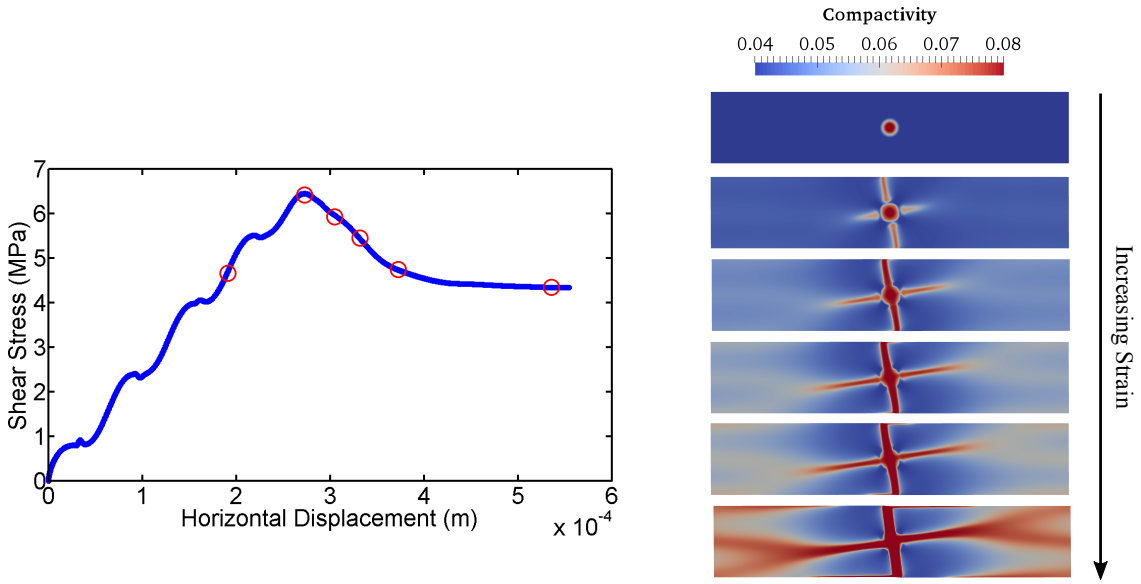

(a) (b)

Figure 3.3: Fault gouge strength evolution and the shear band formation. (a) Stress slip response. (b) The distribution of compactivity at successive time steps corresponding to the order of the red circles on (a). At first the specimen is deforming elastically. With the initiation of the shear band from the center inclusion, diagonal bands start to form, and grow to the upper and lower boundary forming the Riedel shear bands, and then the primary Riedel shear band bifurcates to Y bands which fully develop near steady state. (Simulation Parameters: $\chi_o = 0.04$, $c_o = 0.025$, $P = 10$ MPa)

3.4.2 Factors affecting shear localization

The effect of dilatancy

One relevant feature in the STZ formulation is that the inelastic dilatancy coefficient is not prescribed but it evolves as part of the solution. To show this let's consider the theory formulation in homogeneous 1D setting. The evolution of the compactivity reduces to: $\dot{\chi} = \frac{s\dot{\gamma}}{c_o P}(1 - \chi/\hat{\chi}) = \frac{\dot{V}}{\alpha_{eff}}$ It follows that the dilatancy parameter is given by: $\beta = \frac{\dot{V}}{\dot{\gamma}} = \frac{\alpha_{eff}}{c_o}(1 - \chi/\hat{\chi})\mu$ where $\mu = s/p$. Thus the dilatancy evolves as a function of stress, pressure and disorder. In the absence of additional constraints, we hypothesize that α_{eff} and c_o are of the same order of magnitude and we take them to be equal.

We vary c_o to investigate the effect of inelastic dilation on the stress slip response and shear band evolution. The results are shown in Fig. 3.4. As the value of c_o increases, the compactivity increases more slowly, the peak stress increases and more localization is observed. This behavior is characteristic of dilatant media. On the other hand, if c_o becomes small enough the inelastic dilatancy is negligible and occurs almost instantaneously and the subsequent response becomes more ductile-like with no noticeable strain localization.

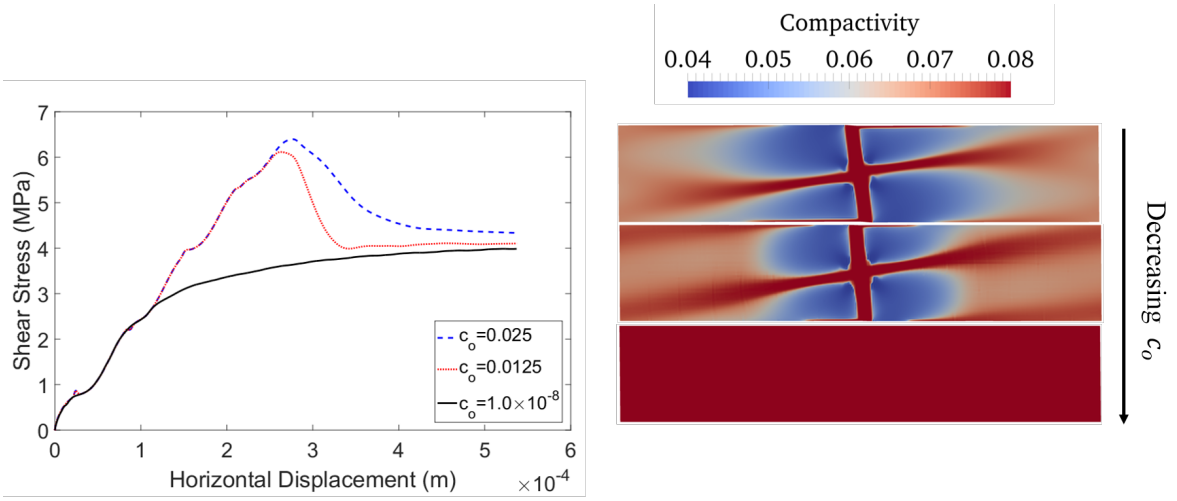

Figure 3.4: Dilatancy effect on strength evolution and strain localization. (a) The stress slip response for different c_o (b) Distribution of compactivity χ for different c_o at final slip. With decreasing value of c_o, the specimen shows a ductile behavior with no noticeable strain localization is formed when c_o is negligible. (Simulation Parameters: $\chi_o = 0.04$, $P = 10$MPa)

The effect of Ramping Protocol (Inertia Effect)

In this section, we investigate the possible inertia effects induced by ramping the shear loading differently from the default case. We keep the steady-state imposed strain rate value constant and a fifth order polynomial is used for strain rate interpolation but we progressively increase the time period over which the ramping occurs. As shown in Fig. 3.5, with the increase of the ramp loading period, the shear band is more distributed, and the Y band development is less distinct than in the default case. Furthermore, with increasing the ramping time, the elastic regime becomes smoother due to the absence of the small stress perturbations carried by the propagating waves. The results suggest that, while the inertia effect doesn't change the overall qualitative features of the strain localization pattern, the Y-band is more mature under quicker ramping. A possible explanation for this is that under

quicker ramping, waves emanate from the top and bottom boundaries and interfere constructively in the middle of the layer causing stronger localization. This may have implications for co-seismic strain localization in which the strain rates increase rapidly at the rupture tip possibly favoring the Y-band formation more. The growth of the reversed diagonal band is not visibly affected by the ramping rate.

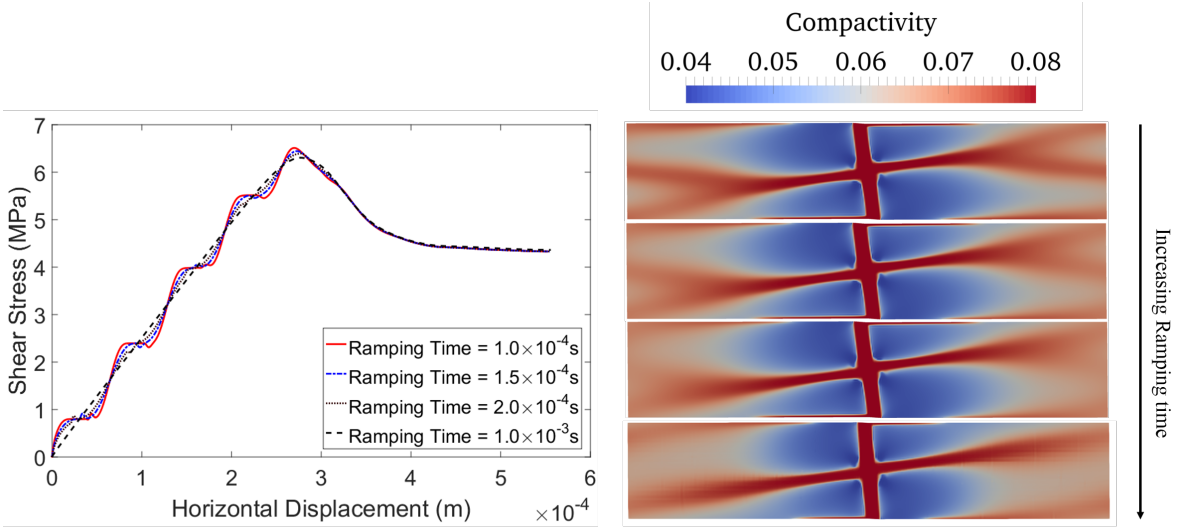

Figure 3.5: Effect of ramping rate on the shear localization. (a) The shear stress slip curve with different ramping time of the imposed strain rate (steady state value = 4/s). (b) The corresponding distribution of compactivity at final slip. With shorter ramping time, the bifurcation from Riedel band to Y band is more observable. Longer ramping time causes smoother elastic response and the Y shear band is not as well developed as with the small ramping time. (Simulation Parameters: $\chi_o = 0.04$, $\chi_o = 0.04$, $P = 10$MPa)

The effect of confining pressure

In this section, we vary the applied confining pressure P on the top and bottom of the fault gouge specimen, and study its effect on strength and shear and evolution. Fig. 3.6 shows that with the increasing confining pressure, the specimen exhibits a brittle to ductile transition. We define a brittle behavior by the existence of a strength drop and localized deformation, whereas in ductile response these features are absent. The observed transition as a function of pressure may be explained as follows. At higher pressures, the minimum flow stress s_o increases. This delays the initiation of plasticity and increases the peak stress as well as the steady state flow stress. However, with increasing pressure,

the characteristic time scale for STZ transition τ decreases (Eq. 3.66) enabling faster accumulation of inelastic strains and disorder (similar to the effect of reducing c_o discussed previously). At low pressure, the plasticity accumulates slowly causing the stress to peak followed by strain softening and brittle behavior. At high pressure, the plasticity accumulates quickly after its initiation and is distributed across the layer leading to gradual saturation of the strength without any softening signatures. This is also reflected in the compactivity plots where strain localization is evident at low pressures but shear bands are diffusive and distributed across the sample width at higher pressure.

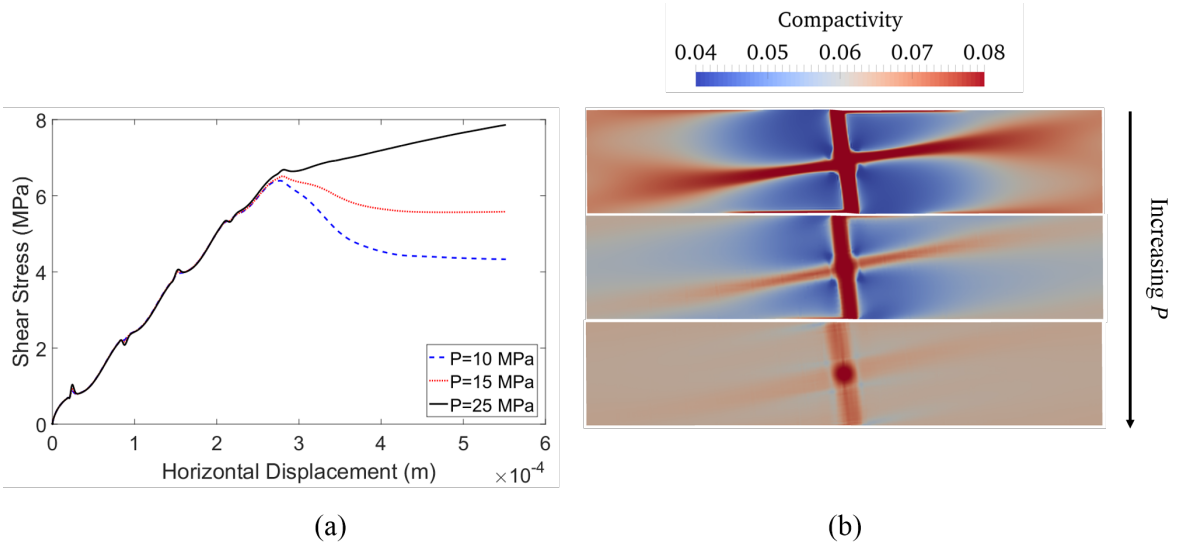

Figure 3.6: Effect of confining pressure on shear localization. (a) Shear slip response with different confining pressure values 10MPa, 15MPa, 25MPa.With increasing pressure, the peak and flow stress increase while the strength drop decreases (b) The compactivity distribution for the different confining pressure at the final slip. From top to bottom, the confining pressure is increasing. The plasticity is distributed across the sample at higher pressure while the strain is more localized in bands at lower pressures. (Simulation Parameters: $\chi_o = 0.04$, $c_o = 0.025$)

The effect of initial compactivity

The initial preparation of the sample may affect its subsequent response. In another amorphous system, namely bulk metallic glasses, it was shown that a well-aged sample exhibits a brittle response whereas a more disordered sample exhibits a ductile response [168]. A similar observation has been documented for granular materials where the initial relative density plays a similar role to the degree of aging. That is, an initially dense sample exhibits a brittle response whereas an initially loose sample

is ductile [120, 169, 170, 171, 172]

Here, we examine the effect of initial disorder on the brittle to ductile transition in sheared confined layers. We consider two cases: one with the default background compactivity $\chi = 0.04$ and the other with higher initial background compactivity $\chi = 0.06$ (closer to steady state value of 0.08). The results are shown in Fig. 3.7, where we plot the stress strain response as well as snapshots of the final compactivity distribution. For higher initial compactivity, and despite the existence of the central inclusion, it is more favorable for the sample to distribute plastic strain across the whole layer. Even if the inelastic deformation starts from the central inclusion, the disorder is high enough everywhere to accommodate plasticity shortly after. This leads to a ductile behavior in the sense that the stress progressively increases towards steady state without exhibiting a peak or strain softening. Furthermore, the plastic deformation is well distributed across the layer with no visible localization. On the other hand, with lower initial compactivity, the behavior is brittle. The inelastic deformation is localized in the center inclusion and the shear bands that grow and propagate out of it. The stress peaks at a certain slip and then goes through strain softening phase before eventually reaching a steady state value.

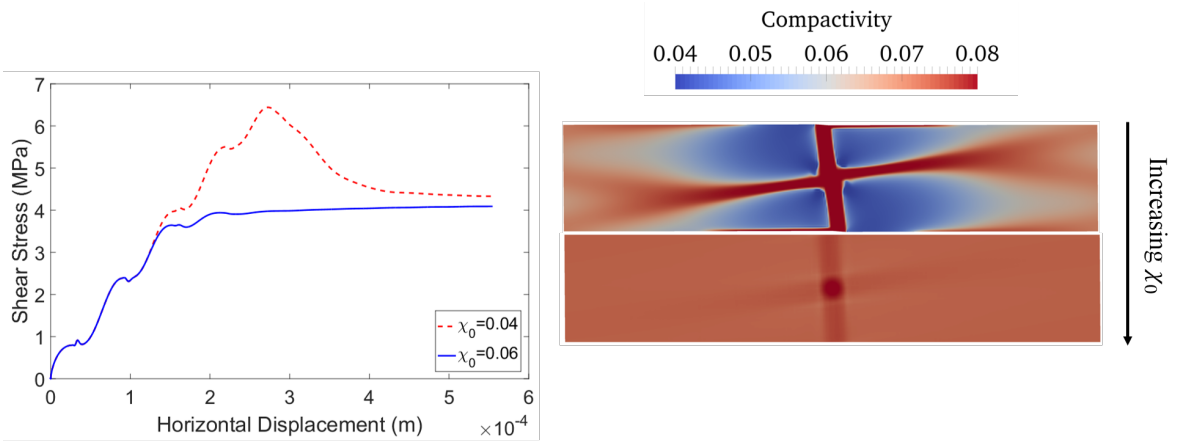

Figure 3.7: Brittle to ductile transition as a function of initial compactivity. (a) Stress slip response with different initial compactivity χ_o. (b) The distribution of compactivity at steady state. With lower initial compactivity, the response is brittle with strain localization softening. (Simulation Parameters: $c_o = 0.025$, $P = 10$MPa)

Compactivity χ is related to porosity [129] and changes in compactivity relates to changes in pore

volume as discussed earlier (assuming incompressibility of the granular particles). Higher initial compactivity corresponds to higher initial porosity. Thus, our results suggest that initially dense layers exhibit brittle response while initially loose layer exhibit a ductile one. The brittle to ductile transition as a function of initial preparation agrees with some experimental observations [173].

We have also tested the response corresponding to a random distribution of the initial compactivity. The random fields have spatial correlations represented by a Gaussian function in the Fourier space with different widths of the frequency filter F. We construct these random fields as follows. We first generate a normal random distribution (pure white noise)and apply a Fourier Transformation to it. Next, in the frequency domain, we apply the Gaussian filter with certain width F. A smaller F value corresponds to longer spatial correlations. Then, we apply an Inverse Fourier Transformation on the filtered field and take the real part of the solution for the random field in space. By varying F value, we could test different initial field correlation effects on the material behavior. Here we show two case with $F = 100$ and $F = 5$. In both cases, the initial random compactivity is between 0.04 and 0.05 . The results are shown in Fig. 3.8. The localization pattern is richer than the default case and exhibit more complexity. Conjugate shear bands emanate from multiple nucleation sites and interact with each other resulting in a complex localization texture. This pattern is qualitatively similar to the localization bands observed in experiments on analogue materials as well as in natural fault zones [119, 174, 175]. With small value of F, the random field for the initial compactivity is more spatially correlated, and more major shear band with larger thickness are formed. With large value F, the random field for initial compactivity is less spatially correlated, and a large number of small thickness conjugate shear bands is formed. The initial conditions may be tuned to generate a wide variety of localization patterns. The influence of different initial conditions on shear band dynamics and establishing a link between the Gaussian filter width and the characteristics of the microstructure [176] will be a focus of a future investigation.

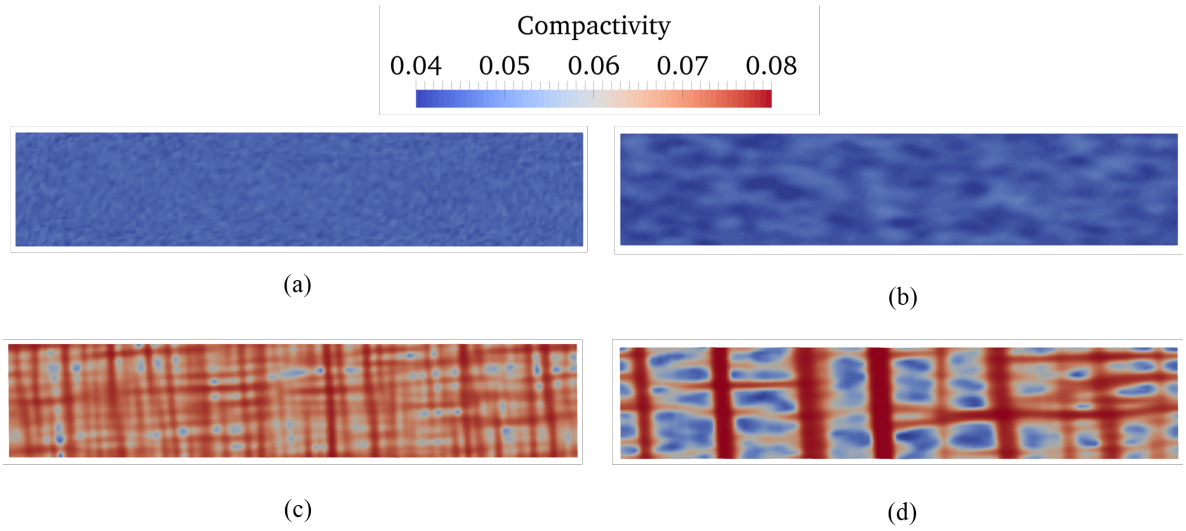

Figure 3.8: Strain localization for random initial compactivity generated using Gaussian filter of width F in the Fourier domain (see text for explanation). (a) The initial random compactivity distribution with $F = 100$ (b) The distribution of compactivity at the steady state with $F = 100$. The random initial compactivity lead to a complex network of shear bands. More shear bands with small thickness are formed with smaller correlation value. (c) The initial random compactivity distribution is uniformly distributed with $F = 5$ (d) The distribution of compactivity at the steady state for $F = 5$.With larger correlation length, the shear band formation are more distinct into several major shear bands. (Simulation Parameters:$\chi_o = 0.04 \sim 0.05$, $c_o = 0.025$, $P = 10$MPa)

The effect of layer thickness

It is natural to expect that the localization pattern depends on the layer thickness since the shear band has a finite length scale and for narrow enough layers, boundary interactions become important. We investigate the evolution of shear bands for three values of the layer thickness: 0.1m, 0.2m, and 0.3m, sheared at the same loading velocity. As shown in Fig. 3.9, for the smallest thickness, the inelastic deformation almost fully saturates the layer and there is no distinct Riedel band. At intermediate thickness, there is more space for the Riedel band to grow and reach the boundary. The Y-band also starts to develop. Boundary interactions still exist as evident by the development and growth of boundary shears at the right bottom and top left edges. For the largest thickness considered, the Y-band bifurcates at an earlier stage. The Riedel shear continues to grow towards the boundaries. However, the development of the boundary shears is delayed due to the absence of interaction of the

boundaries with either the central inclusion or the Riedel bands.

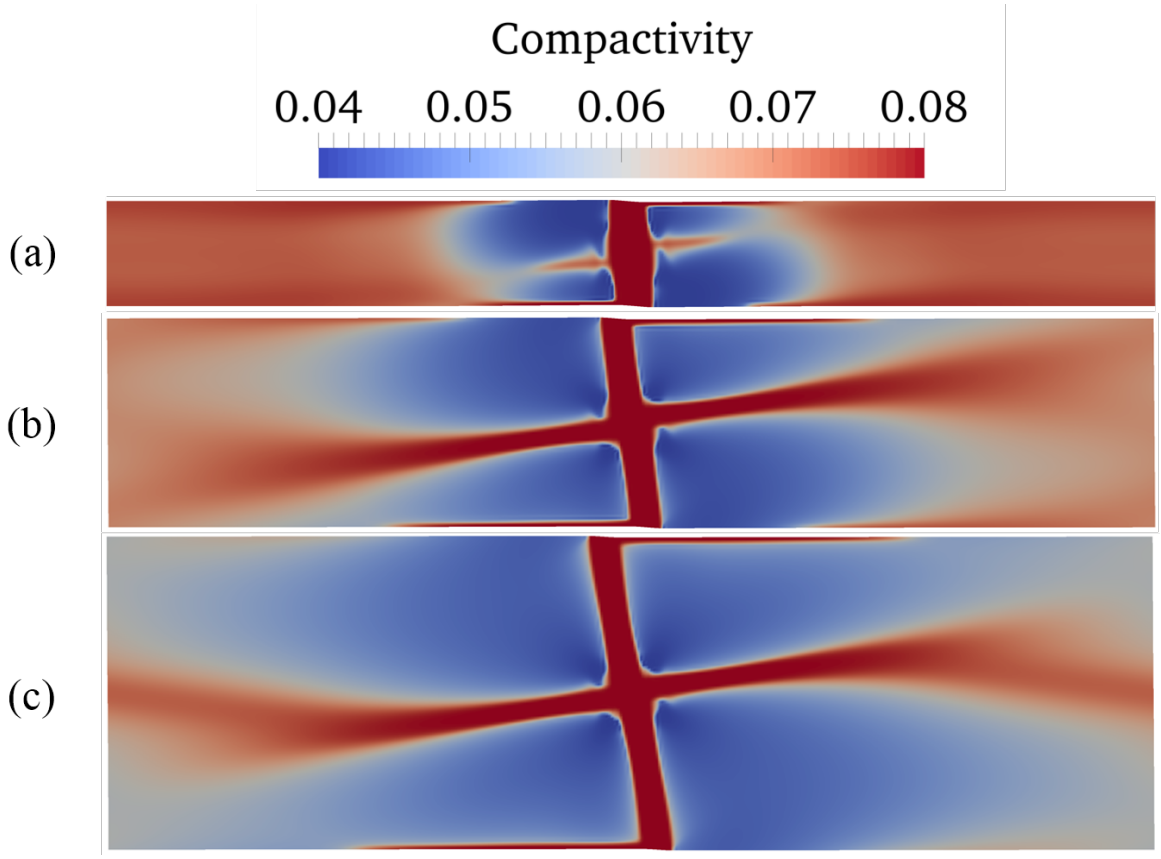

Figure 3.9: Effect of layer thickness on shear localization. (a) Thickness $h = 0.1$m: the shear bands fully saturate the layer and no distinct Riedel band is formed (b) Thickness $h = 0.2$m: The Riedel band forms as well as boundary shears. The Y-band starts to develop (c) Thickness $h = 0.3$m: The Y-band bifurcates at an earlier stage compared to case (b) with less visible boundary shears. (Simulation Parameters:$\chi_o = 0.04$, $c_o = 0.025$, $P = 10$MPa)

The effect of size of the perturbation

The size of the inclusion representing the initial perturbation in the compactivity distribution is an important length scale that contributes to determining the shear band thickness. We have run simulations with different radii of the central inclusion: 0.005m, 0.01m, 0.02m. As shown in Fig. 3.10 as the radius of the inclusion decreases, the thickness of the shear band emanating from the inclusion also decreases. However, the shear band broadens as it propagates due to the nature of the steady state of compactivity in our model. Since we have assumed that the steady state compactivity is constant, accommodation of increasing plastic slip is only possible through increasing the width of the shear

bands which allows accumulation of more plastic strain and strain rate.

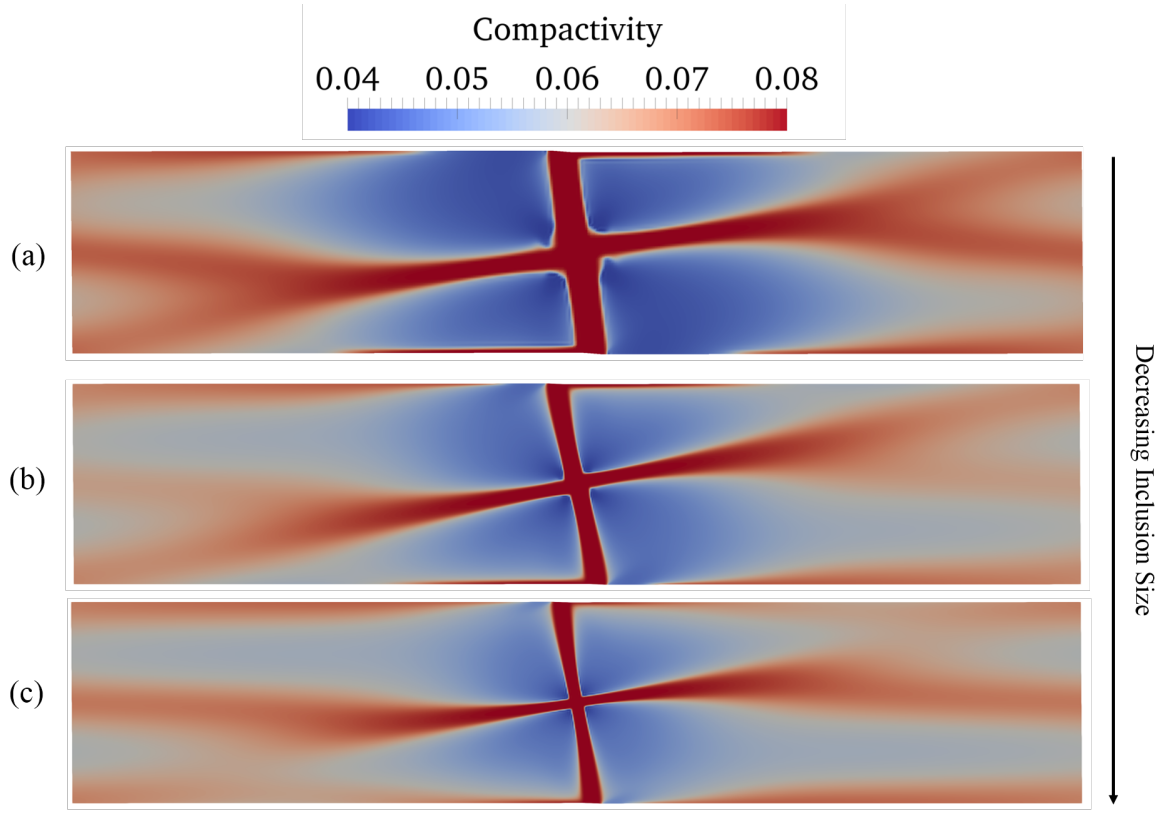

Figure 3.10: Effect of inclusion size on shear localization. (a) The radius of the inclusion circle $r = 0.02$m. (b) The radius of the inclusion circle $r = 0.01$m (c) The radius of the inclusion circle $r = 0.005$m. With smaller inclusion size, the thinner the shear band is. (Simulation Parameters:$\chi_o = 0.04$, $c_o = 0.025$, $P = 10$MPa)

3.5 Discussion

Understanding deformation and failure in granular materials is a problem of both fundamental importance and practical relevance. This is because many natural phenomena as well as industrial processes are controlled by the physics of granular deformation. Earthquakes, and landslides, as well as pouring, transportation, and mixing in food and pharmaceutical industries are just few examples where granular rheology, especially that which involves the shear response due to local particle rearrangement, is of direct relevance. In many circumstances, the granular deformation is not macroscopically uniform but localizes in shear bands. This is particularly the case for crustal faults in which amble evidence exist that co-seismic deformation localizes in thin regions within broad damage zones [124]. In this study,

we presented a numerical model for the evolution of viscoplastic deformation in a sheared granular layer under constant pressure with spatially heterogeneous porosity-like parameter. Using the model, it was possible to investigate the strength evolution and shear band development under different loading conditions.

The viscoplastic formulation adopted here is based on the shear transformation zone (STZ) theory, a non-equilibrium statistical thermodynamic framework for describing rate dependent inelastic deformation in amorphous materials. The STZ theory belongs to the broader class of constitutive laws with internal state variables [177]. Only the initial yield surface is defined but subsequent hardening or softening is computed as part of the solution by integrating the evolution equations of the internal variables. There have been prior fundamental work for investigating localization and plasticity in pressure sensitive materials (See for example, [178, 179, 180, 181, 182, 183]). Most of the prior work has implemented phenomenological constitutive models. One point of departure in the current work is that the primary internal variable, the compactivity, has a clear interpretation as a measure of local disorder in the system and possesses a formal connection to fundamental thermodynamic quantities such as volume and entropy. Furthermore, the flow rule in the STZ formulation is consistent with a microscopic picture of transition dynamics of defects (STZs flipping and sliding). These features make the STZ distinct from other widely used plastic models such as Cam-Clay, Mohr-Coulomb and Drucker-Prager models and enable direct connection with small scale molecular dynamics or discrete element models.

A widely used constitutive model for friction in rocks and granular materials is the rate and state law [135, 136]. Despite its phenomenological nature, the rate and state formulation has led to significant progress in describing several sliding phenomena particularly in bare rock surfaces experiments. The inclusion of the slip rate history, through state variables, in addition to the instantaneous slip rate in evaluating the friction coefficient has been a leap forward from earlier friction laws (see for example, the discussion in [184]). However, the lack of physical interpretation of the state variables in the Dieterich-Ruina laws limits their predictive capability especially when it comes to gouge layers. While in principle, it is possible to include more than one state variable to capture increasingly complex behavior, constraining the evolution equations of these internal variables is not straightforward. An advantage of the STZ theory in that context is that it is based on the laws of thermodynamics and the state variable evolution is constrained by energy flow and entropy evolution. In the past few years, the STZ framework has been successfully extended to incorporate physical phenomena critical

for gouge mechanics such as grain fragmentation [133], flash heating [137], dilation and compaction under combined shear and vibration [129, 134, 148]. Furthermore, extending STZ theory to higher dimensions (2D and 3D) is possible, enabling investigation of strain localization and inhomogeneous plastic deformation. It is not obvious how the rate and state friction may be consistently generalized to higher dimensions, despite some prior notable attempts (e.g.[185])

While the STZ theory provides a powerful framework for describing the multiphysics of spatially extended gouge layers, the physics-based nature of the theory comes at a price: there are more parameters to be constrained in the STZ theory than in the rate and state framework. Fortunately, many of these parameters may be constrained based on physical arguments or from classical experiments. For example, Daub and Carlson [127] have shown, using a simple block slider setup, that it is possible to derive quantities analogous to the direct effect, slip evolution distance, and rate sensitivity parameter, by taking various partial derivatives of the STZ equations at both the transient and steady state limits with respect to strain rate. Using this procedure, experiments like velocity stepping as well as slide-hold-slide tests may be used to constraint several STZ parameters. Other parameters may be freely adjusted to fit experimental observations (see Table 3.1) or derived directly from subscale discrete element models.

The theoretical basis of the STZ framework makes it also possible to connect to more detailed microscopic models such as molecular dynamics and discrete element models. Many experiments and numerical simulations have been done to study the behavior of the glassy material [121, 168, 186, 187]. Different approaches in modeling the plasticity in amorphous system have also been proposed including soft glassy rheology [188], free volume model [189, 190, 191], granular fluidity [159, 160], discrete STZ approach [192] as well as hierarchical continuum-discrete models [193]. Recently, molecular dynamics simulations of glassy systems have made significant progress in identifying STZs using analysis of soft modes [194] or susceptibility of molecular clusters to yielding [195]. By counting the number of STZs in a given volume, the effective temperature may be directly computed using the Boltzmann distribution in STZ density. Thus, a quantitative measure of the effective temperature may be established. Furthermore, microscopic models may help in constraining parameters in the rate factors as well as those connecting the compactivity and volume changes (dilatancy). In principle, it may be possible to do more detailed studies using subscale discrete element models that communicate with the quadrature points of our finite elements. This integrated approach will provide a truly multiscale and predictive formulation for gouge deformation and is a candidate for future work.

The STZ formulation does not just compare well to rate and state friction in capturing basic features of sliding response [127] but it may also highlight additional physics that may help modify the rate and state laws. For example, the internal state variable in the STZ formulation, the compactivity, is driven by the inelastic work rate and not only by the slip (or strain) rate as in the classical evolution laws for the rate and state friction. The dependence of the compactivity on the work rate follows directly form the first law of thermodynamics and suggests that the evolution of the state variable should depend on the stress as well as the strain rate. This remains to be tested in friction experiments by carrying stress stepping tests in addition to velocity stepping ones. Furthermore, there has been some previous notable attempts for incorporating porosity evolution in the classical rate and state law and accounting for inelastic dilatancy [196, 197]. In this prior work the dilatancy factor was assumed to be constant. In the current work, the dilatancy evolves as part of the solution and depends on pressure, stress and disorder.

In this study, we have investigated stress slip response and shear band evolution in sheared granular layers under different conditions of confining pressure, dilation, and loading rates. We have shown that our numerical predictions agree qualitatively with many generic features of gouge deformation reported lab and field observations such as different shear band orientations, brittle to ductile transition with increasing confining pressure, brittle to ductile transition as a function of initial porosity, and increase in the peak strength with increased dilatancy. However, the range of parameters explored here was rather limited. For example, the confining pressure was only increased from 10 MPa to 25 MPa. Strain rates were imposed at 4/s. Seismogenic conditions may require testing gouge response up to hundreds of MPa of confining pressure and at strain rates up to 100 or 1000/s. The range of parameters considered in this study is thus closer to experimental conditions than to field conditions. Although our model is continuum in nature but it is computationally intensive. Higher strain rates and higher pressures (Which decreases the inertia time scales) require use of finer spatial meshes and smaller time steps and high performance computing platforms. Extension to high pressures and strain rates will be the focus of future investigations.

In this study, we have adopted a constant value for the steady state compactivity. This results in a regularization of the strain localization mechanism as it forces the shear band to get wider to accommodate more plastic slip. While this may be justified by the fact that the strain rates considered in this study is orders of magnitude smaller than those where granular inertia lead to significant rate strengthening effects, we would like to note that other scenarios for shear band width variation may be

physically plausible. For example, nonlocal effects due to acoustic vibrations or granular fluidity may further diffuse the shear band and broaden it [130, 198]. On the other hand, thermal effects due to shear heating of fluids or flash heating at grain contacts [124, 137] may lead to rate dependent thinning in the shear band thickness and extreme localization. The competition between these different physical mechanisms is a topic worthy of future investigation.

In this study, We have considered an isotropic formulation of plasticity. No apriori constraint has been imposed on the transition kinematics of the STZs and thus there were no preferred slip directions. The pressure dependence of the response in this case originates from its influence on the volumetric strain. However, several observations exist suggesting that shear bands in geological materials as well as bulk metallic glasses may form in a preferential direction and show asymmetry between compression and tension [199, 200, 201, 202, 203] . Prior work [204, 205] has accounted for this phenomenologically by incorporating explicitly preferred slip plane directions in the formulation of the plastic strain rate tensor. A more physics based approach is still needed in which the anisotropy of the fabric (shape of the granular particles) is incorporated and lead to a bias in the STZ orientations. Some prior work has made progress in this direction by using an extra state variable to account for the particle shape [134]. A more fundamental approach will introduce direction dependent transition probabilities, i.e. direction dependent R factor, in the plastic strain rate expression and relax the proportionality between the STZ orientational bias tensor and the deviatoric stress.

In the last three decades, significant progress has been achieved in testing gouge layers at different pressures and loading rates. However, challenges still exist when it comes to mimicking conditions prevailing during earthquakes. For example, the increase in temperature at large slip velocities and pressures may melt the machine rim. Also, it is hard to confine the gouge layer at high slip rates. Furthermore, most high speed frictional experiments are of the rotary type [206, 207, 208, 209]. This prevents capturing physics associated with rupture propagation or inhomogeneity of slip conditions. The model explored in this study will contribute to closing this knowledge gap. By extending prior work, that has been done in the context of 1D shear zone, through including additional physics related to grain fragmentation [133], flash heating [137], and pore fluid pressurization [126] to the current 2D viscoplastic formulation it will be possible to predict gouge response under extreme condition, capture extreme localization and investigate competition between gouge dilatancy (captured in the current model) and pore fluid thermal pressurization.

In this study, we have considered dry granular layers as a first step. Given that most fault zones are fluid infiltrated, it is important to couple the current viscoplastic formulation with an equation for pore fluid pressure evolution in response to gouge volume changes. Furthermore, at high strain rates, shear heating will be high enough to cause constrained expansion of pore fluids leading to thermal pressurization. Future work will focus on integrating temperature and pore pressure evolution in the current model. Moreover, our recent work [134, 130, 148], inspired by experiments of [166] and discrete element models by [210], suggest that acoustic vibrations may cause transient compaction, alter the stability of sliding in frictional fault gouge, trigger slip, and cause strain delocalization. Extending these results to higher dimensions (2D and 3D) will allow exploring the effect of vibrations on slip, and localization in spatially heterogeneous conditions which may have important implications for triggered earthquakes and slow slip [134]. Finally, we acknowledge that fault zones have 3D structures. The current plane strain formulation can be extended to 3D in a straightforward way. However, the computational cost are orders of magnitude higher. We will report on our ongoing efforts in running a 3D implementation of our numerical method on the National Petascale Computing Facility Blue Waters [211, 212] elsewhere.

3.6 Conclusion

In this study, we present a numerical model for shear defamation in gouge based on finite deformation kinematics and the Shear Transformation Zone (STZ) viscoplasticity framework. Our numerical model generically predicts complex shear band localization pattern similar to what is reported in lab and field observations [118, 119, 213]. Our conclusions are summarized as follows:

1. Complex strain localization patterns emerge, with minimum assumptions, including Riedel, boundary, and Y-bands. The Riedel band follows the direction of the optimally oriented shear plane and emanate first from the initial disorder perturbation. With increase slip, the Y-band starts to emerge and propagate. The boundary shear bands emerge due to the interaction of the Riedel shear and the sample boundaries.

2. With increased dilatancy, the peak strength increases and the response becomes more brittle. At negligible dilatancy, the response is ductile and no shear bands form.

3. With increased pressure, both the peak strength and the steady state flow stress increase. However, the response shows a brittle to ductile transition with increased pressure.

4. With increased initial disorder (aka increased initial porosity) a brittle to ductile transition is also observed. For initially loose layer, the shear stress progressively increases towards the steady state value and the plastic deformation is distributed across the layer. For initially dense layers, the shear stress reaches a peak followed by strain softening and a complex shear band pattern emerges.

5. The full development of the Riedel, boundary, and Y-shears require a thick enough gouge layer. In a thin layer (where the thickness is of roughly the same magnitude as the initial perturbation) the plastic deformation is distributed across the layer and the response is ductile. With progressively increasing the layer thickness, at a constant imposed slip rate, the Riedel and Y-bands develop.

Chapter 4

A Hybrid Finite Element-Spectral Boundary Integral Approach

The content of this chapter has been published on International Journal for Numerical and Analytical Methods in Geomechanics [214].

Ma, X., Hajarolasvadi, S., Albertini, G., Kammer, D., Elbanna, A. A hybrid finite element-spectral boundary integral approach: Applications to dynamic rupture modeling in unbounded domains. International Journal for Numerical and Analytical Methods in Geomechanics. (August):1–22 (2018)

4.1 Introduction

Earthquake ruptures are highly nonlinear and multiscale phenomena. The nonlinearity may arise at different levels. For example, fault friction may depend on the fault slip, slip rate, and deformation history. Thus, the boundary conditions of the fracture problem are nonlinear and the nucleation, propagation, or arrest conditions evolve with time and space and are unknown a priori [215]. Another source of nonlinearity may come from the bulk being loaded beyond its elastic limit, which leads to damage accumulation and inelasticity. In the case of nonplanar faults, the geometric nonlinearity of the fault traces is another contributing factor that may lead to complex patterns of contact and separation. These features usually inhibit the discovery of analytical solutions for this class of problems. Therefore, numerical methods that are capable of treating these nonlinearities are sought to provide insights into the solution behavior. Bulk methods, such as the finite element method (FEM) and finite difference method (FD), as well as boundary integral methods, are among the most widely used approaches for solving these problems.

Aside from the nonlinearity of computational earthquake dynamics, another major challenge is resolving the multi-scale nature of the rupture, which exists in both space and time. Spatially, an earthquake may involve several kilometers of fault rupture, whereas the principal slip surfaces, where most of the displacement is accommodated, may be on the order of few millimeters [112]. Temporally, the time it takes for the stresses to accumulate and initiate an instability is several orders of magnitude larger than the sudden release of energy during an earthquake episode. Hence, a need exists to develop numerical

algorithms that resolve these spatial and temporal scales.

Attempts to do such cycle simulations with domain-based methods are rare, partially because discretization of the entire domain is a computational bottleneck [216]. On the other hand, boundary integral techniques, which confine the calculations to the fault plane and reduce the dimensions of the problem by one as a result, are more accommodating in this sense. A major contribution in the area was made in the work of Lapusta et al. [16]. Not only did the authors manage to integrate the SBI method into rigorous adaptive time-stepping schemes, but they also introduced the concept of mode-dependent time windows, which made it possible to truncate the convolution integrals. These features enable calculations over long durations while capturing the effects of periods with slow tectonic loading marked by episodes of rapid rupture. The main limitation of this method, however, is that it is applicable only to linear-elastic bulks. Furthermore, for problems involving heterogeneities or rough faults, the ability of the method to provide well-defined solutions is compromised, along with the computational efficacy of the method, because it lacks a closed-form representation for the Green's function, which does not allow a straightforward calculation of the spectral transformation of the space convolutions. This makes the computational investigation of problems with rough faults and fault zone complexity extremely expensive.

Unlike SBI methods, domain-based methods are quite flexible in handling material nonlinearities and small-scale heterogeneities [217, 218, 219] as well as complexities of fault geometry [220, 221, 222]. Lower-order formulations [223, 224, 225, 226, 3, 227] and high-order formulations [228, 229, 21] have been developed over the years. The major limitation of these methods, as discussed previously, stems from the need to discretize the entire domain that may be affected by wave propagation. This, additionally, has led to a wide breadth of research on techniques to truncate the domain without affecting the physical solution, such as boundary viscous damping [230], infinite elements [231], and perfectly matching layers [232]. However, all these approaches are prone to artificial reflections, and the absorbing boundaries must be taken far enough from the fault plane or the accuracy of the problem will be compromised.

To overcome the limitations of either method and benefit from their strengths, one may envision combining the two into what we have referred to here as the hybrid method. In this hybrid approach, a domain-based numerical method is used to discretize a confined region, namely a virtual strip, that contains the fault and all near-field nonlinearities or heterogeneities that may potentially affect the

rupture dynamics. This strip is then coupled with linear-elastic homogeneous half spaces on each side through a consistent exchange of displacement and traction boundary conditions, whereas the elasto-dynamic response of these half spaces is captured by SBI.

This idea was first introduced in [233], where a framework was developed to couple FD and SBI in a consistent manner. This hybrid method was then used to investigate the anti-plane propagation of a slip-weakening shear crack in two different settings: (i) a fault with a near-field low-velocity zone, and (ii) a fault embedded in a homogeneous medium with the possibility of co-seismic inelastic strain generation in the vicinity of the fault. In both cases, the method proved to yield results similar to a pure FD scheme, with a smaller computational cost.

In this research, we further extend the hybrid method. Specifically, we formulate the hybrid scheme as a coupling between FEM and SBI in a 2D in-plane setting. This requires a consistent exchange of both the normal and shear components of boundary tractions and displacements. We validate the method by applying it to benchmark problem TPV205-2D from the Southern California Earthquake Center (SCEC). We further demonstrate the capability of the method for handling ruptures in heterogeneous media, first by simulating a 2D in-plane supershear rupture on a crack embedded in a stiff strip; second by simulating a 2D in-plane model with a crack embedded in a low velocity zone.

The remainder of the study is organized as follows. In Section 2, we describe the model setup and introduce the numerical scheme. In Section 3, we summarize the results of the simulations for the SCEC benchmark problem, the supershear propagation in heterogeneous media, and the pulse rupture induced by low velocity fault zone. In Section 4, we discuss the potential of the method as a novel computational earthquake dynamics tool and suggest some future directions. In Section 5, we summarize the conclusions from the hybrid method.

4.2 Model Setup and Numerical Scheme

We consider a 2D in-plane shear problem in domain Ω, with a prescribed traction boundary S_T and a displacement boundary S_u. The fault is on the boundary S_f.

$$\rho \frac{\partial^2 u_i}{\partial t^2} - \frac{\partial \sigma_{ij}}{\partial x_j} - b_i = 0 \quad \text{in } \Omega \tag{4.1}$$

$$\sigma_{ij} n_j = T_i \quad \text{on } S_T \tag{4.2}$$

$$u_i = u_i^0 \quad \text{on } S_u \tag{4.3}$$

$$R_{ki}(u_i^+ - u_i^-) = \delta_k \quad \text{on } S_f \tag{4.4}$$

where u_i is the displacement vector, b_i is the body force vector, Slip is defined by $\delta_i = R_{ij}(u_j^+ - u_j^-)$, where R_{ij} is the rotation matrix that transforms the global coordinates to the local coordinate system of the fault and superscripts $+$ and $-$ indicate the upper and lower fault sides, respectively. If the fault plane is parallel to the x_1 axis, this simplifies to $\delta = u_1^+ - u_1^-$. σ_{ij} is the stress tensor. We assume body forces to be zero and the material behavior to be linear elastic:

$$\sigma_{ij} = \lambda \delta_{ij} \varepsilon_{kk} + 2\mu \varepsilon_{ij} \tag{4.5}$$

where ε_{ij} is the infinitesimal strain tensor and μ, λ the Lamé parameters.

We construct the weak form by computing the dot product of wave equation Eq.4.1 and the weighting function ϕ_i and considering the boundary condition Eq. 4.2 we could get the following weak form of the governing equation as follows:

$$-\int_V \sigma_{ij} \phi_{i,j} dV + \int_{S_T} T_i \phi_i dS + \int_{S_{f^+}} T_i^{f^+} \phi_i dS + \int_{S_{f^-}} T_i^{f^-} \phi_i dS - \int_V \rho \ddot{u}_i \phi_i dV = 0 \tag{4.6}$$

The integral along S_f accounts for the tractions on the fault surfaces. $T_i^{f^+} = \sigma_{ij} n_j^+$ and $T_i^{f^-} = \sigma_{ij} n_j^-$ where n_j^+ and n_j^- are the fault normals for the positive and negative sides of the faults respectively. The shear component of the fault boundary condition is governed by a friction law. Here, a slip-weakening friction law [234] is used. The frictional strength is given by

$$\tau_f(\delta) = \begin{cases} \tau_s - (\tau_s - \tau_r)\delta/\delta_c, & \delta < \delta_c \\ \tau_r, & \delta \geq \delta_c \end{cases} \tag{4.7}$$

where τ_s and τ_r are the peak and residual frictional strength and δ_c the critical slip required for stress to reach the residual value. Continuity of displacements at the fault is preserved (*i.e.*, no slip) if the shear traction is lower than τ_f, otherwise local slip occurs.

4.2.1 Finite Element Method

The FEM has been widely used in solving wave propagation problems because of its capability of modeling fault structures with complex geometry and a bulk constitutive response. We limit the description here to the time integration scheme and the reader is referred to standard textbooks [235, 236] for detailed information about the FEM. The step-by-step time integration approach is a central-difference explicit formulation and follows

$$\dot{u}^{n+1/2} = \dot{u}^{n-1/2} + \Delta t\, M^{-1}(T^n - f^n) \tag{4.8}$$

$$u^{n+1} = u^n + \Delta t\, \dot{u}^{n+1/2} \tag{4.9}$$

where $\dot{}$ represents the partial derivative with respect to time and the superscript n indicates the time step index. A lumped mass matrix is used, which eliminates the need to form a global stiffness matrix, therefore these are all nodal values and the subscript i is omitted. f is the internal force due to the deformation of the solid and Δt the time step. The time stepping of the algorithm must satisfy the stability constraints of the Courant–Friedrichs–Lewy (CFL) condition [237, 235, 236]. The friction law affects the traction boundary condition, hence along the frictional interface Eq. (5.1) becomes

$$\dot{u}^{n+1/2} = \dot{u}^{n-1/2} + \Delta t\, M^{-1}(T_v^n - f^n). \tag{4.10}$$

A detailed explanation of the computation of frictional tractions at the interface T_v based on the fault displacement discontinuity is provided in Appendix C using the traction-at-split node (TSN) method.

4.2.2 Spectral Boundary Integral Method

The boundary integral method has been used extensively since the mid-1980s to study the propagation of cracks. The main advantage of this method is that it eliminates the need to study wave propagation in the entire domain by using integral relationships between the displacement discontinuities and tractions along the crack path [238]. The spectral formulation for this method gives an exact form of such a relationship in the Fourier domain. We use the spectral formulation introduced in [239], where the elastodynamic analysis of each half space is carried out separately. In view of the hybrid method,

where SBI constitutes a boundary condition to the FEM model, we focus the description on modeling a half-space. The relationship between the traction τ_i and the resulting displacements at the boundary of a half-space may be expressed as

$$\begin{aligned}\tau_1^{\pm}(x_1,t) &= \tau_1^{0\pm}(x_1,t) \mp \frac{\mu}{c_s}\dot{u}_1^{\pm}(x_1,t) + f_1^{\pm}(x_1,t)\\ \tau_2^{\pm}(x_1,t) &= \tau_2^{0\pm}(x_1,t) \mp \frac{(\lambda+2\mu)}{c_p}\dot{u}_2^{\pm}(x_1,t) + f_2^{\pm}(x_1,t)\end{aligned} \tag{4.11}$$

where $\pm$ represents upper and lower half-plane, c_p is the pressure wave speed, c_s is the shear wave speed, τ_i^0 indicates the externally applied load (*i.e.*, at infinity); and f_i are linear functionals of the prior deformation history and are computed by the time convolution in the Fourier domain (see Appendix D for more details on the SBI).

The time integration scheme used in the SBI is explicit and given by sampling

$$u_i^{\pm^{n+1}} = u_i^{\pm^n} + \Delta t \dot{u}_i^{\pm^{n+1}} \tag{4.12}$$

where the velocity is found by solving Eq. (5.5), which results in

$$\begin{aligned}\dot{u}_1^{\pm^{n+1}} &= \pm\frac{c_s}{\mu}(f_1^{\pm^{n+1}} + \tau_1^{0\pm} - \tau_1^{\pm^{n+1}})\\ \dot{u}_2^{\pm^{n+1}} &= \pm\frac{c_p}{\lambda+2\mu}(f_2^{\pm^{n+1}} + \tau_2^{0\pm} - \tau_2^{\pm^{n+1}})\end{aligned} \tag{4.13}$$

4.2.3 Hybrid Method

The hybrid method is a combination of the FEM and SBI, although any other domain-based method may be used in lieu of FEM. In the hybrid method, all nonlinearities, such as fault surface roughness or material nonlinearity, as well as small-scale heterogeneities, are contained in a virtual strip of a certain width that is introduced for computational purposes only (Fig. 4.1). Appropriate meshing techniques are then used to discretize and model this strip by using FEM. The rest of the domain, which is now homogeneous and linear-elastic, may be modeled as two half spaces coupled with this strip on each side (S^+, S^-). The elastodynamic response of these half spaces is captured by using the SBI. Through the simulation, the two methods communicate along the virtual boundaries of the strip by exchanging displacement and traction boundary conditions.

The general setup of the hybrid method is shown in Fig. 4.1. The width W_H of the virtual strip

depends on the nature of the problem and may be adjusted to contain the heterogeneities, nonlinearities, and other fault zone complexities. A more elaborate explanation for how this adjustment may be accomplished is offered in the Discussion section.

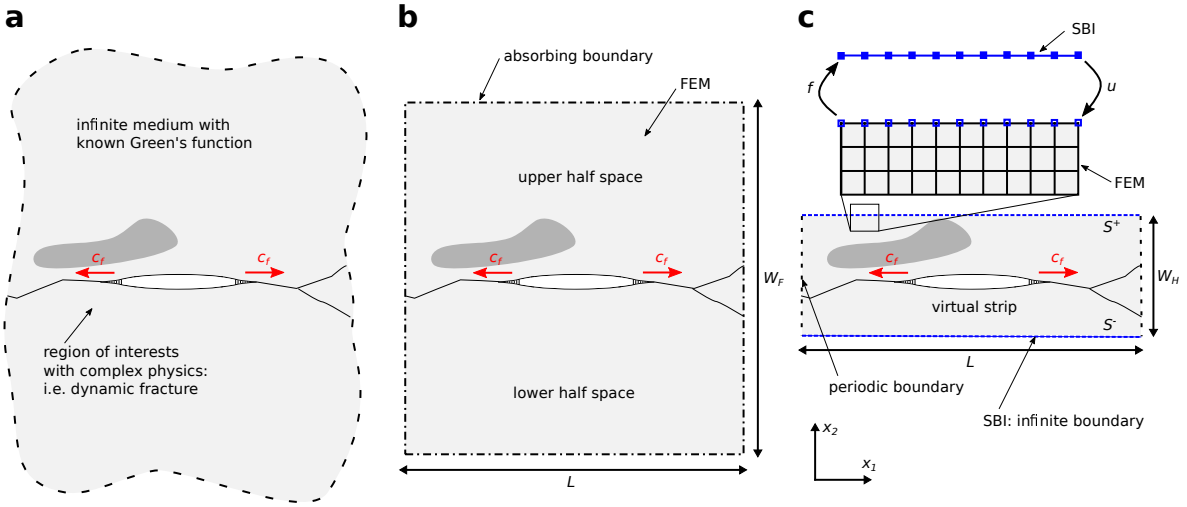

Figure 4.1: Illustration of the hybrid method with coupling of the finite element method (FEM) and spectral boundary integral method (SBI). (a) Schematic illustration of problem of interest. Region of interest with complex physics, such as local heterogeneities and crack branching, is embedded in an infinite medium with known Green's function. (b) Typical FEM simulation needs a discretized area of size LW_F and absorbing boundaries. The simulated medium is relatively large to avoid interference of numerical reflections at the absorbing boundaries with the relevant physics in the region of interest. (c) The hybrid method uses SBI to simulate an infinite boundary, which allows to reduce the zone discretized by FEM to a size of LW_H.

We apply a staggered coupling approach, in which the FEM and SBI share nodes at the (virtual) infinite boundary. The shared nodes are part of the displacement boundary of the FEM. While FEM provides SBI with the tractions along the virtual boundary, SBI returns the displacement that is to be imposed on $S^{\pm}$ of FEM. The detailed step-by-step procedure is as follows

1. Solve full time step within the FEM by solving Eq. (5.1 - 5.2) (FEM interior nodes only).
2. Set interface tractions in the SBI equal to the internal force from FEM: $\tau_i^{n,\mathrm{SBI}} = f_i^{n,\mathrm{FEM}}$, where f_i^n is given through Eq. 5.1.
3. Solve full time step within SBI by solving Eq. (4.13) and (4.12).

4. Set displacements of the shared nodes in FEM equal to displacement in SBI: $u_i^{n+1,\text{FEM}} = u_i^{n+1,\text{SBI}}$.

5. Return to Step 1 to advance to the next time step.

Other approaches with a prediction and correction of the imposed displacement have been tested and have not shown any substantial improvements on the result.

4.3 Results

We validate the hybrid method with three problems. In the first one, we use the SCEC Benchmark Verification exercises [240]. The problem is a dynamic rupture simulation with heterogeneous initial shear stress on the fault. The second problem is a fault embedded in a heterogeneous medium. The third problem is a fault embedded in a Low Velocity Zone (LVZ). For the three problems, we compare the simulation results from the hybrid method with those from the FEM.

4.3.1 SCEC Benchmark Verification

We validate the hybrid method with benchmark problem TPV205-2D from the SCEC Dynamic Rupture Verification exercises. The problem is a 2D in-plane fault, governed by the linear slip-weakening friction law, embedded in a linear-elastic homogeneous bulk under plane strain conditions (see Fig. 4.2(a)). The parameters for the TPV205-2D benchmark are summarized in Table 5.1. The nucleation of rupture is achieved through a 3 km wide overstressed region located at the center of the fault. The initial shear stress on the fault is shown in Fig. 4.2(b), where, in addition to the nucleation patch, there are two other patches of different prestress values from the background uniform initial shear stress. The normal stress is uniform along the entire fault length. On the left and right edges of the fault are two strength barriers with length L_s on each side, which have a high enough static frictional strength to stop the rupture from propagating.

Table 4.1: Problem parameters for the SCEC Benchmark TPV205-2D

Parameter	Symbol	Value
Density (kg/m^3)	ρ	2670.0
Pressure wave speed (km/s)	c_p	6.0
Shear wave speed (km/s)	c_s	3.464
Initial shear stress (nucleation patch) (MPa)	τ_0^{nu}	81.6
Initial shear stress (background) (MPa)	τ_0^{bg}	70.0
Initial shear stress (weak patch) (MPa)	τ_0^{w}	78.0
Initial shear stress (strong patch) (MPa)	τ_0^{s}	68.0
Peak frictional strength (MPa)	τ_s	81.24
Residual frictional strength (MPa)	τ_r	63.0
Slip-weakening critical distance (m)	δ_c	0.40
Fault strength barrier length (km)	L_s	35.0
Fault weakening length (km)	L_W	30.0
Distance between two virtual boundaries (km)	W_H	1.6

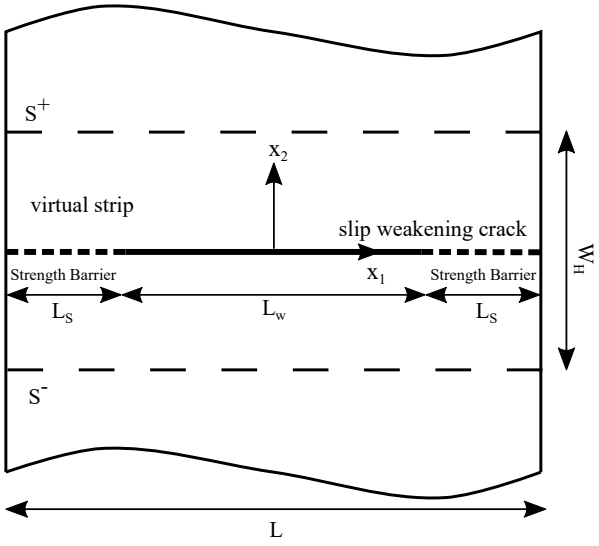

(a)

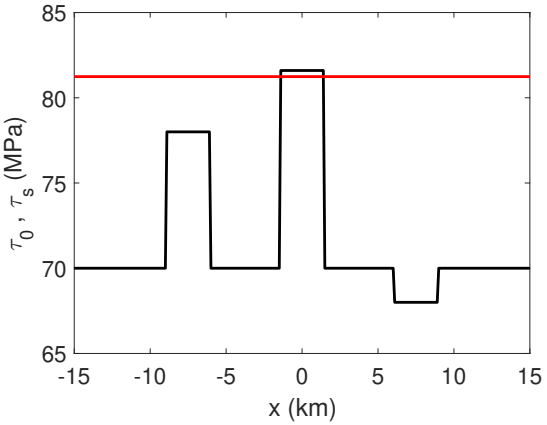

(b)

Figure 4.2: (a) TPV205-2D problem description. The width of the finite element domain is W_H. The fault length is L, with two strength barriers with high-static friction on the left and right edges of the fault with lengths L_s, respectively. The weakening portion of the fault is L_w. (b) Initial shear tractions (in black) on the fault: a strong patch ($\tau_0^w = 68$ MPa), nucleation patch ($\tau_0^{nu} = 81.6$ MPa), and weak patch ($\tau_0^w = 78$ MPa). The static frictional strength is shown in red ($\tau_s = 81.24$ MPa).

We solve the TPV205-2D benchmark with the hybrid method and compare the results with the FEM benchmark results. Fig. 4.3 shows a comparison of the results from the hybrid approach with those of the FEM. Fig. 4.3(a) and 4.3(b) show time history plots of the slip, slip rate, and shear traction at a station at the center of the fault and 4.5 km away from the center, respectively. The results match perfectly. Fig. 4.3(c) shows the spatial distribution of the slip and slip rate with time intervals

of one second, beginning at $t = 1s$ and ending at $t = 5s$. The hybrid scheme accurately captures the rupture nucleation, propagation, and rest. Fig. 4.4(a) shows the variation of the L_2 norm of the error between the solution from the hybrid method and solution from FEM on the fault plane with mesh refinement. The results suggest the hybrid method converges to FEM method with mesh refinement. Fig. 4.4(b) suggests that the absolute error in the slip rate inferred by the two methods at the center of the nucleation zone decreases with mesh refinement. One significant advantage of the hybrid method is its capability of truncating the elastodynamic wave field in the vicinity of the fault plane with no artificial reflections from the virtual boundaries. Specifically for this problem, the full finite element domain is 100 km $\times$ 100 km to ensure that no waves will be reflected from the far-field boundaries. However, in the hybrid scheme, the virtual boundary is chosen at a distance of 0.8 km from the fault plane; thus, we need to discretize a domain of only 100 km $\times$ 1.6 km by FEM. Although the problem under consideration is linear-elastic, it serves the purpose of validating the truncation efficiency of the hybrid scheme. When extrapolated to more complex scenarios, this efficient near-field truncation allows the finite element discretization to be limited within a small strip, leading to potential savings in both computational time and memory cost. Here, for the same mesh size $h = 100m$, solving the TPV205-2D problem by using the FEM takes about 1618 seconds. This value reduces to approximately 62 seconds for the hybrid method, suggesting a speedup of 27 times. The other advantage of the hybrid method over FEM is the computational memory savings. For example, at a $100m$ mesh size, FEM takes approximately 191.4 MB of memory, whereas the hybrid method takes only 58.6 MB. The hybrid method uses only 30 percent of the memory used by the FEM in this case. The savings in computational time and memory cost are expected to become more significant with an increase in problem size and refinement level as we elaborate further in the Discussion section.

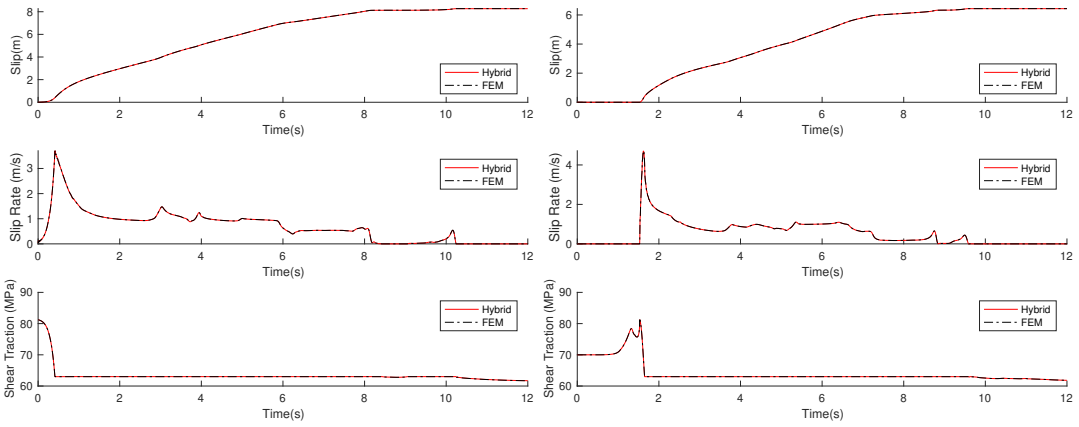

(a) (b)

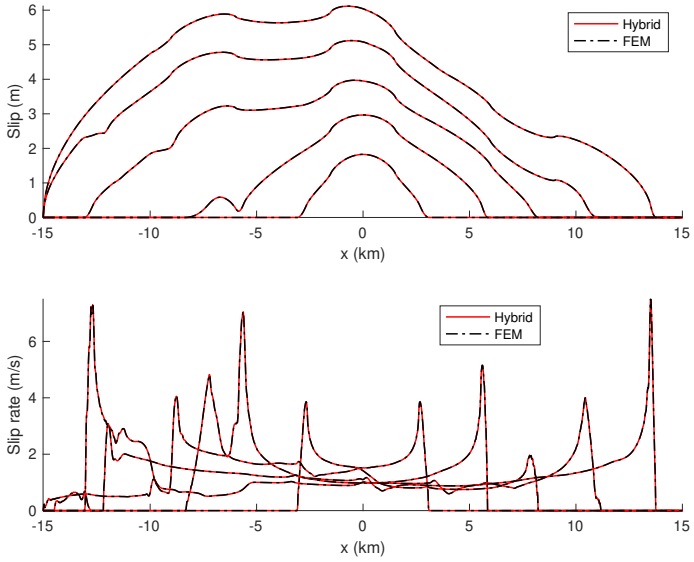

(c)

Figure 4.3: TPV205-2D simulation comparing the hybrid method (in red) with the finite element method (FEM; in black) when using a mesh size of $h = 25m$: (a) Time history of the slip, slip rate, and shear traction at the station in the center of the fault. (b) Time history of the slip, slip rate, and shear traction at a station 4.5 km away from the center of the fault. (c) Snapshots of the slip and slip rate at $t = 1$ s, $t = 2$ s, $t = 3$ s, $t = 4$ s, and $t = 5$ s. The results from the hybrid method match those of the finite element benchmark solution perfectly in the nucleation, propagation, and reset of the rupture. The colored figure is available in the electronic version only.

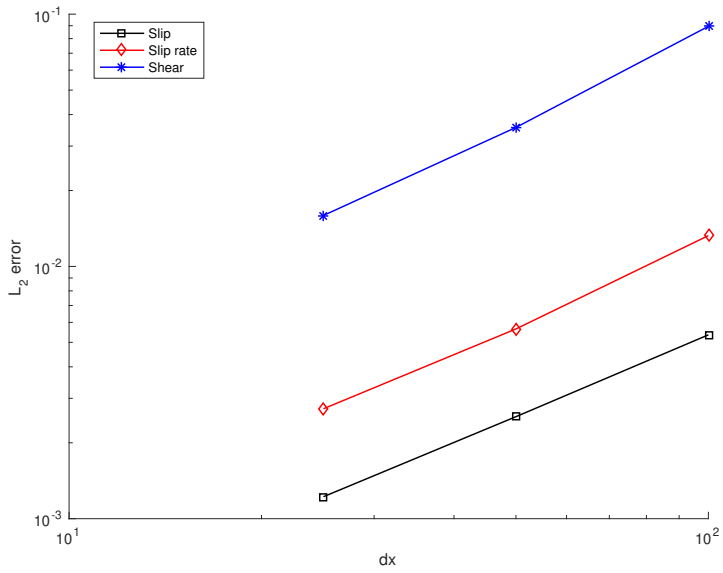

(a)

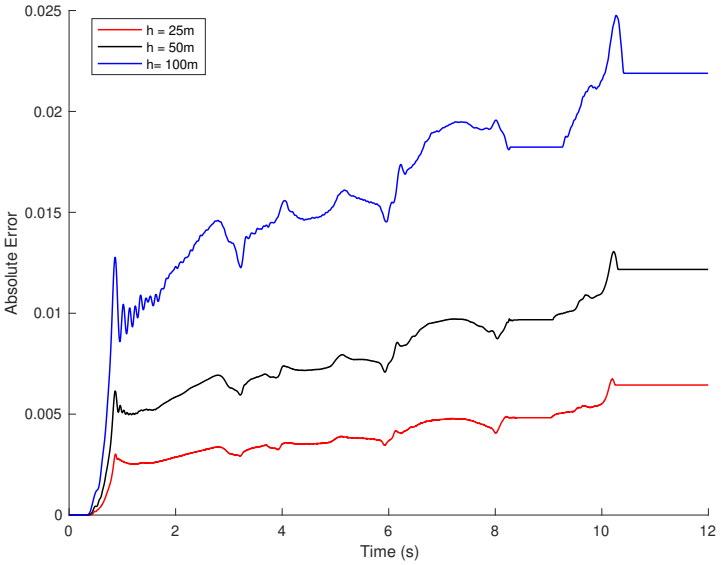

(b)

Figure 4.4: (a) L_2 error for the slip, slip rate, and shear traction versus mesh size. With mesh refinement, the hybrid method converges to the FEM solution, (b) Absolute error of the slip rate measured at the center of the fault and its evolution with respect to time for different mesh sizes, $h = 25m$, $h = 50m$, and $h = 100m$. The error is reduced with mesh refinement. The color figure is available in the electronic version only.

4.3.2 Supershear Rupture Transition in a Heterogeneous Medium

Here, we consider a slip-weakening fault in a heterogeneous medium composed of a central stiff strip and a linear-elastic compliant bulk [241, 242]. The parameters of the problem are summarized in Table 4.2, and the model geometry is described in Fig. 4.5. The initial shear stress is constant along the fault plane except in a central patch where the fault is overstressed to force abrupt nucleation of the dynamic event. The width of the overstressed patch is L_{nuc}, which is the characteristic length scale for frictional instability on linear slip-weakening faults [243]. The normal stress is uniform everywhere. The fault bisects a stiff strip with a total width of $2R$. We choose to locate the virtual boundary at 2.0 km from the fault plane; thus, it is located entirely within the more compliant bulk material.

Table 4.2: Problem parameters for fault-embedded heterogeneous medium

Parameter	Symbol	Value
Density (kg/m^3)	ρ	2670.0
Pressure wave speed (material 1) (km/s)	c_p^{Mat1}	4.8
Shear wave speed (material 1) (km/s)	c_s^{Mat2}	2.771
Pressure wave speed (material 2) (km/s)	c_p^{Mat2}	6.0
Shear wave speed (material 2) (km/s)	c_s^{Mat2}	3.464
Initial shear stress (nucleation patch) (MPa)	τ_0^{nu}	31.0
Initial shear stress (background) (MPa)	τ_0^{bg}	27.5
Peak frictional strength (MPa)	τ_s	30.0
Residual frictional strength (MPa)	τ_r	25.0
Slip-weakening critical distance (m)	δ_c	0.20
Fault length (km)	L	100
Distance between two virtual boundaries (km)	W_H	4.0

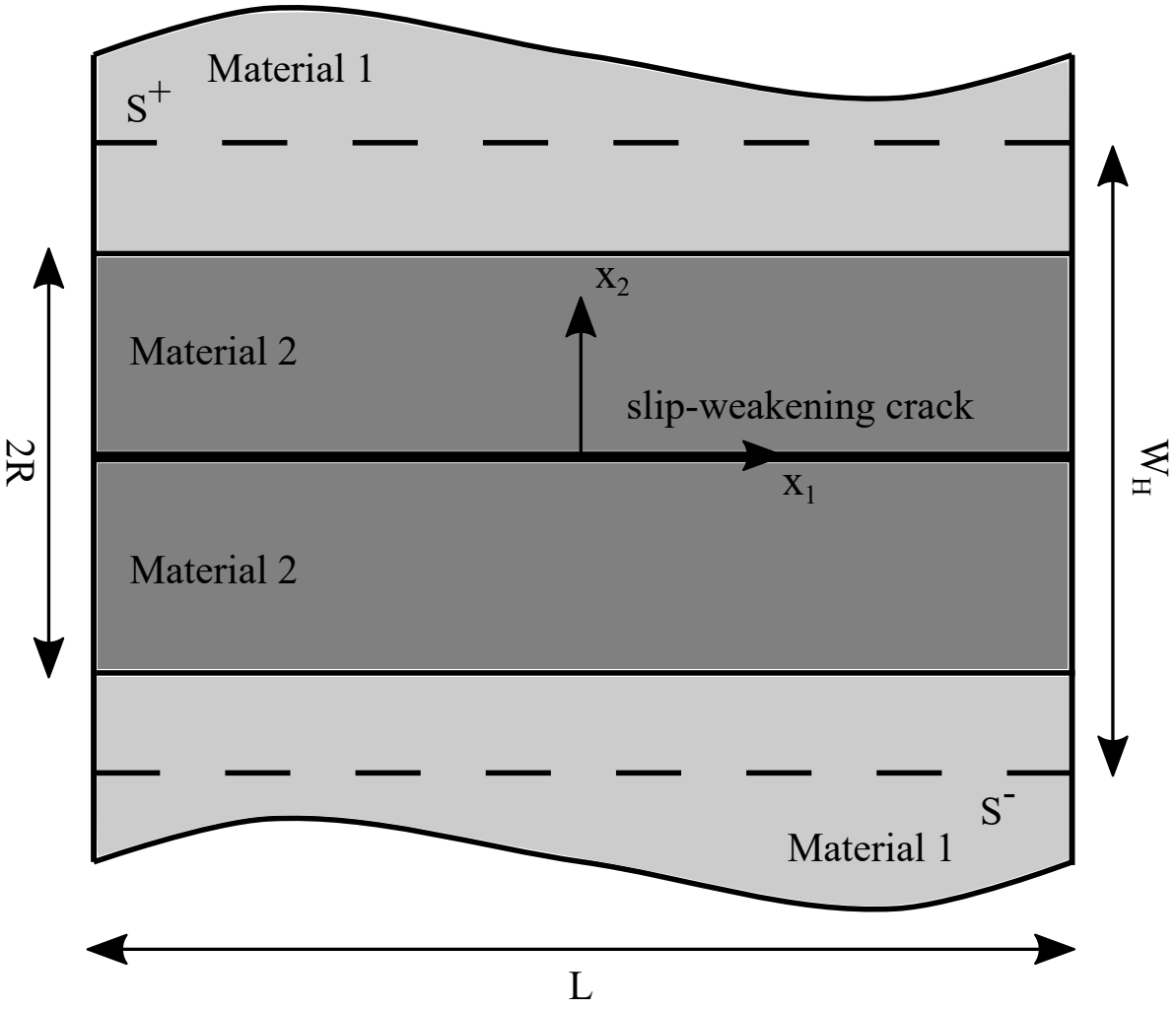

Figure 4.5: Problem geometry description for a fault embedded in a heterogeneous medium. The fault is embedded in a layer with stiffer material properties (material 2), and the surrounding bulk material is material 1. The extension of material 2 from the fault surface is R in each half plane. The virtual boundary is located at $W_H/2$ from the fault surface on each half plane. The length of the fault is L.

We compare the slip, slip rate, and shear traction results from the hybrid method and the FEM (Fig. 4.6(a)) at the center of the fault as well as 4.5 km away from the center (Fig. 4.6(b)). The hybrid method shows excellent agreement with the benchmark finite element solution. Fig. 4.6(c) shows snapshots of the slip and slip rate evolution at times 1, 2, 4, 6, and 8 seconds. Because of the reflection from the bimaterial interface, the reflected waves continuously enhance the rupture and eventually enable the transition from subshear to supershear rupture. Subshear rupture occurs when the rupture speed is slower than the shear wave speed while supershear rupture occurs when the rupture speed exceeds that of the shear wave speed but is lower than the pressure wave speed. The hybrid

method perfectly captures the complexity of the supershear transition through the Burridge–Andrews mechanism [244, 224]. Fig. 4.7 shows the contour of velocity magnitude distribution at the end of the simulation from FEM and the hybrid method. The hybrid method successfully captures the Mach cone signifying the supershear rupture without any artifacts from the domain truncation. The virtual boundaries are perfectly transparent, resulting in no reflection of the Mach cone rays. Fig. 4.8(a) shows L_2 norm of the error between the solution from the hybrid method and the solution from FEM on the fault plane with mesh refinement. The results from the hybrid method converge to ones from FEM with mesh refinement. Fig. 4.8(b) suggests that the absolute error in the slip rate inferred by the two methods at the center of the nucleation zone decreases with mesh refinement. At a 100 m discretization, the simulation time of the hybrid method is approximately 93 seconds, whereas the simulation time of the full FEM is more than 1600 seconds, suggesting the hybrid method is approximately 17 times faster than FEM in this case. Furthermore, in the hybrid scheme, the finite element discretization is limited to a small strip in the vicinity of the fault plane rather than domain-wide discretization. At a 100 m mesh size, the hybrid method uses 77.1 MB of memory, whereas the FEM uses 148 MB. Therefore, the hybrid method uses almost half the memory required by the FEM.

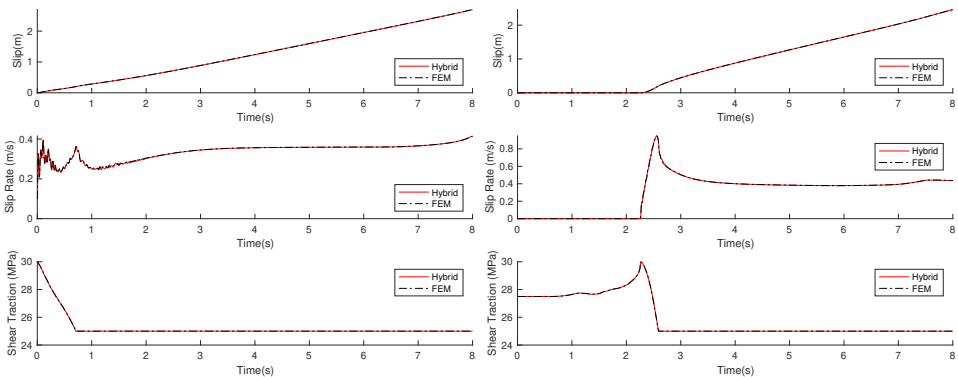

(a) (b)

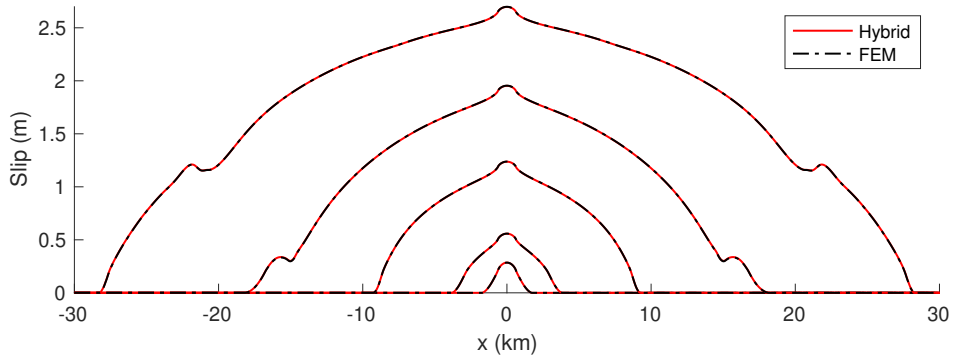

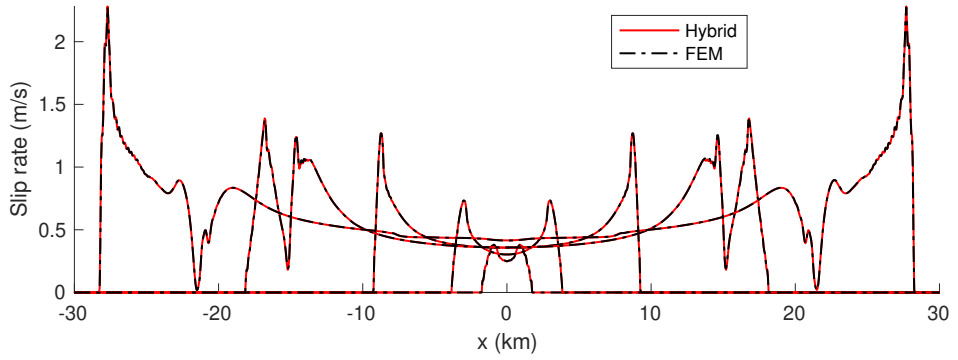

(c)

Figure 4.6: Simulation results for a fault embedded in a heterogeneous medium comparing the hybrid method (in red) and the finite element method (FEM; in black) when using a mesh size of $h = 25m$: (a) Time history of the slip, slip rate, and shear traction at the station in the center of the fault. (b) Time history of the slip, slip rate, and shear traction at the station 4.5 km away from the center of the fault. (c) Snapshots of the slip and slip rate at $t = 1s$, $t = 2s$, $t = 4s$, $t = 6s$, and $t = 8s$. The results from the hybrid method match those from the finite element benchmark solution perfectly in the nucleation, propagation, and reset of the rupture. The color figure is available in the electronic version only.

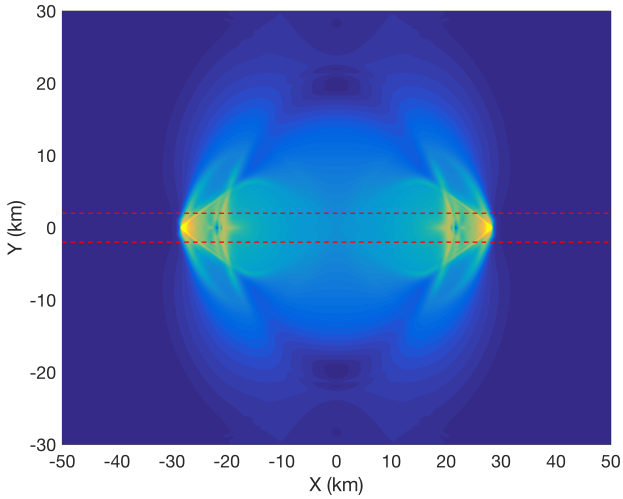

(a)

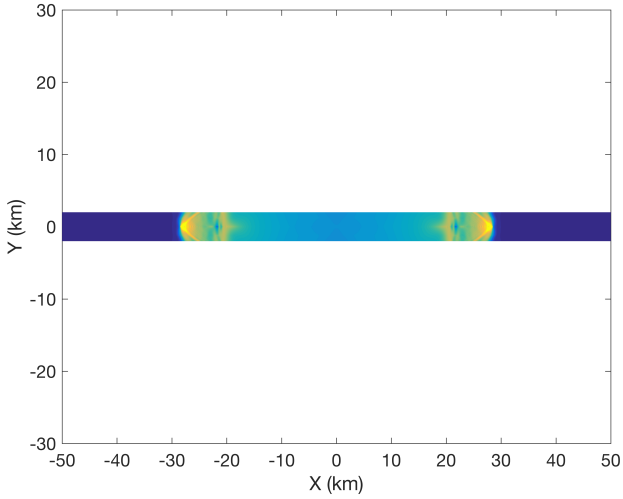

(b)

Figure 4.7: Contour of the velocity magnitude in the field: (a) Finite element method (FEM) results. (b) Hybrid method results. The red dashed line indicates the virtual boundaries located in the hybrid method. The hybrid method captured the truncated Mach cone caused by the supershear rupture. The width of the finite element domain in the hybrid simulation is only 2.4 km, whereas in the FEM simulation, it is 60 km to avoid wave reflection back from the top and bottom boundaries. The hybrid method significantly reduces the computation time and computational memory costs. The color figure is available in the electronic version only.

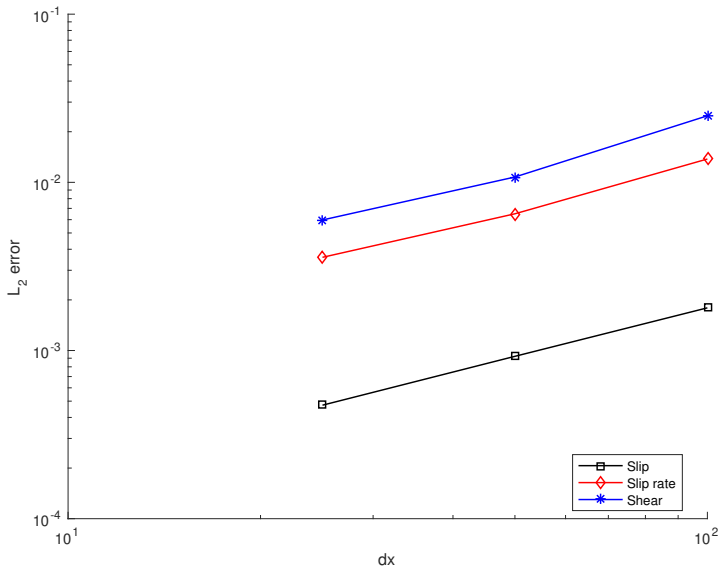

(a)

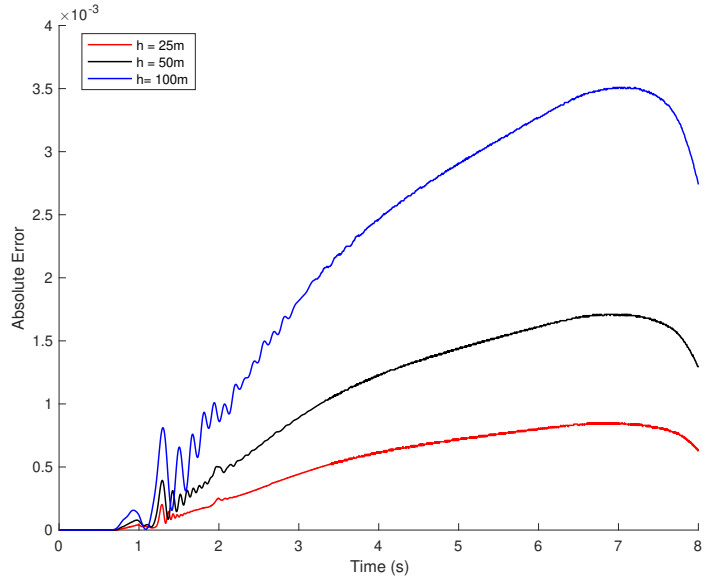

(b)

Figure 4.8: (a) Heterogeneous medium L_2 error for the slip, slip rate, and shear traction versus mesh size. With mesh refinement, the hybrid method converges to the FEM solution, (b) The absolute error of the slip rate measured at the center of the fault and its evolution with respect to time for different mesh sizes, $h = 25m$, $h = 50m$, and $h = 100m$. The error is reduced with mesh refinement. The color figure is available in the electronic version only.

4.3.3 Pulse-like ruptures induced by low velocity fault zones

Low velocity fault zones (LVFZs) are found in most mature faults. The width of the LVFZ is about several hundred meters. These zones cause wave velocity reductions ranging from 20% to 60% [245, 242, 246, 247] relative to the host rock. If the contrast is strong enough, the rupture in the LVFZ can behave as pulses.

In this section, we consider a slip-weakening fault embedded in a LVFZ, with a wave velocity reduction of 20% with respect to the surrounding country rock. The material properties are summarized in Table 4.3. The model geometry is described in Fig. 4.5 but with inverted material properties. The initial shear stress is constant along the fault plane except in a central patch where the fault is overstressed to force abrupt nucleation of the dynamic event. The width of the overstressed patch is 1.6 km. The normal stress is uniform everywhere. The fault plane bisects the LVFZ which has a total width of 1.6 km. We choose to locate the virtual boundary at 1.2 km from the fault plane.

Table 4.3: Problem parameters for fault embedded in low velocity zone

Parameter	Symbol	Value
Density (kg/m^3)	ρ	2670.0
Pressure wave speed (material 1) (km/s)	c_p^{Mat1}	6.0
Shear wave speed (material 1) (km/s)	c_s^{Mat2}	3.464
Pressure wave speed (material 2) (km/s)	c_p^{Mat2}	4.8
Shear wave speed (material 2) (km/s)	c_s^{Mat2}	2.771
Initial shear stress (nucleation patch) (MPa)	τ_0^{nu}	31.0
Initial shear stress (background) (MPa)	τ_0^{bg}	26.67
Peak frictional strength (MPa)	τ_s	30.0
Residual frictional strength (MPa)	τ_r	25.0
Slip-weakening critical distance (m)	δ_c	0.20
Fault length (km)	L	100
Distance between two virtual boundaries (km)	W_H	4.8

We compare the slip, slip rate, and shear traction results from the hybrid method and FEM methods Fig. 4.9(a) at the center of the fault as well as 4.5 km away from the center Fig. 4.9(b). The hybrid method shows excellent agreement with the benchmark finite element solution. Fig. 4.9(c) shows

snapshots of the slip and slip rate evolution at times 1, 2, 4, 6, 8 and 10 seconds. Since the reflection wave from the boundary of the LVFZ is an inversion of the incident wave for a certain range of incidence angels [245], under certain circumstances, the reflected wave could unload the fault, generating a slip pulse. The slip pulse is observed in Fig.4.9(c). After the nucleation of the rupture, due to the reflection from the boundary of the LVFZ, the crack-like rupture splits into a pulse-like rupture and a crack-like rupture. Fig. 4.10(a) shows L_2 norm of the error between the solution from the hybrid method and solution from FEM on the fault plane with mesh refinement. The results suggest the hybrid method converges to the FEM method with mesh refinement. Fig. 4.10(b) suggests that the absolute error in the slip rate inferred by the two methods at the center of the nucleation zone decreases with mesh refinement. The efficient near-field truncation allows the finite element discretization to be limited within a small strip, leading to potential savings in both computational time and memory cost. For the same mesh size $h = 100m$, solving the LVFZ problem by using FEM takes 2288 seconds. This value reduces to 104 seconds for the hybrid method, corresponding to a speedup of 22 times. The saving in memory is significant. For mesh size $h = 100m$, the hybrid method uses approximately 62.7 MB, whereas FEM uses nearly 238 MB. The hybrid method only uses about 26 percent of the memory that FEM uses.

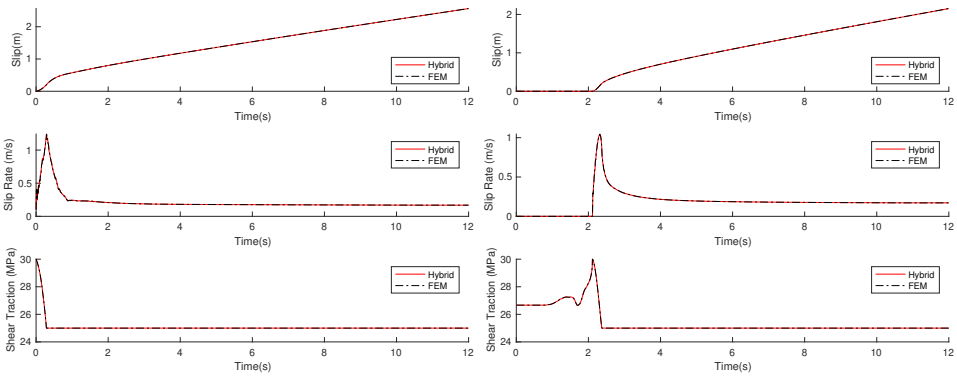

(a) (b)

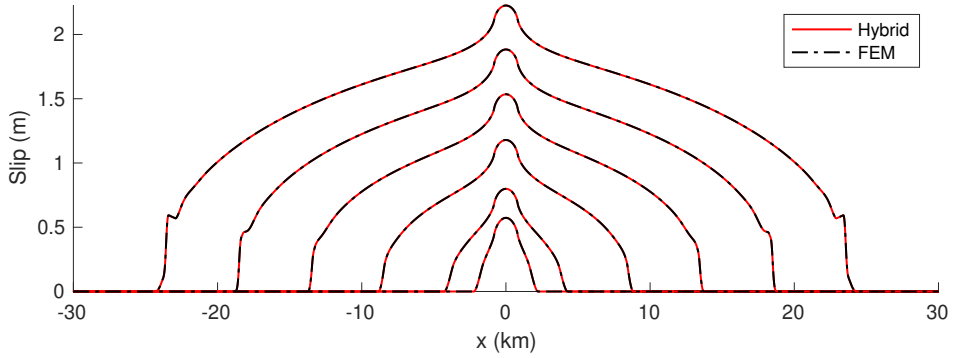

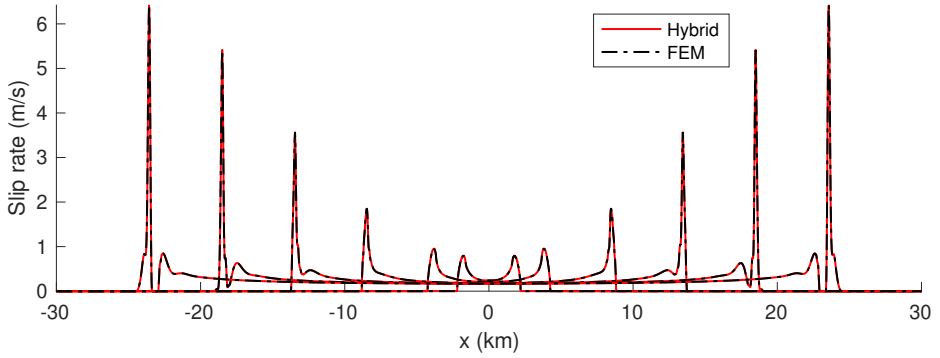

(c)

Figure 4.9: Simulation results for a fault embedded in a heterogeneous medium comparing the hybrid method (in red) and the finite element method (FEM; in black) when using a mesh size of $h = 25m$: (a) Time history of the slip, slip rate, and shear traction at the station in the center of the fault. (b) Time history of the slip, slip rate, and shear traction at the station 4.5 km away from the center of the fault. (c) Snapshots of the slip and slip rate at $t = 1s$, $t = 2s$, $t = 4s$, $t = 6s$, $t = 8s$ and $t = 10s$. The results from the hybrid method match those from the finite element benchmark solution perfectly in the crack to pulse rupture transition

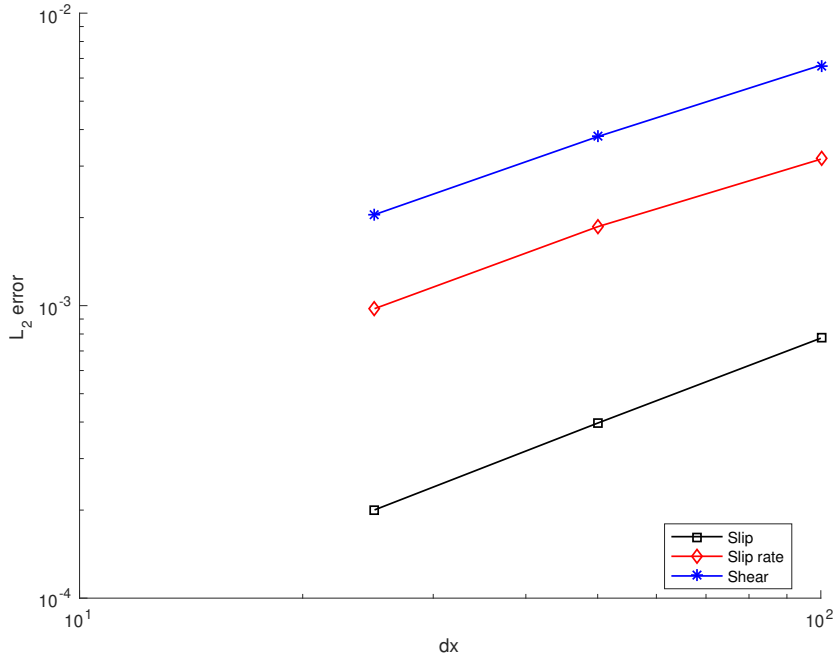

(a)

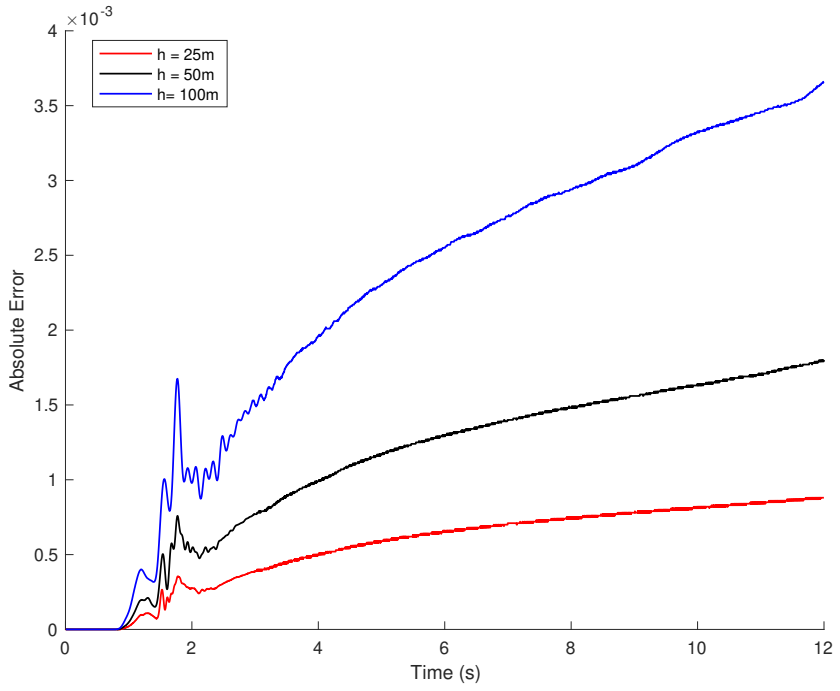

(b)

Figure 4.10: Error evolution of hybrid simulation of fault rupture in a LVZ (a) L_2 error for the slip, slip rate, and shear traction versus mesh size. With mesh refinement, the hybrid method converges to the FEM solution, (b) The absolute error of the slip rate measured at the center of the fault and its evolution with respect to time for different mesh sizes, $h = 25m$, $h = 50m$, and $h = 100m$. The error is reduced with mesh refinement. The color figure is available in the electronic version only.

4.4 Discussion

In the previous section, we validated the hybrid method with a SCEC benchmark problem and further showed its flexibility and performance superiority for problems involving near-field heterogeneities. The method proposed takes its adaptability in handling nonlinearities or heterogeneities from FEM and its computational efficiency from SBI. Furthermore, it owes its excellent performance to the accuracy of the boundary conditions, which eliminate any artificial reflections and make it possible to have the virtual boundaries arbitrarily close to the fault plane as long as the remainder of the domain is linear-elastic and homogeneous. The resulting savings in computational resources may then be redirected to study fault-zone nonlinearities with a higher resolution or large-scale nonlinear problems. We believe this may be the first stepping-stone to realizing long-duration simulations of full earthquake cycles in a bulk that might have material heterogeneity, material nonlinearity, fault geometry complexity, or a combination thereof.

A direct advantage of limiting the spatial discretization to a small area near the fault zone is that the computational cost for solving the discretized bulk is significantly reduced, which may allow small-scale heterogeneities, such as fault branches and shear bands, as well as complex physics within the fault zone, including spontaneous strain localization [248] or small-scale branches, to be incorporated directly into the model.

The spectral boundary integral equation provides an accurate boundary condition irrespective of the wave angle incidence. Therefore, unlike other absorbing boundary conditions, such as infinite elements [231] or even perfectly matching layers [232], where the boundaries must be taken far away from the fault zone to avoid the interference of wave reflections with the physical solution, no artificial reflections are observed in the results obtained from the hybrid method. This result implies that the method may be used as an exact near-field wave truncation algorithm. The consistent exchange of the displacement and traction boundary conditions in this method exploits the same concept as the Dirichlet-to-Neumann maps [249], with the difference that the planar virtual boundaries in the hybrid method make it possible to benefit from solving the real space nonlocal boundary condition as a local boundary condition in the Fourier domain, reducing computational costs and enabling efficient parallelization.

Another advantage of this method over previous forms of coupling between bulk and boundary integral

methods is that it transforms the nonlocal boundary conditions in space to local ones in the Fourier domain, thereby reducing the cost from N^2 to $N\log N$ ([16]). The previous approaches to finite element and boundary integral coupling discretize the spatial convolutions involved in the boundary integral in the real domain, which leads to densely populated stiffness matrices [250].

The savings in computational time and memory shown in the results is significant. If the fault is discretized by N nodes, the number of computational operations will be $O(N^2 W_F/L)$ when a pure FEM scheme is used. Using the SBI method reduces this number to $O(N\log(N))$ [16]. For the hybrid method, we need $N^2 W_H/L$ FEM nodes to discretize the strip between the virtual boundaries. Thus, the number of computational operations for the hybrid method is $O(N^2 W_H/L + N log(N))$. The ratio of computational cost for the hybrid method versus the FEM, therefore, is $O(W_H/W_F + L log(N)/N/W_F)$. For example, for the TPV205-2d SCEC verification problem we have shown, the virtual strip has a width of $W_H = 1.6$km and a length of $L = 100$km and at a mesh size $h = 100m$, the number of discretization points along the fault is $N = 1000$. Therefore, the aforementioned efficiency ratio $W_H/W_F + L log(N)/N/W_F$ is 0.0229. Based on the numerical simulations, we get an efficiency ratio of 0.0383, which is close to the estimated value.

The characteristics of the method discussed above suggest that it may also potentially be used for long-duration earthquake cycle simulations on faults with near-field material heterogeneities, material nonlinearities, or fault surface complexities. Apart from the computational efficiency of the method, the SBI formulation offers an accurate means for truncating the wave field in both dynamic and quasi-dynamic limits, making the hybrid method capable of capturing the effects of both seismic and interseismic phases of the cycle. Moreover, by exploiting the mode truncation and adaptive time-stepping techniques already embedded in the spectral formulation by Lapusta et al. [16], it is possible to resolve the temporal multiscale nature of the rupture in an efficient manner. One can then envision coupling the SBI method with an implicit FEM scheme during the interseismic period to enable this extension.

In [233], the hybrid method was first introduced for coupling bulk and boundary methods in a 2D anti-plane setting. In this study, we have extended the method to 2D in-plane problems. In this case, it is required to couple both the normal and shear components of traction and displacement at the virtual boundaries. Furthermore, because of the existence of fast P-waves and slower S-waves, the time step for integration is limited by the faster P-wave speed. This situation is slightly more complex than

coupling in the anti-plane shear setting, where only one wave speed and one component of displacement exist. Nonetheless, the results presented in this study demonstrate the superior performance of the hybrid method in the 2D in-plane setting and the ability to consistently couple multiple traction and displacement components. With the infrastructure for coupling now available for both in-plane and anti-plane settings, the extension to 3D is straightforward because the kernels in the boundary integral convolution are readily available. In future work, we will consider different extensions of the algorithm, such as including the effect of free surfaces in the boundary integral formulation by using the method of images, coupling 3D FEM with SBI, and representation of more realistic friction laws, such as rate and state friction [135, 136] and shear transformation zone models [167, 251, 157].

Regarding modeling the lateral boundaries at this point, because the length of the fault under consideration is usually much larger than the lateral dimension in which the nonlinear processes or heterogeneities exist, the waves arriving at the lateral boundaries have almost 90-degree incidence angles. Under such circumstances, many of the absorbing boundary conditions, including perfectly matching layers and boundary viscous damping, may be used and will exhibit excellent performance because of the near normal incidence. A possible alternative scenario would be using periodic boundary conditions in the FEM domain that are consistent with the periodic boundary conditions for the boundary integral method. For the problems presented here, the results were found to be insensitive to the choice of lateral boundaries. This is partly due to the existence of unbreakable regions near the fault ends that force the rupture to arrest before reaching the lateral boundaries, or due to the domain length being large enough so that waves did not reach the lateral boundaries.

Even though the hybrid method opens the door to exploring a variety of different problems by offering a more flexible and efficient approach, the applicability of this method has limitations. For example, if heterogeneity or inelasticity exists in the far field, the application of the boundary integral equation would no longer be exact. However, in most cases, it is reasonable to assume that such far-field characteristics of the domain do not have a direct impact on the physical solution because the dynamics of rupture are mostly influenced by the local nonlinearities and heterogeneities. The effects of heterogeneities also depend on their distance from the fault zone and the contrast in their properties from that of the bulk. In ground motion applications, the wave amplitude and phase at a location depend on the wave path. Therefore, in this case, it is reasonable for the hybrid method to be used only as a simulator to predict the source characteristics, such as the fault plane slip and slip rate distribution. These data can then be used as inputs to a wave simulation code to track the propagation in globally

heterogeneous and inelastic media and to predict ground motion.

Another restriction of the method is that for dynamic heterogeneities, such as off-fault plasticity, we usually do not know the region over which the nonlinearities will act a priori. In the case of off-fault plasticity, we can use previous work in the field [23, 252, 253, 219], which implies that inelasticity and damage will be contained in a narrow region near the fault plane. Hajarolasvadi and Elbanna [233] demonstrated the success of the hybrid scheme in modeling anti-plane shear cracks with spontaneous off-fault plastic strain generation by pre-estimating the size of the plastic region and ensuring that the virtual strip completely enclosed the inelasticity. However, in general, an adaptive scheme can also be used. For example, if the inelastic region grows close to the virtual boundaries, we may move the virtual boundaries away from the fault plane and advance the solution on this modified geometry for the next time steps. The solution on the part added to the virtual strip would then need to be accounted for. This can be done directly by using the history of the solution on the previous virtual boundary and applying the representation theorem.

In this study, we implicitly assume that the fault is known a priori. A new fault whose geometry is not a priori known is an important topic to study. One advantage of the proposed hybrid approach is that it can easily adopt volume based discretization techniques with embedded discontinuities such as XFEM [254, 255] or explicit discontinuities such as Discontinuous Galerkin [21]. These methods may replace the continuous Galerkin domain-based method used in this current work. We plan to explore these extensions in the future.

Fluids play an important role in the deformation of the fault zone and the surrounding bulk. One advantage of the hybrid method is that it may enable exploring mechanics of fluid infiltrated fault zones with high resolution representation of fault architecture and poromechanical properties distribution within the FEM domain [256] since the saving in the discretization cost would allow using smaller mesh size in the fault zone. Moreover, there exist boundary integral representations for problems of poroelasticity in half space [257] and viscoelasticity in half space [258]. These formulations may be adapted in the hybrid formulation to model poro- and visco-elastic deformations in the bulk.

4.5 Conclusion

We developed a hybrid numerical scheme by integrating the FEM and SBI methods. This hybrid method enables the simulation of wave propagation in unbounded domains with near-source heterogeneities, material nonlinearities, or a complex fault geometry. Specifically, the method is perfectly suited to modeling problems in which heterogeneities or nonlinearities extend over spatial scales that are too large to be lumped into an interfacial traction separation (or friction) law, but yet are much smaller than the overall dimensions of the domain of interest that is affected by wave propagation. The method is shown to be flexible, accurate, and more efficient than a bulk method such as FEM. The method is primarily useful for earthquake rupture simulations in which the wave source extends primarily in one direction or plane. The main conclusions can be summarized as follows:

1. The hybrid method yields the same results as the pure FEM simulation at a fraction of the discretization cost.

2. The hybrid method significantly reduces the computation cost and memory requirement compared with the FEM because the domain of spatial discretization is truncated.

3. The excellent performance of the hybrid scheme and the absence of artificial reflections from the virtual boundaries suggest that the method may also be used as an accurate near-field wave truncation algorithm.

4. The hybrid method may potentially be used for studying additional small-scale physics within the fault zone and would save memory and other resources that full domain-based discretization numerical schemes would otherwise consume.

5. This method has the potential for use in the field of earthquake cycle simulations in a medium with heterogeneities, nonlinearities, or both because the FEM will capture these features confined in the virtual strip without the need to discretize the entire bulk, whereas the SBI will enable mode truncation and adaptive time stepping to resolve the various scales in time (e.g., both rapid slip and interseismic deformations).

Chapter 5

Dynamic rupture propagation on fault planes with explicit representation of short branches

The content of this chapter has been published on Earth and Planetary Science Letter [259].

Ma, X & Elbanna, A. Dynamic rupture propagation on fault planes with explicit representation of short branches. Earth and Planetary Science Letters. 523:115702 (2019).

5.1 Introduction

The internal structure of fault zones in the upper continental crust exhibits considerable complexity. Mature faults consist of several basic structural elements including: (i) A zone of concentrated shear, the fault core, which is often defined by the presence of extremely comminuted gouge; (ii) A damage zone, with the primary fault core centralized in or bordering that damage zone, in addition to a segmented network of several secondary cores within the damage zone. Damage zones display a greater intensity of deformation relative to the surrounding host rock, and contain features such as secondary faults and fractures, microfractures, folded strata, and comminuted grains; and (iii) host country rock with little or no damage. In general, the intensity of damage increases towards the fault core and the transition from undeformed host rock to damage zone rock is often gradual [260, 261, 262]. Overall, fault zones exhibit a combination of distributed damage as well as discrete anisotropic secondary fractures of different orientations and density [263].

Off-fault damage has been investigated extensively using numerical models that implement either off-fault plastic strain accumulation [264, 253, 265, 266, 267], or continuum damage evolution [268, 269, 270]. The starting point in both approaches is a virgin material that has not experienced damage before. Furthermore, both approaches are found to be prone to numerical localization and have been, for the large part, constrained to scalar damage variables or isotropic formulations [222, 271]. Except for a few pioneering studies, for example [267, 272, 273], that considered off-fault dissipation generated by rough fault surfaces, most of the prior studies considered planar faults with no structural complexity. In particular, the effect of pre-existing anisotropic damage features on rupture dynamics, in both the

elastic and inelastic regimes, remains an area that is under-studied.

An exception to the aforementioned discussion has been the investigation of the critical problem of the influence of a fault branch on the termination or continued propagation of rupture on the main fault [23, 274, 275, 276, 277, 278]. These studies suggest that the rupture may continue to propagate on the main fault without jumping to the branch, or propagate on both the main and secondary faults, or terminate on the main fault and continue on the branch. The fate of the rupture depends on the angle of the branch, the background stress field, and the rupture propagation speed. However, to the best of our knowledge, all these studies have been limited to a single long branch. Short and repeated branches that are routinely mapped in fault zones [279, 263] are largely neglected or homogenized as an effective damage variable. An outstanding challenge in explicit modeling of these anisotropic secondary features has been largely attributed to the prohibitive computational cost in terms of problem size, runtime, and memory requirements of domain-based methods such as finite element or finite difference techniques.

Domain based modeling approaches are very versatile in handing complex geometries and material nonlinearities compared to boundary-based methods such as the spectral boundary integral equation. However, to capture small scale details associated with short fault branches, a very fine mesh must be used to resolve the complex boundaries as well as the multiple stress concentration regions associated with the propagating rupture tips. This fine mesh is generally carried out for a significant portion of the domain to appropriately propagate the seismic waves and avoid artificial reflection from varying the mesh size over small distances. Furthermore, the simulation domain has to be truncated at some distance by imposing absorbing boundary conditions [230, 231, 232] far enough from the fault so that reflections from these boundaries do not affect the solution on the fault plane during the simulation time of interest. As a result, the computation cost of a domain-based method grows as $(L/dx)^3$ in 2D and $(L/dx)^4$ in 3D, making it very challenging to incorporate small scale physics in large scale simulations.

A novel approach in addressing the above challenge has been recently presented by [280], who used discrete finite element model to study co-seismic off-fault damage generation resolving complex rupture process. The numerical method presented by Klinger et al. enabled generation of co-seismic damage patterns that localize into a set of nearly periodic parallel branches. While their formulation is based on continuum damage theory, the damage parameter may numerically localize and eventu-

ally be replaced by a slip-weakening crack. Earlier work by [281] has also provided a framework for spontaneous generation of off-plane faults using a novel formulation of the boundary integral method. However, what continues to be missing in this work is the effect of pre-existing secondary cracks, which is expected to influence the dynamic rupture characteristics high frequency radiation and new damage generation, in a way that is different from co-seismically generated damage in a virgin material. In this study we plan to address this missing piece using a novel numerical scheme that enables incorporating high resolution fault zone physics and geometric structures in dynamic rupture calculations.

Here, we use our recently developed hybrid computational scheme that combines a domain-based numerical method which is used to discretize a confined region encompassing the fault plane and all its related structural and material complexities, with an independent spectral boundary integral formulation that models the exterior linear elastic half spaces [282, 214]. This approach overcomes the limitations of the domain-based methods by limiting the discretization to only a subset of the whole domain but benefits from their flexibility in modeling complex geometry and material nonlinearity. The reduction in the size of the domain to be discretized enables us to use higher resolution within the fault zone to resolve the complexity of the secondary branches while saving computational cost and not compromising the accuracy of long range elastodynamic interactions, which are handled exactly using the spectral boundary integrals. In our prior work [214] we have discussed the novelty of our hybrid formulation in the context of existing literature on coupling boundary and bulk numerical schemes as in [283, 284]. In this study, we will use the hybrid scheme to investigate the dynamics of rupture propagation on a fault plane with multiple short branches mimicking the fish bone architecture idealized in [24, 23].

5.2 Numerical method and model Setup

5.2.1 Hybrid Finite Element-Spectral Integral Equation Method

We solve the initial boundary value problem of dynamic fracture using the recently developed hybrid method [214]. The hybrid method is a combination of the FEM (finite element method) and SBI (spectral boundary integral method), although any other domain-based method may be used in lieu of FEM. In the hybrid method, all nonlinearities, such as fault surface roughness or material nonlinearity, as well as small-scale heterogeneities, are contained in a virtual strip of a certain width that is

introduced for computational purposes only (Fig. 5.1(a)). Appropriate meshing techniques are then used to discretize and model this strip using FEM. The step-by-step time integration approach for the fault nodes is a central-difference explicit formulation as follows:

$$\dot{u}^{n+1/2} = \dot{u}^{n-1/2} + \Delta t\, M^{-1}(T^n - f^n) \tag{5.1}$$

$$u^{n+1} = u^n + \Delta t\, \dot{u}^{n+1/2} \tag{5.2}$$

where $\dot{}$ represents the partial derivative with respect to time and the superscript n indicates the time step index. M is the lumped mass matrix. T_n is the traction on the fault interface based on the fault discontinuity condition. The fault discontinuity condition is implemented using the Traction at Split Nodes (TSN) method [3]. f is the internal force due to the deformation of the solid and Δt the time step.

For the interior nodes in the FEM domain, the step-by-step time integration approach is as follows:

$$\dot{u}^{n+1/2} = \dot{u}^{n-1/2} + \Delta t\, M^{-1}(-f^n) \tag{5.3}$$

$$u^{n+1} = u^n + \Delta t\, \dot{u}^{n+1/2} \tag{5.4}$$

The rest of the domain, which is homogeneous and linear-elastic, may be modeled as two half spaces coupled with this strip on each side (S^+, S^-). The elastodynamic response of these half spaces is modeled using the SBI technique. Throughout the simulation, the two methods communicate along the virtual boundaries of the strip by exchanging displacement and traction boundary conditions. The spectral formulation for this method gives an exact form of such a relationship in the Fourier domain. We use the spectral formulation introduced in [15], where the elastodynamic analysis of each half space is carried out separately. In view of the hybrid method, where SBI constitutes a boundary condition to the FEM model, we focus the description on modeling a half-space. The relationship between the traction τ_i and the resulting displacements at the boundary of a half-space may be expressed as

$$\begin{aligned}
\tau_1^{\pm}(x_1,t) &= \tau_1^{0\pm}(x_1,t) \mp \frac{\mu}{c_s}\dot{u}_1^{\pm}(x_1,t) + f_1^{\pm}(x_1,t) \\
\tau_2^{\pm}(x_1,t) &= \tau_2^{0\pm}(x_1,t) \mp \frac{(\lambda+2\mu)}{c_p}\dot{u}_2^{\pm}(x_1,t) + f_2^{\pm}(x_1,t)
\end{aligned} \tag{5.5}$$

where subscripts 1 and 2 represent fault-parallel and fault-normal direction respectively, $\pm$ represents

upper and lower half-plane, c_p is the pressure wave speed, c_s is the shear wave speed, τ_i^0 indicates the externally applied load (*i.e.*, at infinity); and f_i are linear functionals of the prior deformation history and are computed by the time convolution in the Fourier domain.

The coupling of the two methods is done as follows. The FEM and SBI share nodes at the virtual boundaries introduced to truncate the FEM domain. While FEM provides SBI with the tractions along the virtual boundary, SBI returns the displacement that is to be imposed on $S^{\pm}$ of FEM. The detailed step-by-step procedure is as follows

1. Solve full time step within the FEM by solving Eq. (5.1 - 5.2) (FEM interior nodes only).
2. Set interface tractions in the SBI equal to the internal force from FEM: $\tau_i^{n,\mathrm{SBI}} = f_i^{n,\mathrm{FEM}}$, where f_i^n is given through Eq. 5.1.
3. Solve full time step within SBI by solving Eq. (5.5) for velocity and apply explicit integration scheme to get displacements.
4. Set displacements of the shared nodes in FEM equal to displacement in SBI: $u_i^{n+1,\mathrm{FEM}} = u_i^{n+1,\mathrm{SBI}}$.
5. Return to Step 1 to advance to the next time step.

For a full description of the hybrid scheme, its verification, and some of its prior applications please refer to [214].

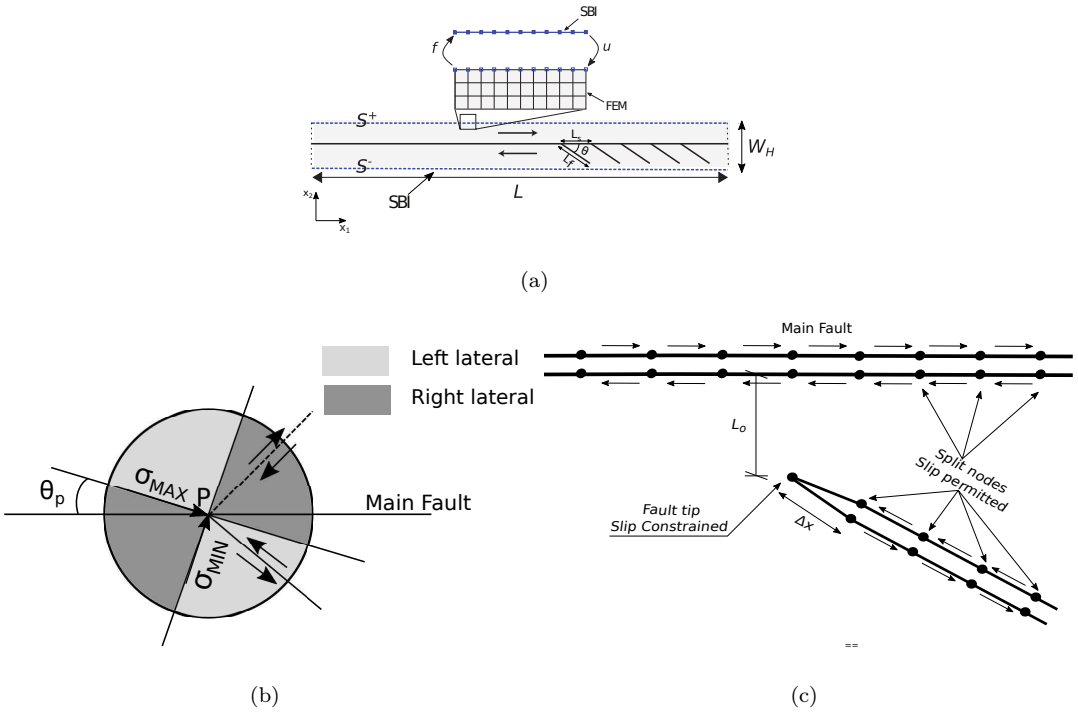

Figure 5.1: Model Setup (a) Schematic of the complex fault zone structure considered in this study. The main fault lies horizontally in the middle of the domain, and the secondary branches are located in a limited region on one side of the fault (tension side). Following [23] we call this setup a fish bone structure. All secondary faults are contained in a narrow virtual strip of dimensions L $\times$ W that is discretized using the Finite element method (FEM). On the upper and lower edges S^+ and S^-, the FEM is coupled with the Spectral Boundary Integral Equation which exactly model the exterior homogeneous elastic half spaces. Tractions and displacements are consistently exchanged between the two methods at the shared nodes. The details of the coupling is outlined in the text. σ_{max} and σ_{min} represents the maximum and minimum principle stresses respectively. θ_p is the angle between the maximum principle stress and the main fault parallel direction. L_s is the spacing between the secondary fault, θ is the angle between the secondary fault and the main fault. L_f is the secondary fault length. (b) The orientation of the principle stresses for the assumed background stress state. The maximum principle stress makes an angle $\theta_p = 19.33^o$ clockwise with the main fault. Also shown is the sense of motion for the secondary faulting consistent with this state of stress. Faults oriented in a dark grey quadrants have a right lateral shear while those oriented in light grey quadrants have left lateral shear. For the faults considered here, the main fault is right lateral while the branches are left lateral. (c) Sketch of the discretization for the main and secondary faults using split nodes. Arrows represent the sense of shear. The secondary fault is shifted L_o away from the main fault. The slip is constrained to be zero at the tips of the secondary fault.

5.2.2 Model Setup

Material and Friction model

In this study, we consider both linear elastic material and elasto-plastic material.

Linear elastic Material

A 2D plane strain elastic model is used to describe the elastic material behavior. The constitutive equation for the linear elastic material is as follows:

$$\sigma_{ij} = \lambda \delta_{ij} \varepsilon_{kk} + 2\mu \varepsilon_{ij} \tag{5.6}$$

where ε_{ij} is the infinitesimal strain tensor and μ, λ are the Lamé parameters.

Elasto-Plastic Material

In this study, we also consider the off-fault material to be idealized with the Drucker-Prager plasticity model [158]. The Drucker-Prager model is closely related to the Mohr-Coulomb model. It describes inelastic deformation in brittle solids arising from frictional sliding of microcracks [183, 253]. We use the Drucker-Prager plasticity model to mimic the inelastic effects on dynamic rupture from cracks on scales that are smaller than the scale of branches. The yield function of the Drucker-Prager plasticity model is given by Eq.5.7,

$$F(\sigma_{ij}) = \sqrt{J_2} - (A + BI_1) \tag{5.7}$$

Here, $I_1 = \sigma_{kk}$ is the first invariant of the Cauchy stress σ_{ij} and $J_2 = s_{ij}s_{ij}/2$ is the second invariant of the deviatoric stress tensor $s_{ij} = \sigma_{ij} - (\sigma_{kk}/3)\delta_{ij}$. Following [253], we take the intermediate principal stress, in the Drucker-Prager formulation, to be the average of the maximum and the minimum principle stress. The constants A and B are determined from experiments and are functions of the cohesion c and the angle of internal friction ϕ that are used to describe the Morh-Coulomb yield surface. When $F(\sigma_{ij}) < 0$, the material response is elastic.

Plastic flow is partitioned between various components of the plastic strain rate tensor by the flow rule. Neglecting the effect of plastic dilatancy we have:

$$\dot{\epsilon}^p_{ij} = \dot{\epsilon}^{eq}_p s_{ij}/(2\sqrt{J_2}) \tag{5.8}$$

Where $\dot{\epsilon}_p^{eq} = \sqrt{2\dot{\epsilon}_{ij}^p \dot{\epsilon}_{ij}^p}$ is the equivalent plastic strain rate. The equivalent plastic strain ϵ_p^{eq} is defined through $\dot{\epsilon}_p^{eq} = d\epsilon_p^{eq}/dt$

Slip-weakening friction model

In this study, all the faults are governed by the slip-weakening friction law [234]. The frictional strength is given by

$$f(D) = \begin{cases} f_s - (f_s - f_d)D/D_c, & D < D_c \\ f_d, & D \geq D_c \end{cases} \tag{5.9}$$

where f_s and f_d are the static and dynamic frictional coefficients and D_c the critical slip required for stress to reach the dynamic value. Continuity of displacements at the fault is enforced (*i.e.*, no slip) if the shear traction is lower than frictional strength, otherwise local slip occurs. [243] defined the characteristic length scale for frictional instability on linear slip-weakening faults. We base our reference length scale for normalizing the spatial scales in our problem on this characteristic length scale term as shown in Eq. 5.10 (omitting the constant term from [243]).

$$L_c = \frac{\mu D_c}{\tau_s - \tau_d} \tag{5.10}$$

Here, μ is the shear modulus, D_c is the characteristic slip distance, τ_s is the static frictional stress and τ_d is the dynamic frictional stress.

Normal Stress Regularization

Due to the complex topology of our fault network, normal stress may be altered on the main fault as well as secondary faults. In order to avoid numerical instability and for the friction model to be compatible with laboratory observations, we include normal stress regularization following priors studies [285, 286].

$$\frac{d\tau}{dt} = -\frac{1}{t^*}(\tau - f\sigma_N) \tag{5.11}$$

where the shear strength τ evolves over a finite time scale (t^*). t^* was taken to be $2\Delta x/c_s$, which is several times larger than the stable time step. Here Δx is the mesh size.

Geometry

We consider our fault system to exist in an infinite medium. A planar horizontal main fault is placed in the middle of the domain with secondary fault branches explicitly modeled as shown in Fig. 5.1(a). The main fault is right lateral and the secondary faults are placed on one side of the fault (on the tension side) starting at a distance L_a from the nucleation zone. This minimizes the effect of these secondary branches on the rupture nucleation. The secondary faults are distributed over a finite length along the main fault and not throughout the whole fault length so that we could explore features of the main fault rupture after it exits the region with the branches. The angle between the secondary faults and main fault is assumed to be θ_f. The secondary faults have constant spacing L_s along the fault strike. The length of each secondary fault is L_f. Vertically, the secondary fault branches are placed a small distance L_o away from the main fault. We note that other approaches may be used to handle the triple junction between the branch fault and the main fault without having to enforce this shift. This may be accomplished by manipulating the kinematics of the split nodes at the junction through either retaining the continuity of the main fault only, or the continuity of the branch fault only, or by assuming that neither fault is continuous and having only one node at the triple junction point as described in [285]. The effect of the various modeling assumptions will be examined in future work. We limit the FEM discretization to a domain of length L and width W_H. The length L is taken to be $100L_c$. The width W_H is much smaller than the length L. The domain width W_H is determined by the length of secondary branches and is taken to be $4L_c$ to ensure that the FEM domain contains the complex fault geometry. All parameters are listed in Table 1.

Table 5.1: Parameters Description

Medium Material Properties	**Value**
Shear Modulus μ	32 GPa
S wave velocity c_s	3.464 $km \cdot s^{-1}$
P wave velocity c_p	6.0 $km \cdot s^{-1}$
Angle of Internal Friction ψ	30.96^o
Maximum Principle Stress direction θ_p	19.33^o
Fault constitutive Parameters	**Value**
Static friction coefficient μ_s	0.6
Dynamic friction coefficient μ_d	0.3
Characteristic slip-weakening distance d_c	0.2 m
Background Stress	**Value**
Background Vertical Stress σ_{yy}	-50.0 MPa
Background Horizontal Stress σ_{xx}	-100.0 MPa
Background Shear Stress σ_{xy}	20.0 MPa
Domain Geometry	**Value**
Reference length scale L_c	500 m
Length of the secondary faults L_f	$1.0L_c$
Spacing between the secondary faults L_s	$1.0L_c$
The off distance of the secondary fault from the main fault L_o	$0.1L_c$
The angle between the secondary fault and the main fault θ_f	30^o
Finite element cell size h	6.25m

Initial and Boundary Condition

We assume the domain is in static equilibrium at time $t = 0$. We consistently resolve the normal stress σ_N and tangential stress τ on all the faults from the background stress σ_{xx}, σ_{yy} and σ_{xy} using Eq. 5.12 .

$$\begin{aligned} \sigma_N &= \sigma_{xx} \sin^2\theta + \sigma_{yy} \cos^2\theta - 2\tau_{xy} \sin\theta \cos\theta \\ \tau &= \sigma_{xx} \sin\theta \cos\theta - \sigma_{yy} \sin\theta \cos\theta + \tau_{xy}(\cos^2\theta - \sin^2\theta) \end{aligned} \tag{5.12}$$

where θ is the angle between secondary faults and the horizontal direction. We nucleate the rupture by overstressing the fault beyond the static friction strength over a localized region in its center with a width L_c. For the medium with elasto-plastic material, we apply a smooth nucleation approach. We use a union of hyperbolic tangent function to smoothly approximate an overstressing region width of L_c to avoid stress concentration from the edges of the nucleation zone. The overstressing region stress level starts at 90 percent of the fault strength and gradually increases over a period of time to reach the fault strength stress level. Other nucleation approaches could also be used such as using consistent initial slip and slip rate profile extracted from quasidynamic simulations for the nucleation process on a planar fault [287].

From [224, 225], the relative strength parameter is defined as $S = (\tau_s - \tau)/(\tau - \tau_d)$, which quantifies the closeness of initial stress to failure relative to the stress drop. For this study, we are considering background stress conditions which correspond to strength parameter $S = 2$ on the main fault. Thus, the ambient stress conditions favor sub-Rayleigh rupture propagation on the main fault.

5.3 Results

To normalize our results, we adopt the following dimensionless quantities for length, time, slip, slip rate, and stress:

- Length, $x^* = x/L_c$
- Time, $t^* = tc_s/L_c$
- Slip, $D^* = D/D_c$
- Slip rate, $V^* = VL_c/(D_c c_s)$
- Stress, $\sigma^*_{ij} = \sigma_{ij}/(-\sigma^0_{yy})$

5.3.1 Elastic Domain

Fig. 5.2 compares several rupture metrics on the main fault plane with and without the short branches. The short branches lead to a reduction in the peak slip rate as well as the accumulated slip on the main fault plane. This may be explained by the fact that when the short branches are activated, the frictional slip on these secondary features contributes to the total energy dissipation leading to reduced slip and slip rate. The increased energy dissipation in the presence of the secondary branches

also slows the rupture on the main fault and decreases the rupture propagation speed at least within the fish bone region. However, there is a slight increase in the slip near the center of the main fault (around $x^* = 0$) for the case with the short branches. The initiation and arrest of ruptures on the secondary branches lead to the generation of seismic signals that are reflected back on the main fault leading to ripples in the slip rate profile that propagate backward and accumulate more slip away from the rupture tip that would not have been generated in the homogeneous medium case. The reduction in slip rate and rupture speed due to increased energy dissipation has also been previously observed in models with off-fault energy dissipation using plasticity [253] or continuum damage theories [270]. The backward propagating ripples, however, is a consequence of the geometric complexity of the model.

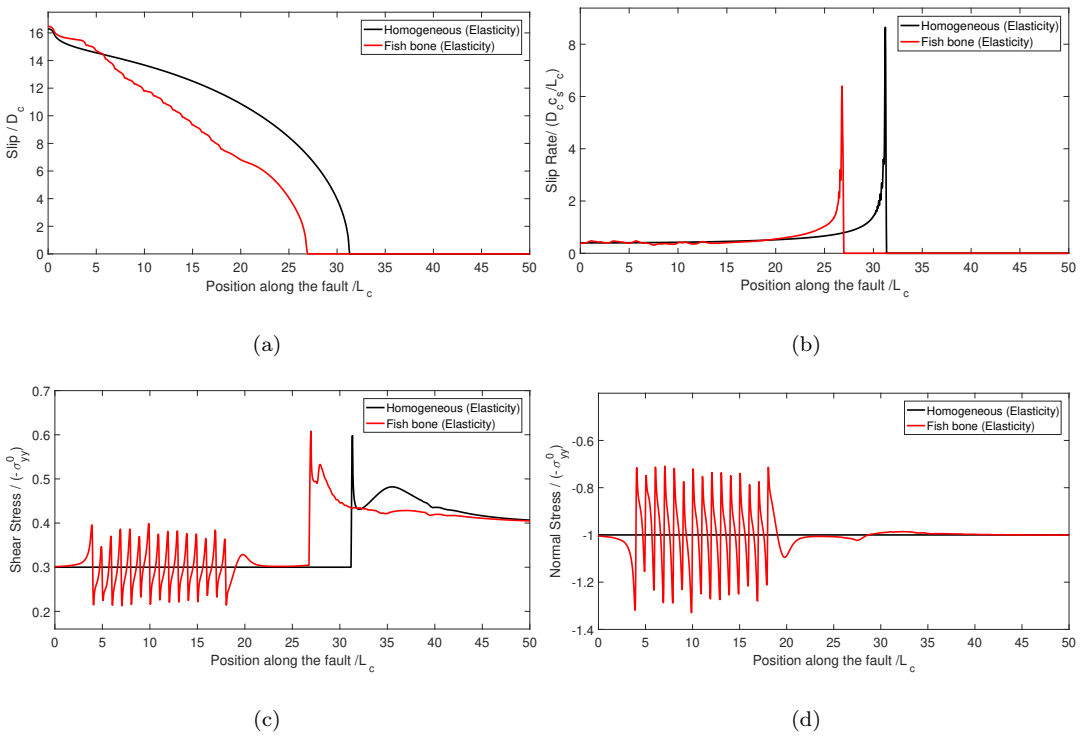

Figure 5.2: Slip, slip rate, shear stress and normal stress distributions on the main fault, at the same point in time, with and without secondary branches for the elastic material case. (a) Slip, (b) Slip rate, (c) Shear stress distribution, and (d) Normal stress distribution. Overall, the fish bone case shows significant post-event stress heterogeneities as well as reduced slip, maximum slip rate, and rupture speed.

The secondary faults have a significant effect on the post-rupture stress distribution. Fig. 5.2(c) and 5.2(d) show that both the shear and normal stress exhibit strong spatial heterogeneities within the

fish bone region after the passage of the rupture front. These strong heterogeneities are absent in the homogeneous medium case. The activation and arrest of slip on the secondary branches lead to the development of normal and shear stress concentrations at their ends which load the main fault nonuniformly. These stress fluctuations lead to both stress increase as well as reduction in both of the normal and shear stress components. In particular, the normal stress is reduced to 70% of its original value at some locations. This may suggest that some configurations of the secondary branches may even lead to fault opening, although we have not observed this yet in the cases we investigated. Furthermore, the shear stress drops to 50% of its corresponding value in the homogeneous case at several points. This is also indicative that geometric complexities may potentially lead to the reversal of the shear stress sense if they cause large enough shear stress fluctuations. This pattern of stress fluctuations on the main fault may be predicted qualitatively using Linear Elastic Fracture Mechanics (LEFM) as has been done in a previous study of dynamic rupture with a single backthrust branch fault [286]. We present an example of such calculations in Appendix E.

Another major result in this study is the influence of secondary branches on the high-frequency generation in the bulk. Fig. 5.3 shows the near-field particle velocity for both cases with and without the secondary branches. For the homogeneous medium, the wave field is smooth almost everywhere with concentration of high frequencies neat the rupture tips. On the other hand, for the medium with branches, we observe coherent wave fronts that are propagating away from the tips and spaced apart periodically, consistent with the periodic distribution of the secondary branches. These coherent fronts are generated due to the constructive interference of seismic radiation from the secondary faults.

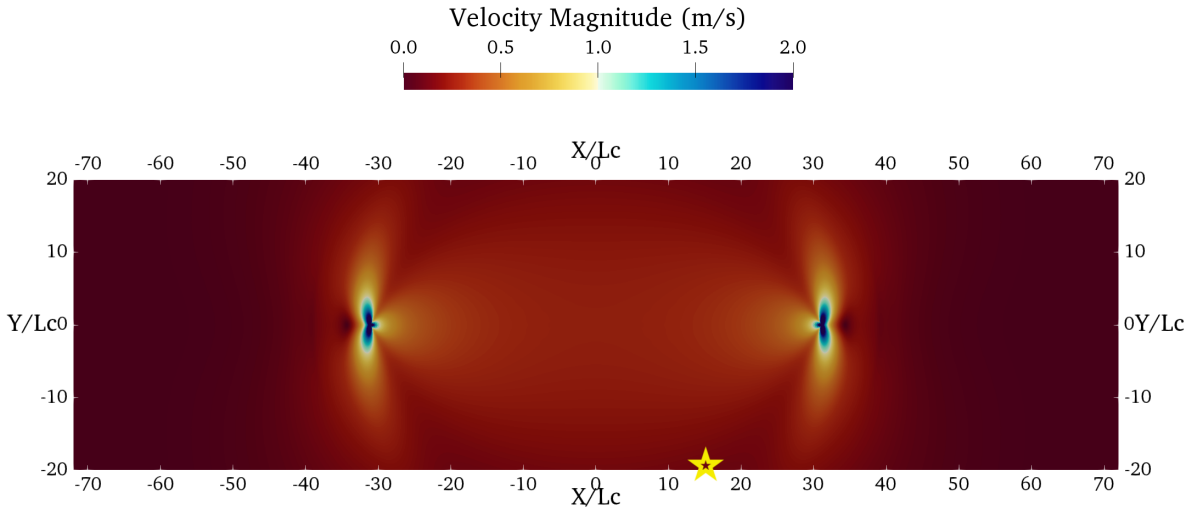

(a)

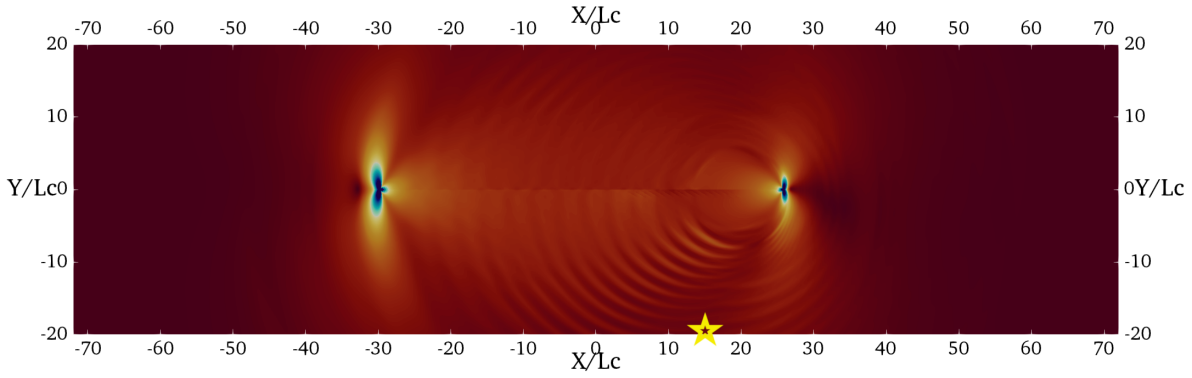

(b)

Figure 5.3: Contours of the bulk velocity field. (a) Homogeneous medium. (b) Domain with fish bone structure. Coherent high frequency generation emerge in the case of the fault with secondary branches (fish bone structure) and propagate away from the fault plane as concentric fringes. These high frequency waves are generated as a result of the constructive interference between the waves emitted by the the secondary branches. In the homogeneous case the high frequency wave field is localized near the rupture fronts.

To demonstrate the enhanced generation of high frequencies for the case with the fish bone structure, we plot in Fig 5.4. the fault-parallel and fault-normal components of the velocity at a station located $20L_c$ from the main fault and represented by the star in Fig. 5.3. Both components of the velocity show high frequency fluctuations in the case of the fault with branches compared to the homogeneous case. The acceleration spectra plotted in Fig. 5.4(c) further prove this point. The fault with small branches has a spectrum that is richer in high-frequency content and furthermore shows an almost flat spectrum in the frequency range 2-20 Hz. This is consistent with observations in [288, 289] and similar to the results from dynamic rupture simulation on rough faults [267]. This suggests that small scale fault branches may be a candidate for explaining near field radiation characteristics of active faults.

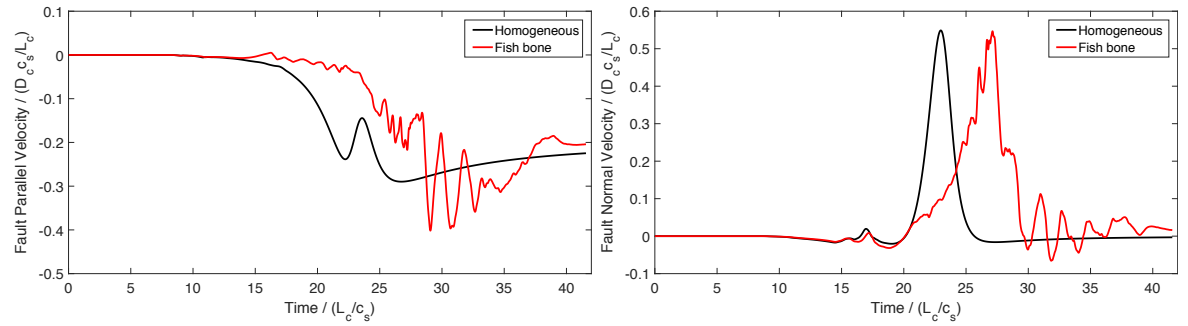

(a)

(b)

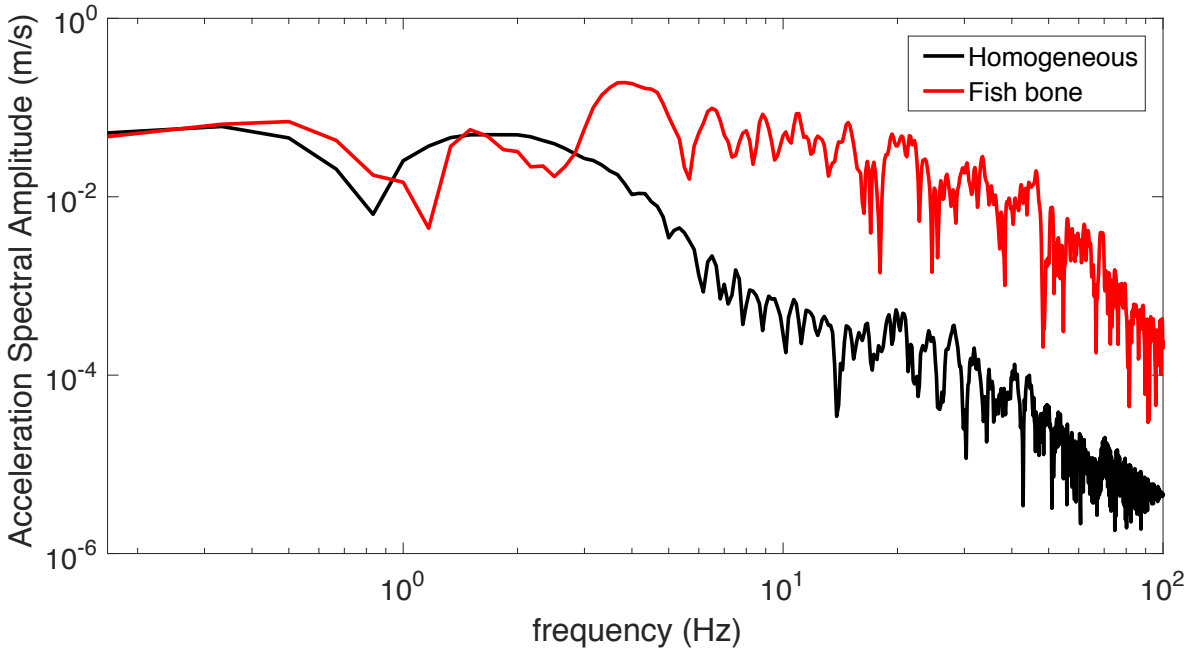

(c)

Figure 5.4: High frequency generation with and without secondary branches. (a),(b) Fault-parallel and fault-normal velocities at a station located at $x^* = 15L_c$ and $y^* = -20L_c$ (c) fault-normal acceleration spectral amplitude at station $x^* = 15L_c$ and $y^* = -20L_c$.

Another effect of the secondary faults is shown in Fig. 5.5 which illustrates the distribution of the normal displacement of the main fault plane. For the homogeneous medium, the fault plane simply rotates. The existence of the secondary branches, however, leads to the development of undulations in the fault plane profile as shown in Fig. 5.5. The stress concentrations corresponding to the secondary faults, load the fault in the normal direction and promote repeated peaks in its vertical profile near the locations where the secondary branches are positioned. While the magnitude of these undulations is small, they may contribute, over several cycles, to the evolution of the main fault roughness.

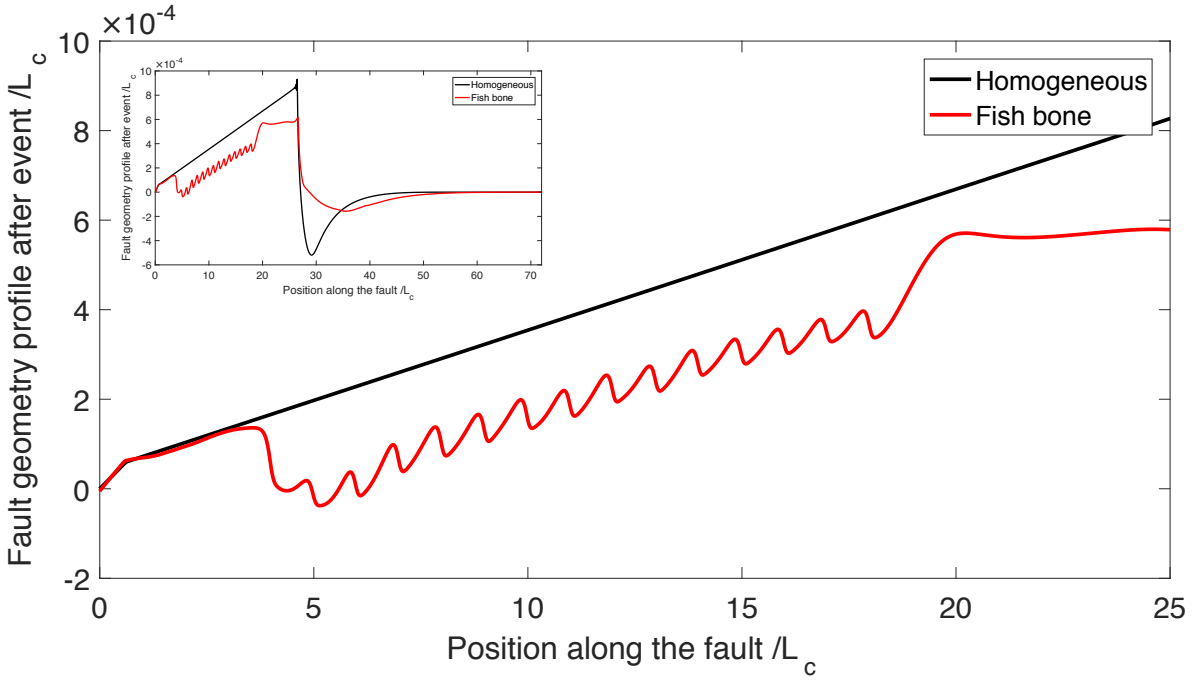

Figure 5.5: Normal displacement distribution with and without secondary branches. The insert figure shows the whole distribution along the full half length of the fault. The secondary faults cause periodic undulations in the main fault profile

To gain further insight into the dynamics of the branch faults, we show in Fig. 5.6 the time evolution of the slip, slip rate, and the rupture speed on one of the secondary faults (the first branch). The secondary fault is triggered dynamically by the main fault rupture as it approaches the branch tip leading to a rapid increase in slip rate and slip over a segment of the branch that is closest to the main fault . As stated in Section 5.2, the background stress favors a sub-Rayleigh rupture propagation on the main fault $S = 2$. However, this is not the case for the secondary faults which are loaded dynamically from the propagating rupture on the main fault in addition to the loading from the background stress field. The insert in Fig. 5.6(a) shows the rupture tip position along the secondary fault versus time, and it suggests that the secondary fault fails in a supershear mode. Interestingly, the background strength parameter for the secondary faults in this case is $S = -8.12$ (See Table 5.2) corresponding to an initially resolved shear stress that is lower than the dynamic frictional stress. Thus, this result suggests that even though the far field background stress favors a sub-Rayleigh rupture propagation on the fault system, the small scale branching faults may fail differently when excited dynamically. This may potentially have important implications for seismic hazard from complex fault zones.

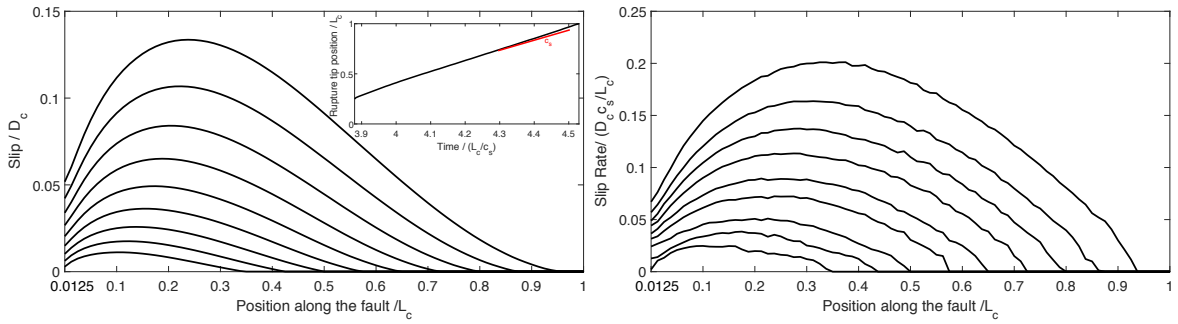

(a) (b)

Figure 5.6: Slip and slip rate distributions on the first secondary fault at consecutive time steps (plotted every 0.02s). (a) Slip, (b) Slip rate. Insert figure in (a) shows the rupture tip position along the secondary fault versus time suggesting that the rupture is propagating at supershear speeds. The fault tip which has zero slip and zero slip rate (See Fig. 5.1(c)) is excluded from the plot for clarity.

5.3.2 Elasto-Plastic Domain

To account for additional energy dissipation mechanisms at a scale smaller than the scale of the secondary branches that we haven't explicitly modeled, we consider the possibility of inelastic strain generation using an elasto-plastic material model. Since we have only considered one level of the secondary branches, the plasticity model may be used as a proxy for small scale damage that is randomly distributed and arising from microcracks or dislocation movement at nano or micro scale. Drucker-Prager plasticity is used as described in Section 5.2.

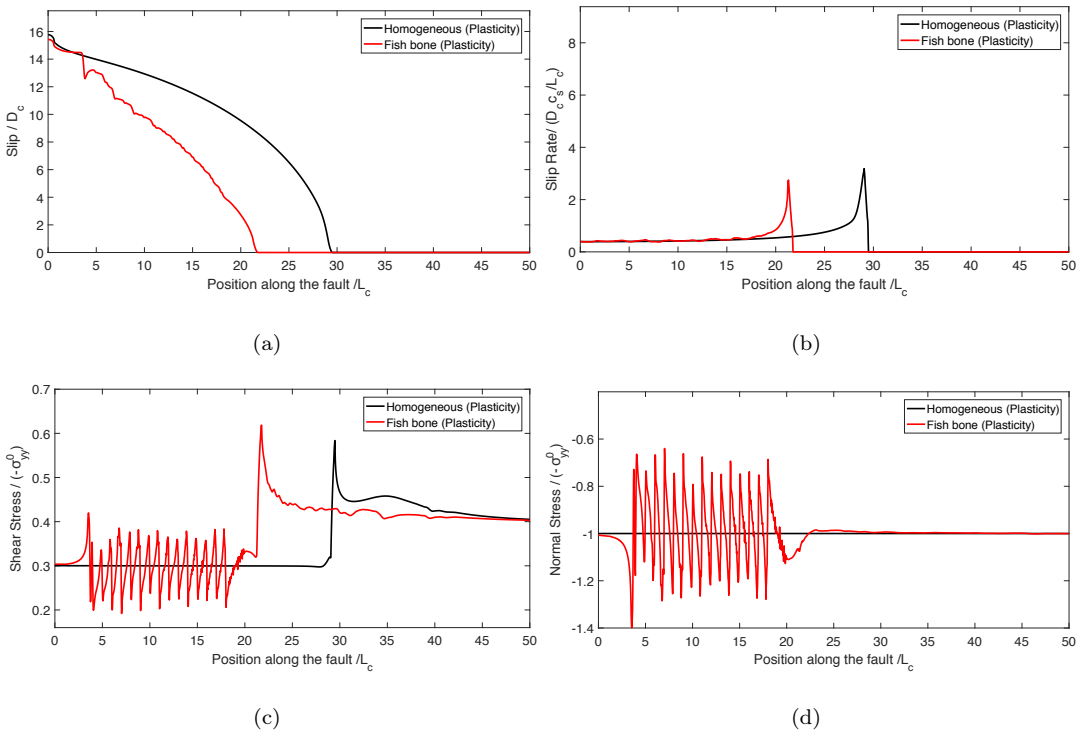

Figure 5.7: Slip, slip rate, shear stress, and normal stress distributions on the main fault, at the same point in time, with and without secondary branches for the elasto-plastic material case. (a) Slip, (b) Slip rate, (c) Shear stress distribution, and (d) Normal stress distribution. Overall, the fish bone case shows significant post-event stress heterogeneities as well as reduced slip, maximum slip rate, and rupture speed. The values of slip and maximum slip rate in the elasto-plastic case are lower than the elastic case.

Fig. 5.7 compares several rupture metrics on the main fault plane with and without the short branches but in the presence of off-fault plasticity. In this case, the rupture may generate off-fault plastic strain if the Drucker-Pragger yield criterion is met. Consistent with the elastic case, the short branches also lead to a reduction in the peak slip rate as well as the accumulated slip on the main fault plane. The frictional slip on the secondary branches contributes to the total energy dissipation leading to reduced slip, slip rate, and rupture propagation speed. However, unlike in the elastic case, there is no slight increase in the slip near the center of the main fault (around $x^* = 0$) for the case with the short branches. Plasticity, which acts as an additional energy sink on its own, has suppressed the backward propagating ripples and greatly reduced their effect. Overall, the slip, the slip rate, and the rupture speed are all lower in this case compared to the case of rupture propagation in an elastic medium.

The effect of the secondary faults on the post-rupture stress distribution persists even with plasticity.

Fig. 5.7(c) and 5.7(d) show that both the shear and normal stress exhibit strong spatial heterogeneities within the fish bone region after the passage of the rupture front. These strong heterogeneities are absent in the homogeneous medium case with off-fault plasticity. The activation and arrest of slip on the secondary branches leads to the development of normal and shear stress concentrations at their ends which load the main fault nonuniformly. These stress fluctuations lead to both stress increase as well as reduction in both of the normal and shear stress components and the amplitude of the fluctuations are very similar to those generated in the elastic case indicating that they are unaffected by plasticity.

The secondary branches, as pre-existing damage features, have strong influence on the off-fault plastic strain distribution as shown in Fig. 5.8. While in the homogeneous case, the plastic strain distribution has the characteristic fan-like shape consistent with previous studies [253, 266, 267], the plastic strain distribution is increasingly non-uniform due to the presence of the short branches. In particular, the spatial extent of the off-fault plasticity in the vicinity of the main fault is greatly reduced within the region that hosts the short branches. Furthermore, the short branches seem to have little or no plastic strain accumulation, suggesting that what should have been bulk plastic strain has collapsed in the form of localized slip along the short secondary fault. However, there is a large increase in the plastic strain accumulation at the ends of the short branches due to the abrupt arrest of the slip and the associated stress concentration. Namely, there is a concentration in plastic strain in the region between the secondary branch tip and the main fault suggesting that even if the branch is not directly connected to the main fault, this region will be severely damaged. Furthermore, there is another region of plastic strain concentration at the far end of the secondary fault. This region also does not extend along the strike of the secondary branches but is slightly bent in another direction suggesting a possible growth plane for the secondary faults if they are allowed to extend.

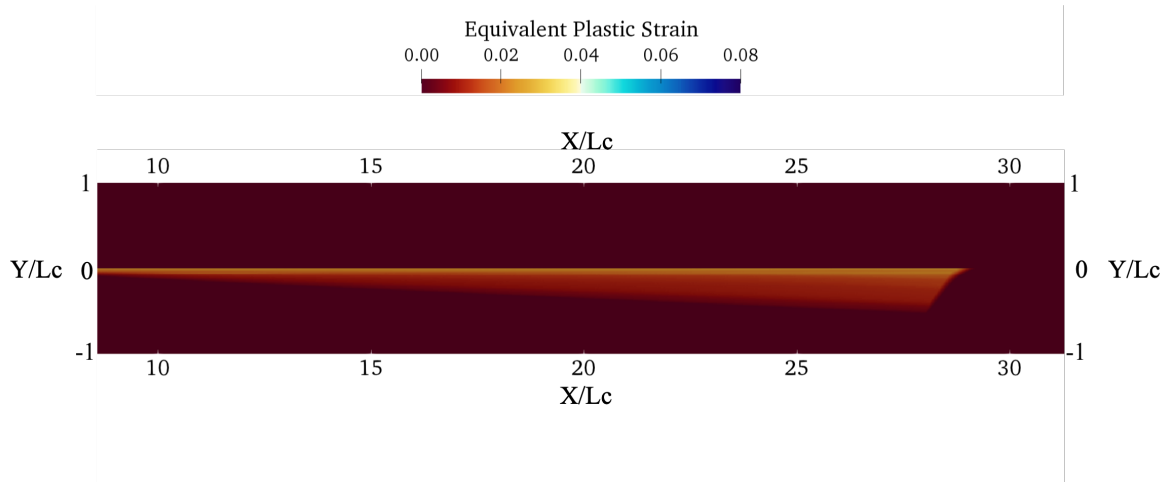

(a)

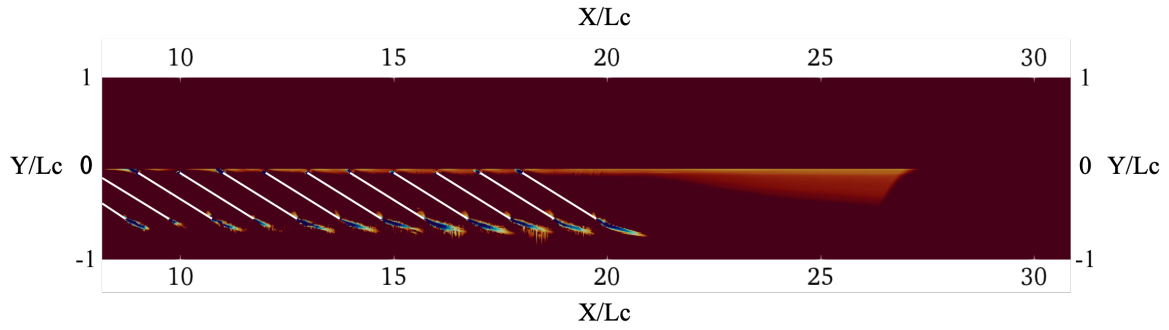

(b)

Figure 5.8: Equivalent Plastic Strain distribution (a) Homogeneous material (b) Fish bone structure. The lines in white are the location of the secondary branches. The vertical dimension is exaggerated for visualization purpose.

5.3.3 Rupture Characteristics with and without plasticity

Fig. 5.9(a) shows the rupture tip position versus time for four cases: the homogeneous medium with and without plasticity, and the fish bone structure with and without plasticity. The slope of these curves gives the rupture propagation speed for each case. The existence of the secondary branches significantly reduces the rupture speed compared to the homogeneous case. The rupture propagation speed generally decreases with off-fault plastic dissipation. The rupture propagates the slowest on the main fault for the case with fish bone structure in elasto-plastic medium. An unexpected observation is that with the existence of the secondary branches, the rupture may temporarily travel faster than the homogeneous case at first and then decelerate (See insert of Fig. 5.9(a)). This may be

explained by the fact that initially the rupture speed on the main fault is small, and that when these secondary branches are activated, they generate waves that may constructively interfere with the main rupture tip, channel energy to this tip, and promote its transient acceleration. As the main rupture accelerates further, this effect is diminished and the secondary faults act primarily as energy sinks, increasing the overall energy dissipation and decelerating the main fault rupture propagation. Once the rupture tip on the main fault moves beyond the fish bone region, it accelerates further approaching the propagation speed of the rupture in the homogeneous case with and without plasticity respectively.

Fig. 5.9(b) shows the maximum slip rate versus rupture tip position for the different cases. The secondary branches lead to a significant reduction in the peak slip rate on the main fault. Cases with off-fault plasticity also show a reduction in the peak slip rate compared to the elastic case. The existence of secondary branches also leads to high-frequency oscillations in the peak slip rate as the rupture propagates, indicative of enhanced radiation efficiency and high-frequency generation. After the rupture on the main fault has propagated beyond the region with the fish bone architecture, the peak slip rate increases and approaches the peak slip rate values for rupture propagation in the homogeneous medium.

Fig. 5.9(c) shows the main fault frictional energy dissipation normalized by the potency at each time step versus the average slip for the fish bone case and the homogeneous case with and without plasticity. The frictional dissipation is calculated by integrating the product of the frictional stress and the slip rate over the fault length and over time $E_f = \int_0^t (\int \tau_f \dot{D} da) dt'$. The potency is defined as the integral of the slip over the fault domain $P = \int D da$. The frictional dissipation normalized by the potency gives a stress-like quantity which may be taken indicative of an average frictional strength on the fault. Thus, the plots shown in Fig. 5.9(c) may be considered as modified effective slip-weakening laws for the fault as a whole. The homogeneous cases with and without plasticity have relatively similar effective stress-slip response. This is because the energy dissipated by off-fault plasticity is smaller than 0.1 percent of the frictional dissipation. Interestingly, the fish bone structure case with plasticity shows the least amount of frictional energy dissipation on the main fault of the four cases. This may be attributed to the other energy dissipation avenues that exist due to the combination of off-fault plasticity and frictional slip on the additional surfaces of the secondary faults. In particular, in the complex fish bone structure, the stress tends to be concentrated at the ends of the secondary faults leading to higher concentration of the plastic strain in this region. This increases the contribution to off-fault energy dissipation on the expense of the energy dissipation by frictional sliding on the main

fault.

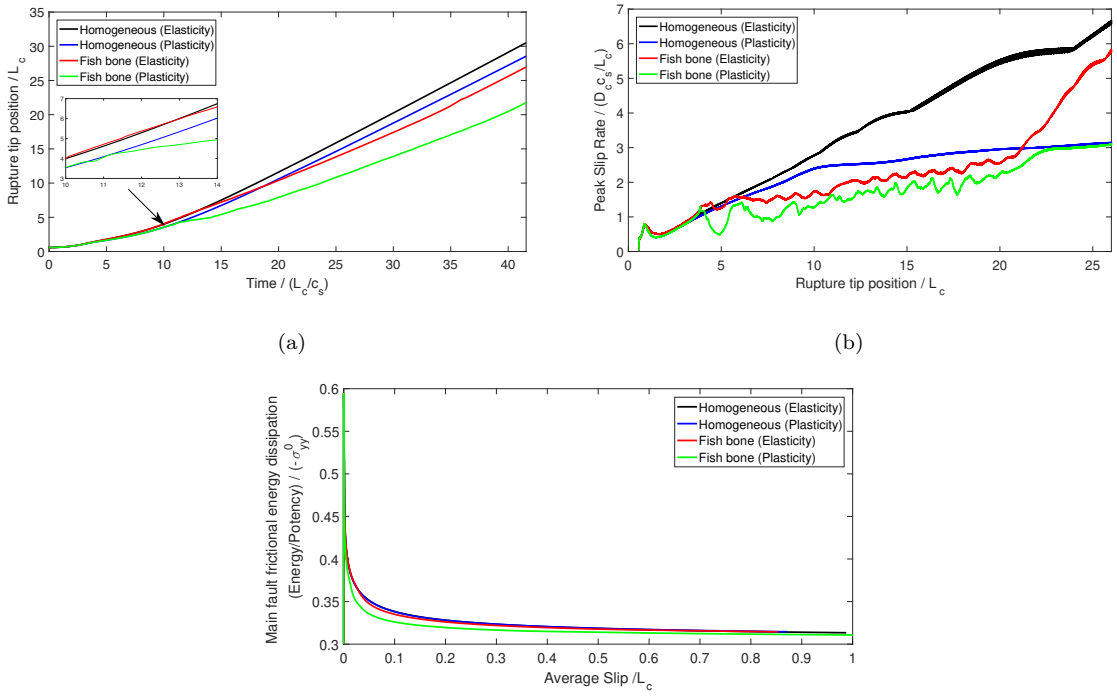

Figure 5.9: Comparison of rupture characteristics in the different cases (a) Rupture Tip position on the main fault as a function of time for the homogeneous and fish bone cases with elastic and elasto-plastic material models. (b) Peak slip rate as a function of rupture tip position on the main fault for homogeneous and fish bone cases with elastic and elastoplastic material models. (c) Frictional dissipation normalized by potency for the main fault in the four different different cases investigated in the manuscript. The homogeneous case with either elastic or elasto-plastic material models shows similar normalized frictional energy dissipation. The fish bone structure with elastic material has lower normalized frictional dissipation on the main fault than the homogeneous case due to off-fault energy dissipation by frictional sliding on the secondary branches. The fish bone structure with plasticity dissipate the least energy on the main fault as frictional heat among the four cases because more energy is being dissipated by the localized plastic deformation at the tips of the secondary faults.

5.3.4 Parametric Study for the Elastic Case

In order to explore the effect of the secondary faults on the rupture characteristics of the main fault, we carried out a limited parametric study by varying some geometric properties of the secondary faults including length L_f , spacing L_s, and the angle with the main fault θ_f.

Effect of secondary fault length

Fig. 5.10 shows a snapshot of slip, slip rate, shear stress, and normal stress distribution on the main fault at a given instant of time. We examine three cases of secondary fault length $L_f = L_c$; $4L_c$; $6L_c$, while keeping all the other parameters the same as in the default case. With increased length of the secondary faults, the rupture speed on the main fault decreases as well as the maximum slip rate as shown in Fig. 5.10(b). However, the oscillations in the slip rate, shown in the insert in Fig. 5.10(b), increase with increasing the secondary faults length. Furthermore, Fig. 5.10(c) and Fig. 5.10(d) show that longer secondary faults promote a more complex pattern in the shear and normal stress perturbations. In particular, not all stress peaks or troughs have the same amplitude. This is because with longer secondary faults, slip is not necessarily accumulated through the whole length of each fault suggesting that some secondary faults may accumulate less slip or their rupture may stop before reaching the far end of the secondary fault. Fig. 5.11 shows the distribution of maximum slip on the secondary faults for different secondary fault length. The results suggest that as the secondary fault length increases, a crack shielding effect emerge; the slip distribution along the secondary faults is non-uniform in the sense that as one secondary fault accumulates large slip, the following one or two accumulate smaller slip, but then comes another secondary fault with large slip, and the pattern continues. The non-uniformity in slip that increases as the secondary fault length increases, leads to non-montonicity in the stress peaks on the main fault with some of the peaks smaller than others. This crack shielding-like phenomenon (sometimes also referred as stress shadowing phenomenon) has been observed both in the experimental work by [290] for tensile cracks as well as numerical simulation results using finite-discrete element method by [280] and other studies modeling spontaneous crack branching [281] and off-fault plasticity[253].

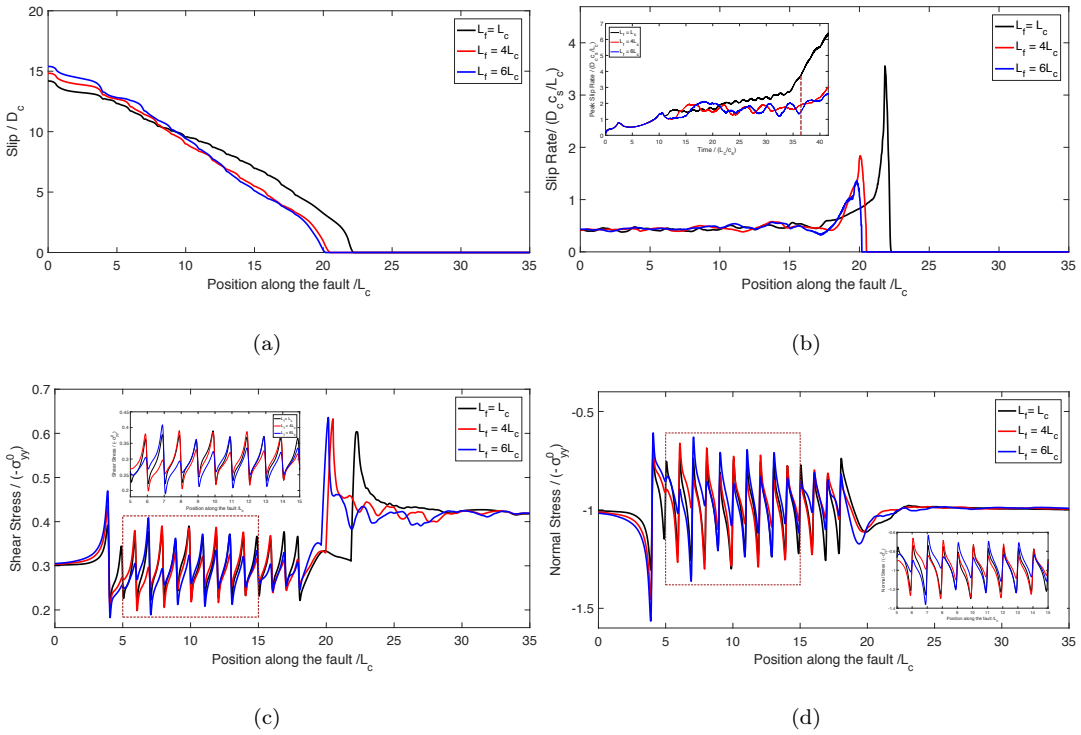

Figure 5.10: Slip, slip rate, shear stress, and normal stress distributions on the main fault, at the same point in time, with different lengths of secondary faults $L_f = L_c, 4L_c, 6L_c$ for the elastic material case. (a) Slip, (b) Slip rate, (c) Shear stress distribution, and (d) Normal stress distribution. Longer secondary faults promote a more complex pattern of stress perturbations on the main fault and lead to further reduction in the main rupture propagation speed.

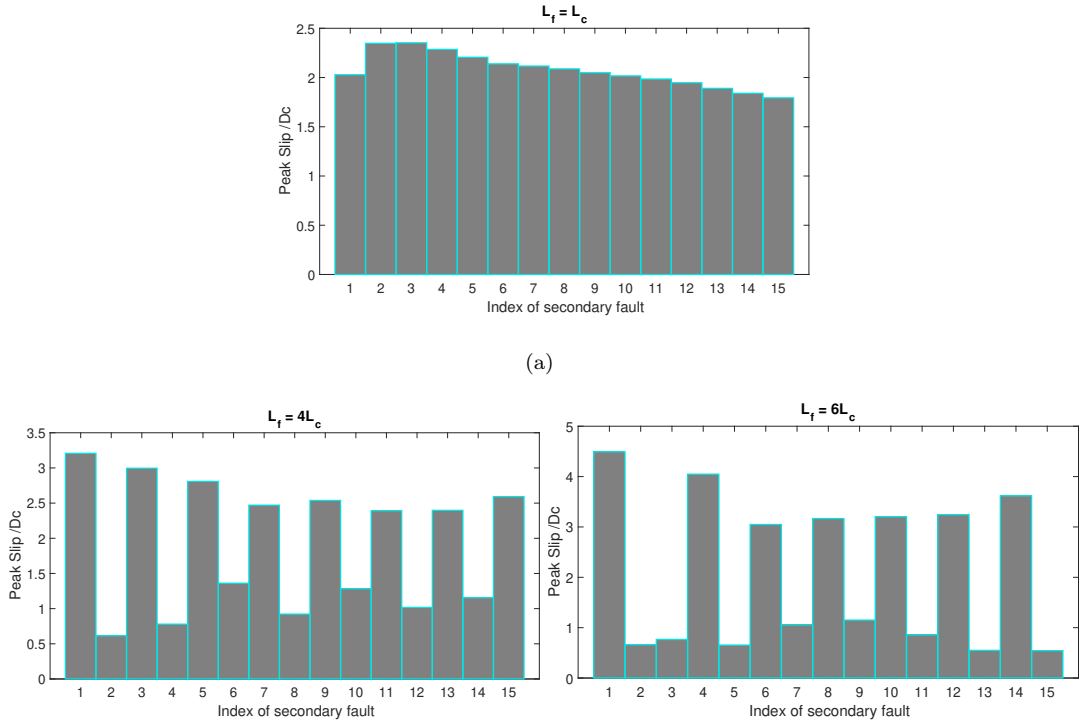

(a)

(b)

(c)

Figure 5.11: Peak Slip distribution on the secondary faults with different length $L_f = L_c$ $L_f = 4L_c$ and $L_f = 6L_c$. The crack shielding effect is more significant in the presence of longer secondary faults.

Effect of spacing distance between secondary faults

Fig. 5.12 shows a snapshot of slip, slip rate, shear stress, and normal stress distribution on the main fault at a given instant of time for three cases of secondary faults spacing $L_s = L_c; 2L_c; 4L_c$. As shown in Fig. 5.12(c) and 5.12(d), as the spacing between the secondary faults increases, the amplitude of perturbations in the shear and normal stresses on main fault increases since each secondary fault accumulates more slip on average than in the case of smaller spacing. With smaller spacing between the secondary faults, the secondary faults are more effective in decelerating the rupture on the main fault. The insert in Fig. 5.12(b) shows that with the increased spacing, the oscillations in the slip rate are spaced at a larger distance but their amplitude increases.

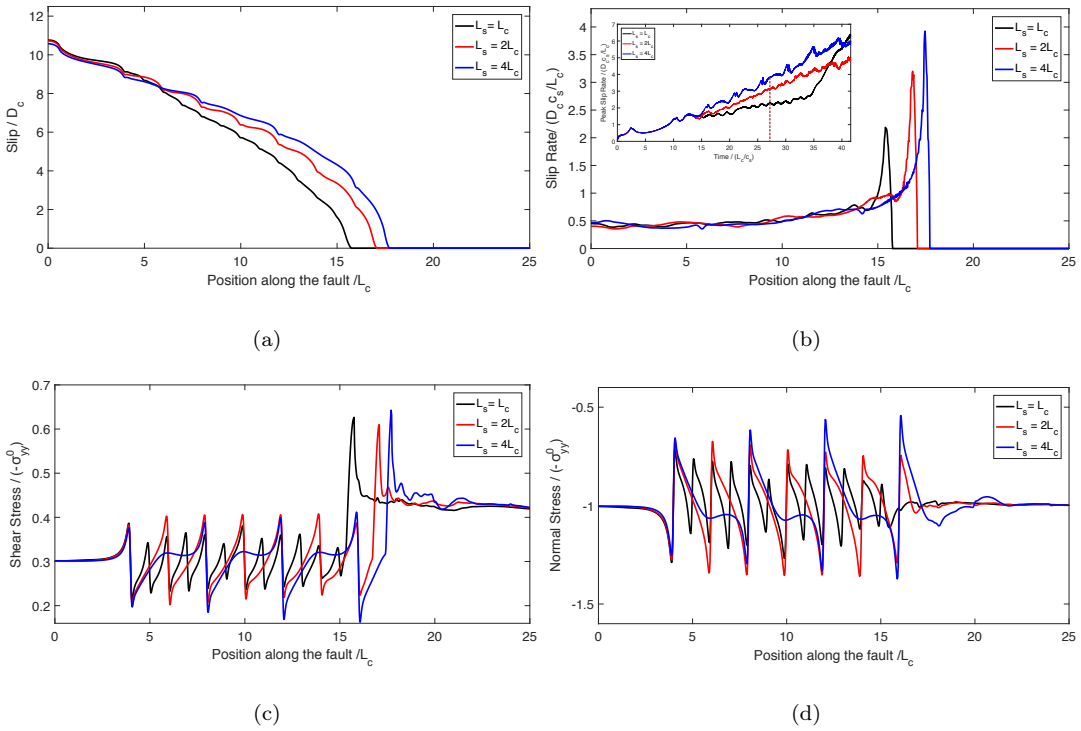

Figure 5.12: Slip, slip rate, shear stress, and normal stress distributions on the main fault, at the same point in time, with different spacing between the secondary faults $L_s = L_c, 2L_c, 4L_c$for the elastic material case. (a) Slip, (b) Slip rate, (c) Shear stress distribution, and (d) Normal stress distribution. Larger spacing between secondary faults promote stronger perturbations in the stress and slip rate on the main fault.

Effect of secondary fault angle with respect to the main fault

While the angle that a secondary fault makes with the main fault may be arbitrary, here we explore a number of different secondary faults orientation that vary around the direction of optimally oriented shear plane computed using the background tectonic stress field and a Mohr-Coulomb failure criterion.

$$\theta = 45^o + \theta_p - \frac{\psi}{2} \tag{5.13}$$

In Eq. 5.13 above, ψ is the angle of internal friction, and θ_p is the angle that the maximum principal stress makes with the horizontal direction. Fig. 5.13 shows the Mohr's circle representing the state of the background stress in the domain. For the parameters shown in Table 5.1, and as demonstrated by the Mohr's circle, the direction of optimally oriented shear plane makes approximately a 50 degree angle clockwise with the direction of the main fault. Accordingly, we consider four cases of orientation

of the branching faults, $\theta = 40^o$, 50^o, 60^o, and 70^o, in addition to the default case, $\theta = 30^o$, discussed earlier. The resolved normal stress, shear stress and the strength parameter S on the secondary faults are summarized in Table 5.2. Fig. 5.14 suggests that the amplitude of the shear and normal stress fluctuations on the main fault have a nonmonotonic trend as the secondary faults are rotated away from the main fault. The case of secondary faults with $\theta = 40^o$ results in the largest amplitude of stress perturbations on the main fault among all the angles considered here. By investigating the slip evolution on the main fault (Fig. 5.15), we have found that the main fault rupture has transitioned into supershear mode when the branch angles are $\theta = 50^o$ and $\theta = 60^o$ while it remains subshear in all the other cases ($\theta = 30^o$, 40, and 70). The resulting slip distribution across the secondary faults for the different branch angles are given by the histograms in Fig. 5.16. The average slip on the secondary faults increases as the branch angle moves towards the optimal orientation (i.e. from $\theta = 30^o$ to $\theta = 40^o$) which is consistent with the increase in the amplitude of stress perturbations on the main fault. Surprisingly, however, the average slip on the secondary faults is lower at $\theta = 50^o$ (the optimal orientation according to the background stress state) and $\theta = 60^o$. The reduction in slip on the secondary faults in these case, despite favorable orientation, is hypothesized to be due to the supershear transition on the main fault which leads to: (1) amplification of slip on the main fault, and (2) rapid exit of the main fault rupture tip from the fish bone region reducing the exposure time of the secondary faults to the impulsive dynamic loading from the main fault rupture tip. This is accompanied by a reduction in the amplitude of stress perturbations on the main fault compared to the case of $\theta = 40^o$. Finally, as the branch angle further increases (e.g. $\theta = 70^o$), the resolved shear stress starts to decrease while the resolved normal stress continues to increase. This makes it more difficult to trigger slip on the secondary branches. Indeed, the case for $\theta = 70^o$ has much smaller average slip value (almost an order of magnitude less) than all the other cases. As a result, the stress perturbations on the main fault in this case is also the smallest. Understanding supershear transition mechanisms in fault systems with complex topology, like the one considered here, and implications for slip partitioning and stress transfer, will be the focus of a future investigation.

Table 5.2: The resolved stress and strength parameter on the secondary fault for different angle. Note that negative sign in the normal stress indicates compression and negative sign in the shear stress indicates left lateral shear.

Secondary fault angle θ_f	**Resolved Normal Stress**	**Resolved Shear Stress**	**Strength Parameter S**
30°	-45.18 MPa	-11.65 MPa	-8.12
40°	-50.96 MPa	-21.15 MPa	1.61
50°	-59.65 MPa	-28.09 MPa	0.75
60°	-70.18 MPa	-31.65 MPa	0.99
70°	-81.30 MPa	-31.39 MPa	2.48

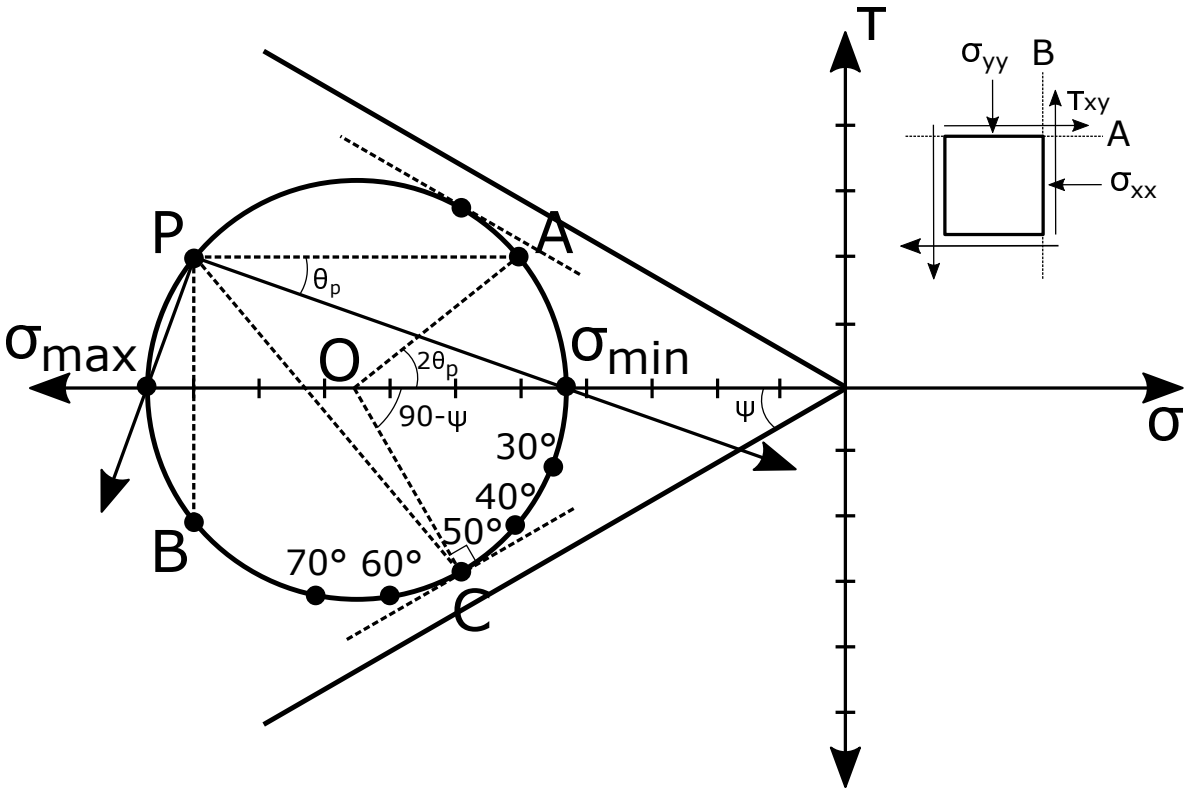

Figure 5.13: Mohr's Circle representation of stress condition. P is the pole point. θ_p is the angle between the horzontal plane and the maximum principle stress plane. ψ is the internal friction angle. Secondary faults with different angles are marked as black dots on the circle.

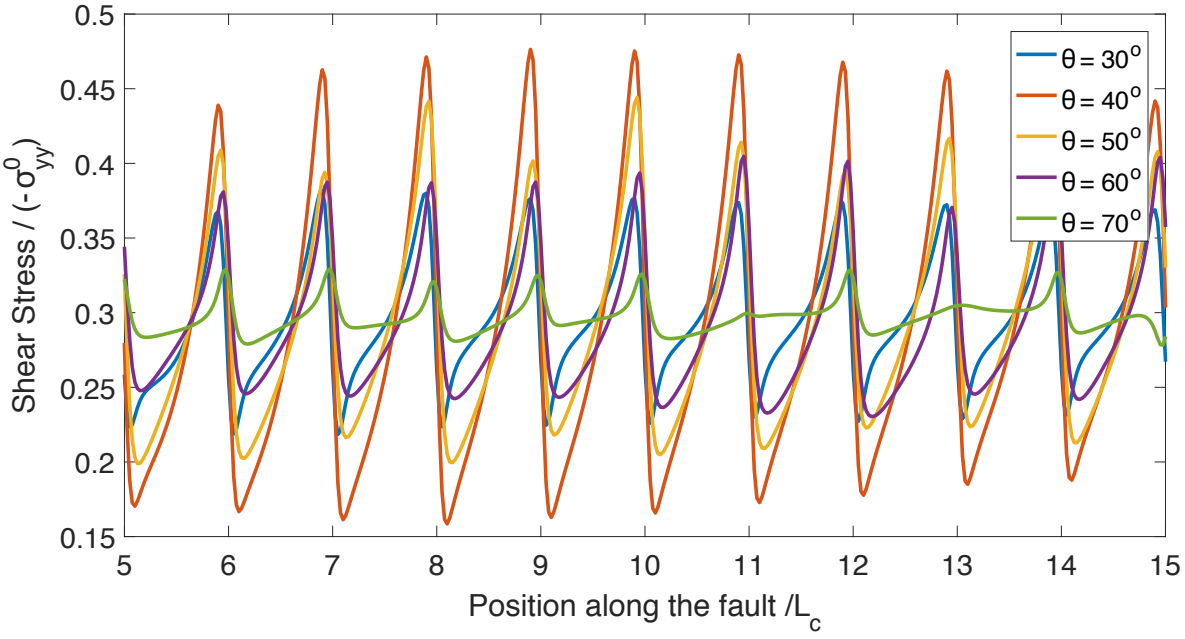

(a)

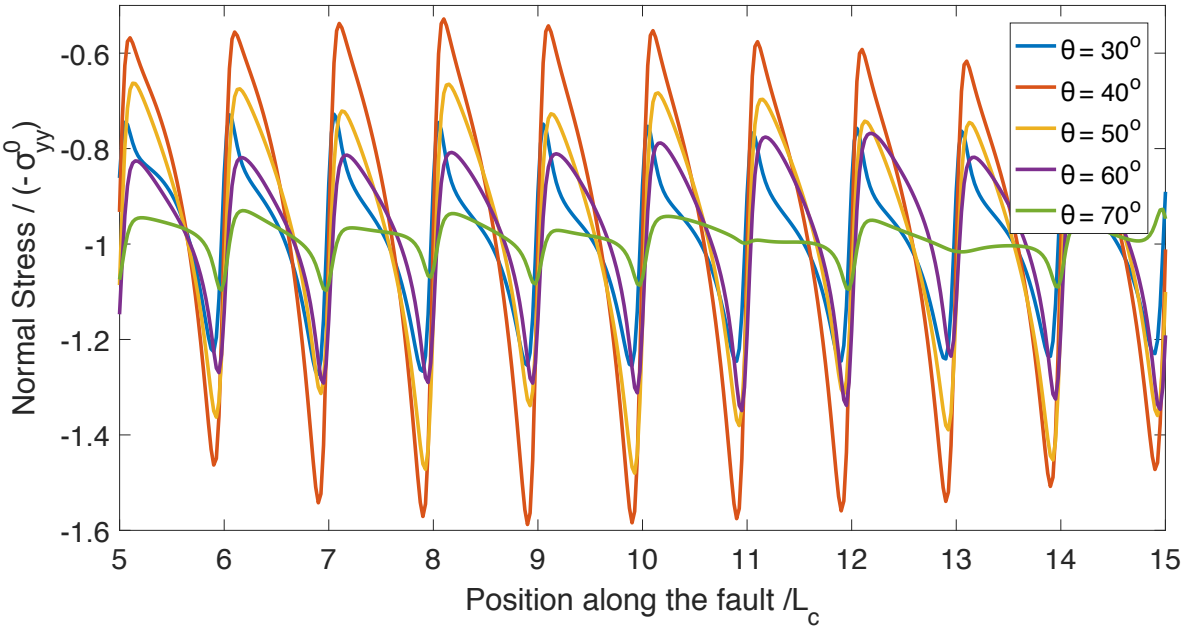

(b)

Figure 5.14: Shear stress and normal stress distributions on the main fault, at the same point in time, for different orientations of secondary faults with respect to the fault parallel direction $\theta = 30, 40, 50, 60, 70$ degrees in the elastic material case. (a) Shear stress distribution, (b) Normal stress distribution. The amplitude of the stress perturbations decrease as the secondary faults rotate away from the optimally oriented shear plane direction ($\theta = 50$ degree).

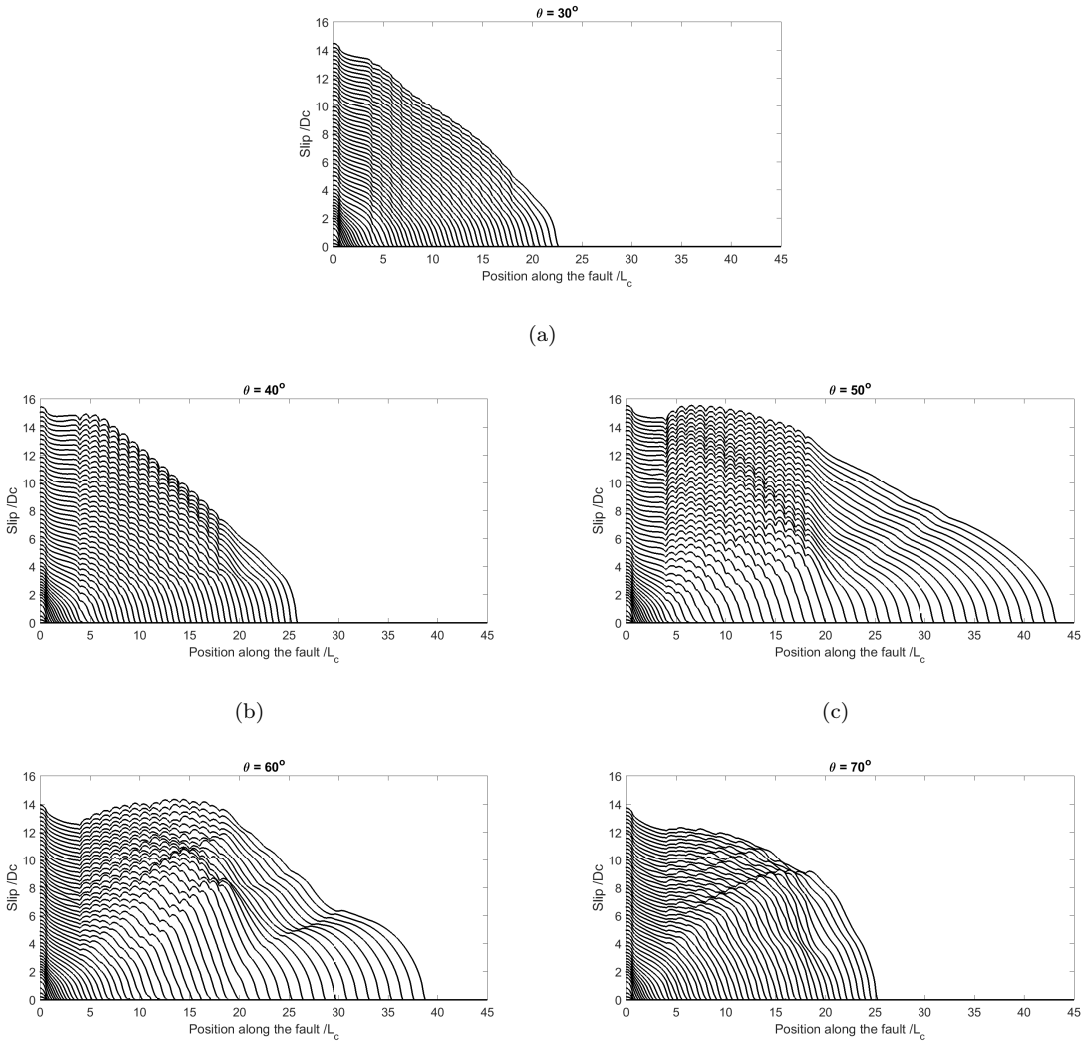

Figure 5.15: Slip line plotted every 0.1s up to $t = 6s$ on the main fault with secondary faults of different angles $\theta = 30^o, 40^o, 50^o, 60^o, 70^o$. Note that the rupture have traversed a much longer distance for cases $\theta = 50^o$ and 60^o than the other cases suggesting that a supershear transition has occurred. The rupture speed in the case with secondary faults $\theta = 50^o$ was found to be $0.92c_p$.

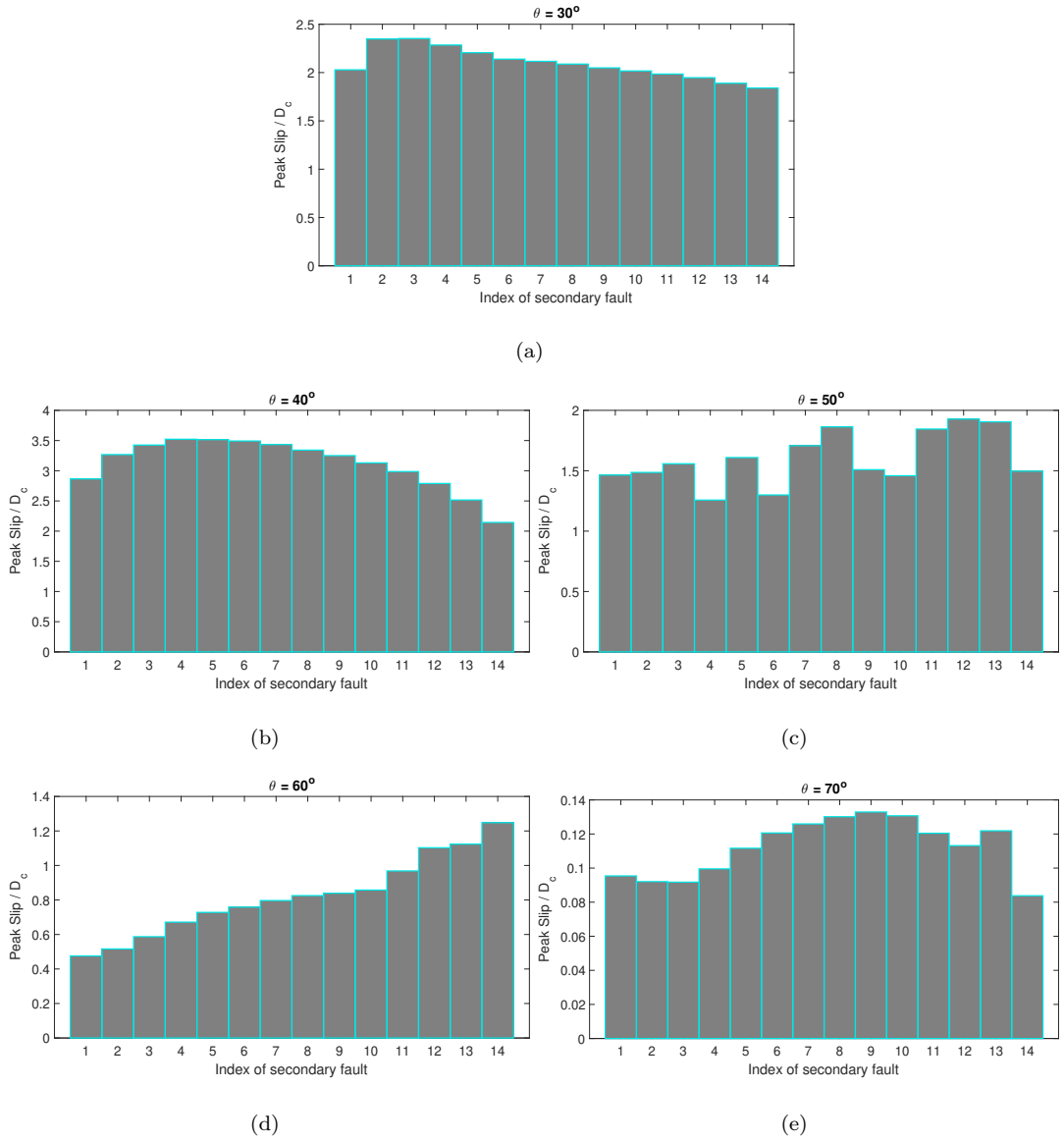

Figure 5.16: Peak Slip distribution on the secondary faults with different angles $\theta = 30^o$, 40^o, 50^o, 60^o, 70^o

5.4 Discussion

Earthquake ruptures are nonlinear multiscale phenomena. A fundamental challenge in earthquake source physics is to resolve this vast range of scales. In this study we have focused on resolving the influence of one of the intermediate spatial scales, namely small scale fault branches, on the rupture dynamics of a single event. These branches are characterized as being small scale since their length is of the order of the reference length scale for nucleation in mature faults.

Our investigation of the effect of explicitly represented small scale branches on rupture dynamics reveals several results that are consistent with the more conventional method of modeling small scale damage as an effective elasto-plastic or continuum damage constitutive relation. For example, slip on these secondary faults increases the overall energy dissipation leading to a reduction in the accumulated slip, maximum slip rate, and rupture propagation speed on the main fault. However, explicit representation of these anisotropic pre-existing slip planes also lead to some novel insights that may not be captured by continuum plasticity models.

For example, the interaction of the main rupture with the short branches leads to strong heterogeneities in the final normal and shear stress distributions. These stress fluctuations may potentially lead to fault opening or reversal in the sign of the shear stress on the main fault, although this has not been observed within the parameter range explored in this study. Interestingly, these stress heterogeneities due to the existence of the secondary branches persist even in the presence of elasto-plastic material response. They do not get smeared or homogenized. The nonuniform stress distribution left over after the seismic event may influence the nucleation, propagation, and arrest of future seismic events. Furthermore, the secondary branches may also act as potential nucleation sites for future ruptures, that do not lie directly on the main fault, but may potentially jump over to its plane. Thus, there is significant potential that this model may form a basis for earthquake complexity.

Moreover, explicit representation of the secondary branches suggest that these features may contribute significantly to the near field high frequency generation. The constructive interference between the seismic radiation from the secondary faults lead to coherent high-frequency generation in the bulk that is strongly correlated to the geometric distribution of the secondary branches. Furthermore, we demonstrated that the near-field acceleration spectrum in the presence of secondary faults is almost flat in the range of 2-20 Hz. This feature has been widely documented in observations [288, 289]. It is also similar to what [267] have observed in dynamic rupture simulations on rough faults. This suggests that complex geometric features, other than fault roughness, such as secondary short branches, may lead to similar coherent high frequency generation patterns.

The secondary faults may act as both energy sinks and energy sources for the main fault. This apparently conflicting role may be explained as follows. As the main fault rupture propagates and the secondary faults are being activated, energy is being dissipated by slip on the secondary faults and therefore the branches act as energy sinks. In the meantime, as the secondary faults are activated

there is dynamic stress drop on these faults. This generates seismic waves that may load the main fault favorably leading to a transient acceleration in the main fault rupture propagation speed or slip rate. Thus, in this limit, the secondary faults may act as energy source. However, this effect depends on the orientation of the secondary fault as well as the stage of the rupture on the main fault (e.g. its current rupture speed). For example, in Fig. 5.9(a) the transient increase in the rupture speed on the main fault happens in the early stages of the rupture where the speed is still lower than the limiting speed. Later in the rupture history, the effect of the secondary fault energy dissipation dominates over the transient dynamic stress transfer and the rupture speed on the main fault decreases.

Different mechanisms have been proposed for fault roughness evolution [261, 291]. These mechanisms include fragmentation, wear, and healing. We have shown here that slip on secondary branches may lead to stress concentrations that load the main fault in a way that leads to undulations in the fault plane with a periodicity comparable to the spacing between the secondary branches. While the amplitude of these undulations is small, they may grow due to repeated ruptures, thus, providing an additional mechanism for fault plane roughness evolution on small scales.

In this study, we have used linear slip-weakening as the fault constitutive model. The rate and state friction framework [135, 136], however, has been successful in interpreting several lab and field observations. While the slip-weakening friction may not be a realistic representation of the fault physics, it is a useful mathematical model that may approximate rate and state friction response, without strong velocity weakening, with the appropriate choice of parameters. In future work, we plan to investigate our results in the framework of rate and state friction with dynamic weakening to explore the role of large dynamic stress drops as well as time dependent post-seismic deformation on the stress concentrations generated by the fish bone structure.

The recent models by [280] provide a pioneering step towards exploration of the influence of co-seismically evolving off-fault damage on rupture dynamics. The current study complements these on-going efforts in the community and provides a step forward towards explicit inclusion of small scale physics in fault zone in the form of pre-existing anisotropic damage features. Continuum damage models and conventional plasticity algorithms are prone to numerical localization. In our case, we pre-define the secondary slip planes based on the background tectonic stress field. While this biases our choice for the fault plane orientations, our results are not mesh dependent. There is a need for development of computational algorithms that may nucleate and grow faults on the fly with minimum

or no mesh dependency. Potential candidates include nonlocal damage and plasticity models [110, 292], extended finite element methods [293, 294], and Discontinuous Galerkin scheme with adaptive mesh refinement [295, 296].

In this study, for modeling energy dissipation at scales smaller than the scale that is explicitly represented by the secondary branches, we adopted the rate-independent Drucker-Prager plasticity model. Without any regularization, the model is prone to artificial strain localization. While the stress concentration at the tips of the secondary branches is physical and necessitates a concentration in the plastic strain, a robust feature in our model that seems to persist at different resolutions, the orientation of the localization band shown in Fig. 5.8 around the tips of the fish bone structures may have a mesh-dependent ingredient. In the results presented here, the reported shear bands are several elements wide in some places but this does not entirely eliminate the mesh sensitivity. In future work, a rate-dependent plasticity model will be used such as rate-dependent Drucker-Prager plasticity model or rate sensitive Shear Transformation Zone theory [110] to avoid or limit the effects of any potential numerical artifacts.

In this study we introduced an application of the recently developed hybrid method which attests to its potential for modeling dynamic rupture with high resolution fault zone physics. While explicit representation of short branches is a start, other candidate applications are also possible. For example, we may use the hybrid method to model strain localization and shear band evolution within the gouge region [110] while maintaining the influence of long range elastic stress transfer in the bulk. Another potential application is to model small-scale damage patterns, as has been done experimentally by [297] to study the transient and steady-state effect of damage patterns on the rupture dynamic. These problems are too challenging for the traditional domain-based numerical schemes but the efficient domain truncation using the hybrid scheme may make them more doable.

Future extensions of this work may include expanding the parametric study initiated here to include nonuniform spacing, orientation, and length of the secondary faults. The ultimate goal would be to use the hybrid scheme to model earthquake cycles in complex fault zone structures bridging both seismic and aseismic episodes and enabling the interplay between dynamics, stress evolution, and geometry to understand the underpinnings of earthquake complexity.

5.5 Conclusion

In this study, we apply our recently developed hybrid numerical scheme to investigate the influence of explicitly represented small scale branches on rupture dynamics. The main conclusions may be summarized as follows:

- The secondary faults increase the overall energy dissipation leading to a reduction in the slip, peak slip rate, and rupture propagation on the main fault.
- The activation of the secondary faults may lead to backward propagating ripples in the slip rate that increases slip far from the rupture tip.
- Rupture activation, propagation, and arrest on the secondary branches lead to a strongly heterogeneous normal and shear stress field on the main fault.
- The interaction of the seismic waves generated by the secondary branches promotes high-frequency generation and generate high-frequency fluctuations on the computed seismograms.
- The secondary branches lead to the evolution of normal undulations in the main fault strike.

Chapter 6

Conclusions and future works

In this research, we focus on modeling earthquake dynamic rupture with high resolution physics. Along this line, first we present a complex fault zone structure and its effect on earthquake dynamic rupture mode transition. And then we look further into the material behavior within the fault zone and develop a non-equilibrium statistical thermodynamics-based viscoplastic framework for modeling granular systems. To address the spatio-temporal complexity of the earthquake source process, we have developed a hybrid computational algorithm for modeling earthquake rupture using a combination of the finite element method and the spectral boundary integral method. Furthermore, we demonstrate the powerful capability of the hybrid approach by solving one of the computationally challenging problem in earthquake dynamic rupture modeling, namely, rupture propagation on a fault plane with multiple short branches. The major contributions and directions of future research are summarized below.

6.1 Contributions

A new supershear transition mechanism:

In Chapter 2, we explored the influence of the existence of a spatially localized off-fault material heterogeneity, represented by off-fault low velocity lens, on the dynamics of rupture propagation on a slip weakening frictional interface. For the first time, to the best of our knowledge, we show that the existence of soft inclusion off the fault plane may promote supershear transition under low prestress conditions. Furthermore, we have conducted a thorough parametric study regarding the soft inclusion geometry and material properties which suggested that the off-fault soft inclusion may have a significant effect on the dynamic rupture characteristics including slip, slip rate, energy dissipation, and the nucleation of the daughter crack through the Burridge-Andrews mechanism. Moreover, this research is already contributing to the ongoing efforts of the earthquake physics community by highlighting the importance of considering material heterogeneity explicitly in the earthquake model and the need for accurately mapping these regions in the field. The research results from this study are published in

Ma and Elbanna [25].

A physics-based model for viscoplasticity and strain localization in gouge media driven by the kinematics of granular rearrangements:
Chapter 3 developed a thermodynamically consistent framework for amorphous plasticity in 2D finitely deformed granular media using the concept of compactivity. The study includes a thorough derivation of a non-equilibrium statistical thermodynamics-based viscoplastic framework for modeling granular systems within the Shear Transformation Zone theory. We realized the thermodynamically consistent framework for amorphous plasticity in a multiphysics finite element framework. The primary goal of this study was to investigate the strain localization behavior in sheared granular material, particularly in dry condition. We conducted numerical simulations with granular material initial conditions consistent with a wide range of experiments. The strain localization formation pattern from this study has a good agreement with the experimental observation. And furthermore, we have applied the numerical model to study effect of different factors on the strain localization such as the initial granular material compactivity, granular layer thickness, confining pressure and etc. We have shown that there are several important factors that govern the brittle to ductile transition in the granular material. The numerical model generically predicts complex shear band localization pattern. The numerical results in this study are published in Ma and Elbanna [110].

A new computationally efficient hybrid numerical scheme for high resolution modeling of earthquake dynamic ruptures:
Chapter 4 developed a hybrid Finite Element-Spectral Boundary Integral approach for modeling earthquake with high resolution and accuracy. This hybrid method enables the simulation of wave propagation in unbounded domains with near-source heterogeneities, material nonlinearities, or a complex fault geometry. The method is shown to be flexible, accurate and more efficient than a bulk method and could handle material heterogeneity and geometry complexity problem which are difficult for the boundary based method. The hybrid approach has the potential for use in the field of earthquake cycle simulation for long term earth sequence study with incorporation of complex fault geometry and material heterogeneity. The research results from this study are published in Ma et al. [214].

A Frontier application: Modeling dynamic rupture in fault zones with explicit modeling of small scale anisotropic discrete damage features:
Chapter 5 investigated the influence of small scale branches on rupture dynamics. This chapter also

demonstrated the powerful capability of the hybrid approach in solving the scale complexity in the earthquake rupture modeling problem. Due to the computational efficiency of the hybrid method, we are able to represent these small scale branches explicitly. By including these small features we observed a strong heterogeneous stress distribution due to the secondary faults' rupture activation, propagation and arrest. We also found out due to the interaction from the seismic generated waves from the secondary faults, high frequency fluctuation is observed on the seismograms and the observed range of high frequency generation is consistent with the field data. This study shows the importance of consideration of these small scale feature on the earthquake dynamic rupture. The research results from this study are published in Ma and Elbanna [259].

6.2 Future works

This dissertation focuses on the theme of modeling earthquake rupture modeling with high resolution physics and the previous works are conducted along this major theme. Thus, directions for future research are also presented along this line. Tho major categories of feature research themes could be identified as: (1) Extension of the Hybrid Finite Element-Spectral Boundary Integral framework to incorporate more physicals models in terms of material nonlinearity and geometry complexity. (2) Application of the hybrid method for earthquake modeling with high fidelity and accuracy. Section 6.2.1 presents ideas for numerical analysis of the hybrid method, to gain deeper understanding of the performance of the hybrid method. Section 6.2.2 presents ideas for the extension of the hybrid method for earthquake long-term cycle simulation by integrating the aseismic periods. Section 6.2.3 presents ideas for modeling spontaneous of damage initiation and propagation during the dynamic rupture.

6.2.1 Numerical analysis of the hybrid scheme

The hybrid scheme has shown an excellent performance in terms of accuracy and efficiency compared to pure finite element method of the same resolution. In particular, for the range of problems discussed in Chapter 5, the hybrid scheme achieves 20 times speed up and 50% reduction in memory requirement compared to FEM with both schemes being implemented in serial. However, so far, we have limited the implementation of the hybrid scheme to the case where we have matched discretization in space and time between the finite element part of the model and the spectral boundary integration scheme. An important direction for future work is to explore the possibility of relaxing these constraints. Specifically, it will be interesting to evaluate the effect of having different spatial discretizations, time

integration algorithms, and time steps between the two domains in the hybrid implementation. It will also be of interest to investigate how the performance of the method changes when using higher order shape functions in the finite element domain as in the spectral FEM formulation or isoparamteric elements with cubic or quartic shape functions. These investigations will help us gain a deeper understanding of the limitations and further potential of the hybrid scheme.

6.2.2 Modeling earthquake cycle with complex fault geometry and material heterogeneity

One of the most important potential future directions in terms of extension of the hybrid earthquake modeling framework is to incorporate modeling earthquake intersesmic period into hybrid earthquake modeling framework. And furthermore, more sophisticated physics-based material model as well as complex fault geometry could be incorporated into the hybrid earthquake modeling framework. The details steps are as follows:

- Incorporate quasi-dynamic earthquake sequence simulation capability into the hybrid earthquake simulation framework. We have already shown initial attempts in earthquake cycle simulation using hybrid method in a 2D antiplane setting with quasi-dynamic approximation with material heterogeneity specifically the existence of low velocity fault zone [298]. Tasks need to be done in this future direction along this line are as follows:
  - Extend the hybrid cycle framework to 2D inplane model and eventually for full 3D.
  - During the seismic period, switch to complete dynamic problem with inertia effect.
- As introduced in the previous chapters, earthquake is a highly nonlinear and complex system. The main goal of this research is toward modeling earthquake rupture with high resolution physics. Therefore, towards modeling earthquake rupture with more realistic condition, more physics-based material model and geometry complexity needs to be considered. Tasks need to be done in this future direction along this line are as follows:
  - Integrate the viscoplasticity framework based on the Shear transformation zone theory which was developed in Chapter 3 into the hybrid earthquake modeling framework. With the integration of the granular modeling framework, this would enrich our understanding of earthquake mechanism.
  - In terms of integrating geometry complexity, after extending the hybrid simulation framework to 3D, the SCEC Community Fault model [299] could be incorporated to study the

effect of fault geometry effect on dynamic rupture and long term earthquake sequence.

- Based on the previous studies, the hybrid scheme shows the excellence performance in terms of accuracy and efficiency. One important future work is to perform a thorough numerical analysis for the hybrid scheme and gain deeper understanding of reason for the high performance of the hybrid method.

6.2.3 Damage evolution and propagating fracture

The current dynamic rupture simulation in the Hybrid framework are conducted with pre-existing faults, the algorithm doesn't allow fault to propagate and damage evolve. In this future direction, we would apply the recently developed Asynchronous Space-Time discontinuous galerkin method [300] into the dynamic rupture study. All elements in the DG method are discontinuous along their common edges, which makes the method intrinsically suitable for modeling fault rupture problem. With the asynchronous feature, the intrinsic adaptive feature in both space and time allows exploring small scale features more accurately and efficiently. As shown in Fig. 6.1, the adaptivity in the space-time occurs asynchronously, which is particularly suitable for problems in dynamics. Specifically, in places where the wave hasn't arrived yet, the mesh may advance more in time. Spatially, the adaptivity in space enables high accuracy in capturing the wave fronts and crack tip stress fields.

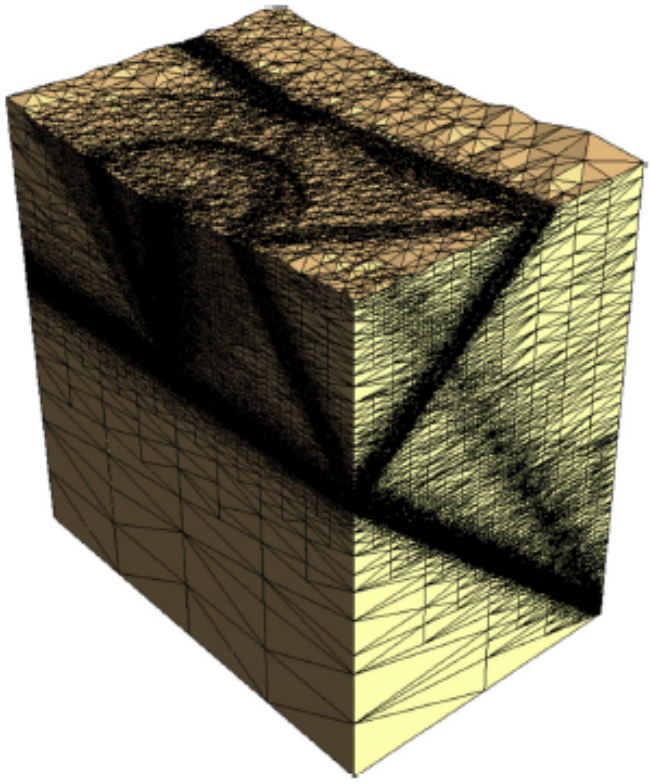

Figure 6.1: Adaptive space mesh for an elastodynamic simulation of crack-tip wave scattering in 2d×time. The vertical direction represents time [300].

Another powerful aspect of the Discontinuous Galerkin method is its flexibility in modeling damage evolution by growing discrete fracture surfaces. Abedi and Haber [300] have demonstrated this feature for Mode I fractures as shown in Fig. 6.2. There, the crack propagates and branches as dictated by the stress field and the mesh seamlessly adapts at each crack tip. We plan to extend the formulation to incorporate Mode II fractures with rate and state frictional boundary conditions and pressure dependent strength in the bulk. Incorporating the capability of spontaneous crack initiation, propagation and secondary fault branching will enable new and unprecedented insights into the mechanics of fault zones.

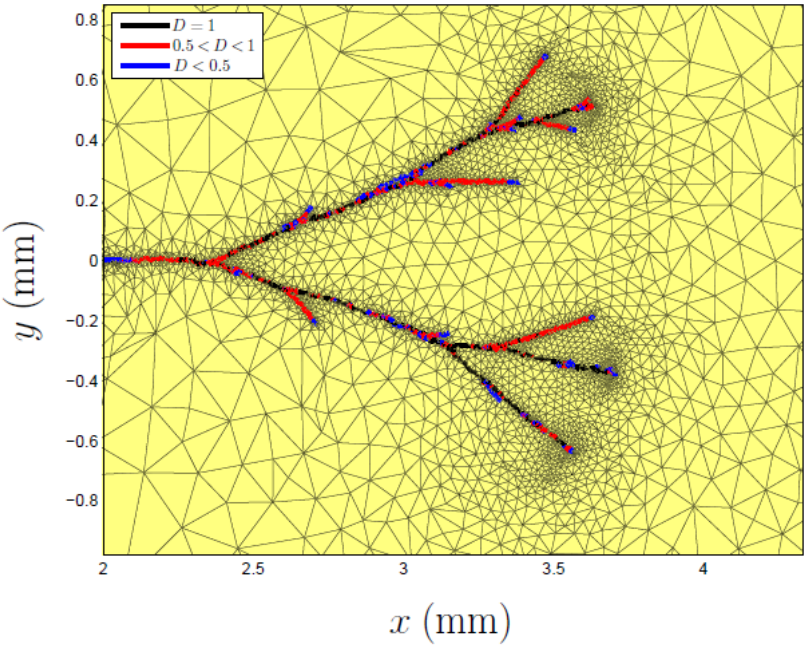

Figure 6.2: Crack propagation using space-time discontinues galerkin method [300].

Bibliography

[1] Hiroyuki Noda, Eric M Dunham, and James R Rice. Earthquake ruptures with thermal weakening and the operation of major faults at low overall stress levels. *Journal of Geophysical Research*, 114(B7):B07302, 7 2009.

[2] D. J. Andrews. A numerical study of tectonic stress release by underground explosions. *Bulletin of the Seismological Society of America*, 63(4):1375, 1973.

[3] Steven M Day. Three-dimensional finite difference simulation of fault dynamics: Rectangular faults with fixed rupture velocity. *Bulletin of the Seismological Society of America*, 72(3):705–727, 1982.

[4] R. Madariaga, K. Olsen, and R. Archuleta. Modeling dynamic rupture in a 3d earthquake fault model. *Bulletin of the Seismological Society of America*, 88(5):1182, 1998.

[5] D. J. Andrews. Test of two methods for faulting in finite-difference calculations. *Bulletin of the Seismological Society of America*, 89(4):931, 1999.

[6] Luis A Dalguer and Steven M Day. Staggered-grid split-node method for spontaneous rupture simulation. *Journal of Geophysical Research*, 112(B2):B02302, 2 2007.

[7] Peter Moczo, Johan O A Robertsson, and Leo Eisner. The Finite-Difference Time-Domain Method for Modeling of Seismic Wave Propagation. *Advances in Geophysics*, 48(06):421–516, 2007.

[8] Geoffrey P. Ely, Steven M. Day, and Jean-Bernard Minster. A support-operator method for 3-d rupture dynamics. *Geophysical Journal International*, 177(3):1140–1150, 2009.

[9] David D. Oglesby, Ralph J. Archuleta, and Stefan B. Nielsen. Earthquakes on dipping faults: The effects of broken symmetry. *Science*, 280(5366):1055–1059, 1998.

[10] David D. Oglesby, Ralph J. Archuleta, and Stefan B. Nielsen. The three-dimensional dynamics of dipping faults. *Bulletin of the Seismological Society of America*, 90(3):616, 2000.

[11] B. T. Aagaard, M. G. Knepley, and C. A. Williams. A domain decomposition approach to implementing fault slip in finite-element models of quasi-static and dynamic crustal deformation. *Journal of Geophysical Research: Solid Earth*, 118(6):3059–3079, 2013.

[12] Shamita Das. A numerical method for determination of source time functions for general three-dimensional rupture propagation. *Geophysical Journal International*, 62(3):591–604, 1980.

[13] D. J. Andrews. Dynamic plane-strain shear rupture with a slip-weakening friction law calculated by a boundary integral method. *Bulletin of the Seismological Society of America*, 75(1):1, 1985.

[14] Alain Cochard and Raúl Madariaga. Dynamic faulting under rate-dependent friction. *Pure and Applied Geophysics PAGEOPH*, 142(3-4):419–445, 1994.

[15] Rice James R Geubelle, Philipppe H. A Spectral Method for Three-Dimensional Fracture Problems. *Journal of the Mechanics and Physics of Solids*, 43(11):1791–1824, 1995.

[16] Nadia Lapusta, James R Rice, Yehuda Ben-Zion, and Gutuan Zheng. Elastodynamic analysis for slow tectonic loading with spontaneous rupture episodes on faults with rate- and state-dependent friction. *Journal of Geophysical Research*, 105:23765, 2000.

[17] J.P. Ampuero. *Étude physique et numérique de la nucléation des séismes*. Grenoble Thèses. Atelier national de reproduction des thèses, 2002.

[18] Y. Kaneko, N. Lapusta, and J.-P. Ampuero. Spectral element modeling of spontaneous earthquake rupture on rate and state faults: Effect of velocity-strengthening friction at shallow depths. *Journal of Geophysical Research: Solid Earth*, 113(B9).

[19] M. Benjemaa, N. Glinsky-Olivier, V. M. Cruz-Atienza, J. Virieux, and S. Piperno. Dynamic non-planar crack rupture by a finite volume method. *Geophysical Journal International*, 171(1):271–285, 2007.

[20] Martin Käser and Michael Dumbser. An arbitrary high-order discontinuous Galerkin method for elastic waves on unstructured meshes - I. The two-dimensional isotropic case with external source terms. *Geophysical Journal International*, 166(2):855–877, 8 2006.

[21] J. de la Puente, J.-P. Ampuero, and M. Käser. Dynamic rupture modeling on unstructured meshes using a discontinuous galerkin method. *Journal of Geophysical Research: Solid Earth*, 114(B10).

[22] Setare Hajarolasvadi and Ahmed E. Elbanna. A new hybrid numerical scheme for modelling elastodynamics in unbounded media with near-source heterogeneities. *Geophysical Journal International*, 211(2):851–864, 2017.

[23] Alexei N B Poliakov, Renata Dmowska, and James R Rice. Dynamic shear rupture interactions with fault bends and off-axis secondary faulting. *Journal of Geophysical Research*, 107(B11):ESE 6–1–ESE 6–18, 2002.

[24] J. M. Sowers, J. R. Unruh, W. R. Lettis, and T. D. Rubin. Relationship of the kickapoo fault to the Johnson Valley and Homestead Valley faults, San Bernardino County, California. *Bulletin of the Seismological Society of America*, 84(3):528–536, 6 1911.

[25] Effect of off-fault low-velocity elastic inclusions on supershear rupture dynamics Effect of off-fault low-velocity elastic inclusions on supershear rupture dynamics Xiao Ma Department of Civil and Environmental Engineering , University of Illinois at Urb. 2015.

[26] Southern California Earthquake Center Caltech.Dataset, 2013.

[27] Y. Ben Zion and C. G. Sammis. Characterization of fault zones. *Pure and Applied Geophysics*, 160(3-4):677–715, 2003.

[28] Y. G Li and P. C. Leary. Fault zone trapped seismic waves. *Bulletin of the Seismological Society of America*, 80(5):1245–1271, October 01 1990.

[29] Yong-Gang Li, Po Chen, Elizabeth S. Cochran, John E. Vidale, and Thomas Burdette. Seismic evidence for rock damage and healing on the san andreas fault associated with the 2004 m 6.0 parkfield earthquake. *Bulletin of the Seismological Society of America*, 96(4B):S349–S363, September 01 2006.

[30] Michael A. Lewis and Yehuda Ben-Zion. Diversity of fault zone damage and trapping structures in the parkfield section of the san andreas fault from comprehensive analysis of near fault seismograms. *Geophysical Journal International*, 183(3):1579–1595, December 01 2010.

[31] M. A. Lewis, Z. Peng, Y. Ben-Zion, and F. L. Vernon. Shallow seismic trapping structure in the san jacinto fault zone near anza, california. *Geophysical Journal International*, 162(3):867–881, September 01 2005.

[32] Hongfeng Yang and Lupei Zhu. Shallow low-velocity zone of the san jacinto fault from local earthquake waveform modelling. *Geophysical Journal International*, 183(1):421–432, October 01 2010.

[33] Yong-Gang Li, Keiiti Aki, David Adams, Akiko Hasemi, and William H. K. Lee. Seismic guided waves trapped in the fault zone of the landers, california, earthquake of 1992. *Journal of Geophysical Research: Solid Earth*, 99(B6):11705–11722, 1994.

[34] Zhigang Peng, Yehuda Ben-Zion, Andrew J. Michael, and Lupei Zhu. Quantitative analysis of seismic fault zone waves in the rupture zone of the 1992 landers, california, earthquake: evidence for a shallow trapping structure. *Geophysical Journal International*, 155(3):1021–1041, December 01 2003.

[35] Hongyi Li, Lupei Zhu, and Hongfeng Yang. High-resolution structures of the landers fault zone inferred from aftershock waveform data. *Geophysical Journal International*, 171(3):1295–1307, December 01 2007.

[36] Yong-Gang Li, John E. Vidale, Steven M. Day, David D. Oglesby, and the SCEC Field Working Team. Study of the 1999 m 7.1 hector mine, california, earthquake fault plane by trapped waves. *Bulletin of the Seismological Society of America*, 92(4):1318–1332, May 01 2002.

[37] Elizabeth S. Cochran, Yong-Gang Li, Peter M. Shearer, Sylvain Barbot, Yuri Fialko, and John E. Vidale. Seismic and geodetic evidence for extensive, long-lived fault damage zones. *Geology*, 37(4):315–318, April 01 2009.

[38] Hongfeng Yang, Lupei Zhu, and Elizabeth S. Cochran. Seismic structures of the calico fault zone inferred from local earthquake travel time modelling. *Geophysical Journal International*, 186(2):760–770, August 01 2011.

[39] Takashi Mizuno, Yasuto Kuwahara, Hisao Ito, and Kin'ya Nishigami. Spatial variations in fault-zone structure along the nojima fault, central japan, as inferred from borehole observations of fault-zone trapped waves. *Bulletin of the Seismological Society of America*, 98(2):558–570, April 01 2008.

[40] Yehuda Ben-Zion, Zhigang Peng, David Okaya, Leonardo Seeber, John G. Armbruster, Naside Ozer, Andrew J. Michael, Serif Baris, and Mustafa Aktar. A shallow fault-zone structure illuminated by trapped waves in the karadere–duzce branch of the north anatolian fault, western turkey. *Geophysical Journal International*, 152(3):699–717, March 01 2003.

[41] Ralph J. Archuleta and Steven M. Day. Dynamic rupture in a layered medium: The 1966 parkfield earthquake. *Bulletin of the Seismological Society of America*, 70(3):671–689, June 01 1980.

[42] Ruth A. Harris and Steven M. Day. Effects of a low-velocity zone on a dynamic rupture. *Bulletin of the Seismological Society of America*, 87(5):1267–1280, October 01 1997.

[43] Yehuda Ben-Zion and Yueqiang Huang. Dynamic rupture on an interface between a compliant fault zone layer and a stiffer surrounding solid. *Journal of Geophysical Research: Solid Earth*, 107(B2):ESE 6–1–ESE 6–13, 2002.

[44] Yihe Huang and Jean-Paul Ampuero. Pulse-like ruptures induced by low-velocity fault zones. *Journal of Geophysical Research: Solid Earth*, 116(B12):– B12307, 2011.

[45] Yihe Huang, Jean-Paul Ampuero, and Don V. Helmberger. Earthquake ruptures modulated by waves in damaged fault zones. *Journal of Geophysical Research: Solid Earth*, 119(4):– 2013JB010724, 2014.

[46] Ralph J. Archuleta. A faulting model for the 1979 imperial valley earthquake. *Journal of Geophysical Research: Solid Earth*, 89(B6):4559–4585, 1984.

[47] Paul Spudich and Edward Cranswick. Direct observation of rupture propagation during the 1979 imperial valley earthquake using a short baseline accelerometer array. *Bulletin of the Seismological Society of America*, 74(6):2083–2114, December 01 1984.

[48] Michel Bouchon, Nafi Toksöz, Hayrullah Karabulut, Marie-Paule Bouin, Michel Dietrich, Mustafa Aktar, and Margaret Edie. Seismic imaging of the 1999 izmit (turkey) rupture inferred from the near-fault recordings. *Geophysical Research Letters*, 27(18):3013–3016, 2000.

[49] Michel Bouchon, Marie-Paule Bouin, Hayrullah Karabulut, M. Nafi Toksöz, Michel Dietrich, and Ares J. Rosakis. How fast is rupture during an earthquake? new insights from the 1999 turkey earthquakes. *Geophysical Research Letters*, 28(14):2723–2726, 2001.

[50] A. Ozgun Konca, Sebastien Leprince, Jean-Philippe Avouac, and Don V. Helmberger. Rupture process of the 1999 mw 7.1 duzce earthquake from joint analysis of spot, gps, insar, strong-motion, and teleseismic data: A supershear rupture with variable rupture velocity. *Bulletin of the Seismological Society of America*, 100(1):267–288, February 01 2010.

[51] Michel Bouchon and Martin Vallée. Observation of long supershear rupture during the magnitude 8.1 kunlunshan earthquake. *Science*, 301(5634):824–826, August 08 2003.

[52] D. P. Robinson, C. Brough, and S. Das. The mw 7.8, 2001 kunlunshan earthquake: Extreme rupture speed variability and effect of fault geometry. *Journal of Geophysical Research: Solid Earth*, 111(B8):– B08303, 2006.

[53] M. Vallée, M. Landès, N. M. Shapiro, and Y. Klinger. The 14 november 2001 kokoxili (tibet) earthquake: High-frequency seismic radiation originating from the transitions between sub-rayleigh and supershear rupture velocity regimes. *Journal of Geophysical Research: Solid Earth*, 113(B7):– B07305, 2008.

[54] Kristoffer T. Walker and Peter M. Shearer. Illuminating the near-sonic rupture velocities of the intracontinental kokoxili mw 7.8 and denali fault mw 7.9 strike-slip earthquakes with global p wave back projection imaging. *Journal of Geophysical Research: Solid Earth*, 114(B2):– B02304, 2009.

[55] Eric M. Dunham and Ralph J. Archuleta. Evidence for a supershear transient during the 2002 denali fault earthquake. *Bulletin of the Seismological Society of America*, 94(6B):S256–S268, December 01 2004.

[56] M. Celebi, R. Kayen, W. L. Ellsworth, J. R. Evans, E. G. Jensen, M. C. Metz, D. J. Nyman, J. W. Roddick, P. Spudich, and C. D. Stephens. Near-field ground motion of the 2002 denali fault, alaska, earthquake recorded at pump station 10. *Earthquake Spectra*, 20(3):597–615, 2004.

[57] Robert Burridge. Admissible speeds for plane-strain self-similar shear cracks with friction but lacking cohesion, December 01 1973.

[58] D. J. Andrews. Rupture velocity of plane strain shear cracks. *Journal of Geophysical Research*, 81(32):5679–5687, 1976.

[59] S. DAS and K. AKI. A numerical study of two-dimensional spontaneous rupture propagation. *Geophysical journal international*, 50(3):643–668, 1977.

[60] SM DAY. 3-dimensional simulation of spontaneous rupture - the effect of nonuniform prestress. *Bulletin of the Seismological Society of America*, 72(6):1881–1902, 1982.

[61] R. Madariaga and K. B. Olsen. Criticality of rupture dynamics in 3-d. *Pure and Applied Geophysics*, 157(11-12):1981–2001, 2000.

[62] E. Fukuyama and K. B. Olsen. A condition for super-shear rupture propagation in a heterogeneous stress field. *Pure and Applied Geophysics*, 159(9):2047–2056, 2002.

[63] G. Festa and J. P Vilotte. Influence of the rupture initiation on the intersonic transition: Crack-like versus pulse-like modes. *Geophysical Research Letters*, 33(15):– L15320, 2006.

[64] Eric M. Dunham. Conditions governing the occurrence of supershear ruptures under slip-weakening friction. *Journal of Geophysical Research: Solid Earth*, 112(B7):– B07302, 2007.

[65] Yi Liu and Nadia Lapusta. Transition of mode ii cracks from sub-rayleigh to intersonic speeds in the presence of favorable heterogeneity. *Journal of the Mechanics and Physics of Solids*, 56(1):25–50, 1 2008.

[66] Zheqiang Shi, Yehuda Ben Zion, Alan Needleman, and Y. BENZION. Properties of dynamic rupture and energy partition in a solid with a frictional interface. *Journal of the Mechanics and Physics of Solids*, 56(1):5–24, 2008.

[67] Nadia Lapusta and Yi Liu. Three-dimensional boundary integral modeling of spontaneous earthquake sequences and aseismic slip. *Journal of geophysical research*, 114(B9), 2009.

[68] Eric G. Daub, M. Lisa Manning, and Jean M. Carlson. Pulse-like, crack-like, and supershear earthquake ruptures with shear strain localization. *Journal of Geophysical Research: Solid Earth*, 115(B5):– B05311, 2010.

[69] Y. Kaneko and N. Lapusta. Supershear transition due to a free surface in 3-d simulations of spontaneous dynamic rupture on vertical strike-slip faults. *Tectonophysics*, 493(3–4):272–284, 10/18 2010.

[70] Sebastian Langer, Louise Olsen-Kettle, and Dion Weatherley. Identification of supershear transition mechanisms due to material contrast at bimaterial faults. *Geophysical Journal International*, 190(2):1169–1180, August 01 2012.

[71] A. A Gabriel, J. P Ampuero, L. A. Dalguer, and P. M. Mai. The transition of dynamic rupture styles in elastic media under velocity-weakening friction. *Journal of Geophysical Research: Solid Earth*, 117(B9):– B09311, 2012.

[72] Andrea Bizzarri. Formulation of a fault governing law at high sliding speeds: Inferences from dynamic rupture models. *Earth and Planetary Science Letters*, 355–356(0):223–230, 11/15 2012.

[73] Andrea Bizzarri and Shamita Das. Mechanics of 3-d shear cracks between rayleigh and shear wave rupture speeds. *Earth and Planetary Science Letters*, 357–358(0):397–404, 12/1 2012.

[74] Jean Elkhoury and Leon Knopoff. Dynamical model of faulting in two dimensions and self-healing of large fractures. *Physical review.E, Statistical, nonlinear, and soft matter physics*, 86(6 Pt 2):066118, 2012.

[75] Anne Le Goff, Pablo Cobelli, and Guillaume Lagubeau. Supershear rayleigh waves at a soft interface. *Physical Review Letters*, 110(23):236101, 2013.

[76] Kenny J. Ryan and David D. Oglesby. Dynamically modeling fault step overs using various friction laws. *Journal of Geophysical Research: Solid Earth*, 119(7):– 2014JB011151, 2014.

[77] B. T. Aagaard, M. G. Knepley, and C. A. Williams. A domain decomposition approach to implementing fault slip in finite-element models of quasi-static and dynamic crustal deformation. *Journal of Geophysical Research: Solid Earth*, 118(6):3059–3079, 2013.

[78] JR Rice and Koji Uenishi. Universal nucleation length for slip-weakening rupture instability under nonuniform fault loading. *Journal of geophysical research*, 108(B1), 2003.

[79] Thomas H. Heaton. Evidence for and implications of self-healing pulses of slip in earthquake rupture. *Physics of the Earth and Planetary Interiors*, 64(1):1–20, 11 1990.

[80] S. Nielsen and R. Madariaga. On the self-healing fracture mode. *Bulletin of the Seismological Society of America*, 93(6):2375–2388, 2003.

[81] A. E. Elbanna. *Pulse like ruptures on strong velocity-weakening frictional interfaces : dynamics and implications. Dissertation (Ph.D.).* California Institute of Technology, Pasadena, CA, U.S., 2011.

[82] K. Aki and P. G. Richards. *Quantitative Seismology.* Univ. Sci.Books, Sausalito, Calif, 2002.

[83] L. B. Freund. *Dynamic Fracture Mechanics.* Cambridge University Press, Cambridge, 1990.

[84] Eric M. Dunham, Pascal Favreau, and J. M. Carlson. A supershear transition mechanism for cracks. *Science*, 299(5612):1557–1559, March 07 2003.

[85] Yoshiaki Ida. Cohesive force across the tip of a longitudinal-shear crack and griffith's specific surface energy. *Journal of Geophysical Research*, 77(20):3796–3805, 1972.

[86] A. C. Palmer and J. R. Rice. The growth of slip surfaces in the progressive failure of over-consolidated clay. *Proceedings of the Royal Society of London.A.Mathematical and Physical Sciences*, 332(1591):527–548, April 03 1973.

[87] James H. Dieterich. Time-dependent friction in rocks. *Journal of Geophysical Research*, 77(20):3690–3697, 1972.

[88] Andy Ruina. Slip instability and state variable friction laws. *Journal of Geophysical Research: Solid Earth*, 88(B12):10359–10370, 1983.

[89] Eric Daub and Jean Carlson. Friction, fracture, and earthquakes, 2010.

[90] A. E. Elbanna and J. M. Carlson. A two-scale model for sheared fault gouge: Competition between macroscopic disorder and local viscoplasticity. *Journal of Geophysical Research: Solid Earth*, 119(6):4841–4859, 2014.

[91] Charles K. C. Lieou, Ahmed Elbanna, Jean Carlson, and Jean M. Carlson. Grain fragmentation in sheared granular flow: Weakening effects, energy dissipation, and strain localization. *Physical review.E, Statistical, nonlinear, and soft matter physics*, 89(2), 2014.

[92] Charles K. C. Lieou, Ahmed Elbanna, J. S. Langer, J. M. Carlson, and J. M. Carlson. Shear flow of angular grains: Acoustic effects and nonmonotonic rate dependence of volume. *Physical review.E, Statistical, nonlinear, and soft matter physics*, 90(3), 2014.

[93] G. Zheng and JR Rice. Conditions under which velocity-weakening friction allows a self-healing versus a cracklike mode of rupture. *Bulletin of the Seismological Society of America*, 88(6):1466–1483, 1998.

[94] J. P Ampuero and Y. Ben-Zion. Cracks, pulses and macroscopic asymmetry of dynamic rupture on a bimaterial interface with velocity-weakening friction. *Geophysical Journal International*, 173(2):674–692, May 01 2008.

[95] Bettina Allmann and Peter Shearer. Global variations of stress drop for moderate to large earthquakes. *Journal of geophysical research*, 114(B1), 2009.

[96] RH SIBSON. Interactions between temperature and pore-fluid pressure during earthquake faulting and a mechanism for partial or total stress relief. *Nature.physical science*, 243(126):66–68, 1973.

[97] Arthur Lachenbruch. Frictional heating, fluid pressure, and the resistance to fault motion. *Journal of geophysical research*, 85(NB11):6097–6112, 1980.

[98] James Rice. Heating and weakening of faults during earthquake slip. *Journal of geophysical research*, 111(B5), 2006.

[99] N. M. Beeler, T. E. Tullis, and D. L. Goldsby. Constitutive relationships and physical basis of fault strength due to flash heating. *Journal of geophysical research*, 113(B1), 2008.

[100] Hiroyuki Noda and Nadia Lapusta. Three-dimensional earthquake sequence simulations with evolving temperature and pore pressure due to shear heating: Effect of heterogeneous hydraulic diffusivity. *Journal of geophysical research*, 115(B12), 2010.

[101] Raehee Han, Takehiro Hirose, Toshihiko Shimamoto, Youngmin Lee, and Jun ichi Ando. Granular nanoparticles lubricate faults during seismic slip. *Geology*, 39(6):599–602, 2011.

[102] Giulio Di Toro, Takehiro Hirose, Stefan Nielsen, Giorgio Pennacchioni, and Toshihiko Shimamoto. Natural and experimental evidence of melt lubrication of faults during earthquakes. *Science*, 311(5761):647–649, 2006.

[103] Hiroyuki Noda, Kyuichi Kanagawa, Takehiro Hirose, and Atsuyuki Inoue. Frictional experiments of dolerite at intermediate slip rates with controlled temperature: Rate weakening or temperature weakening? *Journal of Geophysical Research: Solid Earth*, 116(B7):– B07306, 2011.

[104] Hiroyuki Noda, Eric M. Dunham, and James R. Rice. Earthquake ruptures with thermal weakening and the operation of major faults at low overall stress levels. *Journal of Geophysical Research: Solid Earth*, 114(B7):– B07302, 2009.

[105] Emily Brodsky. Long-range triggered earthquakes that continue after the wave train passes. *Geophysical Research Letters*, 33(15), 2006.

[106] K. R. Felzer and E. E. Brodsky. Decay of aftershock density with distance indicates triggering by dynamic stress. *Nature*, 441(7094):735–738, 2006.

[107] Nicholas J. van der Elst, Emily Brodsky, and Emily E. Brodsky. Connecting near-field and far-field earthquake triggering to dynamic strain. *Journal of geophysical research*, 115(B7), 2010.

[108] Dai F.C. C.Xu and Chen J. Identification and analysis of secondary geological hazards triggered by a magnitude 8.0 wenchuan earthquake. *JOURNAL OF REMOTE SENSING*, 13(4):754–762, 2009.

[109] M. Z. Hossain, C. J Hsueh, B. Bourdin, and K. Bhattacharya. Effective toughness of heterogeneous media. *Journal of the Mechanics and Physics of Solids*, 71(0):15–32, 11 2014.

[110] Xiao Ma and Ahmed Elbanna. Strain localization in dry sheared granular materials: A compactivity-based approach. *Phys. Rev. E*, 98(2):22906, 8 2018.

[111] Anne-Marie Boullier, En-Chao Yeh, Sébastien Boutareaud, Sheng-Rong Song, and Chin-Ho Tsai. Microscale anatomy of the 1999 Chi-Chi earthquake fault zone. *Geochemistry, Geophysics, Geosystems*, 10(3):n/a–n/a, 2009.

[112] Frederick M Chester and Judith S Chester. Ultracataclasite structure and friction processes of the Punchbowl fault, San Andreas system, California. *Tectonophysics*, 295(1-2):199–221, 9 1998.

[113] N De Paola, C Collettini, D R Faulkner, and F Trippetta. Fault zone architecture and deformation processes within evaporitic rocks in the upper crust. *Tectonics*, 27(4):n/a–n/a, 2008.

[114] Michele Fondriest, Steven A F Smith, Giulio Di Toro, Dario Zampieri, and Silvia Mittempergher. Fault zone structure and seismic slip localization in dolostones, an example from the Southern Alps, Italy. *Journal of Structural Geology*, 45:52–67, 2012.

[115] V Heesakkers, S Murphy, and Z Reches. Earthquake Rupture at Focal Depth, Part I: Structure and Rupture of the Pretorius Fault, TauTona Mine, South Africa. *Pure and Applied Geophysics*, 168(12):2395–2425, 12 2011.

[116] Steven A F Smith, Andrea Billi, Giulio Di Toro, and Richard Spiess. Principal Slip Zones in Limestone: Microstructural Characterization and Implications for the Seismic Cycle (Tre Monti Fault, Central Apennines, Italy). *Pure and Applied Geophysics*, 168(12):2365–2393, 12 2011.

[117] N M Beeler, T E Tullis, M L Blanpied, and J D Weeks. Frictional behavior of large displacement experimental faults. *Journal of Geophysical Research: Solid Earth*, 101(B4):8697–8715, 1996.

[118] John M Logan. Brittle phenomena. *Reviews of Geophysics*, 17(6):1121–1132, 1979.

[119] J M Logan. The progression from damage to localization of displacement observed in laboratory testing of porous rocks. *Geological Society, London, Special Publications*, 289(1):75–87, 2007.

[120] Chris Marone. LABORATORY-DERIVED FRICTION LAWS AND THEIR APPLICATION TO SEISMIC FAULTING. *Annual Review of Earth and Planetary Sciences*, 26(1):643–696, 1998.

[121] Chris Marone, C Barry Raleigh, and C H Scholz. Frictional behavior and constitutive modeling of simulated fault gouge. *Journal of Geophysical Research: Solid Earth*, 95(B5):7007–7025, 1990.

[122] Andrew P Rathbun and Chris Marone. Effect of strain localization on frictional behavior of sheared granular materials. *Journal of Geophysical Research: Solid Earth*, 115(B1):n/a–n/a, 2010.

[123] Microscopic and Macroscopic Physics of Earthquakes. In *Geocomplexity and the Physics of Earthquakes*, pages 147–163. American Geophysical Union, 2013.

[124] James R Rice. Heating and weakening of faults during earthquake slip. *Journal of Geophysical Research: Solid Earth*, 111(B5):n/a–n/a, 2006.

[125] John D Platt, John W Rudnicki, and James R Rice. Stability and localization of rapid shear in fluid-saturated fault gouge: 2. Localized zone width and strength evolution. *Journal of Geophysical Research: Solid Earth*, 119(5):4334–4359, 2014.

[126] James R Rice, John W Rudnicki, and John D Platt. Stability and localization of rapid shear in fluid-saturated fault gouge: 1. Linearized stability analysis. *Journal of Geophysical Research: Solid Earth*, 119(5):4311–4333, 2014.

[127] Eric G Daub and Jean M Carlson. Stick-slip instabilities and shear strain localization in amorphous materials. *Phys. Rev. E*, 80(6):66113, 12 2009.

[128] A. M. Hermundstad, E. G. Daub, and J. M. Carlson. Energetics of strain localization in a model of seismic slip. *Journal of Geophysical Research: Solid Earth*, 115(6):1–9, 2010.

[129] Charles K C Lieou, Ahmed E. Elbanna, J. S. Langer, and J. M. Carlson. Shear flow of angular grains: Acoustic effects and nonmonotonic rate dependence of volume. *Physical Review E - Statistical, Nonlinear, and Soft Matter Physics*, 90(3):1–12, 2014.

[130] Konik R Kothari and Ahmed E Elbanna. Localization and instability in sheared granular materials: Role of friction and vibration. *Phys. Rev. E*, 95(2):22901, 2 2017.

[131] Michael L. Falk and James S. Langer. Dynamics of viscoplastic deformation in amorphous solids. *Physical Review E*, 57(6):7192–7205, 1998.

[132] Michael L. Falk and James S. Langer. Deformation and Failure of Amorphous Solidlike Materials. *Annual Review of Condensed Matter Physics*, page 28, 2010.

[133] Charles K C Lieou, Ahmed E. Elbanna, and Jean M. Carlson. Grain fragmentation in sheared granular flow: Weakening effects, energy dissipation, and strain localization. *Physical Review E - Statistical, Nonlinear, and Soft Matter Physics*, 89(2):1–14, 2014.

[134] Charles K. C. Lieou, Ahmed E. Elbanna, and Jean M. Carlson. Dynamic friction in sheared fault gouge: implications of acoustic vibration on triggering and slow slip. *Journal of Geophysical Research: Solid Earth*, 2016.

[135] James H Dieterich. Modeling of rock friction: 1. Experimental results and constitutive equations. *Journal of Geophysical Research: Solid Earth*, 84(B5):2161–2168, 1979.

[136] Andy Ruina. Slip instability and state variable friction laws. *Journal of Geophysical Research: Solid Earth*, 88(B12):10359–10370, 12 1983.

[137] a E Elbanna and J M Carlson. Journal of Geophysical Research : Solid Earth. pages 1–19, 2014.

[138] S F Edwards and R B S Oakeshott. Theory of powders. *Physica A: Statistical Mechanics and its Applications*, 157(3):1080–1090, 1989.

[139] Charles K C Lieou and J. S. Langer. Nonequilibrium thermodynamics in sheared hard-sphere materials. *Physical Review E - Statistical, Nonlinear, and Soft Matter Physics*, 85(6):1–8, 2012.

[140] Eric G. Daub and Jean M. Carlson. A constitutive model for fault gouge deformation in dynamic rupture simulations. *Journal of Geophysical Research*, 113(B12):B12309, 12 2008.

[141] Eric G. Daub, M. Lisa Manning, and Jean M. Carlson. Shear strain localization in elastodynamic rupture simulations. *Geophysical Research Letters*, 35(12):1–5, 2008.

[142] M L Falk and J S Langer. From Simulation to Theory in the Physics of Deformation and Fracture. *MRS Bulletin*, 25(05):40–45, 2000.

[143] M. L. Manning, E. G. Daub, J. S. Langer, and J. M. Carlson. Rate-dependent shear bands in a shear-transformation-zone model of amorphous solids. *Physical Review E - Statistical, Nonlinear, and Soft Matter Physics*, 79(1):1–17, 2009.

[144] M. L. Manning, J. S. Langer, and J. M. Carlson. Strain localization in a shear transformation zone model for amorphous solids. *Physical Review E - Statistical, Nonlinear, and Soft Matter Physics*, 76(5), 2007.

[145] Anael Lemaitre and Jean Carlson. Boundary lubrication with a glassy interface. *Physical Review E - Statistical, Nonlinear, and Soft Matter Physics*, 69(6 1):1–18, 2004.

[146] Eric G. Daub and Jean M. Carlson. Friction, Fracture, and Earthquakes. *Annual Review of Condensed Matter Physics*, 1(1):397–418, 2010.

[147] J. S. Langer and M. L. Manning. Steady-state, effective-temperature dynamics in a glassy material. *Physical Review E - Statistical, Nonlinear, and Soft Matter Physics*, 76(5):1–9, 2007.

[148] Charles K C Lieou, Ahmed E Elbanna, J S Langer, and J M Carlson. Stick-slip instabilities in sheared granular flow: The role of friction and acoustic vibrations. *Phys. Rev. E*, 92(2):22209, 8 2015.

[149] Behrooz Ferdowsi, Michele Griffa, Robert A Guyer, Paul A Johnson, Chris Marone, and Jan Carmeliet. Three-dimensional discrete element modeling of triggered slip in sheared granular media. *Phys. Rev. E*, 89(4):42204, 4 2014.

[150] A N Stroh B.A. Bilby L.R.T. Gardner. Continuous distributions of dislocations and the theory of plasticity. *Proc. XIth ICTAM*, VIII:35–44, 8 1957.

[151] Kroner.E. Kontinuumstheorie der Versetzungen und Eigenspannungen. In *Kontinuumstheorie der Versetzungen und Eigenspannungen*. Springer, 1958.

[152] E H LEE. ELASTIC-PLASTIC DEFORMATION AT FINITE STRAINS. *JOURNAL OF APPLIED MECHANICS*, 36(1):1–&, 1969.

[153] Leonid Pechenik. Dynamics of shear-transformation zones in amorphous plasticity: Nonlinear theory at low temperatures. *Physical Review E - Statistical, Nonlinear, and Soft Matter Physics*, 72(2):1–12, 2005.

[154] J. S. Langer. Shear-transformation-zone theory of plastic deformation near the glass transition. *Physical Review E - Statistical, Nonlinear, and Soft Matter Physics*, 77(2):1–14, 2008.

[155] M E Gurtin, E Fried, and L Anand. *The Mechanics and Thermodynamics of Continua*. The Mechanics and Thermodynamics of Continua. Cambridge University Press, 2010.

[156] J S Langer and M L Manning. Steady-state, effective-temperature dynamics in a glassy material. *Phys. Rev. E*, 76(5):56107, 11 2007.

[157] Eran Bouchbinder and J S Langer. Nonequilibrium thermodynamics of driven amorphous materials. I. Internal degrees of freedom and volume deformation. *Physical Review E*, 80(3):31131, 9 2009.

[158] D. C. Drucker and W. Prager. Soil mechanics and plastic analysis or limit design. *Quarterly of Applied Mathematics*, 10(2):157–165, 1952.

[159] David L Henann and Ken Kamrin. A predictive, size-dependent continuum model for dense granular flows. *Proceedings of the National Academy of Sciences*, 110(17):6730–6735, 2013.

[160] Qiong Zhang and Ken Kamrin. Microscopic Description of the Granular Fluidity Field in Nonlocal Flow Modeling. *Phys. Rev. Lett.*, 118(5):58001, 1 2017.

[161] Derek Gaston, Chris Newman, Glen Hansen, and Damien Lebrun-Grandié. MOOSE: A parallel computational framework for coupled systems of nonlinear equations. *Nuclear Engineering and Design*, 239(10):1768–1778, 2009.

[162] Benjamin S Kirk, John W Peterson, Roy H Stogner, and Graham F Carey. libMesh : a C++ library for parallel adaptive mesh refinement/coarsening simulations. *Engineering with Computers*, 22(3):237–254, 12 2006.

[163] Satish Balay, Shrirang Abhyankar, Mark F. Adams, Jed Brown, Peter Brune, Kris Buschelman, Lisandro Dalcin, Victor Eijkhout, William D. Gropp, Dinesh Kaushik, Matthew G. Knepley, Dave A. May, Lois Curfman McInnes, Karl Rupp, Barry F. Smith, Stefano Zampini, Hong Zhang, and Hong Zhang. {PETS}c {W}eb page. \url{http://www.mcs.anl.gov/petsc}, 2017.

[164] D A Knoll and D E Keyes. Jacobian-free Newton–Krylov methods: a survey of approaches and applications. *Journal of Computational Physics*, 193(2):357–397, 2004.

[165] Joseph E Bowles. *Foundation analysis and design*. McGraw-Hill Education (India) Private Limited, 2012.

[166] Nicholas J. Van Der Elst, Emily E. Brodsky, Pierre Yves Le Bas, and Paul A. Johnson. Auto-acoustic compaction in steady shear flows: Experimental evidence for suppression of shear dilatancy by internal acoustic vibration. *Journal of Geophysical Research: Solid Earth*, 117(9):1–18, 2012.

[167] Eran Bouchbinder and J. S. Langer. Nonequilibrium thermodynamics of driven amorphous materials. I. Internal degrees of freedom and volume deformation. *Physical Review E*, 80(3):031131, 9 2009.

[168] Chris H. Rycroft and Frédéric Gibou. Simulations of a stretching bar using a plasticity model from the shear transformation zone theory. *Journal of Computational Physics*, 231(5):2155–2179, 2012.

[169] B M Carpenter, D M Saffer, and C Marone. Frictional properties of the active San Andreas Fault at SAFOD: Implications for fault strength and slip behavior. *Journal of Geophysical Research: Solid Earth*, 120(7):5273–5289, 2015.

[170] Silvio B Giger, Stephen F Cox, and Eric Tenthorey. Slip localization and fault weakening as a consequence of fault gouge strengthening — Insights from laboratory experiments. *Earth and Planetary Science Letters*, 276(1):73–84, 2008.

[171] Samuel H Haines, Bryan Kaproth, Chris Marone, Demian Saffer, and Ben van der Pluijm. Shear zones in clay-rich fault gouge: A laboratory study of fabric development and evolution. *Journal of Structural Geology*, 51:206–225, 2013.

[172] André Niemeijer, Derek Elsworth, and Chris Marone. Significant effect of grain size distribution on compaction rates in granular aggregates. *Earth and Planetary Science Letters*, 284(3):386–391, 2009.

[173] Chris Marone and C H Scholz. Particle-size distribution and microstructures within simulated fault gouge. *Journal of Structural Geology*, 11(7):799–814, 1989.

[174] Samuel H Haines, Bryan Kaproth, Chris Marone, Demian Saffer, and Ben van der Pluijm. Shear zones in clay-rich fault gouge: A laboratory study of fabric development and evolution. *Journal of Structural Geology*, 51:206–225, 2013.

[175] Karen Mair and Chris Marone. Friction of simulated fault gouge for a wide range of velocities and normal stresses. *Journal of Geophysical Research: Solid Earth*, 104(B12):28899–28914, 1999.

[176] Adam R Hinkle, Chris H Rycroft, Michael D Shields, and Michael L Falk. Coarse graining atomistic simulations of plastically deforming amorphous solids. *Phys. Rev. E*, 95(5):53001, 5 2017.

[177] J R Rice. Inelastic constitutive relations for solids: An internal-variable theory and its application to metal plasticity. *Journal of the Mechanics and Physics of Solids*, 19(6):433–455, 1971.

[178] José E Andrade and Ronaldo I Borja. Capturing strain localization in dense sands with random density. *International Journal for Numerical Methods in Engineering*, 67(11):1531–1564, 2006.

[179] Ronaldo I Borja. Cam-Clay plasticity. Part V: A mathematical framework for three-phase deformation and strain localization analyses of partially saturated porous media. *Computer Methods in Applied Mechanics and Engineering*, 193(48):5301–5338, 2004.

[180] Ronaldo I Borja and José E Andrade. Critical state plasticity. Part VI: Meso-scale finite element simulation of strain localization in discrete granular materials. *Computer Methods in Applied Mechanics and Engineering*, 195(37):5115–5140, 2006.

[181] Thomas Poulet and Manolis Veveakis. A viscoplastic approach for pore collapse in saturated soft rocks using REDBACK: An open-source parallel simulator for Rock mEchanics with Dissipative feedBACKs. *Computers and Geotechnics*, 74:211–221, 2016.

[182] J R Rice and J W Rudnicki. A note on some features of the theory of localization of deformation. *International Journal of Solids and Structures*, 16(7):597–605, 1980.

[183] J W Rudnicki and J R Rice. Conditions for the localization of deformation in pressure-sensitive dilatant materials. *Journal of the Mechanics and Physics of Solids*, 23(6):371–394, 1975.

[184] James R Rice, Nadia Lapusta, and K Ranjith. Rate and state dependent friction and the stability of sliding between elastically deformable solids. *Journal of the Mechanics and Physics of Solids*, 49(9):1865–1898, 2001.

[185] Norman H Sleep, Eliza Richardson, and Chris Marone. Physics of friction and strain rate localization in synthetic fault gouge. *Journal of Geophysical Research: Solid Earth*, 105(B11):25875–25890, 2000.

[186] Antoine Le Bouil, Axelle Amon, Sean McNamara, and Jérôme Crassous. Emergence of Cooperativity in Plasticity of Soft Glassy Materials. *Phys. Rev. Lett.*, 112(24):246001, 6 2014.

[187] Craig E Maloney and Anaël Lema\^\itre. Amorphous systems in athermal, quasistatic shear. *Phys. Rev. E*, 74(1):16118, 7 2006.

[188] Peter Sollich, Fran çLequeux, Pascal Hébraud, and Michael E Cates. Rheology of Soft Glassy Materials. *Phys. Rev. Lett.*, 78(10):2020–2023, 3 1997.

[189] Lallit Anand and Cheng Su. A constitutive theory for metallic glasses at high homologous temperatures. *Acta Materialia*, 55(11):3735–3747, 2007.

[190] A S Argon. Plastic deformation in metallic glasses. *Acta Metallurgica*, 27(1):47–58, 1979.

[191] Frans Spaepen. Homogeneous flow of metallic glasses: A free volume perspective. *Scripta Materialia*, 54(3):363–367, 2006.

[192] Babak Kondori, A Amine Benzerga, and Alan Needleman. Discrete shear-transformation-zone plasticity modeling of notched bars. *Journal of the Mechanics and Physics of Solids*, 111:18–42, 2018.

[193] Shingo Urata and Shaofan Li. A multiscale shear-transformation-zone (STZ) model and simulation of plasticity in amorphous solids. *Acta Materialia*, 155:153–165, 2018.

[194] M L Manning and A J Liu. Vibrational Modes Identify Soft Spots in a Sheared Disordered Packing. *Phys. Rev. Lett.*, 107(10):108302, 8 2011.

[195] Sylvain Patinet, Damien Vandembroucq, and Michael L Falk. Connecting Local Yield Stresses with Plastic Activity in Amorphous Solids. *Phys. Rev. Lett.*, 117(4):45501, 7 2016.

[196] Paul Segall and James R. Rice. Dilatancy, compaction, and slip instability of a fluid-infiltrated fault. *Journal of Geophysical Research: Solid Earth*, 100(B11):22155–22171, 11 1995.

[197] Norman H Sleep. Frictional heating and the stability of rate and state dependent frictional sliding. *Geophysical Research Letters*, 22(20):2785–2788, 1995.

[198] Ken Kamrin and Georg Koval. Nonlocal Constitutive Relation for Steady Granular Flow. *Phys. Rev. Lett.*, 108(17):178301, 4 2012.

[199] Sean R Agnew and Özgür Duygulu. Plastic anisotropy and the role of non-basal slip in magnesium alloy AZ31B. *International Journal of Plasticity*, 21(6):1161–1193, 2005.

[200] M R Barnett. A taylor model based description of the proof stress of magnesium AZ31 during hot working. *Metallurgical and Materials Transactions A*, 34(9):1799–1806, 9 2003.

[201] Akhtar S Khan, Amit Pandey, Thomas Gnäupel-Herold, and Raja K Mishra. Mechanical response and texture evolution of AZ31 alloy at large strains for different strain rates and temperatures. *International Journal of Plasticity*, 27(5):688–706, 2011.

[202] Srihari Kurukuri, Michael J Worswick, Dariush Ghaffari Tari, Raja K Mishra, and Jon T Carter. Rate sensitivity and tension-compression asymmetry in AZ31B magnesium alloy sheet. *PHILOSOPHICAL TRANSACTIONS OF THE ROYAL SOCIETY A-MATHEMATICAL PHYSICAL AND ENGINEERING SCIENCES*, 372(2015, SI), 5 2014.

[203] I Ulacia, N V Dudamell, F Gálvez, S Yi, M T Pérez-Prado, and I Hurtado. Mechanical behavior and microstructural evolution of a Mg AZ31 sheet at dynamic strain rates. *Acta Materialia*, 58(8):2988–2998, 2010.

[204] L Anand and C Gu. Granular materials: constitutive equations and strain localization. *Journal of the Mechanics and Physics of Solids*, 48(8):1701–1733, 2000.

[205] L Anand and C Su. A theory for amorphous viscoplastic materials undergoing finite deformations, with application to metallic glasses. *Journal of the Mechanics and Physics of Solids*, 53(6):1362–1396, 2005.

[206] G Di Toro, D L Goldsby, and T E Tullis. Friction falls towards zero in quartz rock as slip velocity approaches seismic rates. *NATURE*, 427(6973):436–439, 1 2004.

[207] G Di Toro, R Han, T Hirose, N De Paola, S Nielsen, K Mizoguchi, F Ferri, M Cocco, and T Shimamoto. Fault lubrication during earthquakes. *NATURE*, 471(7339):494+, 3 2011.

[208] Raehee Han, Toshihiko Shimamoto, Takehiro Hirose, Jin-Han Ree, and Jun-ichi Ando. Ultralow Friction of Carbonate Faults Caused by Thermal Decomposition. *Science*, 316(5826):878–881, 2007.

[209] T SHIMAMOTO. A new rotary-shear high-speed frictional testing machine : its basic design and scope of research. *Jour. Tectonic Res. Group of Japan*, 39:65–78, 1994.

[210] Behrooz Ferdowsi, Michele Griffa, Robert A Guyer, Paul A Johnson, Chris Marone, and Jan Carmeliet. Acoustically induced slip in sheared granular layers: Application to dynamic earthquake triggering. *Geophysical Research Letters*, 42(22):9750–9757, 2015.

[211] Brett Bode, Michelle Butler, Thom Dunning, Torsten Hoefler, William Kramer, William Gropp, and Wen-mei Hwu. The {B}lue {W}aters Super-System for Super-Science. In *Contemporary High Performance Computing*, Chapman & Hall/CRC Computational Science, pages 339–366. Chapman and Hall/CRC, 4 2013.

[212] William Kramer, Michelle Butler, Gregory Bauer, Kalyana Chadalavada, and Celso Mendes. Blue Waters Parallel I/O Storage Sub-system. In Prabhat and Quincey Koziol, editors, *High Performance Parallel I/O*, pages 17–32. CRC Publications, Taylor and Francis Group, 2015.

[213] David R Scott, Chris J Marone, and Charles G Sammis. The apparent friction of granular fault gouge in sheared layers. *Journal of Geophysical Research: Solid Earth*, 99(B4):7231–7246, 1994.

[214] Xiao Ma, Setare Hajarolasvadi, Gabriele Albertini, David S. Kammer, and Ahmed E. Elbanna. A hybrid finite element-spectral boundary integral approach: Applications to dynamic rupture modeling in unbounded domains. *International Journal for Numerical and Analytical Methods in Geomechanics*, (August):1–22, 2018.

[215] Steven M. Day, Luis a. Dalguer, Nadia Lapusta, and Yi Liu. Comparison of finite difference and boundary integral solutions to three-dimensional spontaneous rupture. *Journal of Geophysical Research*, 110(B12):B12307, 2005.

[216] Brittany A Erickson, Eric M Dunham, and Arash Khosravifar. A Finite Difference Method for Off-fault Plasticity throughout the Earthquake Cycle. *Journal of Mechanics and Physics of Solids*, 2016.

[217] Benchun Duan and Steven M Day. Inelastic strain distribution and seismic radiation from rupture of a fault kink. *Journal of Geophysical Research*, 113(B12):B12311, 12 2008.

[218] Shuo Ma and D J Andrews. Inelastic off-fault response and three-dimensional dynamics of earthquake rupture on a strike-slip fault. *Journal of Geophysical Research*, 115(B4):B04304, 4 2010.

[219] E M Dunham, D Belanger, L Cong, and J E Kozdon. Earthquake Ruptures with Strongly Rate-Weakening Friction and Off-Fault Plasticity, Part 1: Planar Faults. *Bulletin of the Seismological Society of America*, 101(5):2296–2307, 2011.

[220] V M Cruz-Atienza and J Virieux. Dynamic rupture simulation of non-planar faults with a finite-difference approach. *Geophysical Journal International*, 158(3):939–954, 7 2004.

[221] Víctor M Cruz-Atienza, Jean Virieux, and Hideo Aochi. 3D finite-difference dynamic-rupture modeling along nonplanar faults. *GEOPHYSICS*, 72(5):SM123–SM137, 9 2007.

[222] Kenneth Duru and Eric M Dunham. Dynamic earthquake rupture simulations on nonplanar faults embedded in 3D geometrically complex, heterogeneous elastic solids. *Journal of Computational Physics*, 305(C):185–207, 1 2016.

[223] David M Boore, Kenneth L Larner, and Keiiti Aki. Comparison of two independent methods for the solution of wave-scattering problems: Response of a sedimentary basin to vertically incident {<}i{>}SH{<}/i{>} waves. *Journal of Geophysical Research*, 76(2):558–569, 1 1971.

[224] D J Andrews. Rupture propagation with finite stress in antiplane strain. *Journal of Geophysical Research*, 81(20):3575, 1976.

[225] S Das and K Aki. A numerical study of two-dimensional spontaneous rupture propagation. *Geophysical Journal International*, 50(3):643–668, 9 1977.

[226] Ralph J Archuleta and Steven M Day. Dynamic rupture in a layered medium: The 1966 Parkfield earthquake. *Bulletin of the Seismological Society of America*, 70(3):671–689, 1980.

[227] Jean Virieux and Raul Madariaga. Dynamic faulting studied by a finite difference method. *Bulletin of the Seismological Society of America*, 72(2):345–369, 1982.

[228] Y Kaneko, N Lapusta, and J.-P. Ampuero. Spectral element modeling of spontaneous earthquake rupture on rate and state faults: Effect of velocity-strengthening friction at shallow depths. *Journal of Geophysical Research*, 113(B9):B09317, 9 2008.

[229] Ossian O'Reilly, Eric M Dunham, and Jan Nordström. Simulation of Wave Propagation Along Fluid-Filled Cracks Using High-Order Summation-by-Parts Operators and Implicit-Explicit Time Stepping. *SIAM Journal on Scientific Computing*, 39(4):B675–B702, 2017.

[230] J Lysmer and R L Kuhlemeyer. Finite dynamic model for infinite media. *journal of Engineering Mechanics Division*, 95:859–878, 1969.

[231] Peter Bettess. Infinite elements. *International Journal for Numerical Methods in Engineering*, 11(1):53–64, 1977.

[232] Jean-Pierre Berenger. A perfectly matched layer for the absorption of electromagnetic waves, 1994.

[233] Setare Hajarolasvadi and Ahmed E Elbanna. A new hybrid numerical scheme for modelling elastodynamics in unbounded media with near-source heterogeneities. *Geophysical Journal International*, 211(2):851–864, 11 2017.

[234] Yoshiaki Ida. Cohesive force across the tip of a longitudinal-shear crack and Griffith's specific surface energy. *Journal of Geophysical Research*, 77(20):3796–3805, 7 1972.

[235] Junuthula Narasimha Reddy. *An introduction to the finite element method*, volume 2. McGraw-Hill New York, 1993.

[236] Thomas J R Hughes. *The finite element method: linear static and dynamic finite element analysis*. Courier Corporation, 2012.

[237] R Courant, K Friedrichs, and H Lewy. Über die partiellen Differenzengleichungen der mathematischen Physik. *Mathematische Annalen*, 100(1):32–74, 12 1928.

[238] Steven M Day, Luis A Dalguer, Nadia Lapusta, and Yi Liu. Comparison of finite difference and boundary integral solutions to three-dimensional spontaneous rupture. *Journal of Geophysical Research: Solid Earth*, 110(12):1–23, 2005.

[239] M Scot Breitenfeld and Philippe H Geubelle. Numerical analysis of dynamic debonding under 2D in-plane and 3D loading. *International Journal of Fracture*, 93(1-4):13–38, 1998.

[240] R. A. Harris, M. Barall, R. Archuleta, E. Dunham, B. Aagaard, J. P. Ampuero, H. Bhat, V. Cruz-Atienza, L. Dalguer, P. Dawson, S. Day, B. Duan, G. Ely, Y. Kaneko, Y. Kase, N. Lapusta, Y. Liu, S. Ma, D. Oglesby, K. Olsen, A. Pitarka, S. Song, and E. Templeton. The SCEC/USGS Dynamic Earthquake Rupture Code Verification Exercise. *Seismological Research Letters*, 80(1):119–126, 2009.

[241] Gabriele Albertini and David S. Kammer. Off-fault heterogeneities promote supershear transition of dynamic mode II cracks. *Journal of Geophysical Research: Solid Earth*, 122(8):6625–6641, 2017.

[242] Xiao Ma and A. E. Elbanna. Effect of off-fault low-velocity elastic inclusions on supershear rupture dynamics. *Geophysical Journal International*, 203(1):664–677, 2015.

[243] Koji Uenishi and James R. Rice. Universal nucleation length for slip-weakening rupture instability under nonuniform fault loading. *Journal of Geophysical Research: Solid Earth*, 108(B1), 2003.

[244] Robert Burridge. Admissible Speeds for Plane-Strain Self-Similar Shear Cracks with Friction but Lacking Cohesion. *Geophysical Journal of the Royal Astronomical Society*, 35(4):439–455, 1973.

[245] Yihe Huang and Jean-paul Ampuero. Pulse-like ruptures induced by low-velocity fault zones. 116(December):1–13, 2011.

[246] Yihe Huang, Jean-Paul Ampuero, and Don V Helmberger. Earthquake ruptures modulated by waves in damaged fault zones. *Journal of Geophysical Research: Solid Earth*, 119(4):3133–3154, 4 2014.

[247] Yihe Huang, Gregory C Beroza, and William L Ellsworth. Stress drop estimates of potentially induced earthquakes in the Guy-Greenbrier sequence. *Journal of Geophysical Research: Solid Earth*, 121(9):6597–6607, 9 2016.

[248] Xiao Ma and Ahmed Elbanna. A Model for Athermal Strain Localization in Dry Sheared Fault Gouge. 1 2017.

[249] Isaac Harari, Igor Patlashenko, and Dan Givoli. Dirichlet-to-Neumann Maps for Unbounded Wave Guides. *Journal of Computational Physics*, 143(1):200–223, 6 1998.

[250] J Bielak and R C MacCamy. Symmetric finite element and boundary integral coupling methods for fluid-solid interaction. *Quart. Appl. Math.*, 49(1):107–119, 1991.

[251] Eran Bouchbinder and J. S. Langer. Nonequilibrium thermodynamics of driven amorphous materials. II. Effective-temperature theory. *Physical Review E*, 80(3):031132, 9 2009.

[252] James R Rice, Charles G Sammis, and Robert Parsons. Off-fault secondary failure induced by a dynamic slip pulse. *Bulletin of the Seismological Society of America*, 95(1):109–134, 2005.

[253] Elizabeth L Templeton and James R Rice. Off-fault plasticity and earthquake rupture dynamics: 1. Dry materials or neglect of fluid pressure changes. *Journal of Geophysical Research: Solid Earth*, 113(9):1–19, 2008.

[254] Fushen Liu and Ronaldo I Borja. An extended finite element framework for slow-rate frictional faulting with bulk plasticity and variable friction. *International Journal for Numerical and Analytical Methods in Geomechanics*, 33(13):1535–1560.

[255] Fushen Liu and Ronaldo I Borja. Extended finite element framework for fault rupture dynamics including bulk plasticity. *International Journal for Numerical and Analytical Methods in Geomechanics*, 37(18):3087–3111.

[256] Joshua A White and Ronaldo I Borja. Stabilized low-order finite elements for coupled solid-deformation/fluid-diffusion and their application to fault zone transients. *Computer Methods in Applied Mechanics and Engineering*, 197(49):4353–4366, 2008.

[257] Y.-S. Chen, W.-C. Lo, J.-M. Leu, and Alexander H.-D. Cheng. Effect of Impermeable Boundaries on the Propagation of Rayleigh Waves in an Unsaturated Poroelastic Half-Space. *Journal of Mechanics*, 26(4):501–511, 2010.

[258] M J Danyluk, P H Geubelle, and H H Hilton. Two-dimensional dynamic and three-dimensional fracture in viscoelastic materials. *International Journal of Solids and Structures*, 35(28):3831–3853, 1998.

[259] Xiao Ma and Ahmed Elbanna. Dynamic rupture propagation on fault planes with explicit representation of short branches. *Earth and Planetary Science Letters*, 523:115702, 2019.

[260] Frederick M. Chester, James P. Evans, and Ronald L. Biegel. Internal structure and weakening mechanisms of the San Andreas Fault. *Journal of Geophysical Research: Solid Earth*, 98(B1):771–786, 1 1993.

[261] Y. Ben-Zion and C. G. Sammis. Characterization of Fault Zones. *Pure and Applied Geophysics*, 160(3):677–715, 3 2003.

[262] Heather M. Savage and Emily E. Brodsky. Collateral damage: Evolution with displacement of fracture distribution and secondary fault strands in fault damage zones. *Journal of Geophysical Research: Solid Earth*, 116(3), 2011.

[263] Christie D. Rowe, Catherine Ross, Mark T. Swanson, Stephen Pollock, Nils R. Backeberg, Naomi A. Barshi, Charlotte E. Bate, Samantha Carruthers, Sophie Coulson, Kelian Dascher-Cousineau, Nicolas Harrichhausen, Andrés F. Peña Castro, Haylea Nisbet, Paul Rakoczy, Jacek Scibek, Hendrik Smith, Matthew S. Tarling, Alexander Timofeev, and Erik Young. Geometric Complexity of Earthquake Rupture Surfaces Preserved in Pseudotachylyte Networks. *Journal of Geophysical Research: Solid Earth*, 123(9):7998–8015, 9 2018.

[264] D. J. Andrews. Rupture dynamics with energy loss outside the slip zone. *Journal of Geophysical Research*, 110(B1):B01307, 1 2005.

[265] S. Hok, M. Campillo, F. Cotton, P. Favreau, and I. Ionescu. Off-fault plasticity favors the arrest of dynamic ruptures on strength heterogeneity: Two-dimensional cases. *Geophysical Research Letters*, 37(2):n/a–n/a, 1 2010.

[266] E. M. Dunham, D. Belanger, L. Cong, and J. E. Kozdon. Earthquake Ruptures with Strongly Rate-Weakening Friction and Off-Fault Plasticity, Part 1: Planar Faults. *Bulletin of the Seismological Society of America*, 101(5):2296–2307, 10 2011.

[267] Eric M. Dunham, David Belanger, Lin Cong, and Jeremy E. Kozdon. Earthquake ruptures with strongly rate-weakening friction and off-fault plasticity, part 2: Nonplanar faults. *Bulletin of the Seismological Society of America*, 101(5):2308–2322, 2011.

[268] Yehuda Ben-Zion and Zheqiang Shi. Dynamic rupture on a material interface with spontaneous generation of plastic strain in the bulk. *Earth and Planetary Science Letters*, 236(1-2):486–496, 7 2005.

[269] Shiqing Xu, Yehuda Ben-Zion, Jean Paul Ampuero, and Vladimir Lyakhovsky. Dynamic Ruptures on a Frictional Interface with Off-Fault Brittle Damage: Feedback Mechanisms and Effects on Slip and Near-Fault Motion. *Pure and Applied Geophysics*, 0 2015.

[270] Harsha S. Bhat, Ares J. Rosakis, and Charles G. Sammis. A Micromechanics Based Constitutive Model for Brittle Failure at High Strain Rates. *Journal of Applied Mechanics*, 79(3):031016, 2012.

[271] Carsten Uphoff, Sebastian Rettenberger, Michael Bader, Elizabeth H. Madden, Thomas Ulrich, Stephanie Wollherr, and Alice-Agnes Gabriel. Extreme scale multi-physics simulations of the tsunamigenic 2004 sumatra megathrust earthquake. In *Proceedings of the International Conference for High Performance Computing, Networking, Storage and Analysis on - SC '17*, pages 1–16, New York, New York, USA, 2017. ACM Press.

[272] Zheqiang Shi and Steven M Day. Rupture dynamics and ground motion from 3-D rough-fault simulations. *Journal of Geophysical Research: Solid Earth*, 118(3):1122–1141, 3 2013.

[273] Yuval Tal, Bradford H. Hager, and Jean Paul Ampuero. The Effects of Fault Roughness on the Earthquake Nucleation Process. *Journal of Geophysical Research: Solid Earth*, 123(1):437–456, 1 2018.

[274] Nobuki Kame, James R. Rice, and Renata Dmowska. Effects of prestress state and rupture velocity on dynamic fault branching. *Journal of Geophysical Research: Solid Earth*, 108(B5):1–21, 2003.

[275] Harsha S. Bhat, Renata Dmowska, James R. Rice, and Nobuki Kame. Dynamic slip transfer from the Denali to totschunda faults, Alaska: Testing theory for fault branching. *Bulletin of the Seismological Society of America*, 94(6 SUPPL. B):202–213, 2004.

[276] Ronald L. Biegel, Charles G. Sammis, and Ares J. Rosakis. Interaction of a Dynamic Rupture on a Fault Plane with Short Frictionless Fault Branches. *Pure and Applied Geophysics*, 164(10):1881–1904, 10 2007.

[277] Carl-Ernst Rousseau and Ares J. Rosakis. Dynamic path selection along branched faults: Experiments involving sub-Rayleigh and supershear ruptures. *Journal of Geophysical Research*, 114(B8):B08303, 8 2009.

[278] Takehito Suzuki. Damage-tensor-based nondimensional parameters governing secondary faulting behavior. *Tectonophysics*, 600:205–216, 7 2013.

[279] Marieke Rempe, Thomas Mitchell, Jörg Renner, Stuart Nippress, Yehuda Ben-Zion, and Thomas Rockwell. Damage and seismic velocity structure of pulverized rocks near the San Andreas Fault. *Journal of Geophysical Research: Solid Earth*, 118(6):2813–2831, 6 2013.

[280] Yann Klinger, Kurama Okubo, Amaury Vallage, Johann Champenois, Arthur Delorme, Esteban Rougier, Zhou Lei, Earl E. Knight, Antonio Munjiza, Claudio Satriano, Stephane Baize, Robert Langridge, and Harsha S. Bhat. Earthquake Damage Patterns Resolve Complex Rupture Processes. *Geophysical Research Letters*, pages 279–287, 2018.

[281] Ryosuke Ando and Teruo Yamashita. Effects of mesoscopic-scale fault structure on dynamic earthquake ruptures: Dynamic formation of geometrical complexity of earthquake faults. *Journal of Geophysical Research*, 112(B9):B09303, 9 2007.

[282] Setare Hajarolasvadi and Ahmed E. Elbanna. A new hybrid numerical scheme for modelling elastodynamics in unbounded media with near-source heterogeneities. *Geophysical Journal International*, 211(2):851–864, 11 2017.

[283] J. Bielak, Kostas Loukakis, Yoshiaki Hisada, and Chiaki Yoshimura. Domain Reduction Method for Three-Dimensional Earthquake Modeling in Localized Regions, Part I: Theory. *Bulletin of the Seismological Society of America*, 93(2):817–824, 4 2003.

[284] C. Yoshimura, Jacobo Bielak, Yoshiaki Hisada, and Antonio Fernández. Domain Reduction Method for Three-Dimensional Earthquake Modeling in Localized Regions, Part II: Verification and Applications. *Bulletin of the Seismological Society of America*, 93(2):825–841, 4 2003.

[285] N. DeDontney, J. R. Rice, and R. Dmowska. Finite Element Modeling of Branched Ruptures Including Off-Fault Plasticity. *Bulletin of the Seismological Society of America*, 102(2):541–562, 4 2012.

[286] Shiqing Xu, Eiichi Fukuyama, Yehuda Ben-Zion, and Jean-Paul Ampuero. Dynamic rupture activation of backthrust fault branching. *Tectonophysics*, 644-645:161–183, 3 2015.

[287] Yi Liu and Nadia Lapusta. Transition of mode II cracks from sub-Rayleigh to intersonic speeds in the presence of favorable heterogeneity. *Journal of the Mechanics and Physics of Solids*, 56(1):25–50, 1 2008.

[288] David J Wald and Thomas H Heaton. Spatial and temporal distribution of slip for the 1992 Landers, California, earthquake. *Bulletin of the Seismological Society of America*, 84(3):668–691, 6 1994.

[289] Xiaodong Chen. Near-field ground motion from the Landers earthquake. 1 1995.

[290] D. Ngo, Y. Huang, A. Rosakis, W. A. Griffith, and D. Pollard. Off-fault tensile cracks: A link between geological fault observations, lab experiments, and dynamic rupture models. *Journal of Geophysical Research: Solid Earth*, 117(B1):n/a–n/a, 1 2012.

[291] Emily E. Brodsky, James D. Kirkpatrick, and Thibault Candela. Constraints from fault roughness on the scale-dependent strength of rocks. *Geology*, 44(1):19–22, 1 2016.

[292] Simon Preuss, Robert Herrendörfer, Taras Gerya, Jean-Paul Ampuero, and Ylona van Dinther. Seismic and aseismic fault growth lead to different fault orientations. *EarthArXiv*, 2019.

[293] Fushen Liu and Ronaldo I. Borja. An extended finite element framework for slow-rate frictional faulting with bulk plasticity and variable friction. *International Journal for Numerical and Analytical Methods in Geomechanics*, 33(13):1535–1560, 9 2009.

[294] Fushen Liu and Ronaldo I. Borja. Extended finite element framework for fault rupture dynamics including bulk plasticity. *International Journal for Numerical and Analytical Methods in Geomechanics*, 37(18):3087–3111, 12 2013.

[295] Christian Pelties, Josep de la Puente, Jean-Paul Ampuero, Gilbert B Brietzke, and Martin Käser. Three-dimensional dynamic rupture simulation with a high-order discontinuous Galerkin method on unstructured tetrahedral meshes. *Journal of Geophysical Research: Solid Earth*, 117(B2):n/a–n/a, 2 2012.

[296] C. Pelties, A.-A. Gabriel, and J.-P. Ampuero. Verification of an ADER-DG method for complex dynamic rupture problems. *Geoscientific Model Development*, 7(3):847–866, 5 2014.

[297] R.L. Biegel, H.S. Bhat, C.G. Sammis, and A.J. Rosakis. The effect of asymmetric damage on dynamic shear rupture propagation I: No mismatch in bulk elasticity. *Tectonophysics*, 493(3-4):254–262, 10 2010.

[298] Mohamed Ezzeldin Abdelmeguid, Xiao Ma, and Ahmed Elbanna. A Novel Hybrid Finite Element-Spectral Boundary Integral Scheme for Modeling Earthquake Cycles: Application to Rate and State Faults with Low-Velocity Zones. *EarthArXiv*, 2019.

[299] A. Plesch, J. H. Shaw, C. Benson, W. A. Bryant, S. Carena, M. Cooke, J. Dolan, G. Fuis, E. Gath, L. Grant, E. Hauksson, T. Jordan, M. Kamerling, M. Legg, S. Lindvall, H. Magistrale, C. Nicholson, N. Niemi, M. Oskin, S. Perry, G. Planansky, T. Rockwell, P. Shearer, C. Sorlien, M. P. Suss, J. Suppe, J. Treiman, and R. Yeats. Community Fault Model (CFM) for Southern California. *Bulletin of the Seismological Society of America*, 97(6):1793–1802, dec 2007.

[300] Reza Abedi and Robert B. Haber. Riemann solutions and spacetime discontinuous galerkin method for linear elastodynamic contact. *Computer Methods in Applied Mechanics and Engineering*, 270:150 – 177, 2014.

[301] C. T. (Chin-Teh) Sun and Z.-H. Jin. *Fracture mechanics*. Academic Press, 2012.

Appendix A

Driving Force Derivation

We start with the equation of motion of a body in R^3

$$\rho \ddot{u} = \nabla \cdot \sigma \tag{A.1}$$

Multiply both sides by the particle velocity and integrate over the whole volume to get:

$$\begin{aligned} \int_V \rho \ddot{u}_i \dot{u}_i dV &= \int_V \sigma_{ij,j} u_i dV \\ &= \int_V (\sigma_{ij} \dot{u}_i)_{,j} dV - \int_V \sigma_{ij} \dot{u}_{i,j} dV \\ &= \int_{C+\Gamma} \sigma_{ij} \dot{u}_i n_j dV - \int_V \sigma_{ij} \dot{u}_{i,j} dV \end{aligned} \tag{A.2}$$

Where V is the volume of the continuum body bounded in the far field by a contour C and includes a surface of discontinuity within it that is covered by the contour Γ as shown in Figure A.1.

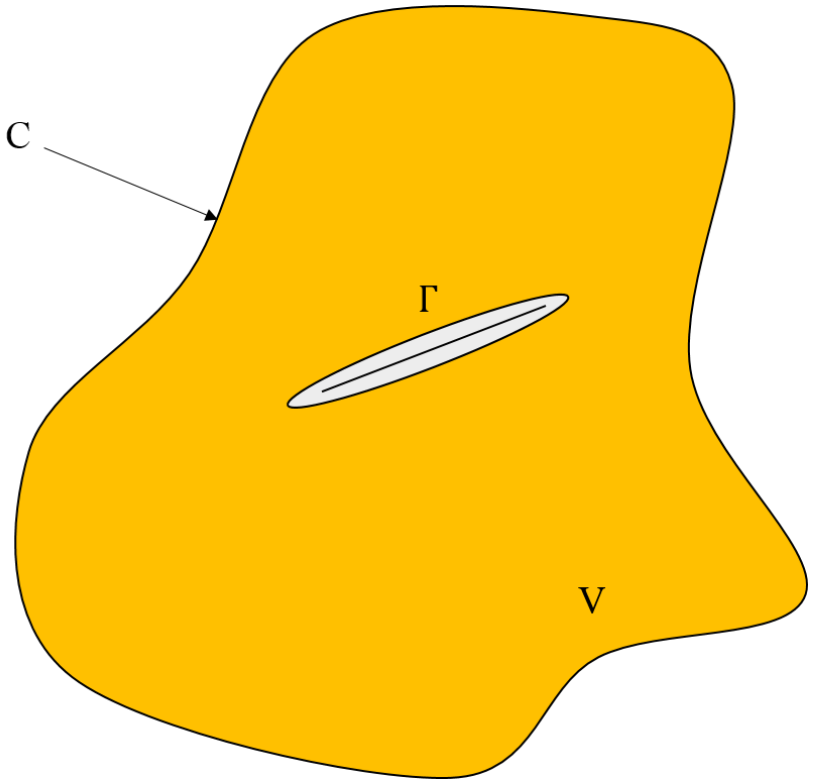

Figure A.1: Arbitrary Domain V with an embedded fault surface Γ. The domain V is bounded by contour C.

Rearranging terms we get:

$$\int_V \rho \ddot{u}_i \dot{u}_i dV + \int_V \sigma_{ij} \dot{u}_{i,j} dV - \int_C \sigma_{ij} \dot{u}_i n_j dV = \int_\Gamma \sigma_{ij} \dot{u}_i n_j dV \tag{A.3}$$

But the total stress is the sum of the initial stress and the elastic stress change:

$$\sigma_{ij} = \sigma^o_{ij} + C_{ijkl} u_{k,l} \tag{A.4}$$

Moreover by using Reynold's transport theorem the rate of change of kinetic energy (T) can be written as:

$$\frac{dT}{dt} = \frac{d}{dt} \int_V \frac{1}{2} \rho \dot{u}_i \dot{u}_i dV = \int_V \rho \ddot{u}_i \dot{u}_i dV + \int_\Gamma \frac{1}{2} \rho \dot{u}_i \dot{u}_i v_r n_j dS \tag{A.5}$$

Where the surface integral is taken only along Γ since C is fixed in space and large enough to include the whole fault. Here v is the velocity by which the contour Γ is moving and n is the normal to contour surface. The normality condition cancels the contribution of the last term in (A.5) for an in-plane shear

rupture. Hence we will drop this term out in the subsequent discussion (If we allow for crack opening then this term will assume nonzero value)

Similarly the rate of change of strain energy (w) can be found from:

$$\begin{aligned}\int_V \sigma_{ij}\dot{u}_{i,j}dV &= \int_V \sigma^o_{ij}\dot{u}_{i,j}dV + \int_V C_{ijkl}u_{k,l}\dot{u}_{i,j}dV \\ &= \int_V \sigma^o_{ij}\dot{u}_{i,j}dV + \frac{d}{dt}\frac{1}{2}\int_V C_{ijkl}u_{k,l}\dot{u}_{i,j}dV \\ &= \int_V \sigma^o_{ij}\dot{u}_{i,j}dV + \frac{dw}{dt}\end{aligned} \tag{A.6}$$

Combining all the above we arrive at the following Power Identify:

$$\frac{dT}{dt} + \frac{dw}{dt} - \int_C \sigma_{ij}\dot{u}_i n_j dS = \int_\Gamma (\sigma_{ij} - \sigma^o_{ij})\dot{u}_i n_j d\Gamma \tag{A.7}$$

We may recognize the contour integral over the far fixed contour C as the rate of change of energy radiation. If C is taken far enough then its contribution to the energy balance during rupture propagation is zero. In this case the energy balance reduces to:

$$\frac{dT}{dt} + \frac{dw}{dt} = \int_\Gamma (\sigma_{ij} - \sigma^o_{ij})\dot{u}_i n_j d\Gamma \tag{A.8}$$

Where

$$T = \frac{1}{2}\int_V \rho\dot{u}_i\dot{u}_i dV \tag{A.9}$$

Is the kinetic energy and

$$w = \frac{1}{2}\int_V C_{ijkl}u_{k,l}u_{i,j}dV \tag{A.10}$$

Is the strain energy for a linearly elastic solid.

In 2D domain the discontinuous surface will reduce to a line, and rate of change of the driving force is given by the following formula:

$$\frac{dF}{dt} = \frac{1}{l}\int_0^l (\tau_o - \tau)\dot{u}dx \tag{A.11}$$

In (A.11) the work rate integral was normalized by l which is the instantaneous crack length.

Appendix B

Stress (material model) update algorithm

Here we describe the algorithm for the plastic strain rate and stress (material model) update in the Moose framework.

Algorithm 1: Stress (material model) update

for $t < t_{total}$ **do**
  At time $t = t_n$, χ_n, u_{x_n}, u_{y_n} are known
  Calculate $\dot{\chi}_n$, the total deformation gradient $\mathbf{F}_n$
  Calculate equivalent stress $\bar{s}$ and the yield strength s_0
  if $\bar{s} - s_0 > 0$ *(plasticity)* **then**
    Formulate the residual for each plastic strain rate: $R^i_{j+1} = \dot{\lambda}^i_j - \dot{\lambda}^i_{j+1}$
    while $|R| \geq tolerance$ **do**
      Formulate Jacobian: $jac = \frac{dR}{d\dot{\lambda}}$
      Newton-Raphson Solve for $\dot{\lambda}^i_{j+1}$
      Update plastic deformation gradient: $\mathbf{F}^p$
      Update elastic deformation gradient: $\mathbf{F}^e = \mathbf{F}\mathbf{F}^{p^{-1}}$
      Update Cauchy-Green Strain tensor: $\mathbf{C}^e = \mathbf{F}^{e^T}\mathbf{F}^e$
      Update Green-Lagrangian Strain tensor: $\mathbf{E}^e = \frac{1}{2}(\mathbf{C}^e - \mathbf{I})$
      Update Pk2 Stress: $\mathbf{T} = \mathbf{L} : \mathbf{E}^e$
      Update Cauchy Stress: $\sigma = J^{e^{-1}}\mathbf{F}^e : \mathbf{T} : \mathbf{F}^{e^T}$
    end while
  else *elasticity*
    Update Pk2 Stress: $\mathbf{T} = \mathbf{L} : \mathbf{E}^e$
    Update Cauchy Stress: $\sigma = J^{e^{-1}}\mathbf{F}^e : \mathbf{T} : \mathbf{F}^{e^T}$
  end if
  Calculate the updated χ_{n+1}, the displacement $u_{x_{n+1}}$, $u_{y_{n+1}}$ through Residual equation

$$\mathbf{R} = \begin{bmatrix} R_\chi \\ R_u \end{bmatrix} = 0$$

  The terms in the Residual equations are provided to **Moose** through **Kernel**

$$R_\chi = \underbrace{\int_\Omega \dot{\chi}\phi dV}_{\text{HeatTimeDerivative } \mathbf{Kernel}} - \underbrace{\int_\Omega (1 - \frac{\chi}{\hat{\chi}})(\frac{\mathbf{s} : \mathbf{D}^p_{dev}}{Pc_o})\phi dV}_{\text{HeatSource } \mathbf{Kernel}}$$

$$R_u = \underbrace{\int_\Omega (\nabla \cdot \sigma)\phi dV}_{\text{Stress Divergence } \mathbf{Kernel}} - \underbrace{\int_\Omega \rho\ddot{u}\phi dV}_{\text{Inertia } \mathbf{Kernel}}$$

end for

Appendix C

Traction-at-Split-Node method

The traction-at-split node (TSN) method presented here is adopted from [238] with modifications for the 2D in-plane problem.

As shown in Fig. C.1, a given fault plane node is split into plus- and minus-side parts. The interaction between the two half-split nodes is only through the traction acting on the interface between them. The plus- and minus-side nodes have respective masses of M^+ and M^- and experience the elastic restoring forces f^+ and f^-. At time $t + \Delta t/2$, D'Alembert's principle leads to a force balance, including the inertial force for each split node. When the central difference scheme is used in time, the velocity $\dot{u}_v^{\pm}(t + \Delta t/2)$ and displacement $u_v^{\pm}(t + \Delta t)$ components at the arbitrary split nodes (i, j) are:

$$\dot{u}_v^{\pm}(t + \Delta t/2) = \dot{u}_v^{\pm}(t - \Delta t/2) + \Delta t(M^{\pm})^{-1} \cdot \{f_v^{\mp}(t) \mp aT_v(t) \pm aT_v^0\} \tag{C.1}$$

$$u_v^{\pm}(t + \Delta t) = u_v(t) + \Delta t\dot{u}_v^{\pm}(t + \Delta t/2) \quad v = x_1, x_2 \tag{C.2}$$

where a is the area of the fault surface associated with the split node at (j,k), Δt is the time step, T_v is the fault plane traction vector at node (j,k), and T_v^0 is the initial equilibrium value of T_v.
By enforcing the continuity of the tangential velocity ($\dot{u}_1^+ - \dot{u}_1^- = 0$) and the continuity of normal displacement ($u_2^+ - u_2^- = 0$) and plugging Eq. C.1 and Eq. C.2 into the two continuity equations, we were able to derive the sticking traction $\tilde{T}_1$ and $\tilde{T}_2$ as follows:

$$\tilde{T}_1 = \frac{\Delta t^{-1}M^+M^-(\dot{u}_1^+ - \dot{u}_1^-) + M^-f_1^+ - M^+f_1^-}{a(M^+ + M^-)} + T_1^0 \tag{C.3}$$

$$\tilde{T}_2 = \frac{\Delta t^{-1}M^+M^-[(\dot{u}_2^+ - \dot{u}_2^-) + \Delta t^{-1}(u_2^+ - u_2^-)] + M^-f_2^+ - M^+f_2^-}{a(M^+ + M^-)} + T_2^0 \tag{C.4}$$

The jumping condition of the fault will be satisfied if the fault traction T_v is:

$$T_v = \begin{cases} \tilde{T}_1, & v = x_1, \quad \tilde{T}_1 \leq \tau_f \\ \tau_c, & v = x_1 \quad \tilde{T}_1 > \tau_f \\ \tilde{T}_2, & v = x_2, \quad \tilde{T}_2 \leq 0 \\ 0, & v = x_2, \quad \tilde{T}_2 > 0 \end{cases} \tag{C.5}$$

The formulation above enforces the jump and parallel conditions for the fault. It also governs the fault behavior at all times, such as at nucleation, arrest of rupture, and subsequent reactivation and arrest of rupture.

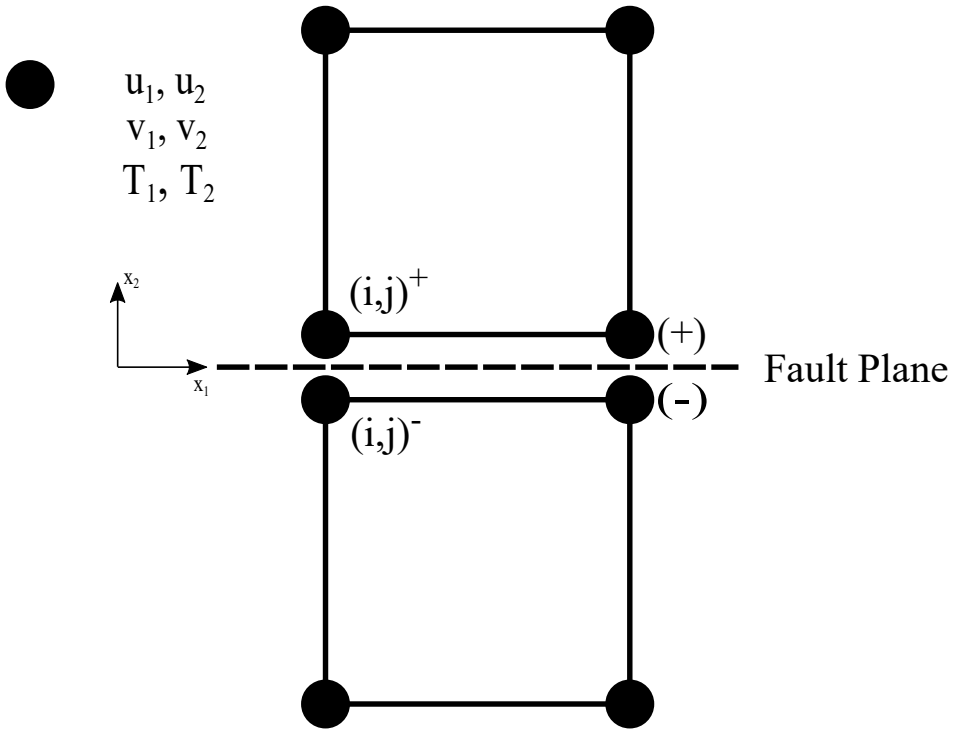

Figure C.1: Illustration of the traction-at-split-node method. The node (i,j) indicates the nodes on the fault. The displacements u_1, u_2 are the displacements in two directions at the fault nodes, the velocities v_1, v_2 are the velocities in two directions at the fault nodes, and the stresses T_1, T_2 are the stresses in two directions at the fault nodes.

Appendix D

Independent Spectral Formulation

The material in this section is extensively borrowed from [239], in which a more general treatment of the problem is provided.

$$u_1(x_1, x_2, t) = \phi_{,1}(x_1, x_2, t) + \psi_{,2}(x_1, x_2, t) \tag{D.1}$$

$$u_2(x_1, x_2, t) = \phi_{,2}(x_1, x_2, t) - \psi_{,1}(x_1, x_2, t) \tag{D.2}$$

where

$$c_p^2 \Delta\phi = \frac{\partial^2 \phi}{\partial t^2}, \quad c_s^2 \Delta\psi = \frac{\partial^2 \psi}{\partial t^2}$$

We examine one particular spectral component:

$$[\phi(x_1, x_2, t), \psi(x_1, x_2, t)] = e^{iqx_1}[\Phi(x_2, t; q), \Psi(x_2, t; q)] \tag{D.3}$$

The Laplace transform of a function f is introduced as

$$\hat{f}(p) = L[f(t)] = \int_0^\infty e^{-pt} f(t) \mathrm{d}t$$

Therefore,

$$\begin{aligned} \frac{\partial^2 \hat{\Phi}}{\partial x_2^2}(x_2, p; q) &= q^2 \alpha_p^2 \hat{\Phi}(x_2, p; q) \\ \frac{\partial^2 \hat{\Psi}}{\partial x_2^2}(x_2, p; q) &= q^2 \alpha_s^2 \hat{\Psi}(x_2, p; q) \end{aligned} \tag{D.4}$$

where

$$\alpha_p = \sqrt{1 + \frac{p^2}{q^2 c_p^2}}, \quad \alpha_s = \sqrt{1 + \frac{p^2}{q^2 c_s^2}}$$

For $x_2 > 0$

$$\hat{\Phi}(x_2, p; q) = \hat{\Phi}_0(p; q) e^{-|q|\alpha_p x_2} \tag{D.5}$$

$$\hat{\Psi}(x_2, p; q) = \hat{\Psi}_0(p; q) e^{-|q|\alpha_s x_2} \tag{D.6}$$

Substituting Eq. D.5 and Eq. D.6 in Eq. D.1 and Eq. D.2 gives

$$\begin{aligned} \hat{u}_1(x_1, x_2, t) &= e^{iqx_1} \left(iq\hat{\Phi}_0(p; q) e^{-|q|\alpha_p x_2} - |q|\alpha_s \hat{\Psi}_0(p; q) e^{-|q|\alpha_s x_2} \right) \\ \hat{u}_2(x_1, x_2, t) &= e^{iqx_1} \left(-|q|\alpha_p \hat{\Phi}_0(p; q) e^{-|q|\alpha_p x_2} - iq\hat{\Psi}_0(p; q) e^{-|q|\alpha_s x_2} \right) \end{aligned} \tag{D.7}$$

We are primarily concerned with tractions along $x_2 = 0$. Therefore,

$$u_j(x_1, x_2 = 0^+, t) = U_j(t; q) e^{iqx_1} \tag{D.8}$$

Thus,

$$\hat{U}_1(p; q) = iq\hat{\Phi}_0(p; q) - |q|\alpha_s \hat{\Psi}_0(p; q) \tag{D.9}$$

$$\hat{U}_2(p; q) = -|q|\alpha_p \hat{\Phi}_0(p; q) - iq\hat{\Psi}_0(p; q) \tag{D.10}$$

Solving for $\hat{\Phi}_0(p; q)$ and $\hat{\Psi}_0(p; q)$ yields

$$\hat{\Phi}_0(p; q) = \frac{-iq\hat{U}_1(p; q) + |q|\alpha_s \hat{U}_2(p; q)}{q^2(1 - \alpha_s\alpha_p)}, \quad \hat{\Psi}_0(p; q) = \frac{|q|\alpha_p \hat{U}_1(p; q) + iq\hat{U}_2(p; q)}{q^2(1 - \alpha_s\alpha_p)} \tag{D.11}$$

$$\begin{aligned} \hat{u}_1 = e^{i|q|x_1} \Bigg\{ & \hat{U}_1(p; q) \frac{e^{-|q|\alpha_p x_2} - \alpha_s\alpha_p e^{-|q|\alpha_s x_2}}{1 - \alpha_s\alpha_p} \\ & + \hat{U}_2(p; q) \frac{iq\alpha_s}{|q|(1 - \alpha_s\alpha_p)} (e^{-|q|\alpha_p x_2} - e^{-|q|\alpha_s x_2}) \Bigg\} \end{aligned} \tag{D.12}$$

$$\begin{aligned} \hat{u}_2 = e^{i|q|x_1} \Bigg\{ & \hat{U}_1(p; q) \frac{iq\alpha_p}{|q|(1 - \alpha_s\alpha_p)} (e^{-|q|\alpha_p x_2} - e^{-|q|\alpha_s x_2}) \\ & + \hat{U}_2(p; q) \frac{e^{-|q|\alpha_s x_2} - \alpha_s\alpha_p e^{-|q|\alpha_p x_2}}{1 - \alpha_s\alpha_p} \Bigg\} \end{aligned} \tag{D.13}$$

Using the stress-strain relation $\sigma_{ij} = \lambda\delta_{ij}u_{k,k} + \mu(u_{i,j} + u_{j,i})$ and writing the shear stress components along the fault as $\tau_j(x_1, t) = \sigma_{2j}(x_1, x_2 = 0^+, t) = T_j(t; q)e^{iqx_1}$ yields

$$\hat{T}_1(p; q) = -\mu|q| \frac{\alpha_p(1 - \alpha_s^2)}{1 - \alpha_s\alpha_p} \hat{U}_1(p; q) + i\mu q \Big(2 - \frac{1 - \alpha_s^2}{1 - \alpha_s\alpha_p} \Big) \hat{U}_2(p; q) \tag{D.14}$$

$$\hat{T}_2(p; q) = -i\mu q \Big(2 - \frac{1 - \alpha_s^2}{1 - \alpha_s\alpha_p} \Big) \hat{U}_1(p; q) - \mu|q| \frac{\alpha_s(1 - \alpha_s^2)}{1 - \alpha_s\alpha_p} \hat{U}_2(p; q) \tag{D.15}$$

Decoupling the equations and extracting the instantaneous response gives

$$\hat{T}_1(p;q) = -\frac{\mu}{c_s} p\hat{U}_1(p;q) - \mu\Big\{|q|\frac{4\alpha_s\alpha_p - (1+\alpha_s^2)}{\alpha_s(1-\alpha_s^2)} - \frac{p}{c_s}\Big\}\hat{U}_1(p;q) \tag{D.16}$$

$$\hat{T}_2(p;q) = -\frac{(\lambda+2\mu)}{c_p} p\hat{U}_1(p;q) - \Big\{|q|\mu\frac{4\alpha_s\alpha_p - (1+\alpha_s^2)}{\alpha_p(1-\alpha_s^2)} - \frac{\lambda+2\mu}{c_s} p\Big\}\hat{U}_2(p;q) \tag{D.17}$$

for the upper half-plane. Similar expressions can be obtained for the lower half-plane. In the time domain, these relationships translate to

$$\begin{aligned}
\tau_1^{\pm}(x_1,t) &= \tau_0(x_1,t) \mp \frac{\mu}{c_s}\frac{\partial u_1^{\pm}}{\partial t} + f_1^{\pm}(x_1,t),\\
\tau_2^{\pm}(x_1,t) &= \tau_0(x_1,t) \mp \frac{(\lambda+2\mu)}{c_p}\frac{\partial u_2^{\pm}}{\partial t} + f_2^{\pm}(x_1,t),
\end{aligned} \tag{D.18}$$

where f is a linear functional of the prior deformation history and can be expressed in terms of its spectral components as $f_j(x_1,t) = F_j(t;q)e^{iqx_1}$. These components are given in [239] as

$$\begin{aligned}
F_1^{\pm}(t;q) =& \mp \mu|q| \int_0^t H_{11}(|q|c_s t')U_1^{\pm}(t-t';q)|q|c_s \mathrm{d}t' + i(2-\eta)\mu q U_2^{\pm}(t;q)\\
&+ i\mu q \int_0^t H_{12}(|q|c_s t')U_2^{\pm}(t-t;q)|q|c_s \mathrm{d}t',\\
F_2^{\pm}(t;q) =& \mp \mu|q| \int_0^t H_{22}(|q|c_s t')U_2^{\pm}(t-t';q)|q|c_s \mathrm{d}t' - i(2-\eta)\mu q U_1^{\pm}(t;q)\\
&- i\mu q \int_0^t H_{12}(|q|c_s t')U_1^{\pm}(t-t';q)|q|c_s dt',
\end{aligned} \tag{D.19}$$

where $\eta = c_p/c_s$ and H_{ij} are the convolution kernels, which are defined by the following inverse Laplace transforms

$$\begin{aligned}
H_{11}(T) =& L^{-1}\left[\frac{s^2\sqrt{s^2+\eta^2}}{\sqrt{s^2+\eta^2}\sqrt{s^2+1}-\eta} - s\right],\\
H_{12}(T) =& L^{-1}\left[\frac{\eta s^2}{\eta - \sqrt{s^2+\eta^2}\sqrt{s^2+1}} + \eta\right],\\
H_{22}(T) =& L^{-1}\left[\frac{s^2\sqrt{s^2+1}}{\sqrt{1+s^2/\eta^2}\sqrt{s^2+1}-1} - \eta s\right],
\end{aligned} \tag{D.20}$$

where $s = p/|q|c_s$ is the nondimensional Laplace transform variable. The kernels can be inverted numerically.

Appendix E

Linear Elastic Fracture Mechanics analysis on the stress perturbation on the main fault

Here we present an example calculation of using Linear Elastic Fracture Mechanics to predict the stress perturbation pattern on the main fault due to the presence of a secondary fault in its vicinity. We idealize the secondary fault as a Mode II finite length crack in an infinite domain. From [301], the stress distribution around the crack tip in this case is given by Eq. E.1

$$\begin{aligned}
\sigma_{xx} &= -\frac{K_{II}}{\sqrt{2\pi r}} \sin\frac{\phi}{2}(2 + \cos\frac{\phi}{2}\cos\frac{3\phi}{2}) \\
\sigma_{yy} &= \frac{K_{II}}{\sqrt{2\pi r}} \sin\frac{\phi}{2}\cos\frac{\phi}{2}\cos\frac{3\phi}{2} \\
\sigma_{xy} &= \frac{K_{II}}{\sqrt{2\pi r}} \cos\frac{\phi}{2}(1 - \sin\frac{\phi}{2}\sin\frac{3\phi}{2})
\end{aligned} \tag{E.1}$$

where K_{II} is the stress intensity factor for Mode II fracture. ϕ and r are the angle and radius in the polar coordinate system. The geometry model is defined as shown in Fig. E.1.

From Eq. E.1, we compute the stress tensor σ from which we may compute the normal traction component σ_n and the tangential component τ on the main fault as given by Eq. E.2:

$$\begin{aligned}
\mathbf{T} &= \sigma\mathbf{n} \\
\sigma_N &= \mathbf{T}\cdot\mathbf{n} \\
\tau &= \sqrt{|\mathbf{T}|^2 - \sigma_N}
\end{aligned} \tag{E.2}$$

Where $\mathbf{n}$ is the vector normal to plane of the main fault. The results are plotted in Fig. E.2, and give a pattern for the stress perturbation expected from a branch that qualitatively agrees with the numerical results shown in the study.

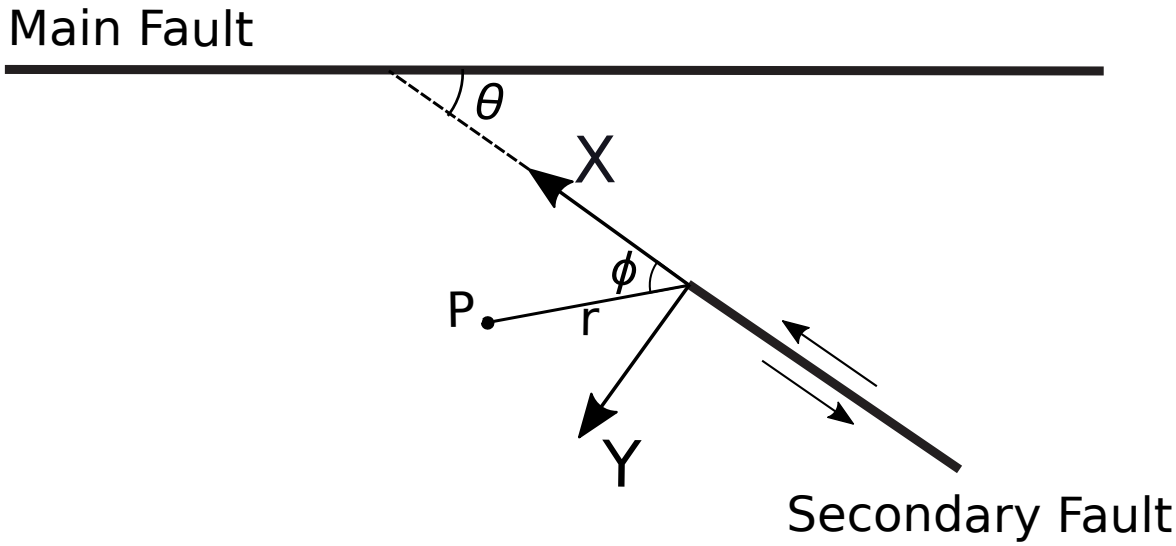

Figure E.1: Model geometry setup for Linear Elastic Fracture Mechanics analysis. The origin of the coordinate system is set at the near end of the secondary fault. The polar coordinates are defined with radius r and angle ϕ. The angle between the main fault and the secondary fault is θ. The shear on the secondary fault is left lateral.

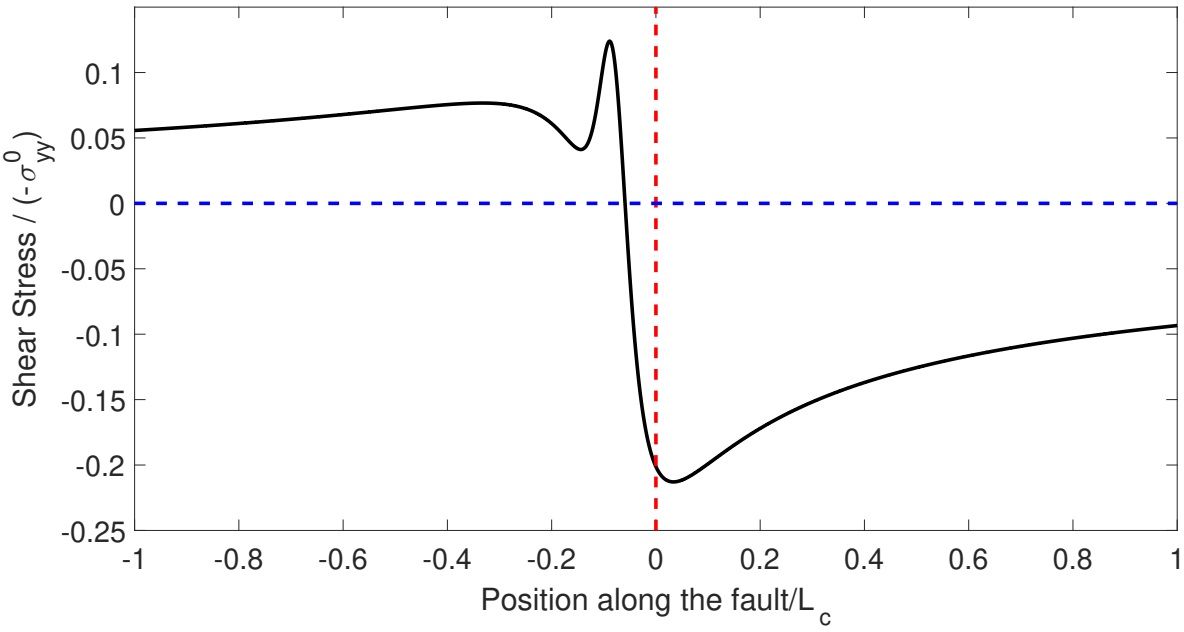

(a)

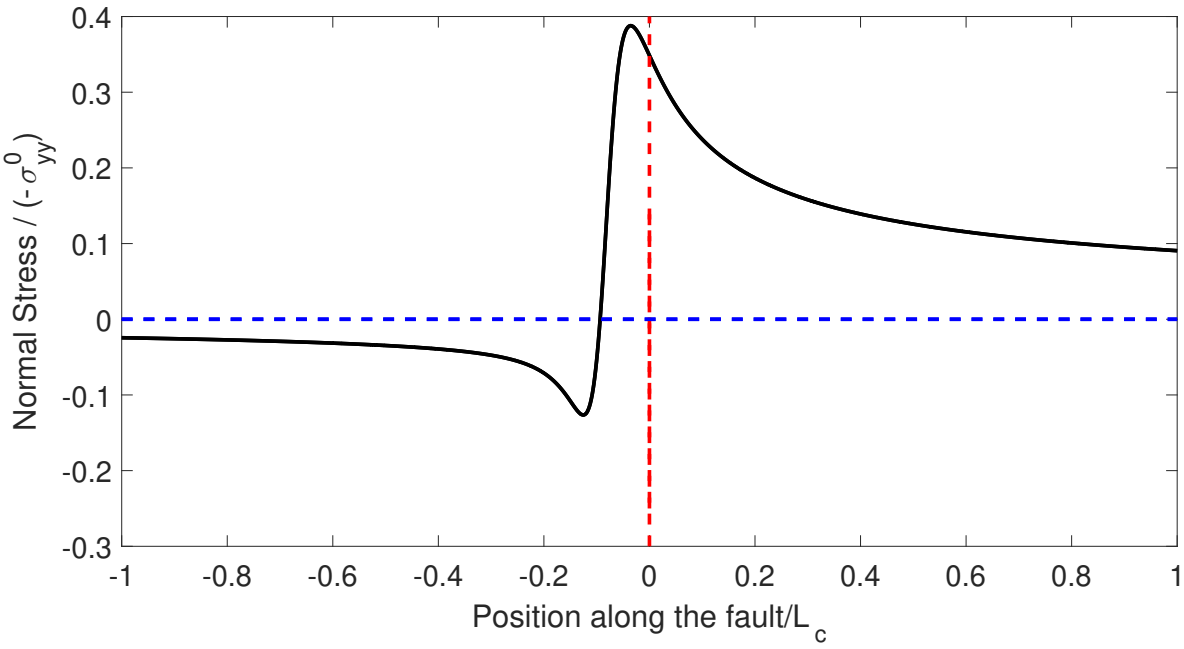

(b)

Figure E.2: Shear and normal stress distribution along the main fault by applying LEFM analysis at the near end of the secondary fault. The secondary fault is located near the position 0 (indicated by the red dash line). The sign of the shear and normal stress switches around the secondary fault position (indicated by the blue dash line). The LEFM analysis gives a stress perturbation pattern that is in qualitative agreement with the results from numerical simulations.